Modeling and simulation of general imperfect interfaces using phase-field-theory

von der Fakultät Maschinenbau
der Technischen Universität Dortmund
zur Erlangung des akademischen Grades

Doktor-Ingenieur (Dr.-Ing.)

genehmigte Dissertation

von

Henning Lammen

aus Dortmund

Vorsitz:	Prof. Dr.-Ing. U. A. Handge
Referent:	Prof. Dr.-Ing. J. Mosler
Korreferenten:	Prof. Dr. S. Conti
	apl. Prof. PD Dr.-Ing. A. Zabel
Tag der Einreichung:	11.10.2024
Tag der mündlichen Prüfung:	07.03.2025

Bibliografische Information Der Deutschen Bibliothek
Die Deutsche Bibliothek verzeichnet diese Publikation in der Deutschen Nationalbibliografie; detaillierte bibliografische Daten sind im Internet über **http://dnb.d-nb.de/** abrufbar.

Bibliographic information published by Die Deutsche Bibliothek
Die Deutsche Bibliothek lists this publication in the Deutsche Nationalbibliografie; detailed bibliographic data is available in the Internet at **http://dnb.d-nb.de/**.

Schriftenreihe des Instituts für Mechanik

Herausgeber: Institut für Mechanik
Fakultät Maschinenbau
Technische Universität Dortmund
Leonhard-Euler-Str. 5
D-44227 Dortmund

Druck: Koffler DruckManagement GmbH

Als Manuskript gedruckt. Printed in Germany.

ISSN 2191-0022
ISBN 978-3-947323-52-4

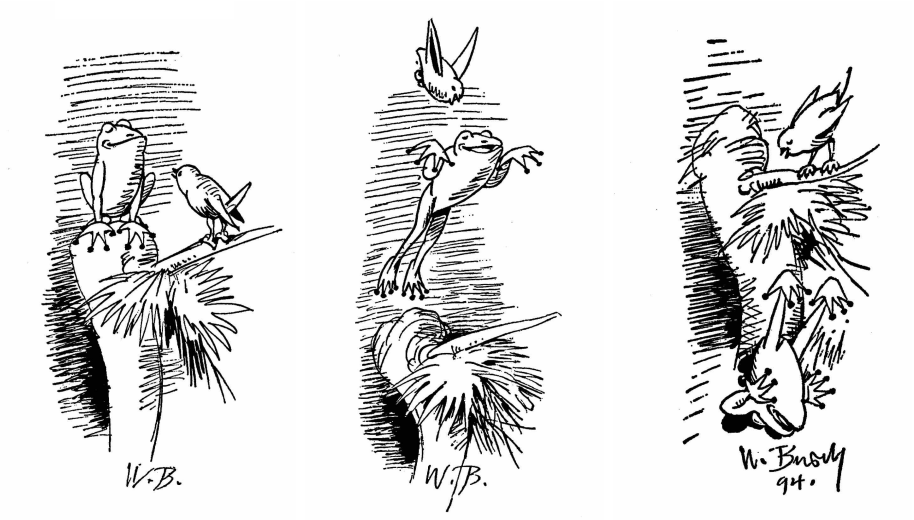

"Wenn einer, der mit Mühe kaum
Geklettert ist auf einen Baum,
Schon meint, daß er ein Vogel wär,
So irrt sich der."

Wilhelm Busch (1832 – 1908)

Acknowledgements

This thesis including its research was developed at my time as a PhD student at the Institute of Mechanics from 2018 to 2024. During my work I was fortunate to be surrounded by encouraging and supporting people. With the help of these, I have grown personally and scientifically, enabling me to finalize this thesis. I would like to use the following paragraphs to express my gratitude to all those who have accompanied me along the way.

First of all I would like to thank my doctoral supervisor and mentor, Prof. Jörn Mosler. You encouraged me to follow my ideas and continuously supported me scientifically and personal during my work. Your open office door and our inspiring discussions were a great driving force behind this work. Additionally, I would link to thank Prof. Sergio Conti for accepting to follow this thesis with joint scientific research and as co-referee of the examination. I enjoyed the synergy and the warm atmosphere at our fruitful meetings. I also thank Prof. Andreas Zabel for being the third referee of the examination committee as well as Prof. Ulrich Handge for chairing the examination.

I would especially like to thank the whole team of the Institute of Mechanics. The congenial working atmosphere at the Institute has made the last few years special and will always remain in my memory. I especially enjoyed the joint social events like the Christmas parties, our institute trips or the evenings at conferences. In particular, my gratitude goes to Prof. Andreas Menzel, who contributed a great share of this atmosphere with his calm and open style , to Kerstin Walter and Christina “Tina” McDonagh for helping in many administrative tasks and for organizing and filling many of the social events and to Matthias Weiß for his support regarding hardware and software.

My sincere thank goes to Dr. Kai Langenfeld and Dr. Christian Sievers for the enjoyable time spent together in the shared office as well as to Nils Cwiekala, PhD, Dr. Fabian Guhr, Dr. Isabelle Noll, Tillmann Wiegold and Hendrik Wilbür for many Doppelkopf evenings and the shared memories in our Bachelors, Masters and doctoral studies. In addition, I would like to thank Dr. Serhat Aygün, Dr. Thorsten Bartel, Dr. Rolf Bertelsen, Merlin Bödecker, Samuel Brabender, Dr. Karsten Buckmann, Klas Feike, Volker Fohrmeister, Tim Furlan, Gian-Luca Geuken, Dilek Güzel, Marius Harnisch, Dr. Tim Heitbreder, Dr. Raphael Holtermann, Dr. Tobias Kaiser, Dr. Patrick Kurzeja, Alexander Niehüser, Justice Olatunbosun, Prof. Richard Ostwald, Felix Rörentrop, Dr. Lars Rose, Markus Schewe, Dr. Robin Schulte, Lennard Sobisch, Dr. Leon Sprave and Dr. Carina Witt.

Finally, I would like to thank my friends and family for their unconditional support, understanding and love throughout my academic journey and beyond. Without your encouragement, I would not have had this great opportunity. Time with you is always both, a refreshing break and a source of motivation for me.

Dortmund, Mai 2025 Henning Lammen

Zusammenfassung

Mechanische Grenzflächen auf der Mikroskala beeinflussen die effektiven makroskopischen Eigenschaften von Materialien in verschiedenen Formen wie Scherbändern oder Korngrenzen in Nanomaterialien. Auf der makroskopischen Skala treten Grenzflächen zum Beispiel in Form von Rissen oder Grenzen von tektonischen Platten auf.

Mechanische Grenzflächen können als kohärent oder nicht kohärent charakterisiert werden. Während das Verschiebungsfeld bei kohärenten Grenzflächen stetig ist treten bei nicht kohärenten Grenzflächen Diskontinuitäten auf. Kohärente Grenzflächen können durch ein zusätzliches konstitutives Modell abhängig von der Verformung der Grenzfläche beschrieben werden. Ein typisches Beispiel ist die Hyperelastizität. Durch die entstehenden tangentialen Spannungen in der Grenzfläche sind Sprünge im Spannungsvektor möglich. Ist diese Energie der kohärenten Grenzfläche konstant spricht man von perfekten Grenzflächen. Für perfekte Grenzflächen ist sowohl das Verschiebungsfeld als auch das Feld der Spannungsvektoren stetig. Nicht kohärente Grenzflächen hingegen lassen sich als Kohäsivzonen oder generalisierte Grenzflächen beschreiben. Für Kohäsivzonen ist das Grenzflächenmodell nur abhängig vom Verschiebungssprung. Dadurch lassen sich Spannungsvektoren über die Grenzfläche übertragen. Der Spannungsvektor ist kontinuierlich. Generalisierte Grenzflächen sind abhängig von der Öffnung sowie der Deformation der Grenzfläche und bilden den allgemeinsten Fall. Hier treten sowohl Diskontinuitäten im Spannungsvektor als auch in der Verschiebung auf.

In der vorliegenden Arbeit werden für kohärente hyperelastische Grenzflächen sowie Kohäsivzonenmodelle Phasenfeldbeschreibungen für finite Deformationen vorgestellt. Durch die Approximation mit der Phasenfeldmethode können Problemstellungen mit veränderlichen Grenzflächen beschrieben werden ohne die Geometrie der Grenzfläche exakt zu parametrisieren. Diese wird durch ein weiteres Feld, das Phasenfeld, mit einer internen Länge beschrieben, so dass ein diffuser Bereich entsteht. Die Grenzfläche wird also durch ein Volumen approximiert. Bei abnehmender interner Länge konvergiert die Phasenfeldbeschreibung zur Beschreibung mit scharfer Grenzfläche im Sinne der Γ-Konvergenz. Des Weiteren sind die Evolution und Entstehung neuer Grenzflächen in der Methode intrinsisch enthalten. Durch numerische Beispiele werden die verschiedenen Möglichkeiten der Modelle herausgestellt.

Abstract

Mechanical interfaces at the microscale influence the effective macroscopic properties of materials in various forms such as shear bands or grain boundaries in nanomaterials. On the macroscopic scale, interfaces occur, for example, in the form of cracks or boundaries between tectonic plates.

Mechanical interfaces can be characterized as coherent interfaces or non-coherent interfaces. While the displacement field is continuous across coherent interfaces, discontinuities occur in the case of non-coherent interfaces. Coherent interfaces can be described by an additional constitutive model depending on the deformation of the interface. A classic example is hyperelasticity. The additional constitutive model allows for jumps in the stress vector as tangent stresses occur in the interface. If the energy of the coherent interface is constant one speaks of perfect interfaces. For perfect interfaces, both, the displacement field and the stress vector are continuous. By way of contrast, non-coherent interfaces can be described as cohesive zone models or generalized interfaces. For cohesive zone models, the interface model only depends on the displacement jump. This allows stress vectors to be transferred across the interface leading to a continuous stress vector field. Generalized interfaces depend on the opening and the deformation of the interface and represent the most general case. Here, discontinuities over the interface occur in the stress vector field as well as in the displacement.

In this thesis finite strain phase field approximations for the two latter cases – interface elasticity and cohesive zone models – are presented. By using the phase field method, free boundary problems with evolving interfaces can be described and solved without an exact description and parametrization of the interface's geometry. In contrast to sharp interface formulations, the interface is approximated as a diffuse volume with an order parameter – the phase field – and an internal length scale. With vanishing internal length the phase field description converges towards the sharp interface formulation in the sense of Γ-convergence. Furthermore, the nucleation and evolution of interfaces is included within the method without any additional cost. The wide range of capabilities of the novel descriptions are highlighted by numerical examples.

Publications

Parts of this thesis are based on peer-reviewed journal articles, which were either published or submitted during the progress of this thesis.

[80] H. Lammen, J. Mosler: *On the approximation of surface elasticity theory by means of phase-field theory.*, Proc. Appl. Math. Mech., 19:e201900375, 2019.

[81] H. Lammen, S. Conti, J. Mosler: *A finite deformation phase field model suitable for cohesive fracture*, Journal of the Mechanics and Physics of Solids, 178:105349, 2023.

[79] H. Lammen, S. Conti, J. Mosler: *Approximating arbitrary traction-separation-laws by means of phase-field theory – Mathematical foundation and numerical implementation*, Journal of the Mechanics and Physics of Solids, 197:106038, 2023.

The author of this thesis contributed essential aspects with regard to the outline of the theory, carried out all of the numerical implementations and simulations, and prepared articles [79–81]. In this thesis, several parts of the publications [79–81] are cited. However, changes to notations, citation numbering, chapter numbering, figure placement and others are made to increase the readability of the thesis. Sections taken from the publications are highlighted by the corresponding citation right after the section title. Italic remarks at the end of sections highlight major differences in formulations/notations. Quotations of the articles within a section are highlighted by quotation marks and the corresponding citation. At the submission of this thesis, publication [79] was not yet published but submitted. Thus, citations from this publication refer to a preliminary version. Between this preliminary version and the final publication only minor differences are present, which are not relevant to the content. The preliminary version is marked with an asterisk in citations ([79, $*$]).

Contents

Notation

General notation

The operations mostly used in the thesis are summarized here. All other notations are introduced when used.

Tensors In this thesis a three-dimensional Euclidean space is spanned by its Cartesian basis vectors $\boldsymbol{e}_1$, $\boldsymbol{e}_2$ and $\boldsymbol{e}_3$. By applying Einstein's summation convention tensors of arbitrary finite order can be described by their coefficients $\bullet_i$, i.e.,

$$\begin{aligned}
\boldsymbol{a} &= A_i\, \boldsymbol{e}_i \quad , && \text{(first-order tensor)} \\
\boldsymbol{A} &= A_{ij}\, \boldsymbol{e}_i \otimes \boldsymbol{e}_j \quad , && \text{(second-order tensor)} \\
\mathsf{A} &= A_{ijkl}\, \boldsymbol{e}_i \otimes \boldsymbol{e}_j \otimes \boldsymbol{e}_k \otimes \boldsymbol{e}_l \quad , && \text{(fourth-order tensor)}
\end{aligned}$$

For first-order tensors (i.e. vectors) and second-order tensors bold-face italic letters are used. Fourth-order tensors will be highlighted as bold-face upper-case sans-serif letters. Non-bold letters denote scalar values.

Operations A multiplication with a scalar $\alpha \in \mathbb{R}$ as well as a summation of two tensors of the same order are defined component-wise, i.e.,

$$\begin{aligned}
\alpha \boldsymbol{a} &:= \alpha\, a_i\, \boldsymbol{e}_i \,, \\
\alpha \boldsymbol{A} &:= \alpha\, A_{ij}\, \boldsymbol{e}_i \otimes \boldsymbol{e}_j \,, \\
\boldsymbol{a} + \boldsymbol{b} &:= [a_i + b_i]\ \boldsymbol{e}_i \,, \\
\boldsymbol{A} + \boldsymbol{B} &:= [A_{ij} + B_{ij}]\ \boldsymbol{e}_i \otimes \boldsymbol{e}_j \,, \\
\mathsf{A} + \mathsf{B} &:= [A_{ijkl} + B_{ijkl}]\ \boldsymbol{e}_i \otimes \boldsymbol{e}_j \otimes \boldsymbol{e}_k \otimes \boldsymbol{e}_l \,.
\end{aligned}$$

Multiplications of tensors with different orders are classified as **inner** and **dyadic tensor products**.

Inner tensor product Inner tensor products are denoted by dots. The number of dots indicates the number of contractions, i.e.,

$$\begin{aligned}
\boldsymbol{a} \cdot \boldsymbol{b} &:= a_i\, b_i\,, \\
\boldsymbol{A} \cdot \boldsymbol{b} &:= A_{ij}\, b_j\, \boldsymbol{e}_i\,, \\
\boldsymbol{A} \cdot \boldsymbol{B} &:= A_{ij}\, B_{jk}\, \boldsymbol{e}_i \otimes \boldsymbol{e}_k\,, \\
\boldsymbol{A} : \boldsymbol{B} &:= A_{ij}\, B_{ij}\,, \\
\mathbf{A} : \boldsymbol{B} &:= A_{ijkl}\, B_{kl}\, \boldsymbol{e}_i \otimes \boldsymbol{e}_j\,.
\end{aligned}$$

Dyadic tensor product Dyadic tensor products are denoted by $\otimes$ and its modifications $\overline{\otimes}$ and $\underline{\otimes}$. The products read

$$\begin{aligned}
\boldsymbol{a} \otimes \boldsymbol{b} &:= a_i\, b_j\, \boldsymbol{e}_i \otimes \boldsymbol{e}_j\,, \\
\boldsymbol{A} \otimes \boldsymbol{b} &:= A_{ij}\, b_k\, \boldsymbol{e}_i \otimes \boldsymbol{e}_j \otimes \boldsymbol{e}_k\,, \\
\boldsymbol{A} \otimes \boldsymbol{B} &:= A_{ij}\, B_{kl}\, \boldsymbol{e}_i \otimes \boldsymbol{e}_j \otimes \boldsymbol{e}_k \otimes \boldsymbol{e}_l\,, \\
\boldsymbol{A} \,\overline{\otimes}\, \boldsymbol{B} &:= A_{ik}\, B_{jl}\, \boldsymbol{e}_i \otimes \boldsymbol{e}_j \otimes \boldsymbol{e}_k \otimes \boldsymbol{e}_l\,, \\
\boldsymbol{A} \,\underline{\otimes}\, \boldsymbol{B} &:= A_{il}\, B_{jk}\, \boldsymbol{e}_i \otimes \boldsymbol{e}_j \otimes \boldsymbol{e}_k \otimes \boldsymbol{e}_l\,.
\end{aligned}$$

Cross product The cross product, indicated by $\times$ reads

$$\boldsymbol{a} \times \boldsymbol{b} := (a_2 b_3 - a_3 b_2)\, \boldsymbol{e}_1 + (a_3 b_1 - a_1 b_3)\, \boldsymbol{e}_2 + (a_1 b_2 - a_2 b_1)\, \boldsymbol{e}_3$$

for tensors of first order.

Spatial derivatives Spatial derivatives with respect to coordinates X_1, X_2 and X_3 are used throughout the thesis. However, all of the derivatives used here are symbolically based on the Nabla operator defined by

$$\nabla := \frac{\partial}{\partial X_1}\, \boldsymbol{e}_1 + \frac{\partial}{\partial X_2}\, \boldsymbol{e}_2 + \frac{\partial}{\partial X_3}\, \boldsymbol{e}_3\,.$$

By applying the Nabla operator to differentiable tensor-valued fields $\boldsymbol{a}$, different derivatives can be obtained, leading to e.g.

$$\begin{aligned}
\mathrm{Grad}(\boldsymbol{a}) = (\nabla \otimes \boldsymbol{a})^{\mathrm{t}} &:= a_{i,j}\, \boldsymbol{e}_i \otimes \boldsymbol{e}_j\,, && \text{(gradient)}\\
\mathrm{Div}(\boldsymbol{a}) = \nabla \cdot \boldsymbol{a} &:= a_{i,i}\,, && \text{(divergence)}\\
\mathrm{Rot}(\boldsymbol{a}) = \nabla \times \boldsymbol{a} &:= (a_{3,2} - a_{2,3})\, \boldsymbol{e}_1 + (a_{1,3} - a_{3,1})\, \boldsymbol{e}_2 + (a_{2,1} - a_{1,2})\, \boldsymbol{e}_3\,, && \text{(rotation)}
\end{aligned}$$

for tensors of first order. The subscript comma denotes a partial derivative with respect to the following coordinate. A common abbreviation for the gradient of field $\boldsymbol{a}$ is $\nabla \boldsymbol{a}$. When applying the derivatives with respect to the deformed configuration with coordinates x_1, x_2 and x_3, the operations are written in small case letters, i.e., $\mathrm{grad}(\boldsymbol{a})$, $\mathrm{div}(\boldsymbol{a})$, $\mathrm{rot}(\boldsymbol{a})$.

Macauley brackets Macauley bracket $\langle \bullet \rangle_+$ and $\langle \bullet \rangle_-$ are defined by

$$\langle \bullet \rangle_+ := \begin{cases} \bullet & \text{if } \bullet \geq 0 \\ 0 & \text{if } \bullet < 0\,, \end{cases}$$

$$\langle \bullet \rangle_- := \begin{cases} 0 & \text{if } \bullet \geq 0 \\ \bullet & \text{if } \bullet < 0\,, \end{cases}$$

such that $\bullet = \langle \bullet \rangle_+ + \langle \bullet \rangle_-$ where $\bullet$ represents any real number.

Fundamentals of interfaces – curvilinear coordinates

The geometric description of a two-dimensional oriented interface $\Gamma \subset \mathbb{R}^3$ in a surrounding volume (bulk) $\Omega \subset \mathbb{R}^3$ is described by means of curvilinear coordinates $\boldsymbol{\xi} \in \Xi$ with the mapping $\boldsymbol{\Theta} : \Xi \to \Gamma$. $\Xi \subset \mathbb{R}^2$ denotes the two-dimensional parameter space of the curvilinear coordinates. The corresponding covariant basis vectors are defined by $\overline{\boldsymbol{G}}_\alpha = \partial_\alpha \boldsymbol{\Theta}$. They are tangential to the interface. Their contravariant counterparts $\overline{\boldsymbol{G}}^\alpha$ are defined by the relationship $\overline{\boldsymbol{G}}^\alpha \cdot \overline{\boldsymbol{G}}_\beta = \delta^\alpha_\beta$, where

$$\delta^\alpha_\beta := \begin{cases} 1 & \text{if } \alpha = \beta \\ 0 & \text{else} \end{cases}$$

is the Kronecker Delta. The covariant ($\overline{G}_{\alpha\beta}$) and contravariant ($\overline{G}^{\alpha\beta}$) components of the first fundamental form or metric tensor are given by $\overline{G}_{\alpha\beta} = \overline{\boldsymbol{G}}_\alpha \cdot \overline{\boldsymbol{G}}_\beta$ and $\overline{G}^{\alpha\beta} = \overline{\boldsymbol{G}}^\alpha \cdot \overline{\boldsymbol{G}}^\beta$. Consequently, the relationships $\overline{\boldsymbol{G}}_\alpha = \overline{G}_{\alpha\beta}\, \overline{\boldsymbol{G}}^\beta$ and $\overline{\boldsymbol{G}}^\alpha = \overline{G}^{\alpha\beta}\, \overline{\boldsymbol{G}}_\beta$ hold. In order to project quantities to the interface, the interface identity is defined as $\overline{\boldsymbol{I}} := \overline{\boldsymbol{G}}_1 \otimes \overline{\boldsymbol{G}}^1 +$

$\overline{\boldsymbol{G}}_2 \otimes \overline{\boldsymbol{G}}^2$. With an interface normal defined by $\overline{\boldsymbol{N}}$ the interface identity can be rewritten as $\overline{\boldsymbol{I}} = \boldsymbol{I} - \overline{\boldsymbol{N}} \otimes \overline{\boldsymbol{N}}$.

By using curvilinear coordinates, typical operators acting in the bulk can also be defined within the interface. For instance,

$$\begin{aligned}
\overline{\mathrm{Grad}}\,(\overline{\bullet}) &= \frac{\partial \overline{\bullet}}{\partial \xi_1} \otimes \overline{\boldsymbol{G}}^1 + \frac{\partial \overline{\bullet}}{\partial \xi_2} \otimes \overline{\boldsymbol{G}}^2 \,, \\
\overline{\mathrm{Div}}\,(\overline{\bullet}) &= \frac{\partial \overline{\bullet}}{\partial \xi_1} \cdot \overline{\boldsymbol{G}}^1 + \frac{\partial \overline{\bullet}}{\partial \xi_2} \cdot \overline{\boldsymbol{G}}^2 \,, \\
\overline{\mathrm{Det}}\,(\overline{\bullet}) &= \frac{\|\overline{\bullet} \cdot \overline{\boldsymbol{G}}_1 \times \overline{\bullet} \cdot \overline{\boldsymbol{G}}_2\|}{\|\overline{\boldsymbol{G}}_1 \times \overline{\boldsymbol{G}}_2\|} \,, \\
\overline{\mathrm{Cof}}\,(\overline{\bullet}) &= \overline{\mathrm{Det}}\,(\overline{\bullet})\ \overline{\bullet}^{-\mathrm{t}} \,.
\end{aligned}$$

The orientation of the interface allows the definition of two interface sides denoted by Γ_+ and Γ_-, where the interface normal $\overline{\boldsymbol{N}}$ faces from $-$ to $+$. In the reference configuration the interface sides coincide such that $\Gamma = \Gamma_+ \cup \Gamma_- = \Gamma_+ = \Gamma_-$. This is no longer the case in the deformed configuration (Ω_t,Γ_t) at time t for non-coherent interfaces, i.e. with a non-continuous displacement field. Here, in general $\Gamma_{t;+} \neq \Gamma_{t;-}$. The union of both sides defines the total interface $\Gamma_t = \Gamma_{t;+} \cup \Gamma_{t;-}$.

If the interface separates the volume Ω the two created volumes are denoted by Ω_+ and Ω_-. All involved volumes are assumed as open sets such that $\Gamma = \overline{\Omega}_+ \cap \overline{\Omega}_-$ with closures $\overline{\Omega}_+$ and $\overline{\Omega}_-$. This leads to $\Omega = \Omega_+ \cup \Omega_- \cup \Gamma$. The same holds true for the deformed interface $\Gamma_t \subset \Omega_t$ in the deformed bulk Ω_t at time t ($\Omega_t = \Omega_{t;+} \cup \Omega_{t;-} \cup \Gamma_t = \Omega_{t;+} \cup \Omega_{t;-} \cup \Gamma_{t;+} \cup \Gamma_{t;-}$). If $\Omega \backslash \Gamma$ is a connected set, i.e. the interface does not divide the volume, the definition of Ω_+ and Ω_- is not possible. However, the separation in Γ_+ and Γ_- remains the same as it only depends on the orientation of the interface.

Due to the non-continuity of fields, arbitrary mechanical quantities $\bullet$ like the displacement show two possible values at the interface. These are denoted $\bullet_+$ and $\bullet_-$ and read

$$\begin{aligned}
\bullet_+ &:= \lim_{\epsilon \to 0} \bullet(\boldsymbol{X} + \epsilon\, \overline{\boldsymbol{N}}) \quad \text{for } \boldsymbol{X} \in \Gamma_+ \,, \\
\bullet_- &:= \lim_{\epsilon \to 0} \bullet(\boldsymbol{X} - \epsilon\, \overline{\boldsymbol{N}}) \quad \text{for } \boldsymbol{X} \in \Gamma_- \,.
\end{aligned}$$

The so-called jumps over the interface are defined by $[\![\bullet]\!] := \bullet_+ - \bullet_-$. In contrast, the average of the two sides is defined by $\{\!\{\bullet\}\!\} = \frac{1}{2}\,[\bullet_+ + \bullet_-]$.

1 Introduction

1.1 Introduction

1.1.1 Motivation

Interfaces have a significant impact on the (mechanical) properties of materials and structures. Typical examples for interfaces at the micro scale are phase boundaries in nanocomposites [26, 92, 126, 153], grain boundaries [72, 106, 128, 158] or shear bands in ductile materials [62, 164]. For larger scales, cracks [6, 85, 107, 131] or the boundaries of tectonic plates [132, 141] are examples of interfaces. Figure 1.1 provides examples of interfaces at different length scales.

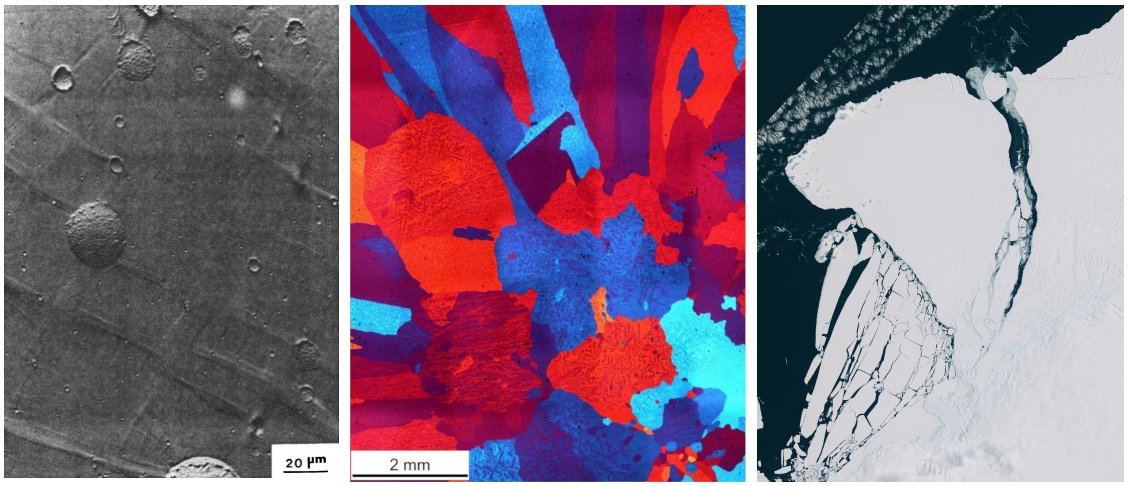

Figure 1.1: Examples of interfaces at different length scales. **left:** Shear bands in a rubber-epoxy nanocomposit under compressive loading (reprint with grateful permission from [1]). **middle:** Grain microstructure of aluminum visualized by a polarized optic micrograph [163, © CC-BY]. **right:** Fracture at the Brunt Ice Shelf (Antarctica) at the break away from icebergs A81 and A81a [49, © ESA Standard Licence].

As the area-to-volume ratio is proportional to the inverse of the characteristic length (length of the representative volume element) the importance of interfaces increases significantly at smaller scales. This is why they are particularly important for nanomaterials (c.f. [45, 58, 59, 98, 113, 156, 170, 172–174]). The size effect induced by the interplay between bulk and interface energies is investigated in [45, 67, 74, 105, 135, 172] among others.

1.2 State of the art

Mechanical interfaces can be separated into coherent interfaces, over which the displacement field remains continuous, and into non-coherent interfaces showing displacement jumps. Examples for the latter are cracks, while phase boundaries correspond to coherent interfaces. A further distinction follows from the regularity of the tractions over the interface. Coherent interfaces can be separated into perfect interfaces, continuous in displacements and tractions, and those where traction jumps are possible. Such jumps correspond to an additional constitutive model within the interface. On the other hand non-coherent interfaces can be classified as cohesive interfaces allowing displacement jumps while preserving a continuous traction field and general interfaces with jumps in displacements and tractions. This thesis mainly focuses on interface elasticity (coherent hyperelastic interfaces with discontinuous tractions) as well as cohesive interfaces. A state of the art review of these two types of interface classifications is presented in the following.

1.2.1 Coherent interfaces — Hyperelastic formulation

As mentioned before, mechanical interfaces can be subdivided into coherent and non-coherent interfaces. Coherent interfaces show a continuous displacement field, but the traction vector might be discontinuous. This section is concerned with coherent interfaces. Although they are not restricted to any particular constitutive framework, focus is on hyperelasticity. The dependency on the deformation gradient leads to stresses tangential to the interface. Pioneering work has been published by Gurtin and Murdoch [64, 65, 111] and has been further elaborated (e.g. [76, 138**?** , 139]).

Coherent interfaces can be either modeled as discrete interfaces or approximated as diffuse interfaces with a finite thickness. Discrete models can be found in [14, 67, 107] within a finite element framework. In [67] two-dimensional finite elements are embedded into the finite element mesh between volume elements. By way of contrast, the eXtended Finite Element Method (XFEM) allowing to approximate interfaces within three dimensional finite elements was employed in [14, 107]. By applying the partition of unity special ansatz functions can be defined which can approximate jumps within a finite element. All discrete interface techniques have in common that their solutions show a mesh dependency or require a change of the ansatz spaces.

In contrast, the phase field method provides a powerful framework to approximate interfaces. By using an additional order parameter, i.e., the phase field, the interface is approximated as a diffuse interface with a finite thickness (as a volume). Within the phase field method the tracking of the interfaces is automatically included. A promising phase field approach to interface elasticity has recently been published in [80, 86, 161, 162].

1.2.2 (Cohesive) Fracture

The second class of interfaces considered in this thesis are non-coherent interfaces, i.e., those characterized by a discontinuous displacement field. Often, they are employed for modeling and predicting failure processes. Applications at the micro-scale are [10, 43, 61, 71, 110, 171] while the works [11, 127, 137, 146] deal with failure at the macroscale. While linear fracture mechanics can often be sufficiently described by using the Griffith criterion [63], non-linear fracture models are often required. "A suitable framework for capturing non-linear failure is given by cohesive zone models. This framework dates back to the pioneering works by Barenblatt [15], Dugdale [46] and also to Hillerborg [70] as far as the numerical implementation is concerned.

In contrast to classic stress-strain based bulk material models, cohesive zone models are described by so-called *traction-separation-laws*. These laws connect the stress vector acting at a material interface to its energetically dual variable being the displacement discontinuity/jump, cf. [2–4, 30, 99, 100, 115, 143, 144]. Illustrative examples of such material interfaces are provided by cracks in quasi-brittle materials or shear bands in ductile metals. In both cases – and again in line with classic bulk material models – cohesive zone models can be defined by postulating a Helmholtz energy and suitable evolution equations. However, and in contrast to bulk material models, this energy depends on the displacement jump – and possibly additional variables. A general framework complying with the fundamental principles in physics such as balance of angular momentum and the second-law of thermodynamics is discussed in [108, 120]." ([79, Sec. 1]) The constitutive models can be categorized into *potential-based* and *non-potential-based* traction-separation laws, cf. [47, 95, 108, 121]. As non-potential based traction-separation laws ([42, 133, 147–149]) fail to fulfill fundamental physical principles (cf. [108, 123]) this thesis deals with potential-based traction-separation laws. Potential-based traction-separation laws rely on an interface potential energy depending on the displacement jump, cf. [115, 122, 143, 169]. Its derivative yields the traction-separation law. Due to their potential-based structure, the models are path-independent – in contrast to the irreversibility of fracture itself. Therefore, extensions to potential-based traction-separation laws introducing internal variables were published e.g. by [60, 97, 112, 129]. "A cohesive zone framework consistent with fundamental physical principles, such as balance of angular momentum, material frame indifference (geometrically exact setting) and the second law of thermodynamics, was elaborated in a series of papers by one of the authors, cf. [66–68, 76, 108, 120]. It bears emphasis that these

fundamental principles are indeed violated for most anisotropic cohesive zone models within a geometrically exact setting." ([81, Sec. 1]).

This thesis only deals with isotropic fracture models. As also pointed out in [76, 108, 120], these models fulfill all fundamental physical principles when a potential-based structure is applied. Regarding cohesive interfaces "[...] isotropy is understood as co-linearity between the stress vector across the interface and its dual variable, the displacement jump. [...] Focusing on thermodynamics, the area-specific Helmholtz energy of isotropic cohesive zone models depends on the norm of the displacement jump as well as on some internal variables, cf. [76, 108, 120].

Material interfaces such as those defining a cohesive zone can be modeled as sharp (a two-dimensional object) or as diffuse (a three-dimensional object). Finite element models falling into the range of the first aforementioned class are presented in [13, 17, 40, 50, 57, 66, 107, 114, 118, 168]. While in [66, 114, 118, 168] interface elements (two-dimensional finite elements) are inserted between bulk elements (three-dimensional finite elements), the works [13, 17, 57, 107] employ the eXtended Finite Element Method (X-FEM) where interfaces can be embedded into bulk finite elements. Finally, approaches based on the isogeometric analysis are elaborated in [40, 50]. Independent of the numerical implementation, modeling interfaces as two-dimensional objects leads to *free boundary problems*. To be more precise, the location as well as the geometry of the evolving interfaces are not known beforehand, but part of the solution. For this reason, the finite element triangulation has to be updated according to the propagation of the interfaces. It bears emphasis that this statement is also true for the X-FEM where the shape functions as well as the numerical integration have to be adapted.

A numerically powerful approximation of free boundary problems is provided by phase field theory. Phase field models approximate the two-dimensional material interfaces by means of three-dimensional objects, i.e. the interfaces show a finite thickness. Focusing on brittle fracture, phase field models are discussed in [22, 102]. One of the major advantages of phase field approximations is that the location and the geometry of the interfaces is described by a field variable (the order parameter), while the underlying finite element triangulation does not need to be updated. Accordingly, the tracking of evolving interfaces is automatically included in phase field models and no special updating of the finite element triangulation or the integration scheme is required. Furthermore, the phase field approximation converges to the underlying sharp interface problem in the sense of Γ-convergence [8], see also [22]. The influence of the phase-field width on the mechanical response is analyzed in [142]." ([81, Sec. 1]).

Phase field approximations of fracture fall into the more general range of gradient damage approaches. Within these approaches the gradient of damage is penalized, introducing an additional length scale. In contrast to standard local damage approaches (neglecting the gradient) this leads to a regularization of the underlying PDE and thus to mesh objective results as far as the finite element implementation is concerned. Examples for different approaches to gradient damage can be found in [87, 94, 124] among others. A comparison of different gradient damage approaches to fracture is presented in [38].

A phase field approach to cohesive fracture is presented in this thesis. For a vanishing interface thickness, a (Γ-) convergence of the phase field approximation to the sharp interface limit can be proven. Besides the Γ-convergence, the intrinsically included tracking of the initiation and evolution of cracks is an additional advantage. A main disadvantage of phase field approaches to fracture is the computational cost. This is mainly caused by the fine spacial discretization required near the crack and by an iterative solution technique applied due to the non-convexity of the underlying (incremental) energy.

"While for brittle fracture, the (Γ-) convergence of phase field models to the underlying sharp interface model has been known for decades, the treatment of non-linear fracture mechanics within the cohesive zone framework is significantly more challenging." ([79, Sec. 1$*$]) "Extensions of the phase field model to cohesive failure are discussed in [35, 52, 53, 81, 90, 91, 150, 165–167][79, Sec. 1$*$] . The cited works can be subdivided into three different groups.

Within the first of these groups [150], three different field variables are introduced: the displacement field, the phase field and an additional field representing the displacement jump. This is in contrast to the mathematical rigorous two-field approximations of brittle fracture such as [8, 54] where the displacement jump is implicitly defined by the displacement field and the phase-field distribution. Most frequently, the framework [150] is employed in order to analyze decohesion at already existing material interfaces such as grain boundaries, cf. [116]. In this case, the distribution of the phase-field is known beforehand and time-invariant. If evolving material interfaces are to be studied, an additional evolution equation is required, cf. [150] and [151].

The second group of phase field models suitable for cohesive fracture is characterized by a two-field formulation – in line with the mathematical rigorous two-field approximations of brittle fracture such as [8, 54]. Models falling into the range of this group can be found in [52, 53, 90, 91, 165–167]. Focusing on a one-dimensional setting, the analytical solution of the coupled problem is computed within the cited works first (under relatively weak assumptions). Subsequently, the total strain is decomposed into an elastic and an inelastic part. The latter, in turn, can be related to the displacement jump. By considering the limiting case (the width of the localization zone converges to zero), a traction-separation-law can be computed. Finally and assuming an isotropic energy, the one-dimensional model is extended to the three-dimensional setting. It appears Lorentz and co-workers were the first who proposed this idea, cf. [90, 91]. First, they employed gradient-enhanced damage models. Later, they also analyzed phase-field models. The reconstruction of the model parameters from the traction-separation law was addressed in [53]. However, since phase-field models are a special subset of gradient-damage models, this modification is relatively straightforward. Although the idea advocated in [90, 91] is indeed sound, some questions remain open. On the one hand, the computation of the displacement jump in a three-dimensional setting is unclear. On the other hand and equally important, convergence of these models to a sharp interface formulations is still an open question from a mathematical point of view.

A mathematically rigorous phase-field approximation of cohesive zone models is introduced in [35]. It is based on the framework of Γ-convergence – in line with the mathematical rigorous two-field approximations of brittle fracture such as [8, 54]. Extensions of this framework are given in [36, 55, 81]. They cover the incorporation of the Microcrack-Closure-Reopening (MCR) effect, a geometrically exact setting (finite deformations) and the consideration of arbitrary hyperelastic bulk material models, cf. [81]. Analogously to models of the second group (see [52, 53, 90, 91, 165, 166]), the traction-separation-law is also implicitly defined within the third group of phase-field approximations. To be more explicit, this law again follows from the degradation function which reduces the stiffness of the pristine material, cf. [35]." ([79, Sec. 1,∗]). The latter extension is introduced in [79]. The extensions elaborated in [79, 81] are presented in detail in this thesis.

1.3 Structure of the thesis

The thesis is organized in three main parts. First, an introduction to general interfaces is presented. In the second part, a phase field approximation of surface elasticity is given before a phase field approximation of cohesive fracture is presented. Finally, the thesis is concluded and an outlook is provided. The chapters are organized as follows:

Introduction to general interfaces: As this thesis deals with the approximation of interfaces, a short introduction to general interfaces is given in this chapter. It covers the kinematics as well as kinetics of the interface and the bulk phase. Fundamental balance laws as well as the basis of constitutive modeling are introduced.

Phase-field approximation of interface elasticity: In this chapter, a phase field approximation of elastic interfaces is presented. A Neo-Hookean type interface model is introduced and approximated by means of to the phase field model. Phase transformations are not considered in this chapter.

Phase-field approximation of cohesive fracture: A mathematically rigorous finite strain phase field model for cohesive fracture is presented. Arbitrary potential-based traction-separation laws can be approximated. In addition, the Microcrack-Closure-Reopening Effect (MCR) is introduced to the model, i.e., cracks only propagate under tension.

2 Introduction to general interfaces

In this chapter the mathematical description of interfaces including their kinematics, balance equations and modeling approaches are summarized. Interested readers are referred to [24, 32, 78, 140] for further details.

2.1 Kinematics

In the following, the kinematics of a volume (bulk) $\Omega \subset \mathbb{R}^{n_{\text{dim}}}$ ($n_{\text{dim}} = 1, 2, 3$) under deformation including an oriented interface $\Gamma \subset \mathbb{R}^{n_{\text{dim}}}$ are described. While Ω and Γ are given in an undeformed (reference) configuration at time $t = t_0$, their counterparts in the deformed (current) configuration at time t are denoted by $\Omega_t \subset \mathbb{R}^{n_{\text{dim}}}$ and $\Gamma_t \subset \mathbb{R}^{n_{\text{dim}}}$. Points in the reference configuration are depicted by $\boldsymbol{X}$ (or $\overline{\boldsymbol{X}}$ on the interface) while $\boldsymbol{x}$ or $\overline{\boldsymbol{x}}$ refer to points in the current configuration. The interface itself is allowed to evolve within the bulk. However, the movement of the interface is connected to the movement of the surrounding bulk.

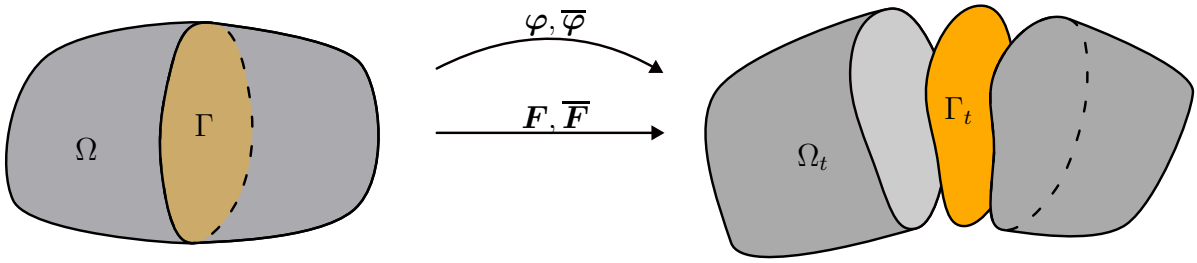

Figure 2.1: Kinematics of interfaces in a continuum. Deformation map $\boldsymbol{\varphi}$ describes the deformation of the bulk while $\overline{\boldsymbol{\varphi}}$ denotes the deformation map of the interface. Their gradients are denoted by $\boldsymbol{F}$ and $\overline{\boldsymbol{F}}$.

The deformation of the structure is defined by means of two mapings. For the bulk the deformation mapping $\boldsymbol{\varphi} : \Omega \times [t_0, t_{\text{end}}] \mapsto \Omega_t$ is introduced, where $[t_0, t_{\text{end}}] \in \mathbb{R}$ defines the time space. The deformed bulk results from the mapping $\Omega_t = \boldsymbol{\varphi}(\Omega, t)$ and the deformed point $\boldsymbol{x}$ is given by

$$\boldsymbol{x} = \boldsymbol{\varphi}(\boldsymbol{X}, t)\,. \tag{2.1}$$

Similarly, the deformation of the interface is given by the map $\overline{\boldsymbol{\varphi}} : \Gamma \times [t_0, t_{\text{end}}] \mapsto \Gamma_t$. The deformed interface reads $\Gamma_t = \overline{\boldsymbol{\varphi}}(\Gamma, t)$. A deformed point on the interface takes the form

$$\overline{\boldsymbol{x}} = \overline{\boldsymbol{\varphi}}(\overline{\boldsymbol{X}}, t)\,. \tag{2.2}$$

The displacements are defined as

$$\boldsymbol{u} := \boldsymbol{x} - \boldsymbol{X}\,, \tag{2.3}$$
$$\overline{\boldsymbol{u}} := \overline{\boldsymbol{x}} - \overline{\boldsymbol{X}}\,. \tag{2.4}$$

The deformation gradients yield

$$\boldsymbol{F} := \frac{\partial \boldsymbol{x}}{\partial \boldsymbol{X}} = \boldsymbol{I} + \frac{\partial \boldsymbol{u}}{\partial \boldsymbol{X}}\,, \tag{2.5}$$
$$\overline{\boldsymbol{F}} := \frac{\partial \overline{\boldsymbol{x}}}{\partial \overline{\boldsymbol{X}}} = \boldsymbol{I} + \frac{\partial \overline{\boldsymbol{u}}}{\partial \overline{\boldsymbol{X}}}\,. \tag{2.6}$$

As the interface deformation depends on the bulk deformation the two deformation maps are connected by the condition $\overline{\boldsymbol{\varphi}}(t, \overline{\boldsymbol{X}}) = \{\!\{\boldsymbol{\varphi}\}\!\}(t, \overline{\boldsymbol{X}}), \forall \overline{\boldsymbol{X}} \in \Gamma$. $\{\!\{\bullet\}\!\}$ denotes the average of a quantity over an interface as defined in Section Notations. As a result deformation gradients (2.5) and (2.6) are linked by

$$\overline{\boldsymbol{F}} = \boldsymbol{F} \cdot \overline{\boldsymbol{I}}. \tag{2.7}$$

Here $\overline{\boldsymbol{I}}$ is the surface identity which can be interpreted as the projection to the interface. It is discussed in more detail in Section Notations.

Both deformation gradients quantify the changes of directed surface elements $\mathrm{d}\boldsymbol{A}$, $\mathrm{d}\overline{\boldsymbol{A}}$ and line elements $\mathrm{d}\boldsymbol{L}$, $\mathrm{d}\overline{\boldsymbol{L}}$. Furthermore, the bulk deformation gradient quantifies the change of infinitesimal volumes $\mathrm{d}V$. To be more precise,

$$\mathrm{d}v := \mathrm{Det}(\boldsymbol{F})\,\mathrm{d}V = J\,\mathrm{d}V\,, \tag{2.8}$$
$$\mathrm{d}\boldsymbol{a} := \mathrm{Cof}(\boldsymbol{F}) \cdot \mathrm{d}\boldsymbol{A} = \mathrm{Det}(\boldsymbol{F})\,\boldsymbol{F}^{-\mathrm{t}} \cdot \mathrm{d}\boldsymbol{A}\,, \tag{2.9}$$
$$\mathrm{d}\boldsymbol{l} := \boldsymbol{F} \cdot \mathrm{d}\boldsymbol{L}\,. \tag{2.10}$$

Similarly, the surface's counterparts read

$$\mathrm{d}\overline{a} := \overline{\mathrm{Det}}(\overline{\boldsymbol{F}})\,\mathrm{d}\overline{A} = \overline{J}\,\mathrm{d}\overline{A}\,, \tag{2.11}$$
$$\mathrm{d}\overline{\boldsymbol{l}} := \overline{\boldsymbol{F}} \cdot \mathrm{d}\overline{\boldsymbol{L}}\,. \tag{2.12}$$

The determinants are abbreviated as $J = \mathrm{Det}(\boldsymbol{F})$ and $\overline{J} = \overline{\mathrm{Det}}(\overline{\boldsymbol{F}})$ here and in the following. The normal of the surface of the bulk is denoted by $\boldsymbol{N}$ in the reference configuration. In addition to the interface normal vector $\overline{\boldsymbol{N}}$, the vector $\widetilde{\boldsymbol{N}}$ is introduced

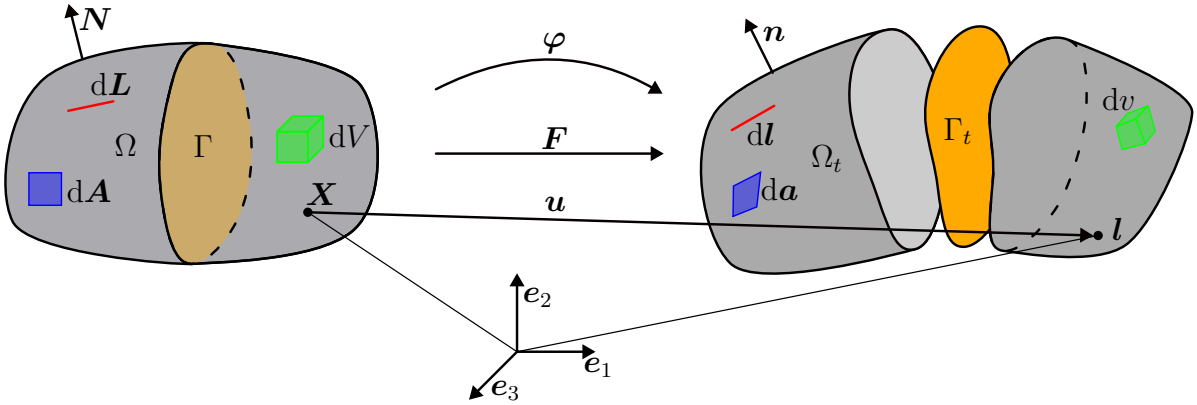

Figure 2.2: Deformation of infinitesimal volume $\mathrm{d}V$, area $\mathrm{d}\boldsymbol{A}$ and line $\mathrm{d}\boldsymbol{L}$ of the bulk from reference configuration to their deformed counterparts $\mathrm{d}v$, $\mathrm{d}\boldsymbol{a}$ and $\mathrm{d}\boldsymbol{l}$ in the current configuration.

as normal vector to the interface boundary. $\widetilde{\boldsymbol{N}}$ is defined by the additional condition of being tangential to the interface (see Figure 2.3). The corresponding normal vectors in the deformed configuration read $\overline{\boldsymbol{n}}$, $\widetilde{\boldsymbol{n}}$ and $\boldsymbol{n}$.

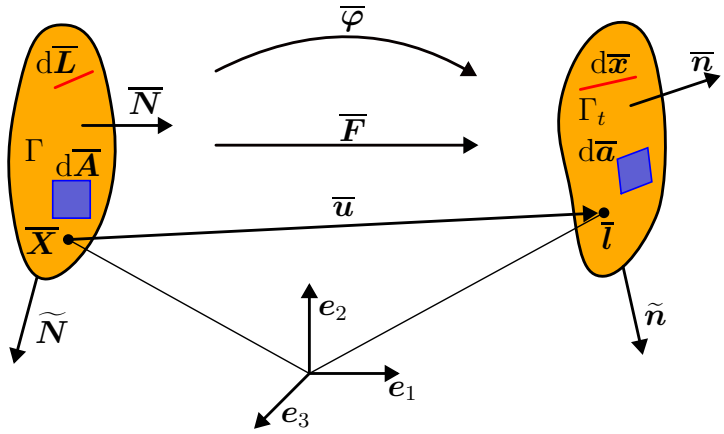

Figure 2.3: Deformation of infinitesimal surface element $\mathrm{d}\overline{\boldsymbol{A}}$ and line element $\mathrm{d}\overline{\boldsymbol{L}}$ of the interface from reference configuration to their deformed counterparts $\mathrm{d}\overline{\boldsymbol{a}}$ and $\mathrm{d}\overline{\boldsymbol{l}}$ in the current configuration.

For a coherent deformation ($[\![\boldsymbol{\varphi}]\!] = \boldsymbol{0}$) the jump of the deformation gradient over the interface is defined by the Hadamard jump condition as stated in [136] for kinematic compatibility. The Hadamard jump condition states that

$$[\![\boldsymbol{F}]\!] = \boldsymbol{a} \otimes \overline{\boldsymbol{N}}, \quad \boldsymbol{a} \in \mathbb{R}^{n_{\mathrm{dim}}}. \tag{2.13}$$

Thus, the jump is represented by a rank-one tensor. The Hadamard jump condition also ensures, that the relationship $\overline{\boldsymbol{F}} = \boldsymbol{F} \cdot \overline{\boldsymbol{I}}$ holds true for $\boldsymbol{F}_+$ and $\boldsymbol{F}_-$, i.e. multiplying

the displacement gradients by $\boldsymbol{I} = \overline{\boldsymbol{I}} + \overline{\boldsymbol{N}} \otimes \overline{\boldsymbol{N}}$ from the right side and considering $[\![\boldsymbol{F}]\!] \cdot \left(\overline{\boldsymbol{N}} \otimes \overline{\boldsymbol{N}}\right) = \boldsymbol{a} \otimes \left(\overline{\boldsymbol{N}} \cdot \overline{\boldsymbol{N}}\right) \otimes \overline{\boldsymbol{N}} = [\![\boldsymbol{F}]\!]$ results in

$$\begin{aligned} [\![\boldsymbol{F}]\!] &= [\![\boldsymbol{F}]\!] \cdot \overline{\boldsymbol{I}} + [\![\boldsymbol{F}]\!] \cdot \overline{\boldsymbol{N}} \otimes \overline{\boldsymbol{N}} \\ &= [\![\boldsymbol{F}]\!] \cdot \overline{\boldsymbol{I}} + [\![\boldsymbol{F}]\!] \end{aligned} \tag{2.14}$$

with the consequence $[\![\boldsymbol{F}]\!] \cdot \overline{\boldsymbol{I}} = \boldsymbol{0}$ or $\boldsymbol{F}_+ \cdot \overline{\boldsymbol{I}} = \boldsymbol{F}_- \cdot \overline{\boldsymbol{I}} = \overline{\boldsymbol{F}}$. As described in Section Notations, the subscript $+$ and $-$ denote quantities on the different sides of the interface.

2.1.1 Strain measures

Several strain measures can be defined by means of the deformation gradients $\boldsymbol{F}$ and $\overline{\boldsymbol{F}}$. In the following, these deformation measures are only defined for the bulk quantities. All strain measures can be formulated analogously for the interface.

In general, a strain tensor should fulfill certain conditions. One of these conditions states, that a rigid body motion should not induce strains. A rigid body movement is defined by

$$\boldsymbol{x} = \boldsymbol{R} \cdot \boldsymbol{X} - \boldsymbol{c}\,, \tag{2.15}$$

with a rotation characterized by rotation tensor $\boldsymbol{R} \in \mathcal{SO}(n_{\mathrm{dim}})$ and a translation $\boldsymbol{c} \in \mathbb{R}^{n_{\mathrm{dim}}}$. In order to exclude the rotation, the deformation gradient is often combined with its transpose defining the right Cauchy-Green deformation tensor

$$\boldsymbol{C} := \boldsymbol{F}^{\mathrm{t}} \cdot \boldsymbol{F}\,. \tag{2.16}$$

When applying a rotation to the deformation gradient such that $\tilde{\boldsymbol{F}} := \boldsymbol{R} \cdot \boldsymbol{F}$ the right Cauchy-Green tensor does not change due to the orthogonality of rotation tensors

$$\tilde{\boldsymbol{C}} := [\boldsymbol{R} \cdot \boldsymbol{F}]^{\mathrm{t}} \cdot [\boldsymbol{R} \cdot \boldsymbol{F}] = \boldsymbol{F}^{\mathrm{t}} \cdot \boldsymbol{R}^{\mathrm{t}} \cdot \boldsymbol{R} \cdot \boldsymbol{F} = \boldsymbol{F}^{\mathrm{t}} \cdot \boldsymbol{F} = \boldsymbol{C}\,. \tag{2.17}$$

As an example of strain measures, the Seth-Hill-family of generalized strains is introduced as

$$\boldsymbol{E}^k = \begin{cases} \dfrac{1}{2} \ln \boldsymbol{C} & \text{if } k = 0 \\[2ex] \dfrac{1}{2\,k} \left[\boldsymbol{C}^k - \boldsymbol{I}\right] & \text{else}\,, \end{cases} \tag{2.18}$$

cf. [44, 69, 117, 145]. As a special case, the Green-Lagrange strain tensor ($k = 1$) is denoted by $\boldsymbol{E}$.

Similarly, the left Cauchy-Green tensor can be defined as

$$\boldsymbol{b} := \boldsymbol{F} \cdot \boldsymbol{F}^{\mathrm{t}}. \tag{2.19}$$

In contrast to $\boldsymbol{C}$, $\boldsymbol{b}$ belongs to the deformed configuration. With its help generalized strain tensors of the form

$$\boldsymbol{e}^k = \begin{cases} \dfrac{1}{2} \ln \boldsymbol{b} & \text{if } k = 0 \\ \dfrac{1}{2\,k} \left[\boldsymbol{I} - \boldsymbol{b}^{-k} \right] & \text{else}\,, \end{cases} \tag{2.20}$$

can be defined. For $k = 1$, the Eulerian-Almansi strain tensor $\boldsymbol{e}$ is introduced as a special case.

A linearized theory can be applied under the assumption of small deformations. The infinitesimal strains are defined by

$$\boldsymbol{\varepsilon} = \nabla \boldsymbol{u}^{\mathrm{sym}} = \frac{1}{2} \left[\nabla \boldsymbol{u} + [\nabla \boldsymbol{u}]^{\mathrm{t}} \right], \tag{2.21}$$

which can be derived from Equations (2.18) or (2.20) by considering a linearization with respect to the undeformed configuration. The linearization of a finite rotation is given by a skew-symmetric tensor. The trace of the infinitesimal strain tensor is used as volume change as $\mathrm{Det}(\boldsymbol{F}) \overset{\mathrm{lin.}}{=} 1 + \mathrm{trace}(\boldsymbol{\varepsilon})$ when assuming a geometrically linearized setting.

2.2 Conservation laws

In the following, the conservation of linear momentum and angular momentum as well as the dissipation inequality are summarized.

2.2.1 Balance of linear momentum

The balance of linear momentum states, that the sum of forces acting at any arbitrary bounded regular subdomain $\mathcal{V}_0 \subset \Omega$ with included interface $\mathcal{I}_0 := \mathcal{V}_0 \cap \Gamma$ results in the change of the linear momentum. As only quasi-static processes are investigated in this thesis the linear momentum of the volume is assumed to vanish. Thus, the sum of forces should also vanish. The forces acting on the arbitrary volume are separated into body forces $\boldsymbol{B}$ (force per volume) acting within $\mathcal{V}_0$ and into surface tractions $\boldsymbol{T}$ (force per area) acting on its boundary $\partial\mathcal{V}_0$. Here and in the following, dead loads are assumed for surface tractions and volume forces. Equivalent external loads on the interface and its

boundary are neglected throughout the thesis. The global form of the balance of linear momentum is formulated as

$$\mathbf{0} = \int_{\mathcal{V}_0} \boldsymbol{B}\, \mathrm{d}V + \int_{\partial\mathcal{V}_0} \boldsymbol{T}\, \mathrm{d}A\,. \tag{2.22}$$

In order to derive the local strong form, the volume is assumed to converge to a local point following the localization theorem. If convergence to a point $\boldsymbol{X} \in \mathcal{V}_0 \backslash \mathcal{I}_0$ is assumed identity

$$\boldsymbol{T} = \boldsymbol{P} \cdot \boldsymbol{N}, \tag{2.23}$$

can be applied, which follows from Cauchy's postulate. $\boldsymbol{P}$ denotes the first Piola-Kirchhoff stress tensor. Subsequently, the divergence theorem can be used to transform the surface integral into a volume integral. After some straightforward operations the strong form of the balance of linear momentum reads

$$\mathrm{Div}\,(\boldsymbol{P}) + \boldsymbol{B} = \mathbf{0} \qquad \forall \boldsymbol{X} \in \Omega \backslash \Gamma\,. \tag{2.24}$$

In contrast, assuming a convergence to an an arbitrary point $\overline{\boldsymbol{X}}$ on the included interface Identity (2.23) as well as the additional identity

$$\widetilde{\boldsymbol{T}} = \overline{\boldsymbol{P}} \cdot \widetilde{\boldsymbol{N}} \tag{2.25}$$

are applied. $\boldsymbol{N} \to \overline{\boldsymbol{N}}$ on $\mathcal{I}_+$ and $\boldsymbol{N} \to -\overline{\boldsymbol{N}}$ on $\mathcal{I}_-$ the integrals of the weak form (2.22) can be reinterpreted within the convergence. $\mathcal{I}_+$ and $\mathcal{I}_-$ denote the two sides of the interface. After the application of the divergence theorem for surfaces (see e.g. [64]) with additional condition $\overline{\boldsymbol{P}} \cdot \overline{\boldsymbol{N}} = \mathbf{0}$ the local form of the balance of linear momentum can be derived as

$$\overline{\mathrm{Div}}\left(\overline{\boldsymbol{P}}\right) + [\![\boldsymbol{P}]\!] \cdot \overline{\boldsymbol{N}} = \mathbf{0} \qquad \forall \overline{\boldsymbol{X}} \in \Gamma\,. \tag{2.26}$$

2.2.2 Balance of angular momentum

The balance of angular momentum states that the angular momentum of any volume $\mathcal{V}_0 \subset \Omega$ referring to any fixed point $\boldsymbol{Y} \in \mathbb{R}^{n_{\mathrm{dim}}}$ changes due to the moments induced by force contributions $\boldsymbol{B}$ and $\boldsymbol{T}$ as defined above. For the special case of quasi-static processes the balance of angular momentum reads

$$\mathbf{0} = \int_{\mathcal{V}_0} \boldsymbol{r} \times \boldsymbol{B}\, \mathrm{d}V + \int_{\partial\mathcal{V}_0} \boldsymbol{r} \times \boldsymbol{T}\, \mathrm{d}A\,. \tag{2.27}$$

Here, $\boldsymbol{r} := \boldsymbol{X} - \boldsymbol{Y}$ indicates the connection vector from fixed point $\boldsymbol{Y}$ to arbitrary point $\boldsymbol{X} \in \mathcal{V}_0$.

With derivations similar to the balance of linear momentum, the local balance of angular momentum can be obtained as

$$\boldsymbol{P}\cdot\boldsymbol{F}^{\mathrm{t}} = \left[\boldsymbol{P}\cdot\boldsymbol{F}^{\mathrm{t}}\right]^{\mathrm{t}} = \boldsymbol{F}\cdot\boldsymbol{P}^{\mathrm{t}} \qquad \forall \boldsymbol{X}\in\Omega\backslash\Gamma\,. \tag{2.28}$$

Similar derivations as for the balance of linear momentum finally lead to the local balance of angular momentum for points on the interface

$$\overline{\boldsymbol{P}}\cdot\overline{\boldsymbol{F}}^{\mathrm{t}} + \overline{\boldsymbol{T}}\otimes[\![\boldsymbol{u}]\!] = \left[\overline{\boldsymbol{P}}\cdot\overline{\boldsymbol{F}}^{\mathrm{t}} + \overline{\boldsymbol{T}}\otimes[\![\boldsymbol{u}]\!]\right]^{\mathrm{t}} = \overline{\boldsymbol{F}}\cdot\overline{\boldsymbol{P}}^{\mathrm{t}} + [\![\boldsymbol{u}]\!]\otimes\overline{\boldsymbol{T}} \qquad \forall\overline{\boldsymbol{X}}\in\Gamma\,. \tag{2.29}$$

Accordingly, cohesive zone models (models that do not depend on $\overline{\boldsymbol{F}}$) require $[\![u]\!]\otimes\overline{\boldsymbol{T}}$ to be symmetric (i.e. $[\![u]\!]\otimes\overline{\boldsymbol{T}} = [[\![u]\!]\otimes\overline{\boldsymbol{T}}]^{\mathrm{t}}$) which is equivalent to isotropy. Consequently, the tractions have to be co-linear to the displacement jump in this case.

2.2.3 Dissipation inequality — Second law of thermodynamics

The dissipation inequality is concerned with the direction of processes. The second law of thermodynamics states, that the dissipation always remains non-negative. For points in the bulk ($\boldsymbol{X}\in\Omega\backslash\Gamma$) the dissipation is defined by

$$\begin{aligned}\mathcal{D} &:= \mathcal{P} - \dot{\Psi}\\ &= \boldsymbol{P}\colon\dot{\boldsymbol{F}} - \dot{\Psi}\\ &= \left[\boldsymbol{P} - \frac{\partial\Psi}{\partial\boldsymbol{F}}\right]\colon\dot{\boldsymbol{F}} - \frac{\partial\Psi}{\partial\boldsymbol{\alpha}}\circ\dot{\boldsymbol{\alpha}} \quad \geq 0 \quad \forall\,\dot{\boldsymbol{F}}\end{aligned} \tag{2.30}$$

for iso-thermal systems. $\mathcal{P} = \boldsymbol{P}\colon\dot{\boldsymbol{F}}$ denotes the stress power and $\Psi(\boldsymbol{F},\boldsymbol{\alpha})$ denotes the Helmholtz energy. The latter one depends on the deformation gradient $\boldsymbol{F}$ as well as on an arbitrary set of internal variables $\boldsymbol{\alpha}$. As the dimension of $\boldsymbol{\alpha}$ is arbitrary, a generalized inner product $\circ$ is applied here and in the following.

Following Coleman and Noll [33] an elastic unloading process is assumed first ($\dot{\boldsymbol{\alpha}} = 0$, $\mathcal{D} = 0$) leading to the thermodynamically stress tensor $\boldsymbol{P} := \partial\Psi/\partial\boldsymbol{F}$ (first Piola-Kirchhoff stress tensor) being dual to the deformation gradient. The reduced dissipation then reads

$$\mathcal{D}^{\mathrm{red}} = \boldsymbol{A}\circ\dot{\boldsymbol{\alpha}} \quad \geq 0 \quad \forall\,\dot{\boldsymbol{\alpha}} \quad \forall\boldsymbol{X}\in\Omega\backslash\Gamma\,, \tag{2.31}$$

where $\boldsymbol{A} := -\partial\Psi/\partial\boldsymbol{\alpha}$ is the thermodynamically dual variable to the internal variable $\boldsymbol{\alpha}$.

Similarly the dissipation in the interface reads

$$\begin{aligned}\overline{\mathcal{D}} &:= \overline{\mathcal{P}} - \dot{\Phi} \\ &= \overline{\boldsymbol{P}} : \dot{\overline{\boldsymbol{F}}} + \overline{\boldsymbol{T}} \cdot [\![\dot{\boldsymbol{u}}]\!] - \dot{\Phi} \quad \geq 0 \\ &= \left[\overline{\boldsymbol{P}} - \frac{\partial \Phi}{\partial \dot{\overline{\boldsymbol{F}}}}\right] : \dot{\overline{\boldsymbol{F}}} + \left[\overline{\boldsymbol{T}} - \frac{\partial \Phi}{\partial [\![\boldsymbol{u}]\!]}\right] \cdot [\![\dot{\boldsymbol{u}}]\!] - \frac{\partial \Phi}{\partial \overline{\boldsymbol{\alpha}}} \circ \dot{\overline{\boldsymbol{\alpha}}} \quad \geq 0 \quad \forall \dot{\overline{\boldsymbol{F}}}, [\![\dot{\boldsymbol{u}}]\!]\end{aligned} \tag{2.32}$$

with interface stress power $\overline{\mathcal{P}} = \overline{\boldsymbol{P}} : \dot{\overline{\boldsymbol{F}}} + \overline{\boldsymbol{T}} \cdot [\![\dot{\boldsymbol{u}}]\!]$ and interface Helmholtz energy $\Phi(\overline{\boldsymbol{F}}, [\![\boldsymbol{u}]\!], \overline{\boldsymbol{\alpha}})$ depending on the interface deformation gradient $\overline{\boldsymbol{F}}$, the displacement jump $[\![\boldsymbol{u}]\!]$ as well as on an arbitrary set of internal variables $\overline{\boldsymbol{\alpha}}$ at the interface. Assuming an elastic unloading ($\dot{\overline{\boldsymbol{\alpha}}} = 0$, $\overline{\mathcal{D}} = 0$) leads to the introduction of $\overline{\boldsymbol{P}} := \partial\Phi/\partial\overline{\boldsymbol{F}}$ and $\overline{\boldsymbol{T}} := \partial\Phi/\partial [\![\boldsymbol{u}]\!]$ as the thermodynamically dual variables to $\overline{\boldsymbol{F}}$ and $[\![\boldsymbol{u}]\!]$. The reduced dissipation finally reads

$$\overline{\mathcal{D}}^{\mathrm{red}} = \overline{\boldsymbol{A}} \circ \dot{\overline{\boldsymbol{\alpha}}} \quad \geq 0 \quad \forall \dot{\overline{\boldsymbol{\alpha}}} \quad \forall \overline{\boldsymbol{X}} \in \Omega \backslash \Gamma \,, \tag{2.33}$$

with dual variable $\overline{\boldsymbol{A}} := -\partial\Phi/\partial\overline{\boldsymbol{\alpha}}$ of the internal variable $\overline{\boldsymbol{\alpha}}$.

2.3 Variational description and free boundary problem

In the following, a variational formulation of interface problems is presented. Within the variational framework balance laws and boundary conditions are introduced by a minimization of the total energy. The variational framework in the field of classical mechanics is well established since centuries (cf. [84]) starting from examples like the brachistochrone [18] up to the solution of modern complex computational problems [28]. Variational descriptions yield numerous advantages such as the elegant mathematical formulation as well as the possibility to apply efficient numerical solution techniques.

Here, incremental energy minimization is used to derive the balance of linear momentum as well as boundary conditions. The technique dates back to pioneering work by [27, 34, 119, 125]. In line with the cited works, the rate of the total energy $\dot{\mathcal{E}}$ of an arbitrary bounded regular subdomain $\mathcal{V}_0 \in \Omega$ in the system is given by

$$\dot{\mathcal{E}} = \dot{\mathcal{E}}^{\mathrm{int}} + \dot{\mathcal{E}}^{\mathrm{ext}} \,, \tag{2.34}$$

with a decomposition into the energy rate $\dot{\mathcal{E}}^{\mathrm{int}}$ resulting from internal quantities like the Helmholtz energies Ψ (bulk) and Φ (interface) and the dissipation functions D (bulk) and $\overline{D}$ (interface) as well as an external energy rate $\dot{\mathcal{E}}^{\mathrm{ext}}$ due to external dead loads $\boldsymbol{B}$

and $\boldsymbol{T}$ as defined in Section 2.2. The interface in arbitrary volume $\mathcal{V}_0$ is denoted by $\mathcal{I}_0 = \mathcal{V}_0 \cap \Gamma$. In general, the energy contributions take the form

$$\dot{\mathcal{E}}^{\text{int}} = \int_{\mathcal{V}_0} \dot{\Psi}(\boldsymbol{F}, \boldsymbol{\alpha}) + D(\boldsymbol{\alpha}, \dot{\boldsymbol{\alpha}})\,\mathrm{d}V + \int_{\mathcal{I}_0} \dot{\Phi}(\overline{\boldsymbol{F}}, [\![\boldsymbol{u}]\!], \overline{\boldsymbol{\alpha}}) + \overline{D}(\overline{\boldsymbol{\alpha}}, \dot{\overline{\boldsymbol{\alpha}}})\,\mathrm{d}A\,, \tag{2.35}$$

$$\dot{\mathcal{E}}^{\text{ext}} = -\int_{\mathcal{V}_0} \boldsymbol{B} \cdot \dot{\boldsymbol{\varphi}}\,\mathrm{d}V - \int_{\partial\mathcal{V}_0} \boldsymbol{T} \cdot \dot{\boldsymbol{\varphi}}\,\mathrm{d}A\,. \tag{2.36}$$

State dependent dissipation functions $D(\boldsymbol{\alpha}, \dot{\boldsymbol{\alpha}})$ and $\overline{D}(\overline{\boldsymbol{\alpha}}, \dot{\overline{\boldsymbol{\alpha}}})$ depend on the internal variables ($\boldsymbol{\alpha}, \dot{\boldsymbol{\alpha}}$ and $\overline{\boldsymbol{\alpha}}, \dot{\overline{\boldsymbol{\alpha}}}$). A stationary point can be found with the condition

$$\delta\dot{\mathcal{E}} = \delta_{\dot{\boldsymbol{\varphi}}}\dot{\mathcal{E}} \cdot \delta\dot{\boldsymbol{\varphi}} + \delta_{\boldsymbol{\alpha}}\dot{\mathcal{E}} \circ \delta\dot{\boldsymbol{\alpha}} + \delta_{\dot{\overline{\boldsymbol{\alpha}}}}\dot{\mathcal{E}} \circ \delta\dot{\overline{\boldsymbol{\alpha}}} \overset{!}{=} 0 \qquad \forall \delta\dot{\boldsymbol{\varphi}}, \delta\dot{\boldsymbol{\alpha}}, \delta\dot{\overline{\boldsymbol{\alpha}}}\,. \tag{2.37}$$

As Condition (2.37) needs to hold for all suitable variations $\delta\dot{\boldsymbol{\varphi}}$, $\delta\dot{\boldsymbol{\alpha}}$, $\delta\dot{\overline{\boldsymbol{\alpha}}}$, conditions

$$\delta_{\dot{\boldsymbol{\varphi}}}\dot{\mathcal{E}} \cdot \delta\dot{\boldsymbol{\varphi}} = \delta_{\dot{\boldsymbol{\varphi}}}\dot{\mathcal{E}}^{\text{int}} \cdot \delta\dot{\boldsymbol{\varphi}} + \delta_{\dot{\boldsymbol{\varphi}}}\dot{\mathcal{E}}^{\text{ext}} \cdot \delta\dot{\boldsymbol{\varphi}} \qquad \overset{!}{=} 0 \qquad \forall \delta\dot{\boldsymbol{\varphi}}\,, \tag{2.38}$$

$$\delta_{\dot{\boldsymbol{\alpha}}}\dot{\mathcal{E}} \circ \delta\dot{\boldsymbol{\alpha}} = \delta_{\dot{\boldsymbol{\alpha}}}\dot{\mathcal{E}}^{\text{int}} \circ \delta\dot{\boldsymbol{\alpha}} \qquad \overset{!}{=} 0 \qquad \forall \delta\dot{\boldsymbol{\alpha}}\,, \tag{2.39}$$

$$\delta_{\dot{\overline{\boldsymbol{\alpha}}}}\dot{\mathcal{E}} \circ \delta\dot{\overline{\boldsymbol{\alpha}}} = \delta_{\dot{\overline{\boldsymbol{\alpha}}}}\dot{\mathcal{E}}^{\text{int}} \circ \delta\dot{\overline{\boldsymbol{\alpha}}} \qquad \overset{!}{=} 0 \qquad \forall \delta\dot{\overline{\boldsymbol{\alpha}}} \tag{2.40}$$

need to hold separately.

First, stationarity condition (2.38) is considered resulting in the balance of linear momentum as well as the boundary conditions of the Neumann boundary. Following [75, 89], a distinction between regular points $\boldsymbol{X} \in \Omega\backslash\Gamma$ and singular points $\overline{\boldsymbol{X}} \in \Gamma$ is made.

Since set $\Omega\backslash\Gamma$ is open, regular points always have a surrounding volume $\mathcal{V}_0 \in \Omega\backslash\Gamma$ with $\boldsymbol{X} \in \mathcal{V}_0$ in which all fields are continuous. For this surrounding volume, the variation of energy rate contribution $\dot{\mathcal{E}}^{\text{int}}$ reduces to

$$\begin{aligned}
\delta_{\dot{\boldsymbol{\varphi}}}\dot{\mathcal{E}}^{\text{int}} \cdot \delta\dot{\boldsymbol{\varphi}} &= \int_{\mathcal{V}_0} \boldsymbol{P} \colon \delta_{\dot{\boldsymbol{\varphi}}}\dot{\boldsymbol{F}}\,\mathrm{d}V \\
&= \int_{\mathcal{V}_0} \boldsymbol{P} \colon \mathrm{Grad}(\delta\dot{\boldsymbol{\varphi}})\,\mathrm{d}V \\
&= \int_{\mathcal{V}_0} -\mathrm{Div}(\boldsymbol{P}) \cdot \delta\dot{\boldsymbol{\varphi}}\,\mathrm{d}V + \int_{\partial\mathcal{V}_0} [\boldsymbol{P} \cdot \boldsymbol{N}] \cdot \delta\dot{\boldsymbol{\varphi}}\,\mathrm{d}A\,,
\end{aligned} \tag{2.41}$$

where identities

$$\boldsymbol{P} \colon \mathrm{Grad}(\delta\dot{\boldsymbol{\varphi}}) = \mathrm{Div}(\delta\dot{\boldsymbol{\varphi}} \cdot \boldsymbol{P}) - \mathrm{Div}(\boldsymbol{P}) \cdot \delta\dot{\boldsymbol{\varphi}}\,, \tag{2.42}$$

$$\int_{\mathcal{V}_0} \mathrm{Div}(\delta\dot{\boldsymbol{\varphi}} \cdot \boldsymbol{P})\mathrm{d}V = \int_{\partial\mathcal{V}_0} [\boldsymbol{P} \cdot \boldsymbol{N}] \cdot \delta\dot{\boldsymbol{\varphi}}\,\mathrm{d}A\,, \tag{2.43}$$

are used to reformulate the variation. Together with the variation of the external energy rate

$$\delta_{\dot{\boldsymbol{\varphi}}}\dot{\mathcal{E}}^{\text{ext}} \cdot \delta\dot{\boldsymbol{\varphi}} = -\int_{\mathcal{V}_0} \boldsymbol{B} \cdot \delta\dot{\boldsymbol{\varphi}}\,\mathrm{d}V - \int_{\partial\mathcal{V}_0} \boldsymbol{T} \cdot \delta\dot{\boldsymbol{\varphi}}\,\mathrm{d}A \tag{2.44}$$

the variation of the total energy rate reads

$$\begin{aligned}\delta_{\dot{\boldsymbol{\varphi}}}\dot{\mathcal{E}}^{\text{int}} \cdot \delta\dot{\boldsymbol{\varphi}} = &\int_{\mathcal{V}_0} -\mathrm{Div}(\boldsymbol{P}) \cdot \delta\dot{\boldsymbol{\varphi}}\,\mathrm{d}V + \int_{\partial\mathcal{V}_0} [\boldsymbol{P}\cdot\boldsymbol{N}] \cdot \delta\dot{\boldsymbol{\varphi}}\,\mathrm{d}A \\ &- \int_{\mathcal{V}_0} \boldsymbol{B} \cdot \delta\dot{\boldsymbol{\varphi}}\,\mathrm{d}V - \int_{\partial\mathcal{V}_0} \boldsymbol{T} \cdot \delta\dot{\boldsymbol{\varphi}}\,\mathrm{d}A \quad \overset{!}{=} 0 \quad \forall\delta\dot{\boldsymbol{\varphi}}.\end{aligned} \tag{2.45}$$

Since this needs to hold for all suitable variations $\delta\dot{\boldsymbol{\varphi}}$, the strong form can be derived as

$$\mathrm{Div}(\boldsymbol{P}) + \boldsymbol{B} = \boldsymbol{0} \qquad \forall \boldsymbol{X} \in \Omega\backslash\Gamma \tag{2.46}$$

$$\boldsymbol{P}\cdot\boldsymbol{N} - \boldsymbol{T} = \boldsymbol{0} \qquad \forall \boldsymbol{X} \in \partial\Omega_{\mathrm{N}}\backslash\Gamma\,. \tag{2.47}$$

where the index N denotes prescribed external tractions at the Neumann boundary $\partial\Omega_{\mathrm{N}}$.

Regarding singular points $\overline{\boldsymbol{X}} \in \Gamma$, any volume $\mathcal{V}_0$ contains a portion of the interface $\mathcal{I}_0 = \mathcal{V}_0 \cup \Gamma \neq \emptyset$. In this case the volume is considered to converge to the interface such that the boundary $\partial\mathcal{V}_0$ converges to the interface sides $\mathcal{I}_+$ and $\mathcal{I}_-$. The normal vectors converge to $\boldsymbol{N} \to \overline{\boldsymbol{N}}$ on $\mathcal{I}_+$ and $\boldsymbol{N} \to -\overline{\boldsymbol{N}}$ on $\mathcal{I}_-$ (see Figure 2.4).

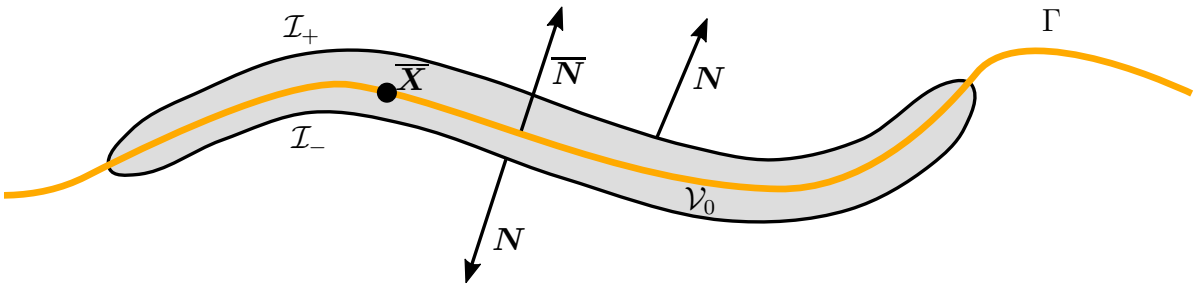

Figure 2.4: Converging volume towards the interface at a singular point $\overline{\boldsymbol{X}}$.

Regarding the energy rates the volume integrals cancel out ($|\mathcal{V}_0| \to 0$). Thus, energy rate contribution $\dot{\mathcal{E}}^{\text{int}}$ reduces to

$$\dot{\mathcal{E}}^{\text{int}} = \int_{\mathcal{I}_0} \overline{\boldsymbol{P}} : \dot{\overline{\boldsymbol{F}}} + \overline{\boldsymbol{T}} \cdot [\![\dot{\boldsymbol{u}}]\!]\,\mathrm{d}A. \tag{2.48}$$

Again, identity

$$\overline{\boldsymbol{P}} : \overline{\mathrm{Grad}}(\delta\dot{\overline{\boldsymbol{\varphi}}}) = \overline{\mathrm{Div}}(\delta\dot{\overline{\boldsymbol{\varphi}}} \cdot \overline{\boldsymbol{P}}) - \overline{\mathrm{Div}}(\overline{\boldsymbol{P}}) \cdot \delta\dot{\overline{\boldsymbol{\varphi}}} \tag{2.49}$$

is applied to derive the variation of the internal energy. In addition, a surface divergence theorem (see e.g. [64]) of the form

$$\int_{\mathcal{I}_0} \overline{\mathrm{Div}}(\delta\dot{\overline{\boldsymbol{\varphi}}} \cdot \overline{\boldsymbol{P}})\,\mathrm{d}A = \int_{\partial\mathcal{I}_0} \delta\dot{\overline{\boldsymbol{\varphi}}} \cdot \overline{\boldsymbol{P}} \cdot \widetilde{\boldsymbol{N}}\,\mathrm{d}\boldsymbol{L} + \int_{\mathcal{I}_0} \overline{\kappa}\,\delta\dot{\boldsymbol{\varphi}} \cdot \overline{\boldsymbol{P}} \cdot \overline{\boldsymbol{N}}\,\mathrm{d}A, \tag{2.50}$$

with curvature $\overline{\kappa}$ is applied. Assuming superficiality in the sence of $\overline{\boldsymbol{P}} \cdot \overline{\boldsymbol{N}} = \boldsymbol{0}$ the last term cancels out (which holds particularly true for the considered coherent interfaces as well as for cohesive zone models). The variation finally reads

$$\begin{aligned}
\delta_{\dot{\boldsymbol{\varphi}}}\dot{\mathcal{E}}^{\mathrm{int}} \cdot \delta\dot{\boldsymbol{\varphi}} &= \int_{\mathcal{I}_0} \overline{\boldsymbol{P}} \colon \delta_{\dot{\boldsymbol{\varphi}}}\dot{\overline{\boldsymbol{F}}} + \overline{\boldsymbol{T}} \cdot \delta_{\dot{\boldsymbol{\varphi}}}[\![\dot{\boldsymbol{u}}]\!]\,\mathrm{d}A \\
&= \int_{\mathcal{I}_0} \overline{\boldsymbol{P}} \colon \overline{\mathrm{Grad}}(\delta_{\dot{\boldsymbol{\varphi}}}\dot{\overline{\boldsymbol{\varphi}}}) + \overline{\boldsymbol{T}} \cdot \delta_{\dot{\boldsymbol{\varphi}}}[\![\dot{\boldsymbol{u}}]\!]\,\mathrm{d}A \\
&= \int_{\mathcal{I}_0} -\overline{\mathrm{Div}}(\overline{\boldsymbol{P}}) \cdot \delta_{\dot{\boldsymbol{\varphi}}}\dot{\overline{\boldsymbol{\varphi}}} + \overline{\boldsymbol{T}} \cdot \delta_{\dot{\boldsymbol{\varphi}}}[\![\dot{\boldsymbol{u}}]\!]\,\mathrm{d}A + \int_{\partial\mathcal{I}_0} \delta_{\dot{\boldsymbol{\varphi}}}\dot{\overline{\boldsymbol{\varphi}}} \cdot \overline{\boldsymbol{P}} \cdot \widetilde{\boldsymbol{N}}\,\mathrm{d}\boldsymbol{L}
\end{aligned} \tag{2.51}$$

In contrast to the volume integrals, the boundary $\partial\mathcal{V}_0$ does not vanish but converges to $\partial\mathcal{V}_0 \to \mathcal{I}_+ \cup \mathcal{I}_- = \mathcal{I}_0$. Consequently, the boundary term can be reformulated as

$$\int_{\partial\mathcal{V}_0} \boldsymbol{T} \cdot \dot{\boldsymbol{\varphi}}\,\mathrm{d}A \to \int_{\mathcal{I}_+=\mathcal{I}_0} \boldsymbol{T}_+ \cdot \dot{\boldsymbol{\varphi}}_+\,\mathrm{d}A + \int_{\mathcal{I}_-=\mathcal{I}_0} \boldsymbol{T}_- \cdot \dot{\boldsymbol{\varphi}}_-\,\mathrm{d}A, \tag{2.52}$$

leading to external energy

$$\dot{\mathcal{E}}^{\mathrm{ext}} = -\int_{\mathcal{I}_0} \boldsymbol{T}_+ \cdot \dot{\boldsymbol{\varphi}}_+ + \boldsymbol{T}_- \cdot \dot{\boldsymbol{\varphi}}_-\,\mathrm{d}A. \tag{2.53}$$

Its variation takes the form

$$\delta_{\dot{\boldsymbol{\varphi}}}\dot{\mathcal{E}}^{\mathrm{ext}} \cdot \delta\dot{\boldsymbol{\varphi}} = -\int_{\mathcal{I}_+=\mathcal{I}_0} \boldsymbol{T}_+ \cdot \delta_{\dot{\boldsymbol{\varphi}}}\dot{\boldsymbol{\varphi}}_+ + \int_{\mathcal{I}_-=\mathcal{I}_0} \boldsymbol{T}_- \cdot \delta_{\dot{\boldsymbol{\varphi}}}\dot{\boldsymbol{\varphi}}_-. \tag{2.54}$$

When applying the relationships

$$\delta_{\dot{\boldsymbol{\varphi}}}\dot{\overline{\boldsymbol{\varphi}}} = \delta_{\dot{\boldsymbol{\varphi}}}\{\!\{\dot{\boldsymbol{\varphi}}\}\!\} = \frac{1}{2}\left[\delta_{\dot{\boldsymbol{\varphi}}}\dot{\boldsymbol{\varphi}}_+ + \delta_{\dot{\boldsymbol{\varphi}}}\dot{\boldsymbol{\varphi}}_-\right] \tag{2.55}$$

$$\delta_{\dot{\boldsymbol{\varphi}}}[\![\dot{\boldsymbol{u}}]\!] = \delta_{\dot{\boldsymbol{\varphi}}}[\![\dot{\boldsymbol{\varphi}}]\!] = \delta_{\dot{\boldsymbol{\varphi}}}\dot{\boldsymbol{\varphi}}_+ - \delta_{\dot{\boldsymbol{\varphi}}}\dot{\boldsymbol{\varphi}}_- \tag{2.56}$$

the variation of the total energy reads

$$\begin{aligned}
\delta_{\dot{\boldsymbol{\varphi}}}\dot{\mathcal{E}} \cdot \delta\dot{\boldsymbol{\varphi}} = \int_{\mathcal{I}_0} &-\frac{1}{2}\overline{\mathrm{Div}}(\overline{\boldsymbol{P}}) \cdot \left[\delta_{\dot{\boldsymbol{\varphi}}}\dot{\boldsymbol{\varphi}}_+ + \delta_{\dot{\boldsymbol{\varphi}}}\dot{\boldsymbol{\varphi}}_-\right] + \overline{\boldsymbol{T}} \cdot \left[\delta_{\dot{\boldsymbol{\varphi}}}\dot{\boldsymbol{\varphi}}_+ - \delta_{\dot{\boldsymbol{\varphi}}}\dot{\boldsymbol{\varphi}}_-\right] \\
&- \boldsymbol{T}_+ \cdot \delta_{\dot{\boldsymbol{\varphi}}}\dot{\boldsymbol{\varphi}}_+ - \boldsymbol{T}_- \cdot \delta_{\dot{\boldsymbol{\varphi}}}\dot{\boldsymbol{\varphi}}_- \\
&+ \int_{\partial\mathcal{I}_0} \frac{1}{2}\overline{\boldsymbol{P}} \cdot \widetilde{\boldsymbol{N}} \cdot \left[\delta_{\dot{\boldsymbol{\varphi}}}\dot{\boldsymbol{\varphi}}_+ + \delta_{\dot{\boldsymbol{\varphi}}}\dot{\boldsymbol{\varphi}}_-\right] \overset{!}{=} 0.
\end{aligned} \tag{2.57}$$

By choosing $\delta_{\dot{\boldsymbol{\varphi}}}\dot{\boldsymbol{\varphi}}_+ \equiv -\delta_{\dot{\boldsymbol{\varphi}}}\dot{\boldsymbol{\varphi}}_-$, the local form

$$\overline{\boldsymbol{T}} - \frac{1}{2}\left[\boldsymbol{T}_+ - \boldsymbol{T}_-\right] = \boldsymbol{0} \qquad \forall \overline{\boldsymbol{X}} \in \Gamma \tag{2.58}$$

is obtained. With the choice $\delta_{\dot{\boldsymbol{\varphi}}}\dot{\boldsymbol{\varphi}}_+ \equiv \delta_{\dot{\boldsymbol{\varphi}}}\dot{\boldsymbol{\varphi}}_-$ the local form reads

$$\overline{\mathrm{Div}}(\overline{\boldsymbol{P}}) + \left[\boldsymbol{T}_+ + \boldsymbol{T}_-\right] = \boldsymbol{0} \qquad \forall \overline{\boldsymbol{X}} \in \Gamma \tag{2.59}$$

$$\overline{\boldsymbol{P}} \cdot \widetilde{\boldsymbol{N}} = \boldsymbol{0} \qquad \forall \overline{\boldsymbol{X}} \in \partial\Gamma_{\mathrm{N}}\,, \tag{2.60}$$

where the index N denotes prescribed external tractions at the Neumann boundary $\partial\Omega_{\mathrm{N}}$. Applying the result of Cauchy's theorem, identity $\boldsymbol{T}_+ + \boldsymbol{T}_- = [\![\boldsymbol{P}]\!] \cdot \overline{\boldsymbol{N}}$ follows, leading to free boundary problem

$$\mathrm{Div}(\boldsymbol{P}) + \boldsymbol{B} = \boldsymbol{0} \qquad \forall \boldsymbol{X} \in \Omega\backslash\Gamma \tag{2.61}$$

$$\overline{\boldsymbol{T}} - \frac{1}{2}\left[\boldsymbol{T}_+ - \boldsymbol{T}_-\right] = \boldsymbol{0} \qquad \forall \overline{\boldsymbol{X}} \in \Gamma \tag{2.62}$$

$$\overline{\mathrm{Div}}(\overline{\boldsymbol{P}}) + \left[\boldsymbol{T}_+ + \boldsymbol{T}_-\right] = \boldsymbol{0} \qquad \forall \overline{\boldsymbol{X}} \in \Gamma \tag{2.63}$$

$$\boldsymbol{P} \cdot \boldsymbol{N} - \boldsymbol{T}_{\mathrm{N}} = \boldsymbol{0} \qquad \forall \boldsymbol{X} \in \partial\Omega_{\mathrm{N}} \tag{2.64}$$

$$\overline{\boldsymbol{P}} \cdot \widetilde{\boldsymbol{N}} = \boldsymbol{0} \qquad \forall \overline{\boldsymbol{X}} \in \partial\Gamma_{\mathrm{N}} \tag{2.65}$$

Next, stationarity condition (2.39) is considered. For $\boldsymbol{\alpha}$ the variation of the total energy rate reduces to Biot's equation (cf. [20])

$$\begin{aligned} \delta_{\dot{\boldsymbol{\alpha}}}\dot{\mathcal{E}} \cdot \delta\dot{\boldsymbol{\alpha}} &= \int_{\mathcal{V}_0} \frac{\partial \Psi}{\partial \boldsymbol{\alpha}} \circ \delta\dot{\boldsymbol{\alpha}} + \delta_{\dot{\boldsymbol{\alpha}}} D \circ \delta\dot{\boldsymbol{\alpha}}\, \mathrm{d}V \\ &= \int_{\mathcal{V}_0} -\boldsymbol{A} \circ \delta\dot{\boldsymbol{\alpha}} + \delta_{\dot{\boldsymbol{\alpha}}} D \circ \delta\dot{\boldsymbol{\alpha}}\, \mathrm{d}V \quad \ni \{0\}\,, \end{aligned} \tag{2.66}$$

where $\boldsymbol{A} = -\partial\Psi/\partial\boldsymbol{\alpha}$ denotes the thermodynamically dual variable to $\boldsymbol{\alpha}$. The local form reads

$$\boldsymbol{A} \in \delta_{\dot{\boldsymbol{\alpha}}} D. \tag{2.67}$$

For $\overline{\boldsymbol{\alpha}}$ the variation of the total energy rate takes the form

$$\begin{aligned} \delta_{\dot{\boldsymbol{\alpha}}}\dot{\mathcal{E}} \cdot \delta\dot{\boldsymbol{\alpha}} &= \int_{\mathcal{I}_0} \frac{\partial \Phi}{\partial \overline{\boldsymbol{\alpha}}} \circ \delta\dot{\overline{\boldsymbol{\alpha}}} + \delta_{\dot{\overline{\boldsymbol{\alpha}}}} \overline{D} \circ \delta\dot{\overline{\boldsymbol{\alpha}}}\, \mathrm{d}A \\ &= \int_{\mathcal{I}_0} -\overline{\boldsymbol{A}} \circ \delta\dot{\overline{\boldsymbol{\alpha}}} + \delta_{\dot{\overline{\boldsymbol{\alpha}}}} \overline{D} \circ \delta\dot{\overline{\boldsymbol{\alpha}}}\, \mathrm{d}A \quad \ni \{0\}\,. \end{aligned} \tag{2.68}$$

$\overline{\boldsymbol{A}} = -\partial\Phi/\partial\overline{\boldsymbol{\alpha}}$ denotes the thermodynamically dual variable to $\overline{\boldsymbol{\alpha}}$. The local form of the evolution equation reads

$$\overline{\boldsymbol{A}} \in \delta_{\dot{\overline{\boldsymbol{\alpha}}}}\overline{D}. \tag{2.69}$$

2.4 Constitutive modeling

In contrast to fundamental physical theorems, constitutive relations are chosen as modeling assumption for each individual problem. They describe the interaction of physical quantities such as strains and stresses.

2.4.1 Bulk modeling

The Helmholtz energy density of the bulk solely depends on the deformation gradient and a set of internal variables

$$\Psi = \Psi(\boldsymbol{F}, \boldsymbol{\alpha}). \tag{2.70}$$

As presented in Section 2.2.3 and following the procedure from Coleman and Noll [33] the first Piola-Kirchhoff stress as dual variable to the deformation gradient $\boldsymbol{F}$ can be derived as

$$\boldsymbol{P} = \frac{\partial\Psi}{\partial\boldsymbol{F}}. \tag{2.71}$$

Rigid body movements ($\boldsymbol{\varphi} = \boldsymbol{R}\cdot\boldsymbol{X} + \boldsymbol{c},\ \boldsymbol{c} \in \mathbb{R}^{n_{\mathrm{dim}}}, \boldsymbol{R} \in \mathcal{SO}(n_{\mathrm{dim}})$) of the body should not affect the energy. As a consequence, the energy has to depend on the right Cauchy-Green strain tensor $\boldsymbol{C} = \boldsymbol{F}^{\mathrm{t}}\cdot\boldsymbol{F}$. The first Piola-Kirchhoff stresses then read

$$\boldsymbol{P} = 2\,\boldsymbol{F}\cdot\frac{\partial\Psi}{\partial\boldsymbol{C}}. \tag{2.72}$$

Since

$$\boldsymbol{P}\cdot\boldsymbol{F}^{\mathrm{t}} = 2\,\boldsymbol{F}\cdot\frac{\partial\Psi}{\partial\boldsymbol{C}}\cdot\boldsymbol{F}^{T} \tag{2.73}$$

is symmetric balance of angular momentum is automatically fulfilled.

By choosing a non-negative, convex dissipation function D with $D(0) = 0$ the second law of thermodynamics (Section 2.2.3), i.e.

$$\mathcal{D}^{\mathrm{red}} = \boldsymbol{A}\circ\dot{\boldsymbol{\alpha}} \quad \geq 0 \quad \forall\,\dot{\overline{\boldsymbol{\alpha}}}\,, \tag{2.74}$$

is fulfilled a priori. However, since only reversible effects are considered throughout the thesis regarding the bulk material, no internal variables $\boldsymbol{\alpha}$ at the bulk are applied in the following.

2.4.2 Interface modeling

The Helmholtz energy density of the interface depends on the surface deformation gradient $\overline{\boldsymbol{F}}$, on the opening of the interface – the displacement jump $[\![\boldsymbol{u}]\!]$ – as well as an arbitrary set of internal variables $\overline{\boldsymbol{\alpha}}$

$$\Phi = \Phi(\overline{\boldsymbol{F}}, [\![\boldsymbol{u}]\!], \overline{\boldsymbol{\alpha}}) \,. \tag{2.75}$$

The procedure of Coleman and Noll [33] results in the dual variables

$$\overline{\boldsymbol{P}} = \frac{\partial \Phi}{\partial \overline{\boldsymbol{F}}} \quad \text{and} \quad \overline{\boldsymbol{T}} = \frac{\partial \Phi}{\partial [\![\boldsymbol{u}]\!]} \,, \tag{2.76}$$

as already described in Section 2.2.3.

Similar to the bulk material, rotation invariance of the energy is enforced by using the right Cauchy-Green tensor

$$\overline{\boldsymbol{C}} := \overline{\boldsymbol{F}}^{\mathrm{t}} \cdot \overline{\boldsymbol{F}} \,. \tag{2.77}$$

Likewise, the rotation-invariant

$$I_1 := \| [\![\boldsymbol{u}]\!] \| \tag{2.78}$$

is chosen leading to isotropic cohesive laws. Choosing these deformation measures, objectivity as well as the balance of angular momentum are fulfilled a priori.

By choosing a non-negative, convex dissipation function $\overline{D}$ with $\overline{D}(0) = 0$ the second law of thermodynamics (Section 2.2.3), i.e.

$$\overline{\mathcal{D}}^{\mathrm{red}} = \overline{\boldsymbol{A}} \circ \dot{\overline{\boldsymbol{\alpha}}} \quad \geq 0 \quad \forall \, \dot{\overline{\boldsymbol{\alpha}}} \,. \tag{2.79}$$

is also fulfilled a priori.

Interfaces can be categorized as perfect interfaces, coherent interfaces, cohesive interfaces or general interfaces. In the following, these interface types are summarized. Table 2.1 presents the resulting boundary problems while Figure 2.5 visualizes the underlying mechanisms.

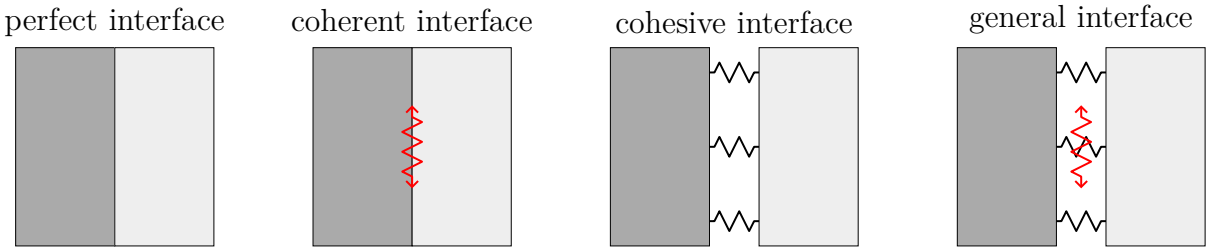

Figure 2.5: Comparison of the mechanisms working in perfect, coherent, cohesive and general interfaces. The symbolized springs denote tractions over the open interface and stresses tangential to the interface.

Perfect interfaces Perfect interfaces are characterized by the constant interface energy density

$$\Phi = \text{const.} \,. \tag{2.80}$$

Consequently, regarding the principle of energy minimization, the interface will always try to minimize its area if $\Phi > 0$.

Coherent interfaces Coherent interfaces were introduced by Gurtin and Murdoch [64, 65, 111]. For coherent interfaces the energy density is assumed to depend only on the surface deformation gradient and internal variables

$$\Phi = \hat{\Phi}(\overline{\boldsymbol{F}}, \overline{\boldsymbol{\alpha}}) \,. \tag{2.81}$$

In this thesis a hyperelastic framework is chosen such that the Helmholtz energy only depends on the deformation gradient $\Phi = \hat{\Phi}(\overline{\boldsymbol{F}})$.

Cohesive interfaces Cohesive interfaces were first presented by Barenblatt [15, 16] and Dugdale [46]. The local Helmholtz energy takes the form

$$\Phi = \hat{\Phi}(\llbracket \boldsymbol{u} \rrbracket, \overline{\boldsymbol{\alpha}}) \,. \tag{2.82}$$

This allows tractions over the open interface. These relationships are called Traction-Separation Laws (TSL). Following boundary problem (Table 2.1) the traction vector is continuous across the interface for this type of model.

General interfaces The interface's energy depends on both – the interface deformation gradient $\overline{\boldsymbol{F}}$ as well as the displacement jump $\llbracket \boldsymbol{u} \rrbracket$

$$\Phi = \hat{\Phi}(\overline{\boldsymbol{F}}, \llbracket \boldsymbol{u} \rrbracket, \overline{\boldsymbol{\alpha}}) \,. \tag{2.83}$$

Consequently, stresses tangential to the interface as well as tractions over the open interface are possible. A summary of the different interface types is given in Table 2.1.

General interfaces $\Phi = \hat{\Phi}(\overline{\boldsymbol{F}}, [\![\boldsymbol{u}]\!], \overline{\boldsymbol{\alpha}})$	Coherent interfaces $\Phi = \hat{\Phi}(\overline{\boldsymbol{F}}, \overline{\boldsymbol{\alpha}})$
$\mathrm{Div}(\boldsymbol{P}) + \boldsymbol{B} = \boldsymbol{0} \quad \forall \boldsymbol{X} \in \Omega \backslash \Gamma$ $\overline{\boldsymbol{T}} - \frac{1}{2}\left[\boldsymbol{T}_+ - \boldsymbol{T}_-\right] = \boldsymbol{0} \quad \forall \overline{\boldsymbol{X}} \in \Gamma$ $\overline{\mathrm{Div}}(\overline{\boldsymbol{P}}) + \left[\boldsymbol{T}_+ + \boldsymbol{T}_-\right] = \boldsymbol{0} \quad \forall \overline{\boldsymbol{X}} \in \Gamma$ $\boldsymbol{P} \cdot \boldsymbol{N} - \boldsymbol{T}_{\mathrm{N}} = \boldsymbol{0} \quad \forall \boldsymbol{X} \in \partial\Omega_{\mathrm{N}}$ $\overline{\boldsymbol{P}} \cdot \widetilde{\boldsymbol{N}} = \boldsymbol{0} \quad \forall \overline{\boldsymbol{X}} \in \partial\Gamma_{\mathrm{N}}$	$\mathrm{Div}(\boldsymbol{P}) + \boldsymbol{B} = \boldsymbol{0} \quad \forall \boldsymbol{X} \in \Omega \backslash \Gamma$ $\overline{\mathrm{Div}}(\overline{\boldsymbol{P}}) + \left[\boldsymbol{T}_+ + \boldsymbol{T}_-\right] = \boldsymbol{0} \quad \forall \overline{\boldsymbol{X}} \in \Gamma$ $\boldsymbol{P} \cdot \boldsymbol{N} - \boldsymbol{T}_{\mathrm{N}} = \boldsymbol{0} \quad \forall \boldsymbol{X} \in \partial\Omega_{\mathrm{N}}$ $\overline{\boldsymbol{P}} \cdot \widetilde{\boldsymbol{N}} = \boldsymbol{0} \quad \forall \overline{\boldsymbol{X}} \in \partial\Gamma_{\mathrm{N}}$
Cohesive interfaces $\Phi = \hat{\Phi}([\![\boldsymbol{u}]\!], \overline{\boldsymbol{\alpha}})$	Perfect interfaces $\Phi = \text{const.}$
$\mathrm{Div}(\boldsymbol{P}) + \boldsymbol{B} = \boldsymbol{0} \quad \forall \boldsymbol{X} \in \Omega \backslash \Gamma$ $\overline{\boldsymbol{T}} - \frac{1}{2}\left[\boldsymbol{T}_+ - \boldsymbol{T}_-\right] = \boldsymbol{0} \quad \forall \overline{\boldsymbol{X}} \in \Gamma$ $\boldsymbol{T}_+ + \boldsymbol{T}_- = \boldsymbol{0} \quad \forall \overline{\boldsymbol{X}} \in \Gamma$ $\boldsymbol{P} \cdot \boldsymbol{N} - \boldsymbol{T}_{\mathrm{N}} = \boldsymbol{0} \quad \forall \boldsymbol{X} \in \partial\Omega_{\mathrm{N}}$	$\mathrm{Div}(\boldsymbol{P}) + \boldsymbol{B} = \boldsymbol{0} \quad \forall \boldsymbol{X} \in \Omega \backslash \Gamma$ $\boldsymbol{T}_+ - \boldsymbol{T}_- = \boldsymbol{0} \quad \forall \overline{\boldsymbol{X}} \in \Gamma$ $\boldsymbol{P} \cdot \boldsymbol{N} - \boldsymbol{T}_{\mathrm{N}} = \boldsymbol{0} \quad \forall \boldsymbol{X} \in \partial\Omega_{\mathrm{N}}$

Table 2.1: Free boundary problems under the assumption of general, coherent, cohesive and perfect interfaces.

3 Phase field approximations of coherent interfaces

In the following a phase field approach to interface elasticity is presented. First, a prototype model for perfect interfaces is introduced. Subsequently, this prototype model is extended to interface elasticity. Finally, numerical examples highlight the capabilities of the novel approach.

3.1 Two-phase systems — A prototype model with perfect interfaces

In two-phase systems, interface Γ separates the two phases Ω_+ and Ω_- such that $\Omega = \Omega_+ \cup \Omega_- \cup \Gamma$ and $\Omega_+ \cap \Omega_- = \emptyset$. Consequently, the total Helmholtz energy of the system consists of three parts

$$\mathcal{E}^{\text{int}}[\boldsymbol{u}] = \int_{\Omega_+} \Psi_+(\boldsymbol{F}_+)\mathrm{d}V + \int_{\Omega_-} \Psi_-(\boldsymbol{F}_-)\mathrm{d}V + \int_{\Gamma} \Phi \,\mathrm{d}A\,, \tag{3.1}$$

where the interface energy density Φ is assumed to be constant. The integrated Helmholtz energy is approximated by using the phase field approach

$$\mathcal{E}^{\text{int}}_{\varepsilon}[\boldsymbol{u}, p] = \int_{\Omega} \Psi(\boldsymbol{F}, p) + \Phi\, f_{\varepsilon}(p, \nabla p)\,\mathrm{d}V\,. \tag{3.2}$$

The subscript ε refers to the phase field setting. A continuous order parameter field or phase field $p \in [0, 1]$ is introduced which can be interpreted as relative volume fraction of phase Ω_+. Accordingly, $p = 1$ coincides with phase Ω_+, whereas $p = 0$ characterize phase Ω_-. The bulk energy density of the mixture phase ($p \in (0, 1)$) is approximated as

$$\Psi(\boldsymbol{F}, p) := p\,\Psi_+(\boldsymbol{F}_+) + (1 - p)\,\Psi_-(\boldsymbol{F}_-)\,. \tag{3.3}$$

The deformation gradient $\boldsymbol{F}_+$ describes the deformations of phases Ω_+ while deformation gradient of phase Ω_- reads $\boldsymbol{F}_-$. Their construction is explained in Section 3.1.1 . The interface energy is approximated by

$$f_\varepsilon(p, \nabla p) := \frac{6}{\varepsilon} p^2 (1-p)^2 + \frac{3}{2} \varepsilon \|\nabla p\|^2 . \tag{3.4}$$

Here, the regularization length ε is related to the thickness of the diffuse interface.

For the one-dimensional minimization problem

$$\min_p \int_{\mathbb{R}} f_\varepsilon(p, \nabla p) \mathrm{d}x \qquad \text{s.t. } p(x=0) = \frac{1}{2} \tag{3.5}$$

the analytical solution takes the form

$$p_{\mathrm{opt}}(X) = \frac{1}{2} \left[\tanh\left(\frac{X}{\varepsilon}\right) + 1 \right] . \tag{3.6}$$

By inserting this solution into the initial interface energy one obtains

$$\int_{\mathbb{R}} f_\varepsilon(p_{\mathrm{opt}}, \nabla p_{\mathrm{opt}}) \, \mathrm{d}V = 1 = \mathcal{H}_\Gamma \tag{3.7}$$

independent of the regularization length ε. $\mathcal{H}_\Gamma$ denotes the Hausdorff measure which can be interpreted as area of the interface. For $n_{\mathrm{dim}} = 1$ a point has a Hausdorff measure of 1. Thus, the phase field approximation is indeed consistent with the underlying sharp interface problem. The solution (3.6) is depicted in Figure 3.1 for varying regularization length ε.

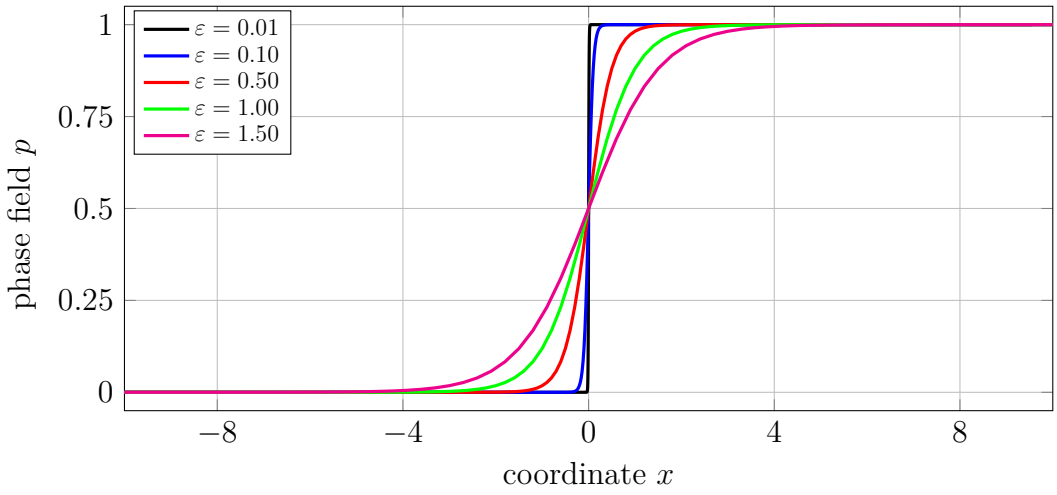

Figure 3.1: Phase-field solutions for one-dimensional minimization problem (3.5) for varying regularization length ε.

The isoline at $p = 1/2$ can be interpreted as a discrete interface. Consequently, the interface normal can be approximated by

$$\overline{\boldsymbol{N}} \approx \overline{\boldsymbol{N}}_p := \frac{1}{\|\nabla p\|} \nabla p \,. \tag{3.8}$$

When introducing the work due to external forces

$$\mathcal{E}^{\mathrm{ext},\Omega}[\boldsymbol{u}] := -\int_\Omega \boldsymbol{B} \cdot \boldsymbol{u} \,\mathrm{d}V - \int_{\partial\Omega} \boldsymbol{T} \cdot \boldsymbol{u} \,\mathrm{d}\boldsymbol{A} \,, \tag{3.9}$$

the total energy of the system reads

$$\mathcal{E}_\varepsilon^{\mathrm{tot}}[\boldsymbol{u}, p] = \mathcal{E}_\varepsilon^{\mathrm{int}}[\boldsymbol{u}, p] + \mathcal{E}^{\mathrm{ext},\Omega}[\boldsymbol{u}] \,. \tag{3.10}$$

$\boldsymbol{B}$ denotes volumetric body forces and $\boldsymbol{T}$ denotes the traction vector on the (external) surface of the body. Solving variational principle

$$(\boldsymbol{u}, p) := \operatorname*{arg\,min}_{(\boldsymbol{u},p)} \mathcal{E}_\varepsilon^{\mathrm{tot}}[\boldsymbol{u}, p] \tag{3.11}$$

results in the fields $\boldsymbol{u}$ and p.

3.1.1 Homogenization

In the transition zones, where both phases coexist, the effective bulk material can be computed by suitable homogenization assumptions. Assuming a constant deformation gradient within each phase (at a certain material point), the respective deformation gradients read

$$\boldsymbol{F}_+ := \boldsymbol{F} + (1-p)\, [\![\boldsymbol{F}]\!] \tag{3.12}$$

$$\boldsymbol{F}_- := \boldsymbol{F} - p\, [\![\boldsymbol{F}]\!] \,, \tag{3.13}$$

with deformation gradient jump $[\![\boldsymbol{F}]\!] = \boldsymbol{F}_+ - \boldsymbol{F}_-$. The bulk energy density of the mixture of the two phases is assumed as

$$\Psi(\boldsymbol{F}, [\![\boldsymbol{F}]\!], p) = p\, \Psi_+(\boldsymbol{F} + (1-p)\, [\![\boldsymbol{F}]\!]) + (1-p)\, \Psi_-(\boldsymbol{F} - p\, [\![\boldsymbol{F}]\!]) \,, \tag{3.14}$$

using the relative volume fractions of the two phases. The jump of the deformation gradient then follows from the local energy minimization problem

$$[\![\boldsymbol{F}]\!]_{\mathrm{opt}} = \min_{[\![\boldsymbol{F}]\!] \in \mathcal{F}} \Psi(\boldsymbol{F}, [\![\boldsymbol{F}]\!], p) \,, \tag{3.15}$$

where the set of admissible deformation gradient jumps $\mathcal{F}$ remains to be defined. In the following, four well established choices are summarized.

	Reuss/Sachs	Rank 1	Partial Rank 1	Taylor/Voigt
kin. compatibility	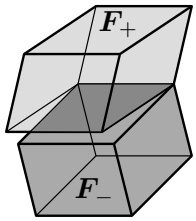	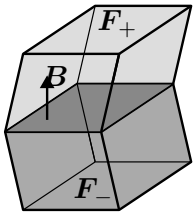	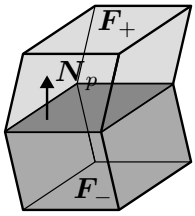	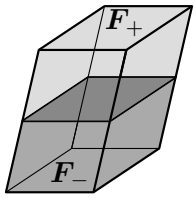
static compatibility	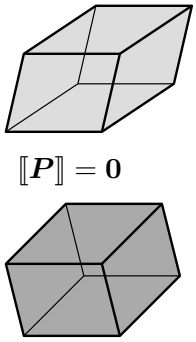	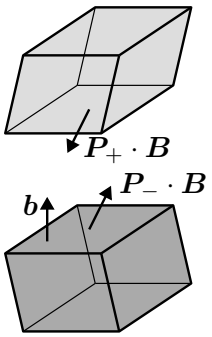	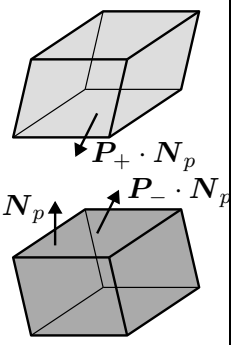	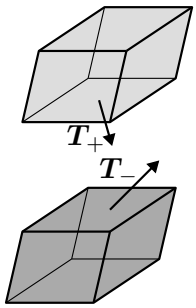
adm. space	$[\![\boldsymbol{F}]\!] \in \mathbb{R}^{3\times3}$	$[\![\boldsymbol{F}]\!] = \boldsymbol{a} \otimes \boldsymbol{B}$ $\boldsymbol{a} \in \mathbb{R}^3, \boldsymbol{b} \in S^2$	$[\![\boldsymbol{F}]\!] = \boldsymbol{a} \otimes \boldsymbol{N}_p$ $\boldsymbol{a} \in \mathbb{R}^3$	$[\![\boldsymbol{F}]\!] = \boldsymbol{0}$

Table 3.1: Overview of the homogenization assumptions: The first two rows depict the kinematic compatibility as well as the static compatibility. The last row defines the admissible displacement gradient jumps.

Taylor-Voigt Taylor and Voigt [152] took the assumption that $\mathcal{F} = \mathcal{F}_{\mathrm{TV}} = \{\boldsymbol{0}\}$ leading to $\boldsymbol{F}_+ = \boldsymbol{F}_- = \boldsymbol{F}$. Therefore, the Taylor-Voigt approach supplies an upper energy bound. With kinematic compatibility as prescribed by the assumption $[\![\boldsymbol{F}]\!] = \boldsymbol{0}$ the Hadamard jump condition (2.13) is fulfilled by definition. However, this assumption does not fulfill equilibrium conditions at the interface. In the setting of phase field approximations the Taylor-Voigt assumption is applied in e.g. [77].

Reuss-Sachs In contrast to the Taylor-Voigt approach, the assumption for the Reuss-Sachs approach [130] is a constant stress tensor, i.e. $[\![\boldsymbol{P}]\!] = \boldsymbol{0}$. This is accomplished in a variational manner by allowing all jumps of the deformation gradient leading to $\mathcal{F} = \mathcal{F}_{\mathrm{RS}} = \mathbb{R}^{3\times3}$. This yields non-compatible kinematics in the sense of the Hadamard

jump condition. The Reuss-Sachs assumption obviously represents a lower energy bound. It can be interpreted as convexification of the energy. In the phase field setting this assumption was made, e.g., in [77].

Rank 1 For the Rank 1 approach, (c.f. [12, 27, 73, 103, 119]), an admissible set of $\mathcal{F} = \mathcal{F}_{\mathrm{R1}} = \{\boldsymbol{a} \otimes \boldsymbol{B} \in \mathbb{R}^{3\times3} : \boldsymbol{a} \in \mathbb{R}^3, \boldsymbol{B} \in S^2\}$ is introduced. $\mathcal{F}_{\mathrm{R1}}$ denotes the set of all tensors in $\mathbb{R}^{3\times3}$ with maximal rank 1. Considering $\boldsymbol{B}$ as normal vector of the interface, the Hadamard jump condition would be fulfilled. This condition guarantees that no displacement jump across the interface occurs, i.e., the displacement field is continuous. Energy minimization (3.15) enforces static compatibility in the sense of $[\![\boldsymbol{P}]\!] \cdot \boldsymbol{B} = \boldsymbol{0}$.

Partial Rank 1 The partial Rank 1 approach as introduced by [109] follows a similar strategy as the Rank 1 approach. The admissible set is defined as $\mathcal{F} = \mathcal{F}_{\mathrm{pR1}} = \left\{\boldsymbol{a} \otimes \overline{\boldsymbol{N}}_p \in \mathbb{R}^{3\times3} : \boldsymbol{a} \in \mathbb{R}^3\right\}$ where $\overline{\boldsymbol{N}}_p$ is defined in (3.8). Kinematic compatibility is evidently fulfilled. However, minimization (3.15) also enforces static equilibrium in the sense of $[\![\boldsymbol{P}]\!] \cdot \overline{\boldsymbol{N}}_p = \boldsymbol{0}$.

Evidently, $\mathbb{R}^{3\times3} = \mathcal{F}_{\mathrm{RS}} \supset \mathcal{F}_{\mathrm{R1}} \supset \mathcal{F}_{\mathrm{pR1}} \supset \mathcal{F}_{\mathrm{TV}} = \{\boldsymbol{0}\}$ follows therefrom. As a consequence, the respective energies fulfill

$$\min_{[\![\boldsymbol{F}]\!]\in\mathcal{F}_{\mathrm{RS}}} \Psi \leq \min_{[\![\boldsymbol{F}]\!]\in\mathcal{F}_{\mathrm{R1}}} \Psi \leq \min_{[\![\boldsymbol{F}]\!]\in\mathcal{F}_{\mathrm{pR1}}} \Psi \leq \min_{[\![\boldsymbol{F}]\!]\in\mathcal{F}_{\mathrm{TV}}} \Psi\,, \tag{3.16}$$

(see (3.15)), where the Taylor-Voigt approach yields an upper bound and the Reuss-Sachs approach yields a lower bound. An illustration of the different assumptions is given in Table 3.1.

3.2 An extended phase field model for coherent interface — Hyperelasticity

In the following, a phase field approximation of interface elasticity theory is elaborated. It requires the redefinition of quantities and operations defined for the sharp interface theory.

3.2.1 Interface operations and quantities

Since the interface energy density depends on the interface deformation gradient $\overline{\boldsymbol{F}}$ an approximation of this quantity is mandatory. As presented in Chapter 2 the interface deformation gradient can be obtained by

$$\overline{\boldsymbol{F}} = \boldsymbol{F} \cdot \overline{\boldsymbol{I}}. \tag{3.17}$$

$\overline{\boldsymbol{I}} := \boldsymbol{I} - \overline{\boldsymbol{N}} \otimes \overline{\boldsymbol{N}}$ denotes the interface identity and projects tensors to an interface with interface normal $\overline{\boldsymbol{N}}$. Within the phase field framework, the interface normal can be approximated by $\overline{\boldsymbol{N}}_p$ (cf. Equation (3.8)). Here and in the following, the subscript p denotes sharp interface quantities and operations approximated at the diffuse interface. A phase field approximation to the interface deformation gradient $\overline{\boldsymbol{F}}_p$ then follows from applying (3.17), i.e.,

$$\overline{\boldsymbol{F}}_p := \boldsymbol{F} \cdot \left[\boldsymbol{I} - \overline{\boldsymbol{N}}_p \otimes \overline{\boldsymbol{N}}_p\right] . \tag{3.18}$$

While the deformation gradient maps line elements, surface elements of the interface are mapped by the interface determinant. The latter is defined by

$$\overline{\mathrm{Det}}\left(\overline{\boldsymbol{F}}\right) := \frac{\|\overline{\boldsymbol{F}} \cdot \overline{\boldsymbol{G}}_1 \times \overline{\boldsymbol{F}} \cdot \overline{\boldsymbol{G}}_2\|}{\|\overline{\boldsymbol{G}}_1 \times \overline{\boldsymbol{G}}_2\|} . \tag{3.19}$$

$\overline{\boldsymbol{G}}_1$ and $\overline{\boldsymbol{G}}_2$ denote two linear independent tangential vectors of the interface (see Notation where the covariant basis vectors are used). In the phase field setting, where no explicit parametrization of the interface is given, these basis vectors do not exist. Nevertheless, it is well known that the covariant basis vectors are tangential to the interface. Using the normed phase field gradient $\overline{\boldsymbol{N}}_p$ two linearly independent tangential vectors can be introduced by

$$\overline{\boldsymbol{G}}_{1,p} = \overline{\boldsymbol{N}}_p \times \boldsymbol{a} \tag{3.20}$$

$$\overline{\boldsymbol{G}}_{2,p} = \overline{\boldsymbol{N}}_p \times \overline{\boldsymbol{G}}_{1,p} , \tag{3.21}$$

with any vector

$$\boldsymbol{a} \in \left\{\boldsymbol{b} \in \mathbb{R}^3 : \|\boldsymbol{b}\| = 1,\, \boldsymbol{b} \neq \pm\overline{\boldsymbol{N}}_p\right\} \tag{3.22}$$

for three-dimensional problems. Consequently, the interface determinant can be approximated by

$$\overline{\mathrm{Det}}_p\left(\overline{\bullet}\right) := \frac{\|\overline{\bullet} \cdot \overline{\boldsymbol{G}}_{1,p} \times \overline{\bullet} \cdot \overline{\boldsymbol{G}}_{2,p}\|}{\|\overline{\boldsymbol{G}}_{1,p} \times \overline{\boldsymbol{G}}_{2,p}\|} . \tag{3.23}$$

The determinant can also be computed from Nanson's formula (i.e., by using the bulk's deformation gradient).

Alternatively, frame-indifferent constitutive models can be defined by introducing the surface right Cauchy-Green tensor $\overline{\boldsymbol{C}} = \overline{\boldsymbol{F}}^T \cdot \overline{\boldsymbol{F}}$. In the case of isotropic materials, one would consider invariants such as $\mathrm{trace}\left(\overline{\boldsymbol{C}}\right)$ and $\mathrm{trace}\left(\overline{\boldsymbol{C}}^2\right)$.

Due to the singularity of the interface identity $\overline{\boldsymbol{I}}$ the interface deformation gradient $\overline{\boldsymbol{F}}$ is singular in the three-dimensional space. However, it is not singular on the interface. In order to obtain the interface inverse, the identity

$$\overline{\boldsymbol{F}}^{-1} = \overline{\boldsymbol{i}} \cdot \overline{\boldsymbol{F}} \tag{3.24}$$

can be applied (c.f. [75]). The spacial interface identity $\overline{\boldsymbol{i}}$ is defined by

$$\overline{\boldsymbol{i}} := \boldsymbol{I} - \overline{\boldsymbol{n}} \otimes \overline{\boldsymbol{n}} \,. \tag{3.25}$$

Here, $\overline{\boldsymbol{n}}$ denotes the interface normal in the deformed configuration. Due to the connection between the interface deformation and the bulk deformation, the deformed interface normal can be obtained by

$$\overline{\boldsymbol{n}} := \frac{\boldsymbol{F}^{-\mathrm{t}} \cdot \overline{\boldsymbol{N}}}{\|\boldsymbol{F}^{-\mathrm{t}} \cdot \overline{\boldsymbol{N}}\|} \,. \tag{3.26}$$

When approximating the initial normal vector $\overline{\boldsymbol{N}}$ by $\overline{\boldsymbol{N}}_p$ the inverse can also be applied in the phase field setting.

A detailed overview of interface quantities and operations working on these is given in [75].

3.2.2 Approximation of the energy contributions

Based on the approximated interface deformation gradient $\overline{\boldsymbol{F}}_p$ (3.18),the interface energy can be approximated as

$$\begin{aligned} \int_\Gamma \Phi(\overline{\boldsymbol{F}}) d\mathrm{A} \quad &= \lim_{\varepsilon \to 0} \inf_p \int_\Omega \Phi(\overline{\boldsymbol{F}}_p) f^\varepsilon\,[p]\, d\mathrm{V} \\ &= \lim_{\varepsilon \to 0} \inf_p \int_\Omega \Phi(\overline{\boldsymbol{F}}_p) \left\{ \frac{3}{2}\,\varepsilon\,\|\nabla p\|^2 + \frac{6}{\varepsilon}\,p^2\,(1-p)^2 \right\} d\mathrm{V}, \end{aligned} \tag{3.27}$$

while the bulk's energy is still given by (see Equation (3.15))

$$\Psi^{\mathrm{red}}(\boldsymbol{F}, p) := \inf_{[\![\boldsymbol{F}]\!] \in \mathcal{F}} \Psi(\boldsymbol{F}, p, [\![\boldsymbol{F}]\!]) \tag{3.28}$$

with

$$\Psi(\boldsymbol{F}, p, [\![\boldsymbol{F}]\!]) = p\,\Psi_+(\boldsymbol{F} - (1-p)\,[\![\boldsymbol{F}]\!]) + (1-p)\,\Psi_-(\boldsymbol{F} - p\,[\![\boldsymbol{F}]\!])\,. \tag{3.29}$$

in line with [109]. Here a Taylor-Voigt homogenization assumption ($\mathcal{F} = \{\boldsymbol{0}\}$) is chosen for computational simplicity. Other homogenization assumptions are presented in Section 3.1.1. The bulk energy density therefore results in

$$\Psi^{\mathrm{red}}(\boldsymbol{F}, p) = (1-p)\,\Psi_{-}(\boldsymbol{F}) + p\,\Psi_{+}(\boldsymbol{F}). \tag{3.30}$$

Similar to the prototype model in Section 3.1 the variational problem of the considered mechanical system takes the form

$$(\boldsymbol{u}, p) := \mathcal{E}_{\varepsilon}^{\mathrm{int}}[\boldsymbol{u}, p] + \mathcal{E}^{\mathrm{ext},\Omega}[\boldsymbol{u}] \tag{3.31}$$

with bulk energy

$$\mathcal{E}_{\varepsilon}^{\mathrm{int}}[\boldsymbol{u}, p] = \int_{\Omega} \Psi^{\mathrm{red}}(\boldsymbol{F}, p) d\mathrm{V} + \int_{\Omega} \Phi(\overline{\boldsymbol{F}}) f^{\varepsilon}[p]\, d\mathrm{V}\,. \tag{3.32}$$

3.3 Implementation by means of the finite element method

In order to solve variational problem (3.31) it is implemented by means of the finite element method. Since the interface is assumed to be invariant with respect to time, only the derivatives with respect to the displacement are given in the following. The Taylor-Voigt assumption is applied here. A more general formulation is presented in [162].

3.3.1 First and second derivatives of the energy — Discrete setting within the finite element method

In the following, the elemental contributions of the derivatives are given. Since the energy is thermodynamically extensive, the total energy results as sum of the elemental contribution. The elemental contributions read

$$\boldsymbol{r}_{\boldsymbol{u}}^{\mathrm{A}} = \boldsymbol{f}_{\boldsymbol{u},\mathrm{int}}^{\mathrm{A}} - \boldsymbol{f}_{\boldsymbol{u},\mathrm{vol}}^{\mathrm{A}} - \boldsymbol{f}_{\boldsymbol{u},\mathrm{sur}}^{\mathrm{A}}\,, \tag{3.33}$$

where superscript A denotes derivatives related to element node A. The force contributions read

$$\boldsymbol{f}_{\boldsymbol{u},\mathrm{int}}^{\mathrm{A}} = \int_{\Omega^e} \left[(1-p)\,\frac{\partial \Psi_{-}}{\partial \boldsymbol{F}} + p\,\frac{\partial \Psi_{+}}{\partial \boldsymbol{F}} + f^{\varepsilon}[p]\,\frac{\partial \Phi}{\partial \overline{\boldsymbol{F}}} : \frac{\partial \overline{\boldsymbol{F}}}{\partial \boldsymbol{F}} \right] \cdot \nabla N^{\mathrm{A}}\, \mathrm{d}V\,, \tag{3.34}$$

$$\boldsymbol{f}_{\boldsymbol{u},\mathrm{vol}}^{\mathrm{A}} = \int_{\Omega^e} N^{\mathrm{A}}\, \rho_0\, \boldsymbol{B}\, \mathrm{d}V\,, \tag{3.35}$$

$$\boldsymbol{f}_{\boldsymbol{u},\mathrm{sur}}^{\mathrm{A}} = \int_{\Omega^e} N^{\mathrm{A}}\, \boldsymbol{T}\, \mathrm{d}V\,. \tag{3.36}$$

The shape functions of node A are denoted as N^{A}. The contributions to the stiffness tensor – the second derivative of the energy with respect to the unknown displacements – read

$$\boldsymbol{K}_{\boldsymbol{uu}}^{\mathrm{AB}} = \int_{\Omega^e} \nabla N^B \bullet \left[(1-p)\, \frac{\partial^2 \Psi_-}{\partial \boldsymbol{F}^2} + p\, \frac{\partial^2 \Psi_+}{\partial \boldsymbol{F}^2} + f^{\varepsilon}\,[p]\, \frac{\partial^2 \Phi}{\partial \boldsymbol{F}^2} \right] \cdot \nabla N^B \,\mathrm{d}V \,. \tag{3.37}$$

$\bullet$ denotes a contraction with respect to the second index. In index notation, derivative $\partial^2\Phi/\partial \boldsymbol{F}^2$ in (3.37) is given by

$$\frac{\partial^2 \Phi}{\partial F_{mn} \partial F_{op}} = \frac{\partial^2 \Phi}{\partial \overline{F}_{mn} \partial \overline{F}_{op}} \frac{\partial \overline{F}_{mn}}{\partial F_{ij}} \frac{\partial \overline{F}_{op}}{\partial F_{kl}} \,. \tag{3.38}$$

The derivative $\partial \overline{\boldsymbol{F}}/\partial \boldsymbol{F}$ reduces to

$$\frac{\partial \overline{\boldsymbol{F}}}{\partial \boldsymbol{F}} = \overline{\boldsymbol{I}} \,\overline{\otimes}\, \boldsymbol{I} \,. \tag{3.39}$$

3.4 Numerical example — Size effect

The capabilities of the elaborated model are presented by analyzing the effective properties of a representative volume element (RVE) with different length l_{RVE} (cf. [67]). This highlights the well-known "the smaller the stiffer" size effect (see. [31]). The cubic representative volume element is presented in Figure 3.2a). A spherical inclusion of diameter $0.8\, l_{\mathrm{RVE}}$ is surrounded by a bulk of the same material. In between an elastic interface is present. The representative volume element is loaded in uni-axial strain with final macroscopic deformation gradient

$$\boldsymbol{F}^{\mathrm{M}} = \begin{bmatrix} 1.05 & 0 & 0 \\ 0 & 1 & 0 \\ 0 & 0 & 1 \end{bmatrix} \,. \tag{3.40}$$

Periodic boundary conditions are considered (cf. [67]). The phase field p is assumed to be time-independent and with an internal length scale $\varepsilon \neq \varepsilon(l_{\mathrm{RVE}})$ independent of the internal length scale of the microstructure.

The phases as well as the interface are described by a time-independent phase field p. For all microstructure sizes, the same internal length $\varepsilon \neq \varepsilon(l_{\mathrm{RVE}})$ is applied. Both bulk materials — inclusion and matrix — are defined by a standard hyperelastic Neo-Hookean material model of the form

$$\Psi_-(\boldsymbol{F}) = \Psi_+(\boldsymbol{F}) = \frac{1}{2}\,\mu\, \left(\mathrm{tr}\, \left(\boldsymbol{F}^{\mathrm{t}} \cdot \boldsymbol{F} \right) - 3 \right) - \mu\, \ln \mathrm{Det}\, \boldsymbol{F} + \frac{1}{2}\,\lambda\, \left(\ln \mathrm{Det}\, \boldsymbol{F} \right)^2 \,. \tag{3.41}$$

The material parameters for both phases are the same and depicted in Table 3.2. The interface energy takes a Neo-Hookean form

$$\Phi(\overline{\boldsymbol{F}}) = \frac{1}{2}\,\overline{\mu}\,\left(\operatorname{tr}\overline{\boldsymbol{F}}^{\mathrm{t}}\cdot\overline{\boldsymbol{F}} - 2\right) - \overline{\mu}\,\ln\overline{\operatorname{Det}}\,\overline{\boldsymbol{F}} \tag{3.42}$$

in line with [75]. All material parameters are taken from [67] and cumulated in Table 3.2.

Bulk		Interface		Geometry
μ	λ	$\overline{\mu}$	ε	l_{RVE}
6160 MPa	10950 MPa	0.1 kN/mm	0.01 mm	varying

Table 3.2: "Numerical analysis of the size effect induced by an interface seperating an inclusion from the surrounding matrix." ([80, Sec. 2]) – Geometry and material parameters.

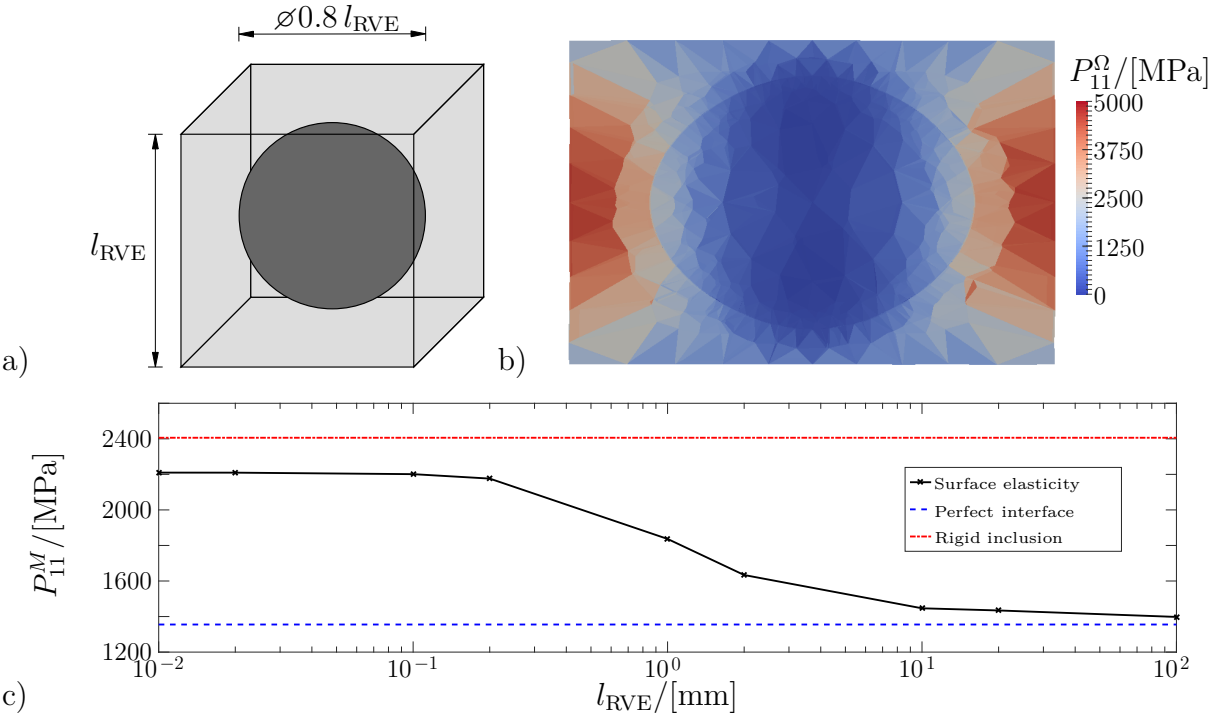

Figure 3.2: "Numerical analysis of the size effect induced by an interface seperating an inclusion from the surrounding matrix. Subfigure a) shows the geometry of the microstructure. In Subfigure b) the bulk stress response P_{11}^{Ω} in the y-z-plane can be seen. The size effect of the structure is visualized in Subfigure c) by means of the macroscopic stress P_{11}^{M} (computed by homogenization, c.f. [67]) versus RVE's length l_{RVE}." ([80, Sec. 2])

"The size effect can be traced back to the different scaling of the interface energy and the bulk energies. Since the surface energy is area specific it decreases slower than the volumetric bulk energies for a decreasing size of the microstructure, i.e.

$\int_\Gamma \Psi_\Gamma / \int_\Omega \Psi_\Omega \sim 1/l_{\mathrm{RVE}}$. Consequently, for sufficiently small microstructures the material response converges to a rigid inclusion, since only the interface energy drives the total energy. Vice versa the material response converges to a homogeneous microstructure with perfect interfaces for sufficiently large microstructures. This effect can be seen in Figure 3.2c), where the results are visualized for a simple tension loadcase. Figure 3.2b) shows the corresponding stress response for a certain length $l_{\mathrm{RVE}} = 0.1\mathrm{mm}$." ([80, Sec. 2]).

The convergence to the rigid inclusion still shows some deviation. This can be drawn back to the phase field width independent of l_{RVE}. For small representative volume elements, the ratio $\varepsilon/l_{\mathrm{RVE}}$ increases significantly effecting the quality of the interface approximation.

Regarding the stress response (Fig. 3.2b)) for $l_{\mathrm{RVE}} = 0.1\mathrm{mm}$ the effect of the interfacial stresses on the bulk stresses is visible. Within the inclusion lower stresses occur as the deformation of the interface becomes more penalized. Therefore, the deformation is larger within the matrix.

3.5 Conclusion

The prototype model presented in Section 3.1 was extended to interface elasticity. By introducing the normed phase field gradient as interface normal the surface deformation gradient of the interface could be computed, which allows to approximate the elastic energy of the interface.

The numerical example proved the capabilities of the approach. A well-known size effect can be explained by the different scalings of bulk and interface energies.

4 Phase-field approximation of cohesive fracture

In the following a phase field model of cohesive fracture is presented. Firstly, a prototype model for brittle fracture approximating Griffith criterion ([63]) is recapitulated. Subsequently, an established phase field approach to cohesive fracture is revisited [35, 36, 55]. This approach is then extended by the following points.

- The fracture energy as well as the strength of the material interface can be prescribed independently – including a rigorous mathematical proof of Γ-convergence.
- Arbitrary isotropic potential-based traction-separation laws can be applied.
- Any hyperelastic bulk material model can be adopted in a geometrically exact setting
- Tension-compression asymmetry (microcrack-closure-reopening (MCR) effect) is accounted for.

Finally, numerical examples underline the predictive capabilities of the novel approach.

4.1 Brittle fracture — A prototype model

A well-established phase field model for brittle fracture approximating the Griffith criterion [63] was introduced in [22, 54]. Since then it has constantly been enhanced by e.g. [6, 9, 104]. In the following, a prototype model is presented based on this established approach.

In general, the integrated Helmholtz energy of a system with sharp interface Γ takes the form

$$\mathcal{E}^{\text{int}} = \int_{\Omega\setminus\Gamma} \Psi(\boldsymbol{F})\mathrm{d}V + \int_{\Gamma} \Phi \,\mathrm{d}\, A\,. \tag{4.1}$$

Under the assumption of a constant interface energy density $\Phi \equiv \gamma$ with Griffith-type critical energy release rate γ the total energy can be simplified to

$$\mathcal{E}^{\text{int}} = \int_{\Omega \setminus \Gamma} \Psi(\boldsymbol{F}) \mathrm{d}V + \gamma \, \mathcal{H}_{\Gamma} \,, \tag{4.2}$$

where $\mathcal{H}_{\Gamma}$ denotes the $n_{\text{dim}} - 1$-dimensional Hausdorff measure, i.e. to the area of the interface. The corresponding phase field approximation is introduced as

$$\mathcal{E}_{\varepsilon}^{\text{int}} = \int_{\Omega} d(p) \, \Psi(\boldsymbol{F}) + \gamma \, f_{\varepsilon}(p, \nabla p) \, \mathrm{d}V \,, \tag{4.3}$$

where $d(p)$ is a degradation function with properties (c.f. [101])

$$d \in \mathcal{C}([0,1]) \tag{4.4}$$

$$d(p_1) > d(p_2) \quad \forall p_1 > p_2 \tag{4.5}$$

$$\left. \frac{\partial d}{\partial p} \right|_{p=0} = 0 \tag{4.6}$$

$$d(0) = 0 \tag{4.7}$$

$$d(1) = 1. \tag{4.8}$$

As a consequence, values close to $p = 1$ describe pristine material, whereas values around $p = 0$ characterize fully broken material. A well-established choice is $d(p) = p^2$, c.f. [9, 22, 39, 54, 101, 104].

The second term in (4.3) refers to the interface energy. In general, the interface density $f_{\varepsilon}(p, \nabla p)$ takes the form

$$f_{\varepsilon}(p, \nabla p) = \frac{1}{c_0} \left[\frac{\vartheta(p)}{4 \, \varepsilon} + \varepsilon \, \|\nabla p\|^2 \right]. \tag{4.9}$$

The geometric crack function $\vartheta(p) \in [0,1]$ fulfills the properties $\vartheta(1) = 0$ and $\vartheta(0) = 1$ (c.f. [165]). It controls the shape of the resulting phase field variable. The prefactor c_0 is defined by

$$c_0 := 2 \int_0^1 \sqrt{\vartheta(p)} \, \mathrm{d}p \,. \tag{4.10}$$

The first term in (4.9) energetically favors phase field values of $p = 1$ denoting pristine material. The following term introduces a regularization penalizing sharp variations of the phase field. Both terms together result in solutions with ∇p proportional to $1/\varepsilon$. The phase field width ε thus controls the width of the smeared interface. Measure $f_{\varepsilon}(p_{\varepsilon}, \nabla p_{\varepsilon}) \mathrm{d}V$ converges weakly to the $n_{\text{dim}} - 1$-dimensional Hausdorff measure $\mathrm{d}\mathcal{H}^{n_{\text{dim}}-1}$

restricted to the jump set of $\boldsymbol{u}$. In the following measure $\mathrm{d}\mathcal{H}^{n_{\mathrm{dim}}-1}$ is abbreviated by $\mathrm{d}A$ for simplicity.

In this thesis, the geometric crack function $\vartheta(p) = (1-p)^2$ is chosen in line with [6, 9, 101, 104]. This leads to interface density

$$f_\varepsilon(p, \nabla p) = \frac{(1-p)^2}{4\,\varepsilon} + \varepsilon \left\|\nabla p\right\|^2 . \tag{4.11}$$

For the one-dimensional minimization problem

$$\min_p \int_{\mathbb{R}} f_\varepsilon(p, \nabla p)\mathrm{d}x \qquad \text{s.t. } p(x=0) = 0 \tag{4.12}$$

enforcing a crack at $x = 0$ ($\Gamma = \{0\}$) the solution takes the form

$$p_{\mathrm{opt}}(X) = 1 - e^{-\frac{|X|}{2\,\varepsilon}} . \tag{4.13}$$

The distribution can be seen in Figure 4.1 for varying regularization length ε. When inserting this solution in the initial interface energy the result proves to be

$$\int_{\mathbb{R}} f_\varepsilon(p_{\mathrm{opt}}, \nabla p_{\mathrm{opt}})\,\mathrm{d}V = 1 = \mathcal{H}_\Gamma \tag{4.14}$$

independent of the regularization length ε. Equation (4.13) also illustrates that the characteristic length scale of the damaged region is ε, as it is shown numerically for several fracture openings in [21, Fig. 4].

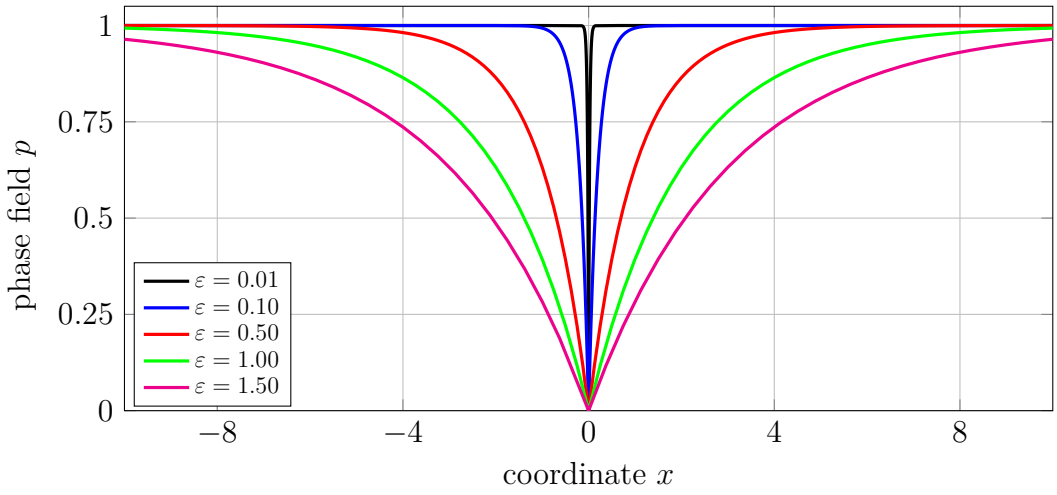

Figure 4.1: Phase-field solutions for the one-dimensional minimization problem (4.12) for varying regularization length ε.

"In order to obtain a well-posed variational problem, we have to overcome the degeneracy of $\mathcal{E}^{\mathrm{int},\Omega}$. To be more precise, the first term in (4.36) is not coercive if $p = 0$ in some region of positive measure. In the literature this is normally solved adding a regularization of the form

$$\mathcal{E}_\varepsilon^{\mathrm{reg},\Omega}[\boldsymbol{u}] := \eta_\varepsilon \int_\Omega \Psi(\boldsymbol{F})\mathrm{d}V \tag{4.15}$$

for some small parameter $\eta_\varepsilon > 0$, see for example [22, Sect. 2.1] or [23, Sect. 2.1]." ([81, Sec. 2])

"By introducing the work due to external forces

$$\mathcal{E}^{\mathrm{ext},\Omega}[\boldsymbol{u}] := -\int_\Omega \rho_0 \boldsymbol{B} \cdot \boldsymbol{u}\,\mathrm{d}V - \int_{\partial\Omega} \boldsymbol{T} \cdot \boldsymbol{u}\,\mathrm{d}A\,, \tag{4.16}$$

the total energy of the system reads

$$\mathcal{E}_\varepsilon^{\mathrm{tot},\Omega}[\boldsymbol{u}, p] = \mathcal{E}_\varepsilon^{\mathrm{int},\Omega}[\boldsymbol{u}, p] + \mathcal{E}_\varepsilon^{\mathrm{reg},\Omega}[\boldsymbol{u}] + \mathcal{E}^{\mathrm{ext},\Omega}[\boldsymbol{u}]\,, \tag{4.17}$$

where $\rho_0 \boldsymbol{B}$ are volumetric body forces and $\boldsymbol{T}$ is the traction vector acting at the (external) surface of the system." ([81, Sec. 2]). A variational description of the underlying free boundary problem is presented in Appendix 6.2.

The unknown fields $\boldsymbol{u}$ and p then follow from the variational principle

$$(\boldsymbol{u}, p) := \operatorname*{arg\,min}_{(\boldsymbol{u},p)} \mathcal{E}_\varepsilon^{\mathrm{tot},\Omega}[\boldsymbol{u}, p]\,. \tag{4.18}$$

"If the sum of the external forces vanishes, in the sense that $\mathcal{E}^{\mathrm{ext},\Omega}[\boldsymbol{u}] = 0$ whenever $\boldsymbol{u}$ is constant, or Dirichlet boundary conditions are imposed on a part of $\partial\Omega$, existence of minimizers (at fixed $\varepsilon > 0$) follows with the direct method of the calculus of variations using strong convergence of p and convexity of Ψ." ([81, Sec. 2])

4.1.1 Microcrack-closure-reopening effect

Cracks are known to only emerge and evolve under tensile states. This tension-compression asymmetry is called Microcrack-Closure-Reopening (MCR) effect. A typical approach to include this behavior in the model is the decomposition of the bulk energy density $\Psi = \Psi_+ + \Psi_-$. Tensile states are covered by the contribution Ψ_+ while compressive states are included in Ψ_-. Damage is then only driven by the tensile contribution of the energy such that Equation (4.3) changes to

$$\mathcal{E}_\varepsilon^{\mathrm{int}} = \int_\Omega d(p)\,\Psi_+(\boldsymbol{F}) + \Psi_-(\boldsymbol{F}) + \gamma\, f_\varepsilon(p, \nabla p)\,\mathrm{d}V\,. \tag{4.19}$$

An overview of the different approaches is given in [39]. For the volumetric-deviatoric decomposition as well as the spectral decomposition an explicit formulation for plane stress

conditions for Hooke's model is possible. It was introduced in [88] and is summerized in Appendix 6.3.

Volumetric-deviatoric decomposition The volumetric-deviatoric decomposition can be found in [83] and [9]. It can be applied for any energy with an existing decomposition into a volumetric Ψ_{vol} and a deviatoric Ψ_{dev} contribution ($\Psi = \Psi_{\text{vol}} + \Psi_{\text{dev}}$). Depending on the Jacobian $J = \text{Det}\, \boldsymbol{F}$ the contributions are characterized as tensile or compressive. The volumetric-deviatoric decomposition takes the form

$$\Psi_+ = \begin{cases} \Psi_{\text{vol}} + \Psi_{\text{dev}} & \text{if } J > 1 \\ \Psi_{\text{dev}} & \text{if } J \leq 1 \end{cases} \tag{4.20}$$

$$\Psi_- = \begin{cases} 0 & \text{if } J > 1 \\ \Psi_{\text{vol}} & \text{if } J \leq 1\,. \end{cases} \tag{4.21}$$

If a small strain setting is adopted, $\text{trace}(\boldsymbol{\varepsilon})$ is applied to measure volume change.

Spectral decomposition Another decomposition can be found in [101, 104] (see also [48, 96]). It is based on the spectral decomposition of the strain tensor. Considering Hooke's model

$$\Psi = \frac{1}{2}\,\lambda\,\text{trace}(\nabla \boldsymbol{u}^{\text{sym}})^2 + \mu\,\nabla \boldsymbol{u}^{\text{sym}} \colon \nabla \boldsymbol{u}^{\text{sym}} \tag{4.22}$$

the decomposition takes the form

$$\Psi_+ = \frac{1}{2}\,\lambda\,\langle \text{trace}(\nabla \boldsymbol{u}^{\text{sym}})\rangle_+^2 + \mu\,\nabla \boldsymbol{u}_+^{\text{sym}} \colon \nabla \boldsymbol{u}_+^{\text{sym}} \tag{4.23}$$

$$\Psi_- = \frac{1}{2}\,\lambda\,\langle \text{trace}(\nabla \boldsymbol{u}^{\text{sym}})\rangle_-^2 + \mu\,\nabla \boldsymbol{u}_-^{\text{sym}} \colon \nabla \boldsymbol{u}_-^{\text{sym}}\,, \tag{4.24}$$

with the Macauley brackets $\langle \bullet \rangle_\pm$ as introduced in the Notations and

$$\nabla \boldsymbol{u}_+^{\text{sym}} = \sum_{i=1}^{n_{\text{dim}}} \langle \lambda_i \rangle_+\, \boldsymbol{N}_i \otimes \boldsymbol{N}_i \tag{4.25}$$

$$\nabla \boldsymbol{u}_-^{\text{sym}} = \sum_{i=1}^{n_{\text{dim}}} \langle \lambda_i \rangle_-\, \boldsymbol{N}_i \otimes \boldsymbol{N}_i\,, \tag{4.26}$$

with the eigenvalues λ_i of $\nabla \boldsymbol{u}^{\text{sym}}$ and its corresponding eigenvectors $\boldsymbol{N}_i$.

It bears emphasis that in general

$$\Psi \neq \Psi(\nabla \boldsymbol{u}_+^{\text{sym}}) + \Psi(\nabla \boldsymbol{u}_-^{\text{sym}})\,. \tag{4.27}$$

Therefore, the Macauley brackets are introduced for the first terms of decomposition (4.23), (4.24), since

$$\operatorname{trace}(\nabla \boldsymbol{u}^{\mathrm{sym}})^2 \neq \operatorname{trace}(\nabla \boldsymbol{u}_+^{\mathrm{sym}})^2 + \operatorname{trace}(\nabla \boldsymbol{u}_-^{\mathrm{sym}})^2 \,. \tag{4.28}$$

The latter terms of Equations (4.23) and (4.24) satisfy

$$\nabla \boldsymbol{u}^{\mathrm{sym}} \colon \nabla \boldsymbol{u}^{\mathrm{sym}} = \nabla \boldsymbol{u}_+^{\mathrm{sym}} \colon \nabla \boldsymbol{u}_+^{\mathrm{sym}} + \nabla \boldsymbol{u}_-^{\mathrm{sym}} \colon \nabla \boldsymbol{u}_-^{\mathrm{sym}} \tag{4.29}$$

due to the symmetric structure of $\nabla \boldsymbol{u}^{\mathrm{sym}}$ and to the orthogonal structure of its eigenvectors $\boldsymbol{N}_i$.

No-tension approach The no-tension approach was introduced to phase field fracture models for linearized kinematics in [39]. However, the key ideas were already published in [56] for damage mechanics. It was first published in [41] for structured media. The main idea is the introduction of a set $\mathcal{K}_+ \subset \mathrm{Sym}$, where $\mathrm{Sym} := \mathrm{Sym}(\mathbb{R}^{n_{\mathrm{dim}} \times n_{\mathrm{dim}}})$ are all symmetric tensors in $\mathbb{R}^{n_{\mathrm{dim}} \times n_{\mathrm{dim}}}$. $\mathcal{K}_+$ contains all strains which are assumed to be linked with crack opening. The compressive energy contribution is defined by

$$\Psi_- := \min_{\boldsymbol{\eta} \in \mathcal{K}_+} \Psi(\nabla \boldsymbol{u}^{\mathrm{sym}} - \boldsymbol{\eta}) = \Psi(\nabla \boldsymbol{u}^{\mathrm{sym}} - \boldsymbol{\eta}^*(\nabla \boldsymbol{u}^{\mathrm{sym}}))\,, \tag{4.30}$$

with

$$\boldsymbol{\eta}^* := \arg\min_{\boldsymbol{\eta} \in \mathcal{K}_+} \Psi(\nabla \boldsymbol{u}^{\mathrm{sym}} - \boldsymbol{\eta})\,. \tag{4.31}$$

The tensile contribution is defined as

$$\Psi_+ := \Psi - \Psi_-. \tag{4.32}$$

Using the no-tension approach the already introduced decompositions as well as several other decompositions are naturally included with a specific choice of $\mathcal{K}_+$ (c.f. [39]). For the original no-tension models a space of $\mathcal{K}_+ = \mathrm{Sym}_+$ is chosen, where $\mathrm{Sym}_+ := \{\boldsymbol{K} \in \mathrm{Sym} : \boldsymbol{a} \cdot \boldsymbol{K} \cdot \boldsymbol{a} \geq 0 \,\forall\, \boldsymbol{a} \in \mathbb{R}^{n_{\mathrm{dim}}}\}$, i.e., the set of all tensile strains.

4.1.2 Self-healing

In isothermal fracture mechanics thermodynamic consistency requires that cracks cannot heal, i.e., $(\dot{p} \leq 0)$. Several approaches have been applied to ensure this irreversibility condition. The three commonly applied approaches are introduced in the following.

Crack boundary conditions Regarding brittle fracture, the phase field variable is only stable at values around 0 (damaged) and 1 (intact). Therefore, when a phase field value reaches a given threshold $p_{\mathrm{th}} \ll 1$ it is fixed to zero as additional boundary condition.

Thus, a crack is enforced at that point for all following time steps. This method is used for example in [22, 134].

Explicit constraint The constraint of a decreasing phase field can also be enforced directly as $\dot{p} \leq 0$. This can be handled for example via an augmented-Lagrange approach (see [157, 160]), an interior point method (see [82, 154, 155]) or the introduction of slack variables (see [19]).

Implicit constraint A third commonly used strategy concerns the driving force of the phase field. It was presented in [104] and has since been used widely. The fundamental idea is the introduction of a monotonic driving force

$$\mathcal{H}_n = \max \left\{ \left. \frac{\partial \Psi}{\partial p} \right|_n , \mathcal{H}_{n-1} \right\} . \tag{4.33}$$

Here, n and $n-1$ correspond to different time steps.

4.1.3 Solution techniques

In general, phase field approximations of fracture show a non-convex energy with respect to its arguments $\boldsymbol{u}$ and p. As a consequence, a standard approach to minimize the energy in a finite element setting often fails. In the following, advanced solution techniques used in literature are presented.

Monolithical minimization Despite the complex structure of the problem, techniques can be elaborated for solving the displacement and the phase field simultaneously. These techniques include modifications of the Jacobian (see [159, 160]) or energy based line searches (see [82]).

Alternate minimization While the total problem is non-convex, the subproblems

$$\boldsymbol{u} = \arg\min_{(\boldsymbol{u})} \mathcal{E}(\boldsymbol{u}, p) \qquad \text{for fixed } p \quad \text{and} \tag{4.34}$$

$$p = \arg\min_{(\boldsymbol{u})} \mathcal{E}(\boldsymbol{u}, p) \qquad \text{for fixed } \boldsymbol{u} \tag{4.35}$$

are convex in many cases. The idea of the alternate minimization algorithm as introduced by [23] is to solve these problems alternating, until convergence is reached. The algorithm is presented in Algorithm 1.

$i \leftarrow 0$
$\boldsymbol{u}^{(i)} \leftarrow \boldsymbol{u}_n$
$p^{(i)} \leftarrow p_n$
while not converged **do**
    $\boldsymbol{u}^{(i)} \leftarrow \arg\min_{\boldsymbol{u}} \mathcal{E}(\boldsymbol{u}, p^{(i-1)})$
    $p^{(i)} \leftarrow \arg\min_{p} \mathcal{E}(\boldsymbol{u}^{(i)}, p)$
    $i \leftarrow i + 1$
end while
$\boldsymbol{u}_n \leftarrow \boldsymbol{u}^{(i)}$
$p_n \leftarrow p^{(i)}$

Algorithm 1: The alternate minimization algorithm.

Backtracking Often, alternate minimization does not converge to the global minimum. With the backtracking approach introduced by [23] energies from previous time steps are compared to energies resulting from the same boundary value problem of the previous time steps but with the latest phase field distribution. By doing so, new predictors can be defined that often converge to the global energy minimum. However, a rigorous mathematical background is missing.

4.2 Review of the phase field approximation of cohesive zone models

The following section is taken from [81, Sec. 2]:

"We summarize here the model proposed in [35, 36, 55] and their main theoretical findings. The key functional takes the form

$$\mathcal{E}_\varepsilon^{\mathrm{int},\Omega}[\boldsymbol{u}, p] := \int_\Omega d_\varepsilon(p)^2 \, \|\nabla \boldsymbol{u}\|^2 + \, f_\varepsilon(p, \nabla p) \, \mathrm{d}V \,, \tag{4.36}$$

where $\Omega \subseteq \mathbb{R}^{n_{\mathrm{dim}}}$ ($n_{\mathrm{dim}} = 1, 2, 3$) is the reference configuration and $\boldsymbol{u} : \Omega \to \mathbb{R}^{n_{\mathrm{dim},\boldsymbol{u}}}$ is the displacement field, the relevant values for $n_{\mathrm{dim},\boldsymbol{u}}$ being $n_{\mathrm{dim},\boldsymbol{u}} = n_{\mathrm{dim}}$ for the physical displacement field, and $n_{\mathrm{dim},\boldsymbol{u}} = 1$ for the scalar approximation, which is appropriate for examples in antiplane shear models. The order parameter (phase field) $p : \Omega \to [0, 1]$ is 1 for pristine material and 0 for fully damaged material, intermediate values represent the states of partial damage which are responsible for cohesive forces in the early stages of, e.g. ductile fracture. The treatment in [35] dealt only with a scalar displacement

field ($n_{\mathrm{dim},\boldsymbol{u}} = 1$), the vector-valued generalization has been treated in [36]. As several expressions are simpler in the scalar case, we shall discuss both in the following.

The first term in (4.36) captures the elastic energy stored in the bulk material. In line with Hooke's model, this energy is quadratic in $\nabla \boldsymbol{u}$. The factor $d_\varepsilon(p)$ accounts for degradation of the bulk material due to damage and shall be discussed in more detail below (see (4.43)).

The second term in (4.36), defined by

$$f_\varepsilon(p, \nabla p) := \frac{(1-p)^2}{4\,\varepsilon} + \varepsilon \left\|\nabla p\right\|^2, \tag{4.37}$$

refers to the interface energy. Parameter ε is related to the thickness of the diffuse interface. The first term in (4.37) penalizes deviations from the state $p = 1$, which corresponds to undamaged material; the second one is a regularization, that penalizes sharp variations of the phase field. Balancing the two, one expects the gradient of p to behave as $1/\varepsilon$, such as in the phase field approximations of brittle fracture models discussed above. For those models, measures $f_\varepsilon(p_\varepsilon, \nabla p_\varepsilon)\mathrm{d}V$ converge weakly to the $n_{\mathrm{dim}} - 1$-dimensional Hausdorff measure $\mathrm{d}\mathcal{H}^{n_{\mathrm{dim}}-1}$ restricted to the jump set of $\boldsymbol{u}$. We recall that $\mathrm{d}\mathcal{H}^{n_{\mathrm{dim}}-1}$ measures area, and for brevity is denoted by $\mathrm{d}A$ in the following. It must be noted that the first term in (4.36) also contains a dependence on both ε and on p. Indeed, the characteristic behavior of ductile fracture, with a fracture energy that increases linearly at small openings and then saturates at large openings, arises from the interaction of all three terms in (4.36). We remark that minimizing (4.37) leads to optimal profiles for p which decay exponentially away from the fractured regions. For example, in one dimension, if one assumes $p(0) = 0$, then the optimal profile is

$$p(x) = 1 - \mathrm{e}^{-|x|/(2\varepsilon)}. \tag{4.38}$$

In contrast, the first term in (4.37) is replaced in the model proposed by Wu [165] by a term with linear growth close to its minimum, leading to sharply localized profiles, see [165, Eq. (3.26)]. (4.38) also illustrates that the characteristic length scale of the damaged region is ε, as was shown numerically for several fracture openings in [21, Fig. 4].

In order to obtain a well-posed variational problem, we have to overcome the degeneracy of $\mathcal{E}^{\mathrm{int},\Omega}$. To be more precise, the first term in (4.36) is not coercive if $p = 0$ in some region of positive measure. In the literature this is normally solved adding a regularization of the form

$$\mathcal{E}_\varepsilon^{\mathrm{reg},\Omega}[\boldsymbol{u}] := \eta_\varepsilon \int_\Omega \|\nabla \boldsymbol{u}\|^2 \mathrm{d}x \tag{4.39}$$

for some small parameter $\eta_\varepsilon > 0$, see for example [22, Sect. 2.1] or [23, Sect. 2.1]. As discussed in [36, Sect. 5] this does not change the convergence properties, provided that $\lim_{\varepsilon\to 0} \frac{\eta_\varepsilon}{\varepsilon} = 0$.

By introducing the work due to external forces

$$\mathcal{E}^{\mathrm{ext},\Omega}[\boldsymbol{u}] := -\int_\Omega \rho_0 \boldsymbol{B}\cdot\boldsymbol{u}\,\mathrm{d}V - \int_{\partial\Omega} \boldsymbol{T}\cdot\boldsymbol{u}\,\mathrm{d}A\,, \tag{4.40}$$

the total energy of the system reads

$$\mathcal{E}_\varepsilon^{\mathrm{tot},\Omega}[\boldsymbol{u},p] = \mathcal{E}_\varepsilon^{\mathrm{int},\Omega}[\boldsymbol{u},p] + \mathcal{E}_\varepsilon^{\mathrm{reg},\Omega}[\boldsymbol{u}] + \mathcal{E}^{\mathrm{ext},\Omega}[\boldsymbol{u}]\,, \tag{4.41}$$

where $\rho_0\boldsymbol{B}$ are volumetric body forces and $\boldsymbol{T}$ is the traction vector acting at the (external) surface of the system. If the sum of the external forces vanishes, in the sense that $\mathcal{E}^{\mathrm{ext},\Omega}[\boldsymbol{u}] = 0$ whenever $\boldsymbol{u}$ is constant, or Dirichlet boundary conditions are imposed on a part of $\partial\Omega$, existence of minimizers (at fixed $\varepsilon > 0$) follows with the direct method of the calculus of variations using strong convergence of p and convexity of $\|\nabla\boldsymbol{u}\|^2$.

The unknown fields $\boldsymbol{u}$ and p then follow from the variational principle

$$(\boldsymbol{u},p) := \operatorname*{arg\,min}_{(\boldsymbol{u},p)} \mathcal{E}_\varepsilon^{\mathrm{tot},\Omega}[\boldsymbol{u},p]\,. \tag{4.42}$$

A comparison of (4.36) to the original phase field approximation for brittle fracture, as advocated for example in [22], reveals two important points: First, (4.36) reduces to the phase field approximation of brittle fracture in [22] if one takes $d_\varepsilon(p) = p$. Indeed, the specific dependence of d_ε on ε discussed below is crucial in order to obtain ductile fracture in the limit. Secondly, the energy density $d_\varepsilon(p)^2\,\|\nabla\boldsymbol{u}\|^2$ does not distinguish between volumetric and deviatoric deformations. In the scalar setting of [35, 55], indeed, ∇u is a vector and one cannot distinguish between volumetric and deviatoric strains. This becomes possible, in principle, within the general vectorial setting presented in [36], but was not discussed there; in particular that framework does not permit distinguishing the elastic behavior in the tensile and compressive damaged zones.

The key novelty of the model proposed in [35] with respect to the classic phase field approximation for brittle fracture [8, 22] is the choice of damage functional d_ε appearing in (4.36). The authors of [35] choose

$$d_\varepsilon(p) := \begin{cases} \min\left\{\sqrt{\varepsilon}\,d(p), 1\right\}, & \text{for } p \in [0,1[\\ 1, & \text{for } p = 1\,, \end{cases} \tag{4.43}$$

where $d(p) \in \mathcal{C}^0\left([0,1[\,,[0,+\infty[\right)$ is a non-decreasing function with the properties

$$d(p) = 0 \text{ if and only if } p = 0, \tag{4.44}$$

$$\lim_{p\to 1}(1-p)d(p) = \ell, \quad \ell \in]0,+\infty[\,. \tag{4.45}$$

Condition (4.44) guarantees that the material is fully damaged only at $p = 0$, and that it retains some strength for any intermediate value $p \in]0,1[$. Condition (4.45) guarantees that $d(p)$ converges sufficiently fast to infinity, if p approaches 1, so that for

$p \geq 1 - O(\ell\sqrt{\varepsilon})$ one has $d_\varepsilon(p) = 1$, as appropriate for undamaged material. A simple example of a function complying with the aforementioned constraints is $d(p) = \ell p/(1-p)$ for any choice $\ell \in]0, \infty[$, for instance $\ell = 1$. This function was already proposed in [35] and is also chosen within the present paper.

It has been shown in [35, 36] that functionals $\mathcal{E}_\varepsilon^{\mathrm{int},\Omega}$ Γ-converge, with respect to the $L^1(\Omega;\mathbb{R}^{n_{\mathrm{dim},\boldsymbol{u}}}) \times L^1(\Omega)$ topology, to

$$\mathcal{E}^{\mathrm{int},\Omega}[\boldsymbol{u},p] := \begin{cases} \int\limits_\Omega h_\ell^{\mathrm{qc}}\left(\nabla \boldsymbol{u}\right) \mathrm{d}V + \int\limits_\Gamma \Phi^0\left(\| \left[\!\left[\boldsymbol{u}\right]\!\right] \|\right) \mathrm{d}A + \ell\, |D^{\mathrm{c}}\boldsymbol{u}|(\Omega), \\ \qquad\qquad \text{if } p = 1\, \mathcal{L}^{n_{\mathrm{dim}}}\text{-a.e. in } \Omega, \boldsymbol{u} \in GBV(\Omega)^{n_{\mathrm{dim},\boldsymbol{u}}}, \\ +\infty, \qquad\qquad \text{otherwise}\,. \end{cases} \tag{4.46}$$

We recall that GBV is the space of generalized functions of bounded variation. These are functions whose distributional gradient can contain regular parts (denoted by $\nabla \boldsymbol{u}$), as well as jump parts concentrated on an $n_{\mathrm{dim}} - 1$-dimensional set $\Gamma = \Gamma_{\boldsymbol{u}}$ (with $[\![\boldsymbol{u}]\!]$ denoting the jump of $\boldsymbol{u}$), and a diffuse singular part, called Cantor part and denoted by $D^{\mathrm{c}}\boldsymbol{u}$. The symbol $|D^{\mathrm{c}}\boldsymbol{u}|(\Omega)$ represents the total variation of measure $D^{\mathrm{c}}\boldsymbol{u}$ over Ω, which can be qualitatively understood as an L^1 norm. We refer to [7] for mathematical background on these function spaces.

Let us address the meaning of Γ-convergence in this setting. The functionals $\mathcal{E}_\varepsilon^{\mathrm{int},\Omega}$ and $\mathcal{E}^{\mathrm{int},\Omega}$ are naturally formulated in terms of different function spaces, and low-energy pairs $(\boldsymbol{u}, p)$ with respect to $\mathcal{E}_\varepsilon^{\mathrm{int},\Omega}$ contain interfaces regularized on the length scale ε. Therefore, pointwise convergence, in the sense that $\mathcal{E}_\varepsilon^{\mathrm{int},\Omega}[\boldsymbol{u}_*, p_*] \to \mathcal{E}^{\mathrm{int},\Omega}[\boldsymbol{u}_*, p_*]$ for any given (fixed) pair $(\boldsymbol{u}_*, p_*)$, would not correctly describe the approximation properties of $\mathcal{E}_\varepsilon^{\mathrm{int},\Omega}$ (and, indeed, it does not hold). The Γ-convergence result of [35, 36] instead states that for any pair $(\boldsymbol{u}_*, p_*)$ the value of $\mathcal{E}^{\mathrm{int},\Omega}[\boldsymbol{u}_*, p_*]$ is the lowest possible limit of the sequence $\mathcal{E}_\varepsilon^{\mathrm{int},\Omega}[\boldsymbol{u}_\varepsilon, p_\varepsilon]$, over all possible sequences $(\boldsymbol{u}_\varepsilon, p_\varepsilon)$ which converge in $L^1(\Omega;\mathbb{R}^{n_{\mathrm{dim},\boldsymbol{u}}}) \times L^1(\Omega)$ to $(\boldsymbol{u}_*, p_*)$. With appropriate coercivity, it implies that minimizers of $\mathcal{E}_\varepsilon^{\mathrm{int},\Omega}$ converge to minimizers of $\mathcal{E}^{\mathrm{int},\Omega}$ up to subsequences. Consequently, the variational problems $\mathcal{E}_\varepsilon^{\mathrm{int},\Omega}$ asymptotically approximate the variational problem $\mathcal{E}^{\mathrm{int},\Omega}$. We refer to [25] for an introduction to the concept of Γ-convergence.

We next discuss the form of the limiting functional in (4.46). The first term in (4.46) contains a bulk energy density $h_\ell^{\mathrm{qc}}\left(\nabla \boldsymbol{u}\right)$. In the scalar ($n_{\mathrm{dim},\boldsymbol{u}} = 1$) case, one can show [35] that $h_\ell^{\mathrm{qc}}\left(\nabla \boldsymbol{u}\right) = \Psi^0(\|\nabla \boldsymbol{u}\|)$, where

$$\Psi^0(\|\nabla \boldsymbol{u}\|) := \begin{cases} \|\nabla \boldsymbol{u}\|^2, & \text{if } \|\nabla \boldsymbol{u}\| \leq \dfrac{1}{2}\ell, \\ \ell\, \|\nabla \boldsymbol{u}\| - \dfrac{1}{4}\,\ell^2, & \text{otherwise}\,. \end{cases} \tag{4.47}$$

Accordingly, the elastic region $\|\nabla \boldsymbol{u}\| < \frac{1}{2}\ell$ is still described by the quadratic term $\|\nabla \boldsymbol{u}\|^2$ characteristic of elastic behavior. If the threshold $\|\nabla \boldsymbol{u}\| = \frac{1}{2}\ell$ is reached, the

displacement jump starts to evolve. As a consequence, the parameter ℓ defines a level separating the space of elastic deformations from the space of inelastic deformations.

In the general case $n_{\mathrm{dim},\boldsymbol{u}} \geq 1$, h_ℓ^{qc} is the quasiconvex envelope of

$$h_\ell(\boldsymbol{H}) := \min\left\{\|\boldsymbol{H}\|^2, \ell\|\boldsymbol{H}\|\right\} = \begin{cases} \|\boldsymbol{H}\|^2, & \text{if } \|\boldsymbol{H}\| \leq \ell, \\ \ell\,\|\boldsymbol{H}\|, & \text{otherwise}\,, \end{cases} \tag{4.48}$$

defined by

$$h_\ell^{\mathrm{qc}}(\boldsymbol{H}) := \inf\left\{\int_{(0,1)^{n_{\mathrm{dim}}}} h_\ell(\boldsymbol{H}+\nabla\boldsymbol{v})dV : \boldsymbol{v} \in \mathcal{C}_0^1([0,1]^{n_{\mathrm{dim}}};\mathbb{R}^{n_{\mathrm{dim},\boldsymbol{u}}})\right\}, \tag{4.49}$$

where $\mathcal{C}_0^1([0,1]^{n_{\mathrm{dim}}};\mathbb{R}^{n_{\mathrm{dim},\boldsymbol{u}}})$ denotes the set of continuously differentiable functions which vanish on the boundary. Qualitatively, the quasiconvex envelope characterizes the effective macroscopic energy of a representative volume element, as obtained after minimizing over all possible kinematically admissible microstructures $\boldsymbol{v}$ which do not affect the boundary data. One can easily see that Ψ^0 as defined in (4.47) is the convex envelope of h_ℓ. In [36, Lemma 2.5] it was shown that h_ℓ^{qc} is strictly larger than its convex envelope, but has the same growth; in particular the interpretation of the meaning of parameter ℓ is unchanged. As the difference is not large, for simplicity we shall focus on the simple expression in (4.47) also in the vectorial case $n_{\mathrm{dim},\boldsymbol{u}} > 1$.

The term $\Phi^0\left(\|\,[\![\boldsymbol{u}]\!]\,\|\right)$ in (4.46) denotes the interface energy density. It depends on the norm of the displacement jump at the interface $[\![\boldsymbol{u}]\!]$. As shown in [35], in the scalar case ($n_{\mathrm{dim},\boldsymbol{u}} = 1$) one has

$$\Phi^0(s) := \inf_{(\alpha,\beta)}\left\{\int_0^1 |1-\beta|\sqrt{d(\beta)^2\,|\alpha'|^2 + |\beta'|^2}\mathrm{d}t : (\alpha,\beta) \in H^1(]0,1[),\right.$$
$$\left.\alpha(0)=0, \alpha(1)=s, \beta(0)=\beta(1)=1\right\} \tag{4.50}$$

with $s := \|\,[\![\boldsymbol{u}]\!]\,\|$. In the vectorial case, a more complex expression was derived in [36]. However, in the case considered here, with elastic energy given by $\|\nabla\boldsymbol{u}\|^2$, their expression reduces to (4.50), again with $s := \|\,[\![\boldsymbol{u}]\!]\,\|$. Therefore, we can focus on this expression.

The energy density Φ^0 defined in (4.50) is nondecreasing, bounded, subadditive, and vanishes only at 0, we refer to [21, 35] for a detailed discussion of its properties. We provide a graphical illustration of $\Phi^0(s)$ in Fig. 4.2 and recall two key properties:

$$\lim_{s\uparrow\infty} \Phi^0(s) = 1\,, \tag{4.51}$$

$$\lim_{s\downarrow 0} \frac{\Phi^0(s)}{s} = \ell\,. \tag{4.52}$$

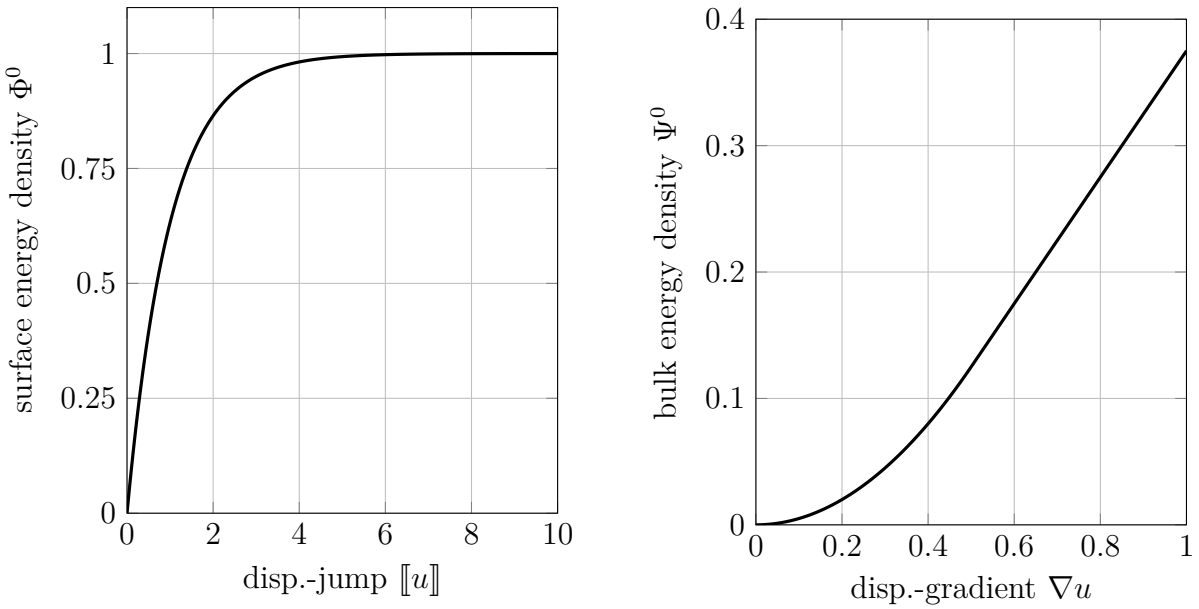

Figure 4.2: Interface energy density $\Phi^0([\![u]\!])$ (left) as well as the bulk energy density $\Psi^0(\nabla u)$ (right) for $d(p) = p/(1-p)$ and $\ell = 1$.

Clearly, $\lim_{s\uparrow\infty} \Phi^0(s)$ represents the interface's energy per unit area at total failure. From a materials science point of view, this corresponds to the fracture energy which can be measured in experiments. According to (4.51), the model predicts a fracture energy per unit area of magnitude 1. Having in mind that $\Phi^0(0) = 0$, Condition (4.52), in turn, shows that the initial slope of the interface's energy density equals ℓ. Since the variable thermodynamically conjugate to $s = \| [\![\boldsymbol{u}]\!] \|$ is an equivalent stress (traction), $\lim_{s\downarrow 0} \frac{\Phi^0(s)}{s}$ is an (equivalent) stress threshold defining the elastic limit. As a consequence, ℓ can be interpreted as the interface's strength. In what follows, the fracture energy is denoted by γ, while the strength of the interface (equivalent stress at crack initiation) is denoted by σ_{c}. With these notations, the phase field approximation as elaborated in [35] is characterized by $\gamma = 1$ (see (4.51)) and $\sigma_{\mathrm{c}} = \ell$ (see (4.52)). Furthermore, the artificial elastic model capturing the bulk's response is not in line with Hooke's model (see (4.47)). These physical restrictions and inconsistencies will be eliminated by the extended phase field model elaborated in this paper.

Due to the aforementioned inconsistencies, the model presented in [35] was modified in [55]. The modified energy reads (in the scalar setting $n_{\mathrm{dim},\boldsymbol{u}} = 1$)

$$\hat{\mathcal{E}}_\varepsilon^{\mathrm{int},\Omega}[u,p] := \int_\Omega d_\varepsilon^2(p)\,\frac{1}{2}c\|\nabla u\|^2 + \gamma\, f_\varepsilon(p,\nabla p)\,\mathrm{d}V\,, \tag{4.53}$$

where damage function $d(p)$ defining d_ε is chosen as $d(p) = p/(1-p)$. Following the proof in [35], it is shown in [55] that functionals $\hat{\mathcal{E}}^{\text{int},\Omega}$ converge (again, in the sense of Γ-convergence with respect to the $L^1(\Omega) \times L^1(\Omega)$ topology) to

$$\hat{\mathcal{J}}^{\text{int},\Omega}[u,p] := \begin{cases} \int_\Omega \hat{\Psi}^0\left(\|\nabla u\|\right) \,\mathrm{d}V + \int_\Gamma \hat{\Phi}^0\left(|[\![u]\!]|\right) \,\mathrm{d}A + |D^{\mathrm{c}}u|(\Omega) \\ \qquad\qquad \text{if } p = 1 \,\mathcal{L}^{n_{\text{dim}}}\text{-a.e. in } \Omega, u \in GBV(\Omega), \\ +\infty \qquad\qquad \text{otherwise}\,. \end{cases} \tag{4.54}$$

Here,

$$\hat{\Psi}^0(\|\nabla u\|) := \begin{cases} \frac{1}{2}c\|\nabla u\|^2, & \text{if } \|\nabla u\| \le \sqrt{\frac{1}{2}\frac{\gamma}{c}}, \\ \sqrt{\frac{1}{2}c\gamma}\,\|\nabla u\| - \frac{1}{4}\gamma, & \text{otherwise} \end{cases} \tag{4.55}$$

is the bulk energy density and

$$\begin{aligned} \hat{\Phi}^0(s) \;:=\; \inf_{(\alpha,\beta)} \Bigg\{ & \int_0^1 \sqrt{\frac{1}{2}c\gamma\beta^2\left|\alpha'\right|^2 + \gamma^2\left(1-\beta\right)^2\left|\beta'\right|^2}\mathrm{d}t : \\ & (\alpha,\beta) \in H^1(]0,1[), \alpha(0) = 0, \alpha(1) = s, \beta(0) = \beta(1) = 1 \Bigg\} \end{aligned} \tag{4.56}$$

denotes the interface energy density. Comparing (4.56) with (4.50), and using $d(p) = p/(1-p)$ which implies $\ell = 1$, one can show that $\hat{\Phi}^0(s) = \gamma\Phi^0(\sqrt{\frac{c}{2\gamma}}s)$. The limits in (4.51) and (4.52) then become

$$\lim_{s\uparrow\infty} \hat{\Phi}^0(s) = \gamma \tag{4.57}$$

$$\lim_{s\downarrow 0} \frac{\hat{\Phi}^0(s)}{s} = \sqrt{\frac{1}{2}c\gamma} =: \sigma_{\mathrm{c}}\,. \tag{4.58}$$

(4.57) confirms that γ is indeed the fracture energy. However, (4.58) shows that the strength of the material interface depends on bulk's elastic modulus c and fracture energy γ. Particularly, it is not an independent model parameter – as required by physics. In summary, extended model [55] indeed improves the original model as elaborated in [35]. However, it is still not flexible enough from a physics point of view. An extension of the model is thus the focus of the present paper."

Remark 1 *Optimization problem* (4.50) *can be reformulated by substituting the argument* α*. The same holds true for variants like* (4.56)*. The reformulated interface energy takes the form*

$$\Phi^0(s) := \inf_{(\alpha,\beta)} \left\{ \int_0^1 |1-\beta| \sqrt{s^2\, d(\beta)^2\, |\alpha'|^2 + |\beta'|^2}\, dt : (\alpha,\beta) \in H^1(]0,1[), \right. \\ \left. \alpha(0) = 0, \alpha(1) = 1, \beta(0) = \beta(1) = 1 \right\} \tag{4.59}$$

with $s = [\![u]\!]$*. Both formulations are used in the following.*

4.3 Physically sound interface energy

The model proposed in [35, 36, 55] results in an interface energy controlled by two dependent material parameters. In fact, even the elastic material parameter of the bulk energy influences the interface material properties. In this section the degradation function is extended in order to introduce independent material parameters. Furthermore, the inverse problem of prescribing a traction-separation law and finding the related degradation function is tackled.

4.3.1 Introducing independent interface material parameters

The following section is taken from [81, Sec. 3.1]:

"In order to account for experimentally measured fracture energies and strengths of material interfaces within the model we introduce the functional

$$\tilde{\mathcal{E}}^{\mathrm{int},\Omega}_{\varepsilon,c,\gamma,\sigma_\mathrm{c}}[\boldsymbol{u},p] := \int_\Omega \tilde{d}^2_{\varepsilon,c,\gamma,\sigma_\mathrm{c}}(p)\, \frac{1}{2}\, c\, \|\nabla \boldsymbol{u}\|^2 + \gamma\, f_\varepsilon(p,\nabla p)\, \mathrm{d}V\,. \tag{4.60}$$

It depends on three additional model parameters c, γ and σ_c. The enhanced damage function $\tilde{d}_{\varepsilon,c,\gamma,\sigma_\mathrm{c}}(p)$ in (4.60), which replaces $d_\varepsilon(p)$ entering (4.36), is defined by

$$\tilde{d}_{\varepsilon,c,\gamma,\sigma_\mathrm{c}}(p) := \begin{cases} \min\left\{ \sqrt{\dfrac{2\varepsilon\sigma_\mathrm{c}^2}{\gamma c \ell^2}}\, d(p), 1 \right\}, & \text{for } p \in [0,1[\,, \\ 1, & \text{for } p = 1\,, \end{cases} \tag{4.61}$$

where $d(p) \in \mathcal{C}^0\,(\,[0,1[\,,[0,+\infty[\,)$ is a non-decreasing function as in Section 4.2, and in particular fulfills Conditions (4.44) and (4.45). Comparing Definition (4.61) with (4.43) one obtains the equivalence

$$\tilde{d}_{\varepsilon,c,\gamma,\sigma_\mathrm{c}}(p) = d_{2\varepsilon\sigma_\mathrm{c}^2/\gamma c\ell^2}(p)\,. \tag{4.62}$$

In the following, we will prove that functionals $\tilde{\mathcal{E}}^{\mathrm{int},\Omega}_{\varepsilon,c,\gamma,\sigma_\mathrm{c}}$ Γ-converge in $L^1(\Omega;\mathbb{R}^{n_{\mathrm{dim},\boldsymbol{u}}}) \times L^1(\Omega)$ to

$$\tilde{\mathcal{J}}^{\mathrm{int},\Omega}_{c,\gamma,\sigma_\mathrm{c}}[\boldsymbol{u},p] := \begin{cases} \int_\Omega \tilde{h}^{\mathrm{qc}}_{c,\sigma_\mathrm{c}}\left(\nabla \boldsymbol{u}\right) \,\mathrm{d}V + \int_\Gamma \tilde{\Phi}\left(\| \left[\!\left[\boldsymbol{u}\right]\!\right] \|\right) \,\mathrm{d}A + \sigma_\mathrm{c}|D^\mathrm{c}\boldsymbol{u}|(\Omega), \\ \qquad\qquad \text{if } p = 1\,\mathcal{L}^{n_\mathrm{dim}}\text{-a.e. in } \Omega, \boldsymbol{u} \in GBV(\Omega)^{n_{\mathrm{dim},\boldsymbol{u}}}, \\ +\infty, \qquad\qquad \text{otherwise}\,, \end{cases} \tag{4.63}$$

with bulk energy density $\tilde{h}^{\mathrm{qc}}_{c,\sigma_\mathrm{c}}$ defined as the quasiconvex envelope (see (4.49)) of

$$\tilde{h}_{c,\sigma_\mathrm{c}}(\boldsymbol{H}) := \min\left\{\frac{1}{2}c\|\boldsymbol{H}\|^2, \sigma_c\|\boldsymbol{H}\|\right\} \tag{4.64}$$

and interface energy density

$$\tilde{\Phi}(\| \left[\!\left[\boldsymbol{u}\right]\!\right] \|) := \gamma\Phi^0\left(\frac{\sigma_\mathrm{c}}{\ell\,\gamma}\| \left[\!\left[\boldsymbol{u}\right]\!\right] \|\right), \tag{4.65}$$

where Φ^0 was defined in (4.50). In the scalar case, $\tilde{h}^{\mathrm{qc}}_{c,\sigma_\mathrm{c}}$ reduces to the convex envelope of $\tilde{h}_{c,\sigma_\mathrm{c}}$, and one obtains $\tilde{h}^{\mathrm{qc}}_{c,\sigma_\mathrm{c}}(\nabla\boldsymbol{u}) = \tilde{\Psi}_{c,\sigma_\mathrm{c}}(\|\nabla\boldsymbol{u}\|)$ where

$$\tilde{\Psi}_{c,\sigma_\mathrm{c}}(\|\nabla\boldsymbol{u}\|) := \begin{cases} \dfrac{1}{2}c\|\nabla\boldsymbol{u}\|^2, & \text{if } c\|\nabla\boldsymbol{u}\| \le \sigma_\mathrm{c}\,, \\ \sigma_\mathrm{c}\|\nabla\boldsymbol{u}\| - \dfrac{\sigma_\mathrm{c}^2}{2\,c}, & \text{otherwise}\,. \end{cases} \tag{4.66}$$

We first check that the claimed convergence leads to the desired values of the relevant material properties. First, σ_c would indeed be the strength of the material interface (see (4.66)). Furthermore, Properties (4.51) and (4.52) of Φ^0 imply

$$\lim_{s\uparrow\infty}\tilde{\Phi}\left(s\right) = \lim_{s\uparrow\infty}\gamma\Phi^0\left(\frac{\sigma_\mathrm{c}}{\ell\,\gamma}s\right) = \gamma\,, \tag{4.67}$$

$$\lim_{s\downarrow 0}\frac{\tilde{\Phi}\left(s\right)}{s} = \lim_{s\downarrow 0}\frac{\gamma\,\Phi^0\left(\dfrac{\sigma_\mathrm{c}}{\ell\,\gamma}\,s\right)}{s} = \sigma_\mathrm{c}\,. \tag{4.68}$$

As a consequence, γ would be the fracture energy and σ_c the strength of the material interface.

In order to prove convergence of the functional (4.60) to the sharp interface limit (4.63), a rescaling of the equations is employed. This rescaling allows to embed the novel model characterized by (4.60) into the original framework elaborated in [35, 36]. By doing so, convergence of (4.60) to (4.63) is a direct consequence of the proof presented in [35, 36].

Proof: The aforementioned rescaling reads, for parameters $\lambda, \mu > 0$ chosen below,

$$\omega := \lambda^{-1}\Omega, \quad \tilde{\gamma} := \lambda^{-1}\Gamma, \quad \boldsymbol{U}(\boldsymbol{x}) := \mu\lambda^{-1}\boldsymbol{u}(\lambda x), \quad P(\boldsymbol{x}) := p(\lambda\boldsymbol{x})\,. \tag{4.69}$$

Accordingly, domain Ω is rescaled to ω, while crack Γ is rescaled to $\tilde{\gamma}$ (the tilde symbol is used here, since the fracture energy has already been denoted as γ). Likewise, a rescaled displacement field and a phase field are introduced, a straightforwad computation shows that the resulting gradients comply with $\nabla\boldsymbol{U}(\boldsymbol{x}) = \mu\nabla\boldsymbol{u}(\lambda\boldsymbol{x})$, $\nabla P(\boldsymbol{x}) = \lambda\nabla p(\lambda\boldsymbol{x})$.

By choosing $\lambda = c\,\gamma\,\ell^2/(2\,\sigma_{\mathrm{c}}^2)$, $\mu = c\,\ell/(2\,\sigma_{\mathrm{c}})$ and $\eta = 2\,\sigma_{\mathrm{c}}^2/(c\,\ell^2)$ one obtains

$$c = 2\eta\mu^2\,, \qquad \sigma_{\mathrm{c}} = \eta\ell\mu\,, \qquad \gamma = \eta\lambda\,. \tag{4.70}$$

Furthermore, energy $\tilde{\mathcal{E}}^{\mathrm{int},\Omega}_{\varepsilon,c,\gamma,\sigma_{\mathrm{c}}}[\boldsymbol{u},p]$ can be rewritten as

$$\begin{aligned}
\tilde{\mathcal{E}}^{\mathrm{int},\Omega}_{\varepsilon,c,\gamma,\sigma_{\mathrm{c}}}[\boldsymbol{u},p] &= \int_\Omega \tilde{d}^2_{\varepsilon,c,\gamma,\sigma_{\mathrm{c}}}(p)\,\frac{c}{2}\,\|\nabla\boldsymbol{u}\|^2 + \gamma\left[\frac{(1-p)^2}{4\varepsilon} + \varepsilon\|\nabla p\|^2\right]\mathrm{d}V \\
&= \int_\Omega \tilde{d}^2_{\varepsilon,2\eta\mu^2,\eta\lambda,\eta\ell\mu}(p)\,\eta\mu^2\,\|\nabla\boldsymbol{u}\|^2 + \eta\lambda\left[\frac{(1-p)^2}{4\varepsilon} + \varepsilon\|\nabla p\|^2\right]\mathrm{d}V \\
&= \eta\int_\Omega d^2_{\varepsilon/\lambda}(p)\,\mu^2\,\|\nabla\boldsymbol{u}\|^2 + \frac{(1-p)^2}{4\varepsilon/\lambda} + \frac{\varepsilon}{\lambda}\lambda^2\|\nabla p\|^2\mathrm{d}V \\
&= \eta\lambda^{n_{\mathrm{dim}}}\int_\omega d^2_{\varepsilon/\lambda}(P)\|\nabla\boldsymbol{U}\|^2 + \frac{(1-P)^2}{4\varepsilon/\lambda} + \frac{\varepsilon}{\lambda}\|\nabla P\|^2\mathrm{d}V \\
&= \eta\lambda^{n_{\mathrm{dim}}}\mathcal{E}^{\mathrm{int},\omega}_{\varepsilon/\lambda}[\boldsymbol{U},P]\,,
\end{aligned} \tag{4.71}$$

where identity $\tilde{d}^2_{\varepsilon,2\eta\mu^2,\eta\lambda,\eta\ell\mu}(p) = d_{\varepsilon/\lambda}(p)$ (see (4.62)) has been used and $\mathcal{E}^{\mathrm{int},\omega}_{\varepsilon/\lambda}[\boldsymbol{U},P]$ is the energy defined in (4.36). Accordingly, (4.71) allows indeed to embed the novel model ($\tilde{\mathcal{E}}^{\mathrm{int},\Omega}_{\varepsilon,c,\gamma,\sigma_{\mathrm{c}}}[\boldsymbol{u},p]$; Eq. (4.60)) into the framework already elaborated in [35] ($\mathcal{E}^{\mathrm{int},\omega}_{\varepsilon/\lambda}[\boldsymbol{U},P]$; Eq. (4.36)).

One can analogously derive a similar scaling for the sharp interface energies. For that purpose, it suffices to consider the case $p = 1$ almost everywhere (which is equivalent to $P = 1$ almost everywhere). Comparing (4.64) with (4.48), one obtains

$$\tilde{h}_{c,\sigma_{\mathrm{c}}}(\boldsymbol{H}) = \frac{2\sigma_c^2}{c\ell^2}h_\ell\left(\frac{c\ell}{2\sigma_c}\boldsymbol{H}\right) = \eta h_\ell\left(\mu\boldsymbol{H}\right) \tag{4.72}$$

and therefore

$$\tilde{h}^{\mathrm{qc}}_{c,\sigma_{\mathrm{c}}}(\boldsymbol{H}) = \eta h^{\mathrm{qc}}_\ell\left(\mu\boldsymbol{H}\right)\,. \tag{4.73}$$

Analogously to (4.71), the limiting energy $\tilde{\mathcal{J}}^{\mathrm{int},\Omega}_{c,\gamma,\sigma_\mathrm{c}}[\boldsymbol{u},1]$ can be rewritten as

$$\begin{aligned}\tilde{\mathcal{J}}^{\mathrm{int},\Omega}_{c,\gamma,\sigma_\mathrm{c}}[\boldsymbol{u},1] &= \int_\Omega \tilde{h}^{\mathrm{qc}}_{c,\sigma_\mathrm{c}}(\nabla\boldsymbol{u})\mathrm{d}V + \int_\Gamma \gamma\Phi^0(\frac{\sigma_\mathrm{c}}{\gamma\ell}\| [\![\boldsymbol{u}]\!] \|)\mathrm{d}A + \sigma_\mathrm{c}|D^c\boldsymbol{u}|(\Omega)\\ &= \eta\int_\Omega h^{\mathrm{qc}}_\ell(\mu\nabla\boldsymbol{u})\mathrm{d}V + \eta\lambda\int_\Gamma \Phi^0(\frac{\mu}{\lambda}\| [\![\boldsymbol{u}]\!] \|)\mathrm{d}A + \eta\ell\mu|D^c\boldsymbol{u}|(\Omega)\\ &= \eta\lambda^{n_\mathrm{dim}}\int_\omega h^{\mathrm{qc}}_\ell(\nabla\boldsymbol{U})\mathrm{d}V + \eta\lambda^{n_\mathrm{dim}}\int_{\tilde{\gamma}} \Phi^0(\| [\![\boldsymbol{U}]\!] \|)\mathrm{d}A + \eta\lambda^{n_\mathrm{dim}}\ell|D^c\boldsymbol{U}|(\omega)\\ &= \eta\lambda^{n_\mathrm{dim}}\mathcal{J}^{\mathrm{int},\omega}[\boldsymbol{U},1]\,,\end{aligned} \tag{4.74}$$

where $\mathcal{J}^{\mathrm{int},\omega}[\boldsymbol{U},1]$ is the energy corresponding to the sharp interface problem defined in (4.46). By applying [35, Theorem 3] for $n_{\mathrm{dim},\boldsymbol{u}} = 1$, and [36, Theorem 2.1] for $n_{\mathrm{dim},\boldsymbol{u}} \geq 2$, we obtain $\mathcal{E}^{\mathrm{int},\omega}_{\varepsilon/\lambda}[\boldsymbol{U},P] \overset{\Gamma}{\to} \mathcal{J}^{\mathrm{int},\omega}[\boldsymbol{U},P]$, and therefore

$$\tilde{\mathcal{E}}^{\mathrm{int},\Omega}_{\varepsilon,c,\gamma,\sigma_c}[\boldsymbol{u},p] = \eta\lambda^{n_\mathrm{dim}}\mathcal{E}^{\mathrm{int},\omega}_{\varepsilon/\lambda}[\boldsymbol{U},P] \overset{\Gamma}{\to} \eta\lambda^{n_\mathrm{dim}}\mathcal{J}^{\mathrm{int},\omega}[\boldsymbol{U},P] = \tilde{\mathcal{J}}^{\mathrm{int},\Omega}_{c,\gamma,\sigma_\mathrm{c}}[\boldsymbol{u},p] \tag{4.75}$$

which concludes the proof. □

"

Remark 2 *For later purposes the function space of admissible functions d is denoted by*

$$\mathcal{D}_\ell = \left\{ d(p) \in \mathcal{C}^0\left([0,1[\,,[0,+\infty[\right) : d(p) \text{ fulfills (4.44), (4.45), (4.77)} \right\} \tag{4.76}$$

where

$$d(p_1) \leq d(p_2), \qquad \forall p_1, p_2 \in [0,1[\,, \quad p_1 < p_2, \tag{4.77}$$

defines the monotonicity condition of the degradation function. The space of admissible degradation functions can be reduced to functions with $\ell = 1$ without loss of generality. This results from Definition (4.61) of advanced degradation functions where ℓ drops out of the equation when choosing $d^* = \ell\, d$ as degradation function with $d \in \mathcal{D}_1$. Accordingly, function space $\mathcal{D}_1$ is abbreviated as

$$\mathcal{D} := \mathcal{D}_1\,. \tag{4.78}$$

in the following.

4.3.2 Introducing traction-separation laws to the model

The following section is taken from [79, Sec. 3∗]:

"As shown in the previous section, the phase field model suitable for cohesive fracture is based on two functions: (1) the Helmholtz energy capturing the bulk's response (see term $1/2\,c\,\|\nabla \boldsymbol{u}\|$ in Eq. (4.60)) and (2) degradation function $d_{\varepsilon,c,\gamma,\sigma_c}(p)$ $[\dots]$. The remaining functions such as f_ε or $\mathcal{E}^{\text{ext}}$ are kept fixed. Since the bulk's constitutive response assumed within the phase field model is directly inherited by the resulting sharp interface model (see Eq. (4.66)), the choice of the degradation function $d_{\varepsilon,c,\gamma,\sigma_c}(p)$ defines the resulting traction-separation law of the sharp interface limit. According to Eq. (4.61), degradation function $d_{\varepsilon,c,\gamma,\sigma_c}(p)$, in turn, can be defined by its normalized counterpart $d(p)$. Based on this observation, this section is structured as follows:

Subsection 4.3.2.1 $d(p) \;\Rightarrow$ fracture energy, traction-separation-law, cf. Φ,
Subsection 4.3.2.2 $d(p) \;\Leftarrow$ fracture energy, traction-separation-law, cf. Φ.

Since the focus is on isotropic cohesive-zone models, a one-dimensional setting can be adopted – essentially, one deals with the norm of the displacement jump. This can also be seen by computing the cohesive tractions, i.e.,

$$\boldsymbol{T} = \underbrace{\frac{\partial \Phi}{\partial \| [\![\boldsymbol{u}]\!] \|}}_{\text{1D}} \underbrace{\frac{[\![\boldsymbol{u}]\!]}{\| [\![\boldsymbol{u}]\!] \|}}_{\text{3D}} \,. \tag{4.79}$$

"

4.3.2.1 The forward problem: Computation of the traction-separation law (sharp interface problem) for a given degradation function (phase-field model)

The following section is taken from [79, Sec. 3.1∗]:

"In line with Eqs. (4.50) and (4.65), the fracture energy has to be computed only for the normalized case $\gamma = 1$ and $\sigma_c = 1$, and by isotropy it only depends on the norm $\| [\![\boldsymbol{u}]\!] \|$, which for notational simplicity we denote by $[\![u]\!]$ below. For other values, it can be re-scaled. Furthermore, Eq. (4.50) defines this energy for a certain value of $[\![u]\!]$. Consequently, minimization problem (4.50) has to be solved for all admissible displacement jumps. Within the algorithm to be elaborated, this is done for a number of different $[\![u]\!]$ which constitutes an equidistant partition of the interval of interest. For this reason, only one of these steps is considered in what follows.

Variational principle (4.50) can usually not be solved analytically, but it is well-suited for the finite element method. Thus, functional

$$f_h^0([\![u]\!]) := \int_0^1 |1-\beta_h| \sqrt{|[\![u]\!]|^2 \, d(\beta_h)^2 \, |\alpha_h'|^2 + |\beta_h'|^2} \mathrm{d}x \tag{4.80}$$

is introduced, cf. Eq. (4.50). Index h signals the finite element discretization. Since only first derivatives of unknown functions α_h and β_h appear, classic continuous piecewise affine finite elements can be used. In what follows interval $[0,1]$ is discretized by means of n linear finite elements in order to approximate α_h and β_h. The respective nodal degrees of freedom are denoted as $\alpha_h^{(i)}$ and $\beta_h^{(i)}$. By doing so, infinite-dimensional variation problem (4.50) is approximated by its discretized finite-dimensional counterpart

$$\Phi_h^0 := \min_{\alpha_h^{(1)},\beta_h^{(1)},\ldots,\alpha_h^{(n)},\beta_h^{(n)}} f_h^0([\![u]\!]) \,. \tag{4.81}$$

In line with Eq. (4.50), discrete variational principle (4.81) is subjected to constraints. While the incorporation of

$$\alpha_h^{(1)} = 0, \quad \alpha_h^{(n)} = 1, \quad \beta_h^{(1)} = 1, \quad \beta_h^{(n)} = 1 \tag{4.82}$$

is straightforward, the discrete counterpart of $0 \leq \beta \leq 1$ (affine shape functions; extrema are at the nodes)

$$0 \leq \beta_h^{(i)} \leq 1 \qquad \text{for } i = 2, \ldots, n-1 \tag{4.83}$$

has been implemented by means of quadratic programming. It bears emphasis that the fracture energy computed from minimization problem (4.81) (or from its infinite-dimensional counterpart (4.50)) corresponds to the sharp interface limit ($\varepsilon \to 0$)."

4.3.2.2 The inverse problem: Computation of the degradation function (phase-field model) for a given traction-separation law (sharp interface problem)

The following section is taken from [79, Sec. 3.2∗]:

"

Fundamentals For a given $d = d(p)$, the algorithm presented in the previous subsection allows the computation of the normalized fracture energy Φ^0. By re-scaling the real fracture energy is then obtained (see Eq. (4.65)) from which the traction-separation-law can be computed, cf. Eq. (4.79). In this section, the inverse problem is considered. This means that the traction-separation law is considered as given (e.g., from experiments).

Equivalently, the fracture energy can be assumed as known, or its re-scaled counterpart Φ^0. Based on this energy, degradation function $d = d(p)$ is to be identified. Clearly, this can be written as an optimization problem of the type

$$d^{\text{opt}} = \arg\min_{d\in\mathcal{D}} \left\{ \int_0^\infty \left| \Phi^{0,\text{exp}}(s) - \Phi^{0,d}(s) \right|^2 \mathrm{d}s \right\} \text{ with } s := \| \llbracket \boldsymbol{u} \rrbracket \| \,. \tag{4.84}$$

Here, $\Phi^{0,\text{exp}}$ is the prescribed (normalized) fracture energy and $\Phi^{0,d}(s)$ depending on the unknown degradation function $d(p)$ corresponds to the fracture energy obtained from the phase-field model.

For a given displacement jump, $\Phi^{0,d}(s)$ is computed by means of the algorithm presented in Subsection 4.3.2.1. However, since both energies should be identical for arbitrary displacement jumps, the error is integrated over all admissible displacement jumps. Clearly, the choice of the L_2-norm for measuring this error is not mandatory. We remark however that the condition $d \in \mathcal{D}$ already ensures that $\Phi^{0,d}(s)$ has the correct linear leading-order term at small openings, see in particular (4.45). Within the numerical implementation, the set of admissible displacement jumps is discretized leading to the discrete counterpart of Eq. (4.84)

$$d^{\text{opt}} \quad = \quad \arg\min_{d\in\mathcal{D}} \left\{ \sum_i \left| \Phi^{0,\text{exp}}(s_i) - \Phi^{0,d}(s_i) \right|^2 \right\} \tag{4.85}$$

where s_i is an equidistant partition of the space of admissible displacement jumps. Conceptually, problem (4.85) appears to be straightforward to be solved. However, the space $\mathcal{D}$ is infinite-dimensional and the constraints are not trivial, cf. Eqs. (4.44)–(4.45). In the next subsection, approximation space series $\mathcal{D}^{(i)}$ are thus derived. In line with most approximation schemes, they should fulfill the following properties: (1) $\mathcal{D}^{(i)} \subseteq \mathcal{D}$, (2) $\dim \mathcal{D}^{(i)} < \infty$ and (3) $\mathcal{D}^{(i)} \subseteq \mathcal{D}^{(i+1)}$. Clearly, a density property in the sense of $\lim_i \mathcal{D}^{(i)} \to \mathcal{D}$ in a topology that makes (4.85) continuous would be appreciated as well. However, numerical experiments will show that the proposed approximation space is already large enough.

Approximation of function space $\mathcal{D}$ Approximation space $\mathcal{D}^{(i)}$ has to fulfill Conditions (4.44)-(4.45). Inspired by the original choice $d(p) = p/(1-p)$ (see [35, 36, 55, 81]), ansatz

$$d(p) = \frac{\tilde{d}(p)}{1-p} \tag{4.86}$$

is proposed. Here, new function $\tilde{d}(p)$ has to comply with

$$\tilde{d} \in \tilde{\mathcal{D}} := \left\{ \tilde{d} \in \mathcal{C}^0([0,1],[0,1]) : \tilde{d}(0) = 0, \tilde{d}(1) = 1 \right\} . \tag{4.87}$$

Apparently, this choice a priori fulfills $d(p) \in \mathcal{C}^0\,(\,[0,1[\,,[0,+\infty[\,)$ (see Eq. (4.44)), $d(0) = 0$ and $\lim_{p\nearrow 1} d(p)\,(1-p) = 1$ (see Eq. (4.45)). It remains to check that $d^{-1}(0) = \{0\}$ (see Eq. (4.44)), which is equivalent to the same property for $\tilde{d}$, as well as monotonicity, in the sense that $d(p_1) \leq d(p_2)$ for $0 \leq p_1 < p_2 < 1$ (see Eq. (4.77)). The last condition, in the equivalent form $\tilde{d}(p_1)/(1-p_1) \leq \tilde{d}(p_2)/(1-p_2)$ for $0 \leq p_1 < p_2 < 1$, will be enforced numerically within the algorithm.

We remark that, if function $t \mapsto \tilde{d}(\sqrt{t})$ is convex, then problem (4.50) has a unique solution in the cohesive regime [21, Prop. 8.3]. In turn, this implies that the traction depends continuously on the opening s.

Approximation of function space $\tilde{\mathcal{D}}$ In what follows, two different approximations of space $\tilde{\mathcal{D}}$ will be given. They define the approximation space of $d(p)$, in turn, by

$$d \in \mathcal{D}_t := \left\{ \frac{\tilde{d}(p)}{1-p} : \tilde{d}(p) \in \tilde{\mathcal{D}}_t \right\} . \tag{4.88}$$

Space I: Polynomials First, an approximation by means of polynomials is considered. It reads

$$\tilde{\mathcal{D}}_{\text{pol}}^{(n_{\boldsymbol{a}})} = \left\{ \tilde{d}(p) := \sum_{i=1}^{n_{\boldsymbol{a}}+1} a_i\, p^i : a_i \in \mathbb{R},\, \sum_{i=1}^{n_{\boldsymbol{a}}+1} a_i = 1 \right\} . \tag{4.89}$$

Here and in the following $n_{\boldsymbol{a}} = \dim \tilde{\mathcal{D}}_{\text{pol}}^{(n_{\boldsymbol{a}})} = \dim \mathcal{D}_{\text{pol}}^{(n_{\boldsymbol{a}})}$ denotes the dimension of the approximation space. Apparently and as required, this ansatz fulfills $\tilde{d}(p=0) = 0$ and $\tilde{d}(p=1) = 1$. Furthermore, is generates a nested series of ansatz spaces with smooth functions $\tilde{d}$. Clearly, smoothness of $\tilde{d}$ is desired from a numerical point of view. However, it also might lead to spurious oscillations, in particular if the function to be captured is not smooth. As mentioned before, monotonicity of the resulting degradation function $d(p)$ is checked numerically.

Space II: Cubic $\mathcal{C}^2$ splines Besides the $\mathcal{C}^\infty$-smooth polynomials, natural cubic $\mathcal{C}^2$-splines $s(p, \boldsymbol{z}, \boldsymbol{b}) \in \mathcal{S}$ are also considered. Here, $\boldsymbol{z} \in \mathbb{R}^{n_{\boldsymbol{a}}+2}$, $0 = z_0 < z_1 < \cdots < z_{n_{\boldsymbol{a}}+1} = 1$ is the knot vector (equidistant) and $\boldsymbol{a} \in \mathbb{R}^{n_{\boldsymbol{a}}+2}$ contains the function values, such that $s(z_i, \boldsymbol{z}, \boldsymbol{a}) = a_i\ \forall i \in 0, \ldots, n_{\boldsymbol{a}}+1$. Accordingly, $s(z_0, \boldsymbol{z}, \boldsymbol{a}) = 0$ and $s(z_{n_{\boldsymbol{a}}+1}, \boldsymbol{z}, \boldsymbol{a}) = 1$ and the approximation of space $\tilde{\mathcal{D}}$ reads

$$\begin{aligned} &\tilde{\mathcal{D}}_{\text{spl}}^{(n_{\boldsymbol{a}})} := \\ &\left\{ s(p, \boldsymbol{z}, \boldsymbol{a}) \in \mathcal{S} : 0 = z_0 < z_1 < \ldots < z_{n_{\boldsymbol{a}}+1} = 1, \boldsymbol{a} = [0, a_1, \ldots, a_{n_{\boldsymbol{a}}}, 1]^T \right\} . \end{aligned} \tag{4.90}$$

Monotonicity of the resulting degradation function $d(p)$ is again enforced numerically.

Remark $\mathcal{C}^0$-continuous piecewise affine functions also lead to good approximations of the sharp interface fracture energy. However, the resulting finite element implementation showed numerical problems. To be more precise, the implemented staggered algorithm (alternate minimization based on Newton's method) has not always converged. For this reason, $\mathcal{C}^0$-continuous piecewise affine functions will not be considered in the following."

4.3.2.3 Visualization of the admissible parameter spaces for $n_{\boldsymbol{a}} = 2$

For $n_{\boldsymbol{a}} = 2$ a visualization of the admissible parameter space of the polynomial approach (Figure 4.3) as well as the spline approach (Figure 4.4) are presented. The admissible parameter sets are denoted by $\mathcal{A}_{\text{pol}}^{(n_{\boldsymbol{a}})}$ and $\mathcal{A}_{\text{spl}}^{(n_{\boldsymbol{a}})}$ respectively. They are defined by

$$\mathcal{A}_{\text{pol}}^{(n_{\boldsymbol{a}})} := \left\{ \boldsymbol{a} \in \mathbb{R}_a^{\boldsymbol{n}} : \sum_{i=1}^{n_{\boldsymbol{a}}+1} a_i \, p^i \in \tilde{\mathcal{D}} \right\} , \tag{4.91}$$

$$\mathcal{A}_{\text{spl}}^{(n_{\boldsymbol{a}})} := \Big\{ \boldsymbol{a} \in \mathbb{R}_a^{\boldsymbol{n}} : s(p, \boldsymbol{z}, \boldsymbol{a}) \in \tilde{\mathcal{D}}, \tag{4.92}$$

$$0 = z_0 < z_1 < \ldots < z_{n_{\boldsymbol{a}}+1} = 1, \boldsymbol{a} = [0, a_1, \ldots, a_{n_{\boldsymbol{a}}}, 1]^{\text{t}} \Big\} ,$$

with $\tilde{\mathcal{D}}$ as defined in Equation 4.87.

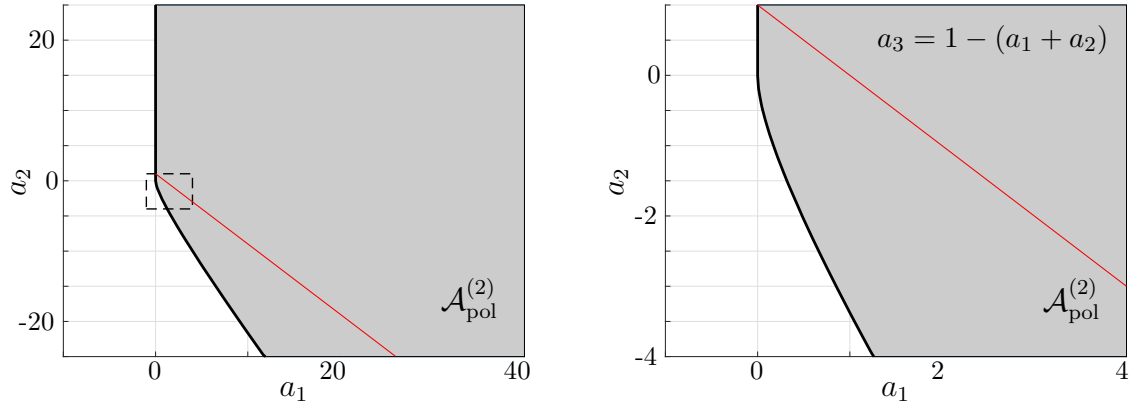

Figure 4.3: Admissible parameter set $\mathcal{A}_{\text{pol}}^{(2)}$ for polynomial-type basis functions (4.89) with $n_{\boldsymbol{a}} = 2$. The value for a_3 is $a_3 = 1 - (a_1 + a_2)$. The subfigure on the right shows a close up of the highlighted area on the left subfigure. The red line highlights the admissible parameter space $\mathcal{A}_{\text{pol}}^{(1)}$ for one free parameter $n_{\boldsymbol{a}} = 1$.

For the polynomial approach, the function spaces are nested in the sense $\tilde{\mathcal{D}}_{\text{pol}}^{(n_{\boldsymbol{a}})} \subset \tilde{\mathcal{D}}_{\text{pol}}^{(n_{\boldsymbol{a}})+1} \; \forall \, n_{\boldsymbol{a}} > 0$. For the admissible parameter sets, this nested structure takes the form

$$\mathcal{A}_{\text{pol}}^{(n_{\boldsymbol{a}})} \times \{0\} \subset \mathcal{A}_{\text{pol}}^{(n_{\boldsymbol{a}}+1)} \quad \forall \, n_{\boldsymbol{a}} > 0. \tag{4.93}$$

In fact

$$\mathcal{A}_{\text{pol}}^{(n_{\boldsymbol{a}})} = \left\{ \boldsymbol{a} \in \mathbb{R}^{n_{\boldsymbol{a}}} : [a_1, a_2, \ldots, a_{n_{\boldsymbol{a}}}, 0]^{\text{t}} \in \mathcal{A}_{pol}^{(n_{\boldsymbol{a}}+1)} \right\} \quad \forall\, n_{\boldsymbol{a}} > 0 \tag{4.94}$$

holds. Figure 4.3 also presents the admissible parameter set for $n_{\boldsymbol{a}} = 0$ as a red line.

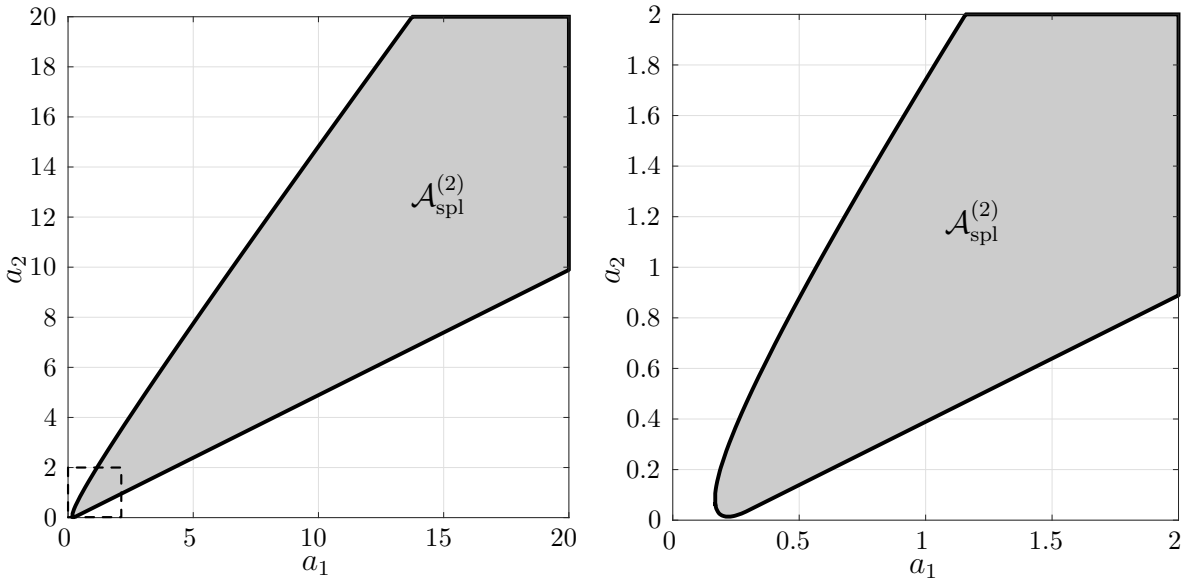

Figure 4.4: Admissible parameter set $\mathcal{A}_{\text{spl}}^{(2)}$ for spline based degradation functions (4.90) with $n_{\boldsymbol{a}} = 2$. The subfigure on the right shows a close up of the highlighted area on the left subfigure.

4.4 Physically sound bulk material

4.4.1 Phase field approximation of hyperelastic bulk models

The following section is taken from [81, Sec. 3.2.1]:

"The phase field model mathematically derived above does not account for a realistic material response in the bulk, cf. Eq. (4.36). In particular, the underlying Helmholtz energy is not invariant with respect to infinitesimal superposed rotations and thus, the resulting stresses are not symmetric. Furthermore, the energy depends only on one model parameter – in contrast to the simplest physically sound energy being Hooke's model which requires two model parameters, e.g. the Lamé coefficients. An ad-hoc modification of the model presented in [35] in order to account for Hooke's law was already advocated in [55]. An approach compatible with finite kinematics was studied in [36]. We develop here a different framework, that allows to choose any hyperelastic

bulk model, and to distinguish between opening and closing of cracks. In contrast to [35, 55], a geometrically exact setting is adopted in what follows.

In order to derive the aforementioned generalized framework, the energy density of the bulk material $\tilde{d}^2_{\varepsilon,c,\gamma,\sigma_c}(p)\,\frac{1}{2}\,c\,\|\nabla \boldsymbol{u}\|^2$ is re-interpreted first. For that purpose, an effective displacement gradient denoted as $\nabla \boldsymbol{u}^{\text{eff}}$ is introduced. Since the total strains in the neighborhood of the interface are proportional to the inverse width of the interface and therefore also proportional to $1/\tilde{d}^2_{\varepsilon,c,\gamma,\sigma_c}(p)$, one obtains

$$\|\nabla \boldsymbol{u}\| \propto \frac{1}{\varepsilon} \propto \frac{1}{\tilde{d}^2_{\varepsilon,c,\gamma,\sigma_c}} \tag{4.95}$$

which, in turn, motivates the introduction of effective displacement gradient

$$\nabla \boldsymbol{u}^{\text{eff}} = \tilde{d}^2_{\varepsilon,c,\gamma,\sigma_c}(p)\nabla \boldsymbol{u} \quad \Rightarrow \quad \|\nabla \boldsymbol{u}\|^{\text{eff}} := \tilde{d}^2_{\varepsilon,c,\gamma,\sigma_c}(p)\|\nabla \boldsymbol{u}\|\,. \tag{4.96}$$

Observing further that the energy density of the phase field $f_\varepsilon(p,\nabla p)$ is also proportional to $1/\varepsilon$ in the interface region, such that

$$f_\varepsilon(p,\nabla p) \overset{\|\nabla p\| \propto \frac{1}{\varepsilon}}{\propto} \frac{1}{\varepsilon} \propto \frac{1}{\tilde{d}^2_{\varepsilon,c,\gamma,\sigma_c}}\,, \tag{4.97}$$

one can re-write the energy density of the bulk material as

$$\tilde{d}^2_{\varepsilon,c,\gamma,\sigma_c}(p)\,\underbrace{\frac{1}{2}\,c\,\|\nabla \boldsymbol{u}\|^2}_{\Psi_*(\nabla \boldsymbol{u})} = \frac{1}{\tilde{d}^2_{\varepsilon,c,\gamma,\sigma_c}(p)}\,\underbrace{\frac{1}{2}\,c\,\left[\|\nabla \boldsymbol{u}\|^{\text{eff}}\right]^2}_{\Psi_*(\nabla \boldsymbol{u}^{\text{eff}})}\,. \tag{4.98}$$

Outside the interface region, $\tilde{d}_{\varepsilon,c,\gamma,\sigma_c}(p)$ is close to 1 and $f_\varepsilon(p,\nabla p)$ vanishes. Thus the aforementioned adjustments do not effect these regions.

Eq. (4.98) provides a natural guideline for the consideration of general hyperelastic models. Suppose the underlying standard hyperelastic model is given in terms of the Green-Lagrange strains $\boldsymbol{E}$ (geometrically exact setting) and the bulk's (standard) energy is denoted as $\Psi_* = \Psi_*(\boldsymbol{E})$. Then, the right hand side of Eq. (4.98) suggests to replace $\Psi_*(\boldsymbol{E})$ by $\Psi_*(\boldsymbol{E}^{\text{eff}})$ where the effective counterpart of $\boldsymbol{E}$ is defined as

$$\begin{aligned}\boldsymbol{E}^{\text{eff}} &:= \frac{1}{2}\left[\left[\nabla \boldsymbol{u}^{\text{eff}}\right]^{\text{t}} \cdot \nabla \boldsymbol{u}^{\text{eff}}\right] + \frac{1}{2}\left[\left[\nabla \boldsymbol{u}^{\text{eff}}\right]^{\text{t}} + \nabla \boldsymbol{u}^{\text{eff}}\right] \\ &:= \tilde{d}^4_{\varepsilon,c,\gamma,\sigma_c}(p)\frac{1}{2}\left[\nabla \boldsymbol{u}^{\text{t}} \cdot \nabla \boldsymbol{u}\right] + \tilde{d}^2_{\varepsilon,c,\gamma,\sigma_c}(p)\nabla \boldsymbol{u}^{\text{sym}}\,.\end{aligned} \tag{4.99}$$

Clearly, other effective deformation measures can be derived in the same way. In line with Eq. (4.98) the final step is the multiplication of $\Psi_*(\boldsymbol{E}^{\text{eff}})$ by prefactor $\tilde{d}^{-2}_{\varepsilon,c,\gamma,\sigma_c}(p)$.

This re-scaling is necessary, since the bulk and the interface energies scale differently. In summary, one thus derives the simple procedure

$$\text{given: } \Psi_* = \Psi_*(\boldsymbol{E}) \quad \Rightarrow \quad \text{phase field model: } \Psi^{\text{eff}}(\boldsymbol{E}, p) := \tilde{d}^{-2}_{\varepsilon,c,\gamma,\sigma_c}(p)\, \Psi_*(\boldsymbol{E}^{\text{eff}}) \tag{4.100}$$

„

4.4.2 Strength of the material interface

The following section is taken from [81, Sec. 3.2.2]:

"The model proposed in Subsection 4.3.1 depends on three parameters associated with the material behavior: fracture energy γ, strength σ_c of the material interface, and effective elastic bulk stiffness c. Since the energy density in the bulk used in Subsection 4.3.1 is not realistic, a physically more sound framework was presented in the previous Subsection. Within this framework, the elastic bulk's response is captured by Ψ_* depending on additional material parameters – for instance, on the Young's modulus and the Poisson ratio. For this reason, parameter c seems to be unnecessary. However, this is not the case, since c serves two purposes. In addition to capturing the bulk's response, the effective stiffness c also implicitly controls the strength of the material, cf. Eq. (4.61). This meaning of c is still required. In order to highlight the different meaning of c, it is renamed by c^*.

The calibration of c^* is implemented here by means of a one-dimensional tensile test. For this test, c^* corresponds to the stress at crack initiation. As far as a phase field approximation is concerned, $\nabla p = \mathbf{0}$ before the crack starts to evolve. Additionally, $p = p_c$ which is defined as truncation point of $d_{\varepsilon,c^*,\gamma,\sigma_c}$, see Eq. (4.61). Starting from these initial conditions, crack initiation is associated with stationarity condition

$$\partial_p \left\{ \Psi^{\text{eff}}(\boldsymbol{E}, p) + \gamma\, f_\varepsilon(p, \mathbf{0}) \right\} = 0\,, \tag{4.101}$$

which is equivalent to

$$\begin{aligned} \frac{1}{\tilde{d}_{\varepsilon,c^*,\gamma,\sigma_c}(p_c)^2} \left.\frac{\partial \Psi_*}{\partial E^{\text{eff}}}\right|_c \left.\frac{\partial E^{\text{eff}}}{\partial \nabla u^{\text{eff}}}\right|_c 2\, \tilde{d}_{\varepsilon,c^*,\gamma,\sigma_c}(p_c) \left.\frac{\partial \tilde{d}_{\varepsilon,c^*,\gamma,\sigma_c}}{\partial p}\right|_c \nabla u - \\ \frac{2}{\tilde{d}_{\varepsilon,c^*,\gamma,\sigma_c}(p_c)^3} \left.\frac{\partial \tilde{d}_{\varepsilon,c^*,\gamma,\sigma_c}}{\partial p}\right|_c \Psi_*(E_c^{\text{eff}}) - \gamma\, \frac{1 - p_c}{2\,\varepsilon} = 0\,, \end{aligned} \tag{4.102}$$

where index c signals values at the moment of crack initiation. Here, a general degradation function $d(p)$, fulfilling Properties (4.44) and (4.45), is used. The values for E_c

and ∇u_c follow from the bulk energy density Ψ_*. The non-bold E and ∇u denote the one-dimensional counterparts of $\boldsymbol{E}$ and $\nabla \boldsymbol{u}$. Using

$$\tilde{d}_{\varepsilon,c^*,\gamma,\sigma_\mathrm{c}}(p_\mathrm{c}) = \sqrt{\frac{2\,\varepsilon\,\sigma_\mathrm{c}^2}{\gamma\,c^*\,\ell^2}}\,d(p_\mathrm{c}) = 1 \tag{4.103}$$

and the left derivative

$$\left.\frac{\partial \tilde{d}_{\varepsilon,c^*,\gamma,\sigma_\mathrm{c}}}{\partial p}\right|_c = \sqrt{\frac{2\,\varepsilon\,\sigma_\mathrm{c}^2}{\gamma\,c^*\,\ell^2}}\left.\frac{\partial d}{\partial p}\right|_c \tag{4.104}$$

one obtains

$$c^* = \frac{\sigma_\mathrm{c}^2\,d^3(p_\mathrm{c})\,(1-p_\mathrm{c})}{2\,\ell^2\,\left.\dfrac{\partial d}{\partial p}\right|_\mathrm{c}\left[\sigma_\mathrm{c}\,\nabla u_\mathrm{c}\,\left.\dfrac{\partial E}{\partial \nabla u}\right|_\mathrm{c} - \Psi_*(E_\mathrm{c})\right]}\,. \tag{4.105}$$

When applying a one-dimensional linear material model of the form $\Psi_*(\nabla u) = 1/2\,c\,\nabla u^2$ ($\sigma_\mathrm{c} = c\,\nabla u_\mathrm{c}$) c^* takes the form

$$\begin{aligned} c^* &= \frac{\sigma_\mathrm{c}^2\,d^3(p_\mathrm{c})\,(1-p_\mathrm{c})}{2\,\ell^2\,\left.\dfrac{\partial d}{\partial p}\right|_\mathrm{c}\left[\sigma_\mathrm{c}\,\nabla u_\mathrm{c} - \dfrac{1}{2}\,c\,\nabla u^2\right]} \\ &= c\,\frac{d^3(p_\mathrm{c})\,(1-p_\mathrm{c})}{\ell^2\,\left.\dfrac{\partial d}{\partial p}\right|_\mathrm{c}}\,. \end{aligned} \tag{4.106}$$

Regarding the convergence $\varepsilon \searrow 0$, the threshold value p_c converges to 1 ($p_\mathrm{c} \nearrow 1$). As a consequence the convergence $d^3(p_\mathrm{c})\,(1-p_\mathrm{c})/(\partial d/\partial p|_\mathrm{c}) \to \ell^2$ as $\varepsilon \searrow 1$ can be proven, resulting in

$$c^* \xrightarrow{\varepsilon\searrow 0} c \tag{4.107}$$

Interestingly and in line with the model elaborated in Subsection 4.3.1, c^* thus converges to the elastic modulus within a geometrically linearized one-dimensional setting. For

damage function $d(p) := p/(1-p)$ and a bulk energy density depending on Green-Lagrange strains E, one obtains

$$\begin{aligned} c^* &= \frac{1}{2}\,\frac{p_{\mathrm{c}}^3\,\sigma_{\mathrm{c}}^2}{\sigma_{\mathrm{c}}\,\nabla u_{\mathrm{c}}\,\left.\dfrac{\partial E}{\partial \nabla u}\right|_{\mathrm{c}} - \Psi_*(E_{\mathrm{c}})} \\ &= \frac{1}{2}\,\frac{p_{\mathrm{c}}^3\,\sigma_{\mathrm{c}}^2}{\sigma_{\mathrm{c}}\,\sqrt{1+2\,E_{\mathrm{c}}}\,\left[\sqrt{1+2\,E_{\mathrm{c}}}-1\right] - \Psi_*(E_{\mathrm{c}})}\,. \end{aligned} \tag{4.108}$$

Considering now the limiting case $\varepsilon \searrow 0$ ($p_{\mathrm{c}} \nearrow 1$) finally leads to simplification

$$c^* = \frac{1}{2}\,\frac{\sigma_{\mathrm{c}}^2}{\sigma_{\mathrm{c}}\,\sqrt{1+2\,E_{\mathrm{c}}}\,\left[\sqrt{1+2\,E_{\mathrm{c}}}-1\right] - \Psi_*(E_{\mathrm{c}})}\,. \tag{4.109}$$

"

4.4.3 Incorporation of the microcrack-closure-reopening effect MCR

The following section is taken from [81, Sec. 3.2.3]:

"In many physical systems, material interfaces can only evolve under tensile stresses. A representative example is given by the propagation of (micro-) cracks. Furthermore, if previously opened cracks are subjected to compressive stresses, the interfaces often recover their original (undamaged) stiffness. This effect is also known as the microcrack-closure-reopening (MCR) effect, cf. [39]. The incorporation of this effects into the phase field model elaborated before is the focus of this subsection.

By starting from the phase field approximation of the bulk's response

$$\Psi^{\mathrm{eff}}(\nabla \boldsymbol{u}, p) = \tilde{d}^{-2}_{\varepsilon,c,\gamma,\sigma_{\mathrm{c}}}(p)\,\Psi_*(\boldsymbol{E}^{\mathrm{eff}}) \tag{4.110}$$

one observes that driving force $\partial_p \Psi^{\mathrm{eff}}$ of the original model cannot account for the MCR effect. To be more precise and due to the structure of Ψ^{eff}, both tensile as well as compressive stresses contribute to this driving force. For this reason, energy Ψ^{eff} is often decomposed into a negative as well as a positive part (in the context of brittle fracture this has been used for example in [39, 56], see also [29] for a mathematical treatment based on similar ideas), i.e.,

$$\Psi^{\mathrm{eff}} = \Psi^{\mathrm{eff}}_- + \Psi^{\mathrm{eff}}_+\,. \tag{4.111}$$

While Ψ^{eff}_- is related to compressive states and hence, does not contribute to the driving force governing crack propagation, Ψ^{eff}_+ precisely accounts for crack initiation and growth.

Since cracking is intrinsically anisotropic in nature, a natural decomposition into tension and compression parts is provided by the spectral decomposition of the strains, e.g.,

$$\boldsymbol{E} = \boldsymbol{E}_- + \boldsymbol{E}_+ \quad \text{with} \quad \begin{aligned} \boldsymbol{E} &= \sum_{i=1}^{3} E^{(i)} \qquad \boldsymbol{N}^{(i)} \otimes \boldsymbol{N}^{(i)} \\ \boldsymbol{E}_+ &= \sum_{i=1}^{3} \max[E^{(i)}, 0] \boldsymbol{N}^{(i)} \otimes \boldsymbol{N}^{(i)} \end{aligned} \tag{4.112}$$

where $E^{(i)}$ are the eigenvalues and $\boldsymbol{N}^{(i)}$ the eigenvectors of $\boldsymbol{E}$. However, such a sound decomposition is – unfortunately – difficult to be implemented for general non-linear hyperelastic models due to two reasons. First, inserting Decomposition (4.112) into a general hyperelastic energy also results in coupling terms of type $\Psi^{\text{coupl}} = \Psi^{\text{coupl}}(\boldsymbol{E}_-, \boldsymbol{E}_+)$. Except for simple (analytical) functions (also for Hooke's model), the adjustment of scaling factor $\tilde{d}^{-2}_{\varepsilon,c,\gamma,\sigma_c}(p)$ is very challenging for these coupling terms. Second and even more important, while the scaling of $\nabla \boldsymbol{u}$ is clear (see effective gradient (4.96)), the scaling of $\boldsymbol{E}_-$ and $\boldsymbol{E}_+$ is not. This is mainly due to the nonlinear dependence of $\nabla \boldsymbol{u}$ on finite strain measurements.

A simplified isotropic measurement suitable for identifying compressive and tensile states is the transformation of (infinitesimal) volume elements, i.e., the trace of the engineering strains (geometrically linearized setting) or the determinant of the deformation gradient (geometrically exact setting), cf. [5, 9]. Suppose the underlying (standard) hyperelastic model is based on a decomposition into a volumetric part $\Psi^{\text{vol}} = \Psi^{\text{vol}}(J)$ (with $J := \det \boldsymbol{F}$, $\boldsymbol{F} := \boldsymbol{I} + \nabla \boldsymbol{u}$) and a deviatoric part Ψ^{dev}. Then energies related to tensile and compressive states can be defined as

$$\Psi_+(\boldsymbol{E}) := \begin{cases} \Psi^{\text{vol}}(\boldsymbol{E}) + \Psi^{\text{dev}}(\boldsymbol{E}) & \text{if } J \geq 1 \\ \Psi^{\text{dev}}(\boldsymbol{E}) & \text{if } J < 1 \end{cases}, \tag{4.113}$$

$$\Psi_-(\boldsymbol{E}) := \Psi_*(\boldsymbol{E}) - \Psi_+(\boldsymbol{E}) = \begin{cases} 0 & \text{if } J \geq 1 \\ \Psi^{\text{vol}}(\boldsymbol{E}) & \text{if } J < 1 \end{cases}. \tag{4.114}$$

Since only the tensile part is related to crack initiation and propagation, Phase field approximation (4.99) is only applied to Ψ_+. By doing so, one obtains the energy of the final model as

$$\Psi^{\text{eff}}(\nabla \boldsymbol{u}, p) = \tilde{d}^{-2}_{\varepsilon,c^*,\gamma,\sigma_c}(p)\, \Psi_+(\boldsymbol{E}^{\text{eff}}) + \Psi_-(\boldsymbol{E})\,. \tag{4.115}$$

„

4.5 Reduction to a geometrically linearized theory

In many cases it is sufficient to consider a geometrically linearized theory. Therefore, the linearization of the phase field model is presented here. As a bulk energy, a linear isotropic elastic Helmholtz energy density of the form

$$\Psi_* = \frac{1}{2}\,\lambda\,\mathrm{trace}(\nabla \boldsymbol{u}^{\mathrm{sym}})^2 + \mu\,\nabla \boldsymbol{u}^{\mathrm{sym}} \colon \nabla \boldsymbol{u}^{\mathrm{sym}} \tag{4.116}$$

is employed. When applying procedure (4.100) it becomes clear that the effective bulk energy takes the form

$$\Psi^{\mathrm{eff}}(\nabla \boldsymbol{u}^{\mathrm{sym}}, p) := \tilde{d}^2_{\varepsilon,c^*,\gamma,\sigma_{\mathrm{c}}}(p)\,\Psi(\nabla \boldsymbol{u}^{\mathrm{sym}})\,. \tag{4.117}$$

Due to the linear structure of $\nabla \boldsymbol{u}^{\mathrm{sym}} := \frac{1}{2}\left[\nabla \boldsymbol{u} + \nabla \boldsymbol{u}^{\mathrm{t}}\right]$ and the quadratic structure of $\Psi(\nabla \boldsymbol{u}^{\mathrm{sym}})$ the degradation function can be fully decoupled from the displacement gradient. This leads to a higher flexibility for possible extensions to the model.

4.5.1 Interface energy density

The procedure to adjust the interface energy density requires only marginal modifications. In particular, the procedure presented in Section 4.4.2 can still be applied. The one-dimensional reduction of the model reads $\Psi = \frac{1}{2}E\nabla u^2$ resulting in

$$c^* \xrightarrow{\varepsilon \searrow 0} E = \frac{\mu\,(3\,\lambda + 2\,\mu)}{\lambda + \mu} \tag{4.118}$$

for the converged case ($\varepsilon \searrow 0$), where E denotes the Young's modulus. Therefore, the model reduces to the simple model presented in Section 4.4.2 with $c = E$ for the one-dimensional case.

4.5.2 Bulk energy density — MCR effect

In order to model the MCR effect, the decomposition

$$\Psi^{\mathrm{eff}}(\nabla \boldsymbol{u}^{\mathrm{sym}}, p) := \tilde{d}^2_{\varepsilon,c,\gamma,\sigma_{\mathrm{c}}}(p)\,\Psi_+(\nabla \boldsymbol{u}^{\mathrm{sym}}) + \Psi_-(\nabla \boldsymbol{u}^{\mathrm{sym}})\,. \tag{4.119}$$

of the Helmholtz energy is considered. The quadratic prefactor d is in line with Section 4.1.

In the following the spectral decomposition introduced by [101] is employed leading to effective bulk energy density

$$\Psi^{\text{eff}}(\nabla \boldsymbol{u}^{\text{sym}}, p) := \tilde{d}^2_{\varepsilon,c,\gamma,\sigma_c}(p) \left[\frac{1}{2}\lambda \left\langle \text{trace}(\nabla \boldsymbol{u}^{\text{sym}}) \right\rangle_+^2 + \mu \nabla \boldsymbol{u}_+^{\text{sym}} : \nabla \boldsymbol{u}_+^{\text{sym}} \right] + \frac{1}{2}\lambda \left\langle \text{trace}(\nabla \boldsymbol{u}^{\text{sym}}) \right\rangle_-^2 + \mu \nabla \boldsymbol{u}_-^{\text{sym}} : \nabla \boldsymbol{u}_-^{\text{sym}} . \tag{4.120}$$

Strains $\nabla \boldsymbol{u}_+^{\text{sym}}$ and $\nabla \boldsymbol{u}_-^{\text{sym}}$ are defined in (4.25) and (4.25).

4.6 Implementational aspects

In the following details on the numerical implementations of the novel phase field approximation to cohesive fracture are presented.

4.6.1 Approximated/convexified damage function

The following section is taken from [79, App. B∗]:

“

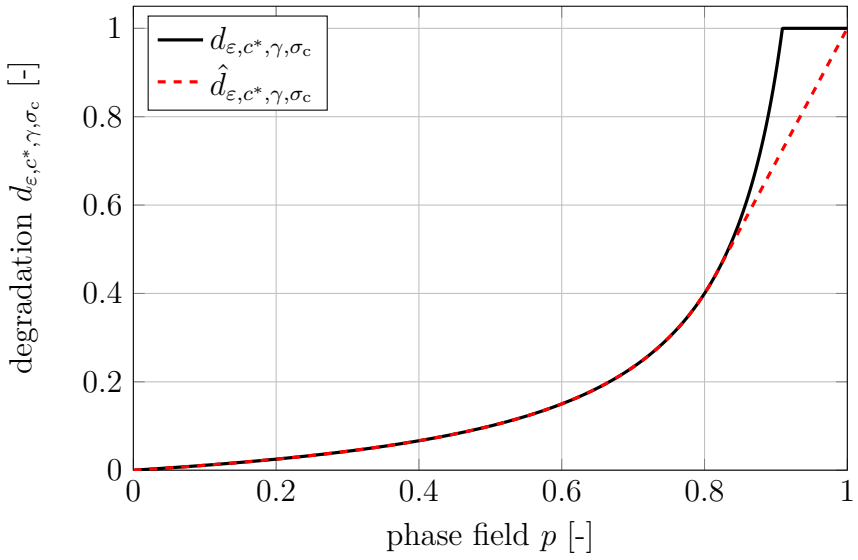

Figure 4.5: Damage functional $d_{\varepsilon,c^*,\gamma,\sigma_c}$ and its approximation/convexification $\hat{d}_{\varepsilon,c^*,\gamma,\sigma_c}$ with $\boldsymbol{a} = [0.5581, 1.3923, -1.1162, 0.1616, 0.0040, 0.0002, -0.0000]^t$ for the polynomial ansatz space. This set of model parameters was also applied for the L-shaped plate in Subsection 4.7.5. The chosen model parameters are $c^* = 2\text{MPa}$, $\gamma = 1\text{N/mm}$, $\sigma_c = 1\text{MPa}$ and $\varepsilon = 0.01\text{mm}$.

The truncation of degradation function (4.61) causes numerical difficulties. Therefore, an approximation/convexification was introduced in [55] for a degradation function of

the type $d(p) = p/(1-p)$. Following the same idea as advocated in [55], function $d_{\varepsilon,c^*,\gamma,\sigma_c}(p)$ is replaced by its linearization in the truncation region, i.e., $d_{\varepsilon,c^*,\gamma,\sigma_c}(p)$ is replaced by

$$\hat{d}_{\varepsilon,c^*,\gamma,\sigma_c}(p) := \begin{cases} d_{\varepsilon,c^*,\gamma,\sigma_c}(p), & p \in [0, p_{\text{th}}[\,, \\ \left.\dfrac{\partial d_{\varepsilon,c^*,\gamma,\sigma_c}(\tilde{p})}{\partial \tilde{p}}\right|_{\tilde{p}=p_{\text{th}}} (p - p_{\text{th}}) + d_{\varepsilon,c^*,\gamma,\sigma_c}(p_{\text{th}}), & p = [p_{\text{th}}, 1]\,. \end{cases} \tag{4.121}$$

Threshold $p = p_{\text{th}}$ is computed from condition $\hat{d}_{\varepsilon,c^*,\gamma,\sigma_c}(1) = 1$, e.g., by means of a Newton scheme. Figure 4.5 shows the approximation/convexification for $\boldsymbol{a} = [0.5581, 1.3923, -1.1162, 0.1616, 0.0040, 0.0002, -0.0000]^{\text{t}}$ (polynomials). This fit corresponds to an exponential traction-separation-law.

"

Remark 3 *An explicit convexified damage function for $d(p) = p/(1-p)$ is presented in Appendix 6.4. It also provides an initial guess for determining p_{th}.*

4.6.2 Influence of the approximated/convexified damage function on the Γ-convergence

It bears emphasis that functions $\hat{d}_{\varepsilon,c^*,\gamma,\sigma_c}$ and $\tilde{d}_{\varepsilon,c^*,\gamma,\sigma_c}$ only differ in the interval $p_{\text{th}} < p < 1$, and that the size of this interval tends to zero as $\varepsilon \searrow 0$. However, the difference does not tend uniformly to zero, hence a more detailed analysis of the difference requires entering the mathematical details of the Γ-convergence proof. The interface energy Φ^0 is identical in the two cases. As a consequence, the identification of the material's strength and the fracture energy in (4.67) and (4.68) remains unchanged. There is, however, a change in the functional form of the elastic energy in the limiting functional, so that the bulk energy is replaced by

$$\hat{\psi}(H) := \begin{cases} \dfrac{H^2}{1 + H^2/4}, & \text{if } H \le H_*\,, \\ H - H_* + H_*^{3/2}/\sqrt{2}, & \text{if } H > H_*\,, \end{cases} \tag{4.122}$$

where H_* is the first positive root of $H^4 + 8H^2 - 32H + 16 = 0$, $H_* \sim 0.591195$. It behaves like the function in (4.47), has the same quadratic expansion at small strains H and shows the same linear behavior at large strains H; the maximum relative difference is approximately 6%. Details are discussed in [81].

The approximation of the degradation function is only applied in multidimensional calculations. For one-dimensional boundary problems the non-truncated degradation function is used when solving for p and the standard, truncated version is applied when solving for u in an alternating minimization scheme. This is in line with [55].

4.6.3 Second law of thermodynamics

The following section is taken from [81, Sec. 4.2]:

"In order to ensure that cracks can only initiate and propagate but never be healed (in a purely mechanical setting), driving force $\left.\dfrac{\partial \Psi}{\partial p}\right|_n$ is replaced by its monotonic counterpart (see [104])

$$\left.\frac{\partial \Psi^{\mathrm{eff}\,*}}{\partial p}\right|_n = \mathcal{H}_n := \begin{cases} \max\left\{\dfrac{\partial \Psi}{\partial p}, \mathcal{H}_{n-1}\right\} & \forall\, n \geq 1 \\ 0 & \text{if } n = 0 \end{cases} \tag{4.123}$$

where $\mathcal{H}_0 = 0$ is chosen as initial conditions. We remark that after this change the model cannot any more be seen as minimization of a functional. In particular, this exits the framework of Γ-convergence. However, numerical experiments indicate that this modification often has only a minor effect on the computed mechanical response."

4.6.4 Implementation by means of the finite element method

The following section is taken from [81, Sec. 4.3]:

"Within each time step, displacement field $\boldsymbol{u}$ as well as phase field p are computed from variational problem

$$(\boldsymbol{u}, p) = \operatorname*{arg\,min}_{(\boldsymbol{u},p)} \left\{ \mathcal{E}^{*,\mathrm{int},\Omega}_{\varepsilon,c^*,\gamma,\sigma_{\mathrm{c}}}[\boldsymbol{u}, p] + \mathcal{E}^{\mathrm{reg},\Omega}_{\varepsilon}[\boldsymbol{u}] - \int_\Omega \rho_0 \boldsymbol{B} \cdot \boldsymbol{u} \mathrm{d}V - \int_{\partial\Omega} \boldsymbol{T} \cdot \boldsymbol{u} \mathrm{d}A \right\}, \tag{4.124}$$

with the final internal energy

$$\mathcal{E}^{*,\mathrm{int},\Omega}_{\varepsilon,c^*,\gamma,\sigma_{\mathrm{c}}}[\boldsymbol{u}, p] := \int_\Omega \hat{d}_{\varepsilon,c^*,\gamma,\sigma_{\mathrm{c}}}(p)^{-2}\, \Psi_+(\boldsymbol{E}^{\mathrm{eff}}) + \Psi_-(\boldsymbol{E}) + \gamma\, f_\varepsilon(p, \nabla p)\, \mathrm{d}V\,. \tag{4.125}$$

Again, $\rho_0 \boldsymbol{B}$ are body forces and $\boldsymbol{T}$ are prescribed tractions. As in (4.42), we included a regularization term with $\eta_\varepsilon \ll \varepsilon$. In practice, the numerical procedure is stable even with $\eta_\varepsilon = 0$, for simplicity we choose this value.

Energy (4.125) is still convex in p, but it cannot be convex in $\boldsymbol{u}$ due to finite deformation. As a matter of fact, bulk energy (4.152) employed within the simulations is not even polyconvex. However, since the elastic deformations are relatively small for the considered example, one expects that the energy is well approximated by linearized elasticity, which, in turn, is characterized by a separately convex energy. For this reason, energy (4.125) is also expected to be almost separately convex for small deformations, and locally polyconvex, so that the variational problem (4.124), as the one in (4.42), has a minimizer. Consequently, alternate minimization can be implemented by means

of a staggered minimization scheme (c.f. [23, 55]). To be more precise and following the algorithm summarized in Algo. 2, the displacement field is computed first, while p is kept fixed. Subsequently, phase field p is optimized and $\boldsymbol{u}$ is fixed. In this step, Eq. (4.123) is adopted if needed. This staggered scheme is performed until convergence is obtained. For multi-dimensional boundary value problems the degradation function in Equation (4.125) is replaced by its $\mathcal{C}^1$ approximation (see Subsection 4.6.1) whereas for one-dimensional simulations, the non-truncated degradation function is used for solving for p in the staggered scheme (c.f. [55]).

1 Given: $(\boldsymbol{u}_{i-1}, p_{i-1})$
2 Initial guess: $(\boldsymbol{u}_i^0, p_i^0) = (\boldsymbol{u}_{i-1}, p_{i-1})$
3 $k = 0$
4 **while** not converged **do**
5 $\quad k \leftarrow k + 1$
6 $\quad$ Solve (4.124) for $\boldsymbol{u}_i^k$ with p_i^{k-1} fixed
7 $\quad$ Solve (4.124) for p_i^k with $\boldsymbol{u}_i^k$ fixed (application of (4.123))
8 **end while**
9 Set $(\boldsymbol{u}_i, p_i) = (\boldsymbol{u}_i^k, p_i^k)$

Algorithm 2: Staggered scheme for time step i

Both aforementioned underlying subproblems are discretized in space by using standard finite element methods with linear shape functions. The first as well as the second derivatives of the (discretized energy) are summarized in Section 4.6.4.1. ”

4.6.4.1 First and second derivatives of the energy – discrete setting within the finite element method

The following section is taken from [81, App. A]:

“The derivatives of Energy (4.124) with respect to the nodal displacements and the nodal phase field variable are given here. Since the energy is an extensive variable, the energy can be additively decomposed into elemental contributions. Accordingly, only derivatives for one element contribution are presented here. They can be written as

$$\boldsymbol{r}_{\boldsymbol{u}}^{\mathrm{A}} = \boldsymbol{f}_{\boldsymbol{u},\mathrm{int}}^{\mathrm{A}} - \boldsymbol{f}_{\boldsymbol{u},\mathrm{vol}}^{\mathrm{A}} - \boldsymbol{f}_{\boldsymbol{u},\mathrm{sur}}^{\mathrm{A}} \tag{4.126}$$

$$r_p^{\mathrm{A}} = f_{p,\mathrm{int}}^{\mathrm{A}}\,, \tag{4.127}$$

where $\boldsymbol{r}_{\boldsymbol{u}}^{\mathrm{A}}$ is the derivative with respect to $\boldsymbol{u}$, while r_p^{A} is the derivative with respect to p. Index $\bullet^{\mathrm{A}}$ signals that the derivatives are related to element node A. The individual terms in Eqs. (4.126) and (4.127) are

$$\boldsymbol{f}_{\boldsymbol{u},\mathrm{int}}^{\mathrm{A}} = \int_{\Omega^e} \frac{\partial \Psi^{\mathrm{eff}}}{\partial \boldsymbol{F}} \cdot \nabla N^{\mathrm{A}} \,\mathrm{d}V \tag{4.128}$$

$$\boldsymbol{f}_{\boldsymbol{u},\mathrm{vol}}^{\mathrm{A}} = \int_{\Omega^e} N^{\mathrm{A}} \,\rho_0 \,\boldsymbol{B} \,\mathrm{d}V \tag{4.129}$$

$$\boldsymbol{f}_{\boldsymbol{u},\mathrm{sur}}^{\mathrm{A}} = \int_{\Omega^e} N^{\mathrm{A}} \,\boldsymbol{T} \,\mathrm{d}V \tag{4.130}$$

$$f_{p,\mathrm{int}}^{\mathrm{A}} = \int_{\Omega^e} \left(\mathcal{H} + \frac{\partial(\gamma \, f_\varepsilon)}{\partial p} \right) N^{\mathrm{A}} + \frac{\partial(\gamma \, f_\varepsilon)}{\partial \nabla p} \cdot \nabla N^{\mathrm{A}} \,\mathrm{d}V \,, \tag{4.131}$$

with N^{A} being the shape function of node A (the same shape functions are used for discretizing $\boldsymbol{u}$ and p). The second derivatives of the energy finally yield

$$\boldsymbol{K}_{\boldsymbol{u}\boldsymbol{u}}^{\mathrm{AB}} = \int_{\Omega^e} \nabla N^B \bullet \frac{\partial^2 \Psi^{\mathrm{eff}}}{\partial \boldsymbol{F}^2} \cdot \nabla N^B \,\mathrm{d}V \tag{4.132}$$

$$K_{pp}^{\mathrm{AB}} = \int_{\Omega^e} N^{\mathrm{A}} \left(\frac{\partial \mathcal{H}}{\partial p} + \frac{\partial^2(\gamma \, f_\varepsilon)}{\partial p^2} \right) N^B \tag{4.133}$$

$$+ \quad \nabla N^{\mathrm{A}} \cdot \frac{\partial^2(\gamma \, f_\varepsilon)}{\partial \nabla p^2} \cdot \nabla N^B \,\mathrm{d}V \,. \tag{4.134}$$

”

4.7 Numerical examples

In the following section, the predictive capabilities of the novel phase field approximation of cohesive zone models are highlighted. First, a simple one-dimensional finite element example using default degradation function $d = p/(1-p)$ is presented. Secondly, the calibration of four benchmark traction-separation-laws is presented. Subsequently, the calibrated traction-separation laws are applied to one-dimensional finite element simulations with a simple quadratic bulk energy. For these models Γ-convergence is proven mathematically in Section 4.3.1 and underlined here by numerical experiments. Similar examples are also presented for a non-linear material. Although no Γ-convergence is proven in this case, the simulations are in line with the expectations.

After the one-dimensional examples, two two-dimensional examples are provided. Firstly, a CT-specimen (notched plate under tension) is investigated. The importance of the traction-separation-law to the crack evolution as well as the global response is emphasized. In addition to the notched plate, an L-shaped boundary problem including a curved crack is analyzed and compared to sharp interface solutions for a non-linear bulk material.

4.7.1 One-dimensional example with a quadratic material model

The following section is taken from [81, Sec. 5.1]:

"In this subsection, cracking in a one-dimensional bar of length $l = 1$ mm and cross-sectional area $A = 1$ mm^2 is numerically analyzed. The bar is clamped on its left hand side, while a displacement of magnitude $\bar{u} = 0.1$mm is applied to the right hand side (within 100 load steps/increments). In order to force the crack to initiate in the center of the bar, the material strength at the center is reduced by one percent at the two elements at the center of the finite element discretization. The bar's bulk material response is captured by linearized elasticity theory, i.e., $\Psi = \frac{1}{2}\, c\, \nabla u^2$. Irreversibility is enforced here in line with [22] and Eq. (4.123) is not applied here. The elastic stiffness, the interface's strength as well as the fracture energy are summarized in Tab. 4.1.

c	σ_c	γ
100 [MPa]	10 [MPa]	2 [N/mm]

Table 4.1: Cracking in a one-dimensional bar: material parameters

For this simplified model, Γ-convergence was proven in this paper. The convergence behavior shall nevertheless be studied here by means of a numerical experiment in which the length parameter controlling the width of the diffuse interface is varied. Simulations based on $\varepsilon = 0.01$ mm, $\varepsilon = 0.005$ mm, $\varepsilon = 0.002$ mm and $\varepsilon = 0.001$ mm are performed. In the region of the interface, an element size h with $\varepsilon/h = 5$ was chosen.

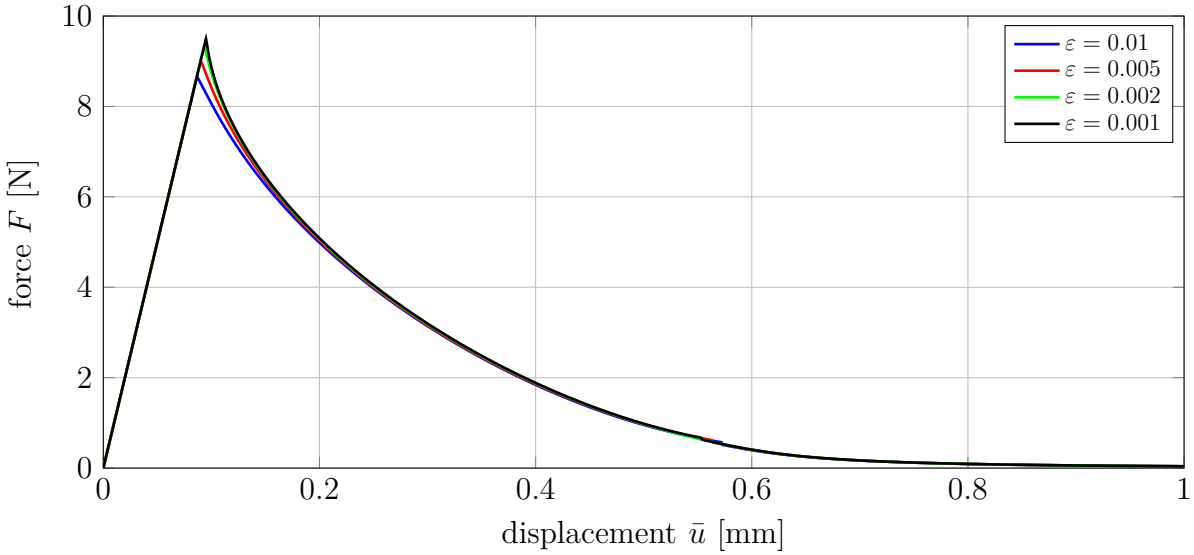

Figure 4.6: Cracking in a one-dimensional bar: Force displacement curves predicted by means of simulations based on different lengths ε

The numerically predicted structural response is given in Fig. 4.6. The diagram shows the prescribed displacement and the resulting reaction force (dual to this displacement). Since the cross-sectional area of the bar is one, the reaction force is equal to the stresses within the bar.

According to Fig. 4.6, a linear elastic response is predicted during the first loading stage. If the prescribed displacement is increased further, the stresses finally reach the material's strength and a crack starts to evolve. This, in turn, leads to softening up to total failure. It can be seen that the predicted strength as well as the fracture energy seem to converge to their prescribed counterparts, if width ε is sufficiently small. The error in strength is 3%, while the error in fracture energy is 4% for the thinnest diffuse interphase."

4.7.2 Identification of the most frequently applied traction-separation-laws

4.7.2.1 Summary of the considered traction-separation-laws

The following section is taken from [79, Sec. 4.1.1∗]:

"In this section, four different, frequently applied traction-separation-laws are considered. They can be either described by their interface energy ($\Phi(\llbracket u \rrbracket)$) or by the resulting traction-separation-law ($t(\llbracket u \rrbracket)$). In what follows both representations will be given.

- **Exponential traction-separation-law**

$$\Phi(\llbracket u \rrbracket) = \gamma \left[1 - \exp\left(- \llbracket u \rrbracket \frac{\sigma_\mathrm{c}}{\gamma} \right) \right] , \tag{4.135}$$

$$t(\llbracket u \rrbracket) = \sigma_\mathrm{c} \exp\left(- \llbracket u \rrbracket \frac{\sigma_\mathrm{c}}{\gamma} \right) . \tag{4.136}$$

- **Linear traction-separation-law**

$$\Phi(\llbracket u \rrbracket) = \begin{cases} \gamma - \dfrac{a}{2} \left[\llbracket u \rrbracket - v \right]^2 , & \text{if } \llbracket u \rrbracket \leq v \, , \\ \gamma, & \text{otherwise} \, , \end{cases} \tag{4.137}$$

$$t(\llbracket u \rrbracket) = \begin{cases} -a \left[\llbracket u \rrbracket - v \right] , & \text{if } \llbracket u \rrbracket \leq v \, , \\ 0, & \text{otherwise} \, , \end{cases} \tag{4.138}$$

with $v := 2\,\gamma/\sigma_\mathrm{c}$ and $a := \sigma_\mathrm{c}/v$.

- **Bilinear traction-separation-law**

$$\Phi(\llbracket u \rrbracket) = \begin{cases} -\dfrac{a_1}{2} \llbracket u \rrbracket^2 + \sigma_\mathrm{c} \llbracket u \rrbracket & \text{if } \llbracket u \rrbracket \leq v_1 \,, \\ \gamma - \dfrac{a_2}{2} \left[\llbracket u \rrbracket - v_2 \right]^2 , & \text{if } \llbracket u \rrbracket \in]v_1, v_2] \,, \\ \gamma, & \text{otherwise} \,, \end{cases} \tag{4.139}$$

$$t(\llbracket u \rrbracket) = \begin{cases} -a_1 \llbracket u \rrbracket + \sigma_\mathrm{c}, & \text{if } \llbracket u \rrbracket \leq v_1 \,, \\ -a_2 \left[\llbracket u \rrbracket - v_2 \right], & \text{if } \llbracket u \rrbracket \in]v_1, v_2] \,, \\ 0, & \text{otherwise} \,. \end{cases} \tag{4.140}$$

with $v_2 := (2\,\gamma - \sigma_\mathrm{c}\, v_1)\,/\sigma_{\mathrm{c},1}$, $a_1 := (\sigma_\mathrm{c} - \sigma_{\mathrm{c},1})/v_1$ and $a_2 := \sigma_{\mathrm{c},1}/(v_2 - v_1)$. Additional parameters v_1 and $\sigma_{\mathrm{c},1}$ define the crack opening and the material strength after the first linear part.

- **Limit traction-separation-law**

$$\Phi(\llbracket u \rrbracket) = \begin{cases} \sigma_\mathrm{c} \llbracket u \rrbracket & \text{if } \llbracket u \rrbracket \leq \dfrac{\gamma}{\sigma_\mathrm{c}} \,, \\ \gamma, & \text{otherwise} \,, \end{cases} \tag{4.141}$$

$$t(\llbracket u \rrbracket) = \begin{cases} \sigma_\mathrm{c}, & \text{if } \llbracket u \rrbracket \leq \dfrac{\gamma}{\sigma_\mathrm{c}} \,, \\ 0, & \text{otherwise} \,. \end{cases} \tag{4.142}$$

We remark that for the limit traction-separation law a simple explicit formula for $\tilde{d}$ can be derived, see [79, App. D∗]."

4.7.2.2 The forward problem: Computation of the traction-separation law (sharp interface problem)

Before solving the inverse problem, the forward problem of solving optimization problem (4.50) is investigated.

As described in Section 4.3.2.1 Problem (4.50) has two natural upper bounds. Firstly, if $\beta \equiv 1$ it follows $|\beta'|^2 = 0$. In addition, following Condition (4.45), $|1 - \beta| \sqrt{d(\beta)^2} \overset{\beta \uparrow 1}{\to} \ell$ holds. Consequently, the integral results in

$$\Phi^0 \leq \ell \, |\llbracket u \rrbracket| \quad \forall \, |\llbracket u \rrbracket| > 0 \tag{4.143}$$

if α monotonously increases as a first upper limit of the minimization. The second upper limit can be reached by only allowing evolution of α ($\alpha' > 0$) if $\beta = 0$ such that $d(\beta)^2 \, |\alpha'| = 0$. If β is chosen as

$$\beta(t) = \min \{3t,\, 1,\, 3\,(1 - t)\} \tag{4.144}$$

the integral produces

$$\Phi^0 \leq 1 \quad \forall\, |[\![u]\!]| > 0 \tag{4.145}$$

as second upper limit. The two limits can be rediscovered in the two main properties of the interface energy density

$$\lim_{|[\![u]\!]| \uparrow \infty} \Phi^0(|[\![u]\!]|) = 1\,, \tag{4.146}$$

$$\lim_{|[\![u]\!]| \downarrow 0} \frac{\Phi^0(|[\![u]\!]|)}{|[\![u]\!]|} = \ell\,. \tag{4.147}$$

as described above.

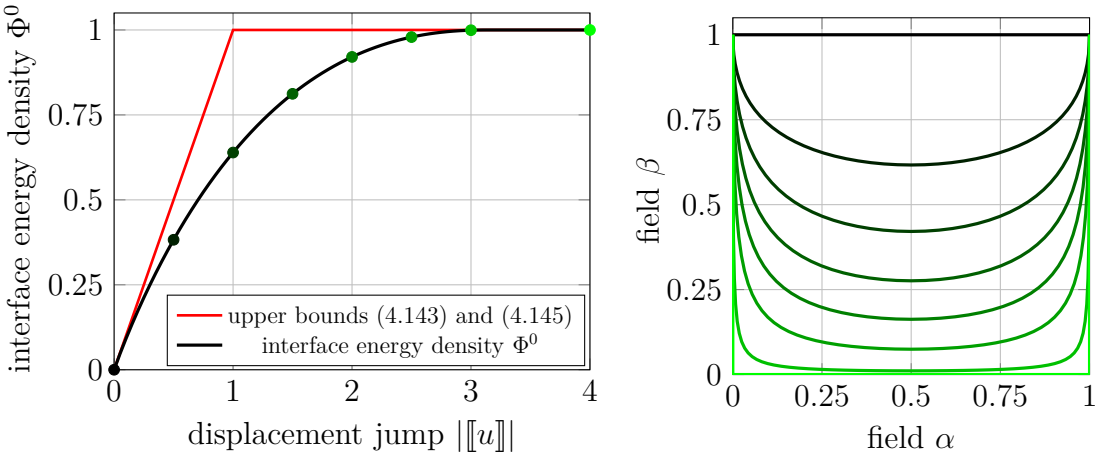

Figure 4.7: Optimization problem (4.50) for $d(p) = p/(1-p)$. The upper bounds described in (4.143) and (4.145) are highlighted in red. The subfigure on the right shows the optimal arguments α and β for displacements jumps highlighted in the left subfigure. The solution is calculated using the methods described in Section 4.3.2.1.

Figure 4.7 (left) presents the solution of Φ^0 for $d(p) = p/(1-p)$. The optimal arguments α and β are depicted in Figure 4.7 (right). Details on the numerical treatment can be found in Section 4.3.2.1. The figure also shows the natural upper bounds as described in (4.143) and (4.145). Clearly, the upper bounds correspond to the initial slope as well as to the convergence limit for $\| [\![u]\!] \|$ characterized by the interface material parameters σ_c and γ. The optimal arguments for displacement jumps close to zero as well as very large displacement jumps does behave as described above.

4.7.2.3 The inverse problem: Computation of the degradation function (phase-field model)

The following section is taken from [79, Sec. 4.1.2∗]:

"Due to scaling (4.65) of the interface energy, it is sufficient to consider the normalized case $\sigma_c = 1$ and $\gamma = 1$. For this choice, numerical experiments have shown that complete softening/failure occurs before a maximum displacement jump of $[\![u]\!]_{\max} = 3$ is reached. Consequently, precisely this maximum jump is chosen in what follows. As far as the bilinear traction-separation-law is concerned, the additional parameters are chosen as $\sigma_{c,1} = 0.25$, and $v_1 = 1$.

Evolution of the error within the algorithm The proposed optimization algorithm according to Subsections 4.3.2.1 and 4.3.2.2 is used in order to identify the degradation function (phase-field model) for the four prescribed traction separation laws (i) exponential, (ii) linear, (iii) bilinear and (iv) limit law, cf. Subsection 4.7.2.1. For that purpose, the two approximations of the space of admissible degradation functions as elaborated in Subsection 4.3.2.2 are considered. Starting from relatively coarse approximations (number of degrees of freedom), the approximation space is enriched up to seven degrees of freedom. The computed model parameters are summarized in 6.5.

The error of the identified degradation functions in terms of the L_2-norm

$$r_{\boldsymbol{a}^{\text{opt}}} = \inf_{d(p)} \left\{ \int_0^\infty \left| \Phi^{0,\exp}(s) - \Phi^{0,d}(s) \right|^2 \mathrm{d}s \right\} \text{ with } s := \| [\![u]\!] \| \tag{4.148}$$

is presented in Fig. 4.8. The left diagram in Fig. 4.8 corresponds to the approximation of the degradation function by means of polynomials and the right diagram to cubic splines. All diagrams show the error (4.148) depending on the approximation space (number of degrees of freedom; $n_{\boldsymbol{a}}$) for the different traction-separation laws. It is observed that the accuracy of the prediction is indeed improved by increasing the approximation space ($n_{\boldsymbol{a}}$). Furthermore, the so-called limit traction-separation-law is approximated best. The resulting error is less than 10^{-12} already for a single degree of freedom, and thus, it cannot be illustrated in the diagram. This might be related to the fact that infinitely many choices of $\tilde{d}$ exist which reproduce exactly the limit traction-separation-law, see [79, Sec. 4.1.2∗]. The least good approximation is obtained for the bilinear traction-separation law. By analyzing the resulting traction-separation-laws it will be shown that all approximations capture the underlying sharp interface model very well."

4.7.2.4 Visualization of the error for $n_{\boldsymbol{a}} = 2$

Figures 4.9 and 4.10 present the admissible parameter spaces for a parameter vector of two dimensions ($n_{\boldsymbol{a}} = 2$). While Figure 4.9 shows the error for each traction-separation law as a colorplot over the admissible domain of the polynomial approach, Figure 4.10

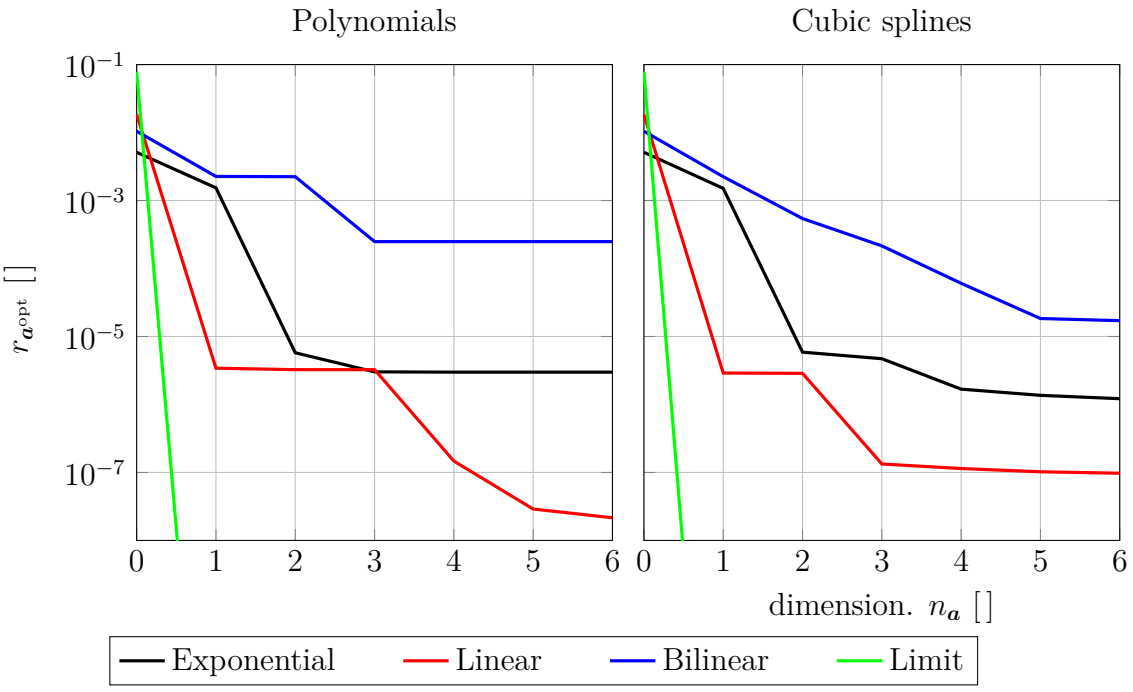

Figure 4.8: Error $r_{\boldsymbol{a}^{\mathrm{opt}}}$ according to Eq. (4.148) for the different prescribed traction-separation laws and the different approximation spaces for the degradation function. (left) approximation by means of polynomials and (right) approximation by means of cubic splines. While the y-axis shows the error, the x-axis corresponds to the number of degrees of freedom of the respective approximation.

corresponds to the spline ansatz. The white lines in Figure 4.9 additionally display the one-dimensional admissible parameter space, which is a subset of the two-dimensional space.

For the exponential, linear and bilinear traction-separation laws, the optimal parameters are unique and located at smaller values of a_1. For the admissible parameter space of the polynomial ansatz functions a_1 controls the initial slope of the degradation function as $d'(p=0) = a_1/(1-p)$. For the spline approach, parameter a_1 defines the first function value of function $\tilde{d}$ at the first knot point and therefore mainly influences the initial slope. A plateau of the error function can be seen for higher values of a_1 in the polynomial approach. Similarly, a plateau exits for the spline approach. In these plateaus all parameter vectors lead to the limit traction separation law which defines the upper bound of minimization problem (4.50). This is in line with [79, Appendix D∗], where the non-uniqueness of the problem regarding the limit law is mathematically proven. This missing injectivity results in non-unique parameter vectors for the limit traction-separation law. While the parameter vector has no influence on the sharp interface solution (Eq. (4.50)) it does on the numerical results and may cause additional numerical costs in the diffuse finite element simulation. In order to reduce this impact,

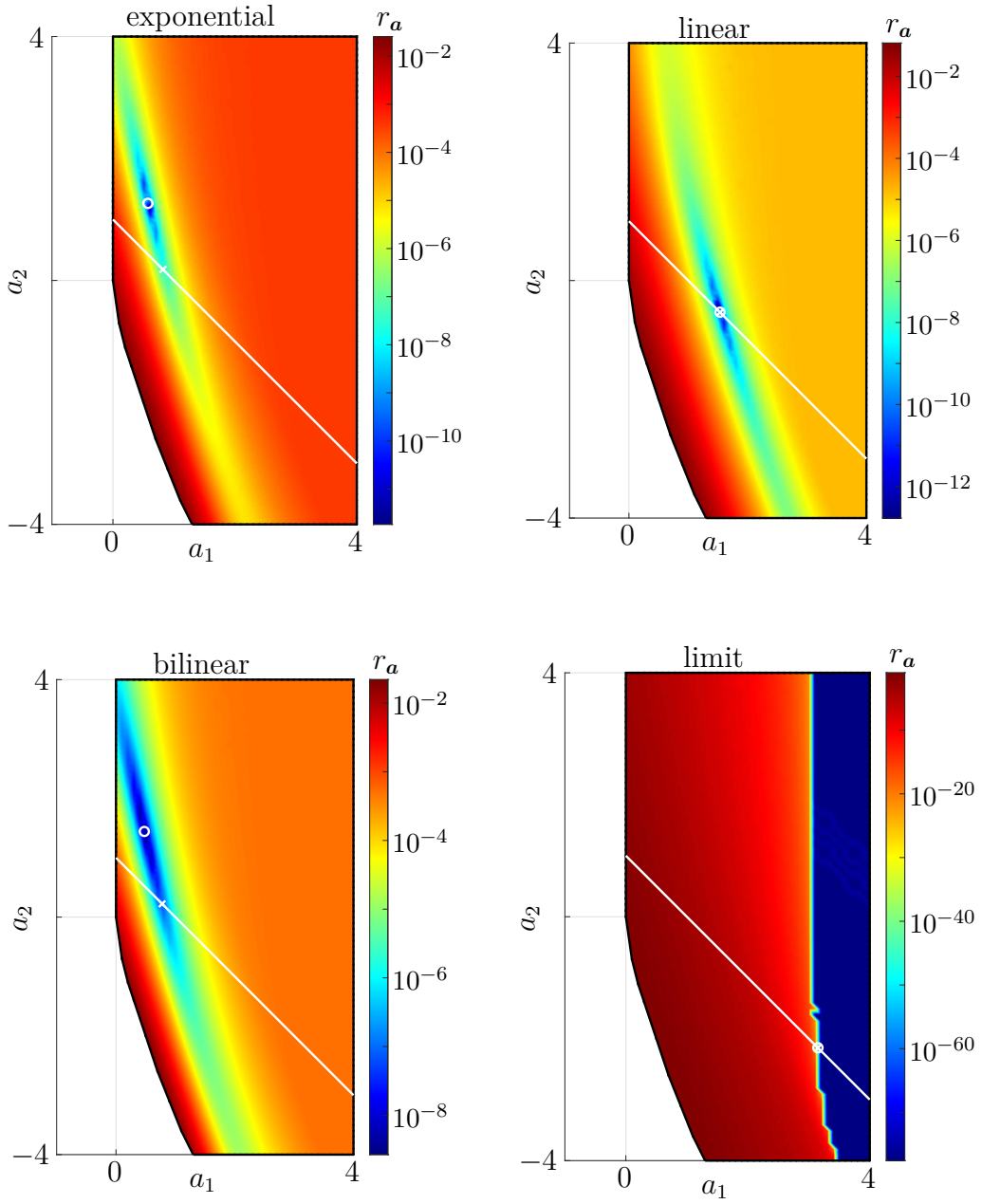

Figure 4.9: Error $r_{\boldsymbol{a}}$ over the admissible parameter set $\mathcal{A}$ for all four traction-separation laws using the polynomial approach. The white ∘ represents the optimal parameter vector. The one-dimensional subset is visualized with the optimal parameter denoted by ×.

the smallest parameter a_1 resulting in an error under a given tolerance is chosen for the optimization in one dimension, locating it at the boundary of the plateau. For higher

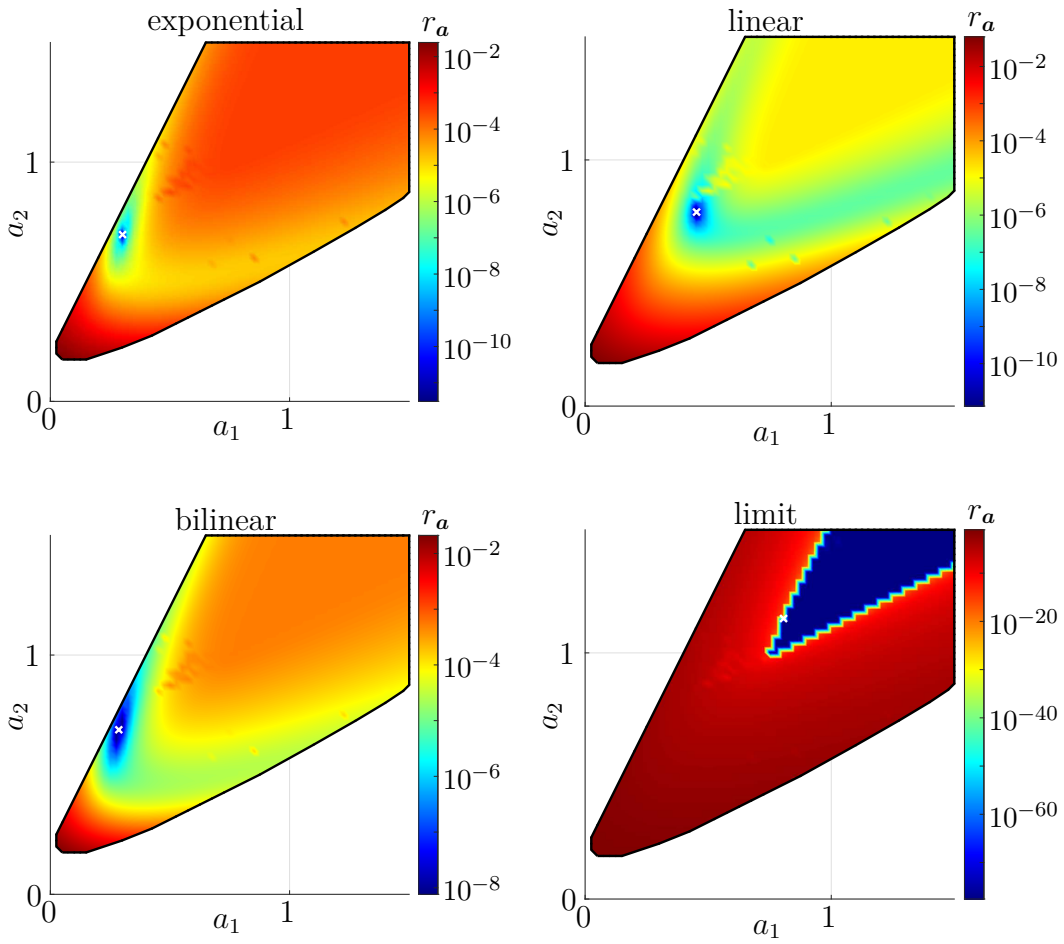

Figure 4.10: Error $r_{\boldsymbol{a}}$ over the admissible parameter set $\mathcal{A}$ for all four traction-separation laws using the spline approach. The white $\times$ represents the computed optimal parameter vector.

dimensions, the initial guess for the parameter vector $\boldsymbol{a}$ is updated individually for each approach as described above.

4.7.3 1D FEM Simulations – Predicted traction-separation laws

The following section is taken from [79, Sec. 4.1.2$*$]:

"In order to analyze the traction-separation laws corresponding to the computed degradation functions (phase field model), 1D finite element simulations are performed. They also allow the investigation of the influence of the length parameter (thickness of the diffuse interface) on the results. The degradation functions used within the computations correspond to the largest/best approximation spaces with $n_{\boldsymbol{a}} = 6$. First, a linear bulk material model will be applied, as resulting from Section 4.3. Here Γ-convergence to the

sharp interface limit it proven mathematically. A nonlinear model is applied in a second step."

4.7.3.1 Linear bulk material model

The following section is taken from [79, Sec. 4.1∗]:

"In order to analyze the traction-separation-laws corresponding to the computed degradation functions (phase-field model), 1D finite element simulations are performed. They also allow to investigate the influence of the length parameter (thickness of the diffuse interface) on the results. The degradation functions used within the computations correspond to the largest/best approximation spaces with $n_{\boldsymbol{a}} = 6$.

As a 1D-benchmark, a truss subjected to tensile loading is considered. Length l and cross-sectional area A of the truss, together with the material parameters, are summarized in Tab. 4.2.

Material parameter			Geometry parameter	
E	σ_{c}	γ	l	A
100 MPa	10 MPa	2 N/mm	1 mm	1 mm^2

Table 4.2: 1D finite element analysis of a truss subjected to tension: Material parameters and geometry.

In order to trigger localization, a small imperfection is placed in the center of the rod (1% reduction of the material's strength).

The structural responses as predicted by the phase field method for different degradation functions and phase field widths are shown in Fig. 4.11. For the sake of comparison, the sharp interface solution (see 6.6) is also presented. According to Fig. 4.11, the exponential traction-separation law is approximated best. This is due to its smoothness and the considered ansatz spaces for the degradation function. The linear law is also well represented. However, the kink at the fully softened state is artificially smoothened – again as expected from the properties of the ansatz spaces. In the same line of thought, the bilinear law leads to one additional smoothing point and thus to small fluctuation. Nevertheless, the peak strength, the overall fracture energy as well as the shape of the traction-separation-law are reasonably captured in all cases. Only for the limit traction-separation-law, a too coarse phase field width leads to an overshoot of the materials strength. However, as evident from Fig. 4.11, this error can be reduced by simply decreasing the length parameter. Finally, it is noted that although the chosen ansatz space indeed influences the resulting interface energy and the implied traction-separation-law, this interaction is not trivial. For instance, using an affine space for $\tilde{d}$ yields the nonlinear degradation function $d(p) = \tilde{d}(p)/(1-p)$ and the respective interface energy is also not affine. Consequently, the properties of $\tilde{d}$ are neither inherited by Φ nor by $\boldsymbol{t}(\boldsymbol{u})$."

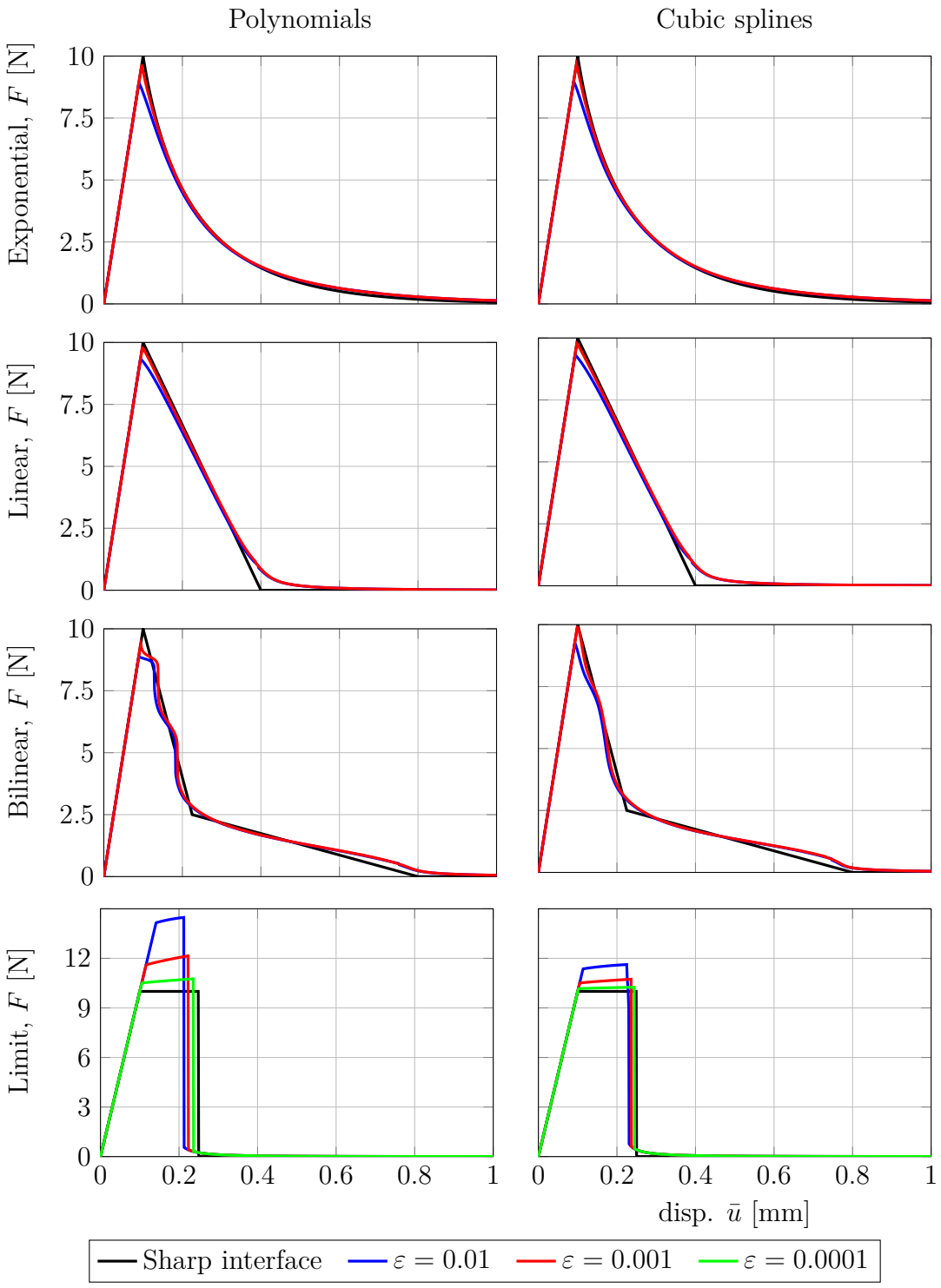

Figure 4.11: 1D finite element analysis of a truss subjected to tension: force-displacement diagrams obtained from the phase-field model for different degradation functions. The underlying sharp interface solution is also shown for the sake of comparison.

4.7.3.2 Non-linear bulk material model

Additionally to the linear material model, one-dimensional finite element simulations are performed with non-linear bulk material model

$$\Psi = \frac{\mu}{2}\left[[\nabla u + 1]^2 - 1 - 2\,\log(\nabla u + 1)\right] + \frac{\lambda}{2}\nabla u^2 \tag{4.149}$$

of Neo-Hookean type with Lamé parameters λ and μ. Together with the length l and the cross-section area A the material parameters are presented in Table 4.3. Artificial parameter c^* is computed via Eq.(4.109).

Material parameter					Geometry parameter	
λ	μ	σ_c	γ	c^*	l	A
20 MPa	150 MPa	400 MPa	1200 N/mm	243.118 MPa	1 mm	1 mm^2

Table 4.3: 1D finite element analysis of a truss subjected to tension: Material parameters and geometry. Artificial parameter c^* is computed via Eq.(4.109).

The crack location is triggered by a small imperfection of 1% of the material's strength in the center of the rod. In the region of the crack a ratio of $\varepsilon/h = 5$ for the element size h is chosen. The load is applied with an increment of $\Delta\bar{u} = 0.01\,\text{mm}$.

The resulting force displacement diagrams are depicted in Figure 4.12. Similar to the linear setting, a satisfying agreement can be observed comparing the finite element solutions to the sharp interface reference solutions. The reference solutions are obtained via the procedure explained in Appendix 6.6. For the exponential, linear and bilinear cases only small deviations can be observed. The largest deviation in these three laws can be seen for the bilinear law at the non-differentiability. Here, the diffuse interface solution smears the kink present in the sharp interface solution. This deviation can be traced back to the limiting regularity of investigated approximation spaces.

Regarding the limit traction-separation law a similar behavior compared to the linear setting can be observed. The approximation of the material's strength is too large for the linear setting when using larger regularization lengths ε. However, a convergence to the chosen material's strength can still be observed for smaller regularization lengths. In contrast to the linear setting, the truncation point for full fracture is not met sufficiently. As is visible in Section 4.7.2.4 (Figures 4.9 and 4.10) the solution of the approximation of the limit traction-separation-law is not unique for both fitting approaches. While the resulting degradation function yields the same converged sharp interface energy, it yields different results in the diffuse interface finite element simulations. Nevertheless, a convergence to the sharp interface solution can be observed.

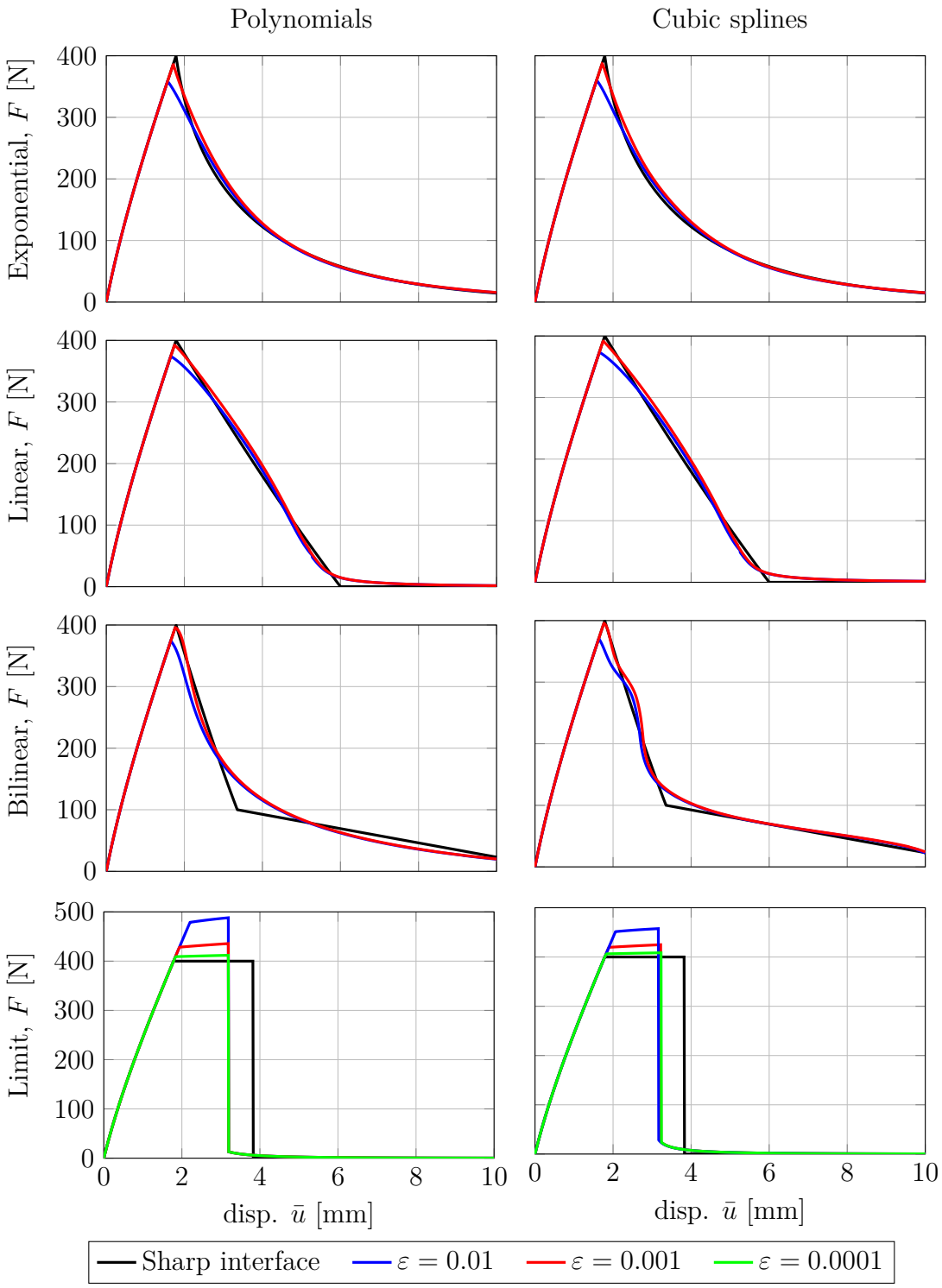

Figure 4.12: "1D finite element analysis of a truss subjected to tension: force-displacement diagrams obtained from the phase-field model for different degradation functions. The underlying sharp interface solution is also shown for the sake of comparison." ([79, Sec. 4.1∗]). A geometrically exact setting as well as material model (4.149) is applied.

4.7.4 CT-specimen — Notched plate under tension

4.7.4.1 Geometrically linearized setting

The following section is taken from [79, Sec. 4.2∗]:

"Next, a two-dimensional CT-specimen is analyzed (notched plate under tension). Plane stress conditions, a geometrically linearized setting and Hooke's model are adopted (Young's modulus E and Poisson's ratio ν). The boundary value problem as well as the model parameters are summarized in Fig. 4.13. Loading is controlled by prescribing the top and the bottom displacement in increments of $\Delta\bar{u} = 0.000005\,\text{mm}$, cf. Fig. 4.13. Since the degradation function is not differentiable at the onset of crack initiation, which might cause numerical problems, an approximation/convexification similar to that in [55] and [81] is applied, cf. Section 4.6.1.

Due to the symmetry of the problem, the geometry of the crack is known beforehand, i.e., starting at the notch, a horizontal crack propagates. In order to analyze the influence of the traction-separation law on the structural response, three computations are performed: (1) based on an exponential traction-separation law, (2) linear law and (3) bilinear law. These computations are either based on a polynomial or a spline approximation of the degradation function resulting in six computations in total. For both approximations, $n_{\boldsymbol{a}} = 6$.

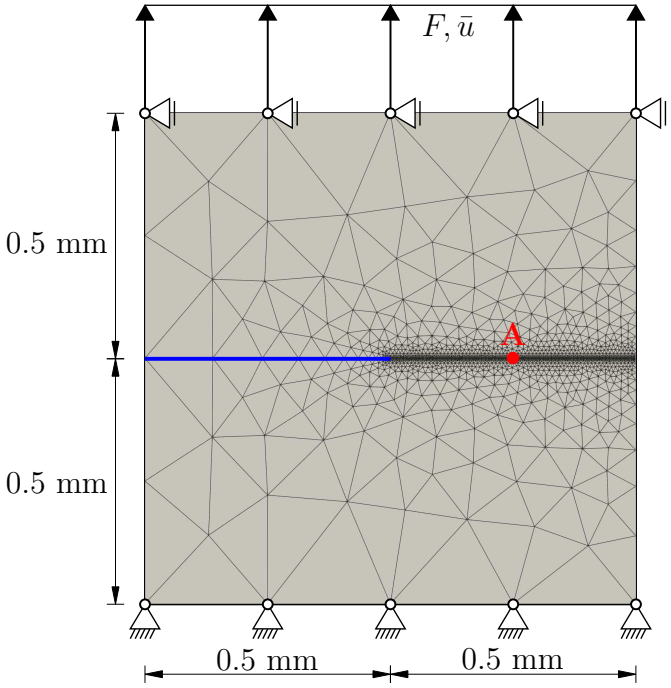

Material parameters	
E	2000.00 MPa
ν	0.30
σ_c	4.00 MPa
γ	0.02 N/mm
c^*	2000.00 MPa
ε	0.01 mm

Figure 4.13: CT-specimen – Notched plate under tension: Geometry, finite element discretization, boundary conditions and model parameters. The plate has a thickness of 1 mm. Plane stress conditions are assumed. The pre-notch is highlighted in blue color.

Fig. 4.14 shows the computed structural responses by means of the load-displacement diagram (F vs. $\bar{u}$).

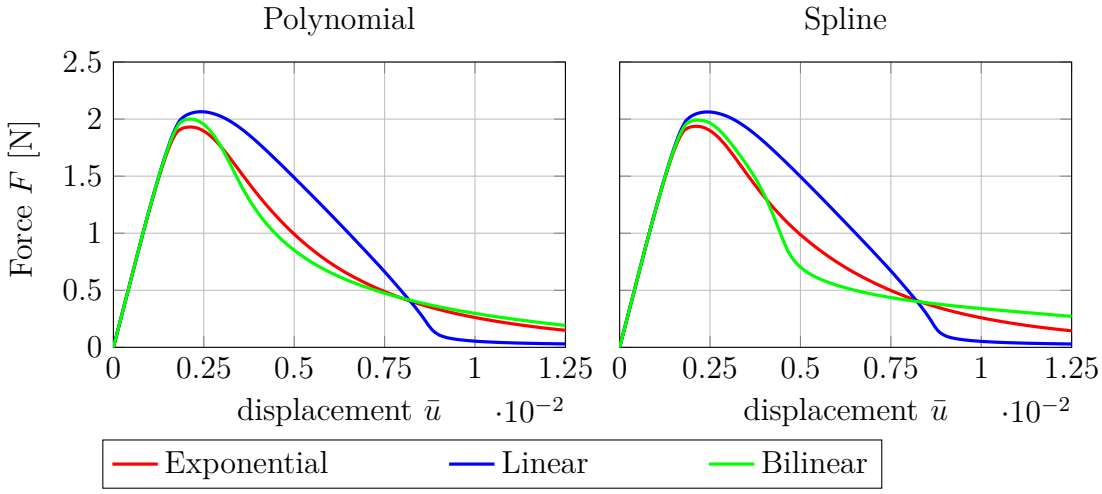

Figure 4.14: CT-specimen – Notched plate under tension: Force-displacement diagrams obtained from the different approximations (polynomial and spline approximation of the degradation function) and three different traction-separation laws (exponential, linear and bilinear).

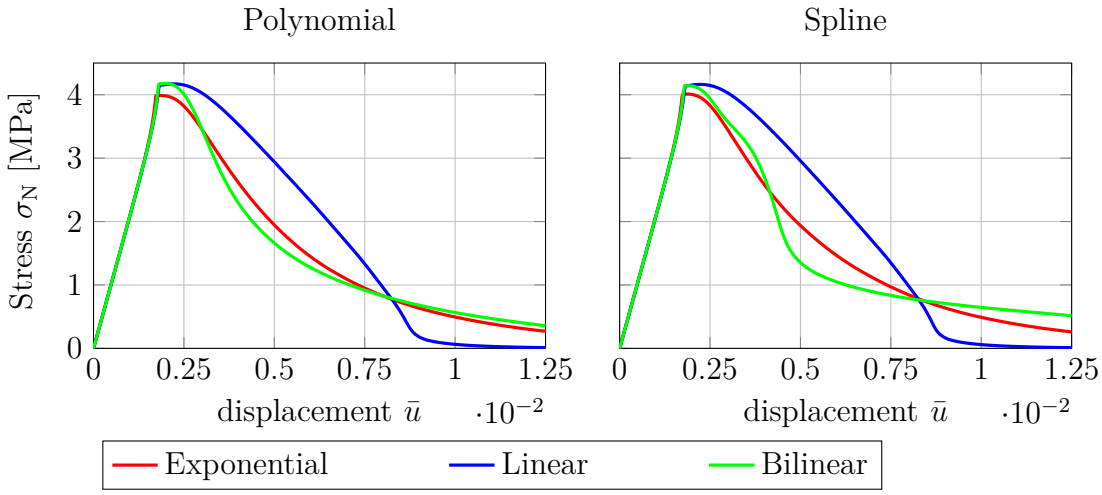

Figure 4.15: CT-specimen – Notched plate under tension: Normal stresses σ_N at point A versus prescribed displacement $\bar{u}$ (point A is defined in Figure 4.13). The results correspond to the different approximations (polynomial and spline approximation of the degradation function) and three different traction-separation laws (exponential, linear and bilinear).

Due to the cross-sectional area of the final crack (0.5 mm$\times$ 1.0 mm=0.5 mm^2) and the strength σ_c=4.00 MPa, a maximum force of roughly 2 N is expected. This is indeed

confirmed in Fig. 4.14. Furthermore, it can be seen that the shape of the traction-separation law indeed influences the structural response – although the total fracture energy and the strength are identical in all simulations.

A similar mechanical response as that in Fig. 4.14, is also observed at point A, see Fig. 4.13. The mechanical response – here in the form of σ_N vs. $\bar{u}$ – again depends on the shape of the underlying traction-separation law, cf. Figure 4.15.

The maximum peak stress is close to 4.0 MPa and thus in line with the material's strength σ_c."

4.7.4.2 Geometrically exact setting

The notched plate under tensile loading is also investigated for a non-linear material behavior under plane stress assumptions. The bulk's response is modeled by means of a neo-Hooke energy

$$\Psi_+ = \begin{cases} \frac{1}{2} G \operatorname{tr}(\bar{\boldsymbol{C}} - \boldsymbol{I})^2 + \frac{1}{2} K (J-1)^2 & \text{if } J \geq 1 \,, \\ \\ \frac{1}{2} G \operatorname{tr}(\bar{\boldsymbol{C}} - \boldsymbol{I})^2 & \text{if } J < 1 \,, \end{cases} \tag{4.150}$$

$$\Psi_- = \begin{cases} 0 & \text{if } J \geq 1 \,, \\ \\ \frac{1}{2} K (J-1)^2 & \text{if } J < 1 \,, \end{cases} \tag{4.151}$$

where the material parameters are given in Figure 4.13. Here, $K = \lambda + \frac{2\mu}{3}$ is the bulk modulus, $G = \mu$ is the shear modulus, $J := \det \boldsymbol{F}$ is the determinant of deformation gradient and $\bar{\boldsymbol{C}} := J^{-\frac{2}{3}} \boldsymbol{F}^{\mathrm{t}} \boldsymbol{F}$ denotes the deviatoric part of the right Cauchy-Green tensor. Equidistant loading steps of $\Delta u = 0.000005$ mm are applied. The global responses are depicted in Figure 4.16 in form of force displacement diagrams for the exponential, linear and bilinear traction-separation laws. For all traction-separation laws $n_{\boldsymbol{a}} = 6$ is chosen for the polynomial as well as the spline ansatz spaces.

The global response in form of the force over displacement depicted in Figure 4.16 shows similar results compared to the linear bulk material. The maximal forces are met for all traction-separation laws but the limit case. The shape is mainly influenced by the corresponding traction-separation law.

A main difference to the geometrically linearized setting can be seen in the local behavior. As Figure 4.17 suggests, the material's strength is slightly exceeded within the numerical simulation. However, this only occurs in a small region at the crack tip. Thus, it has no significant influence on the overall maximal force. With a converging phase field width, the maximal stresses are expected to converge to the material's strength.

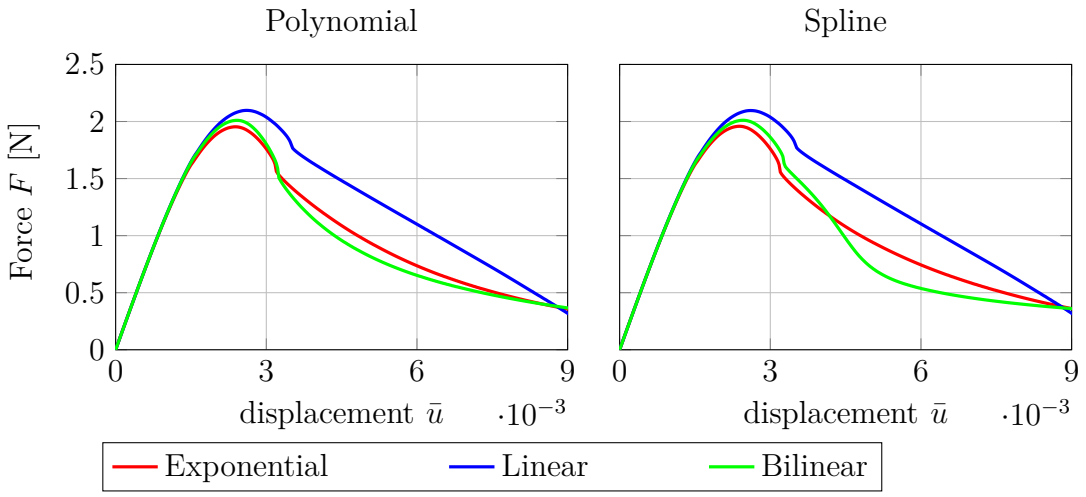

Figure 4.16: "CT-specimen – Notched plate under tension: Force-displacement diagrams obtained from the different approximations (polynomial and spline approximation of the degradation function) and three different traction-separation laws (exponential, linear and bilinear)." ([79, Sec. 4.2∗]). A geometrically exact theory is applied.

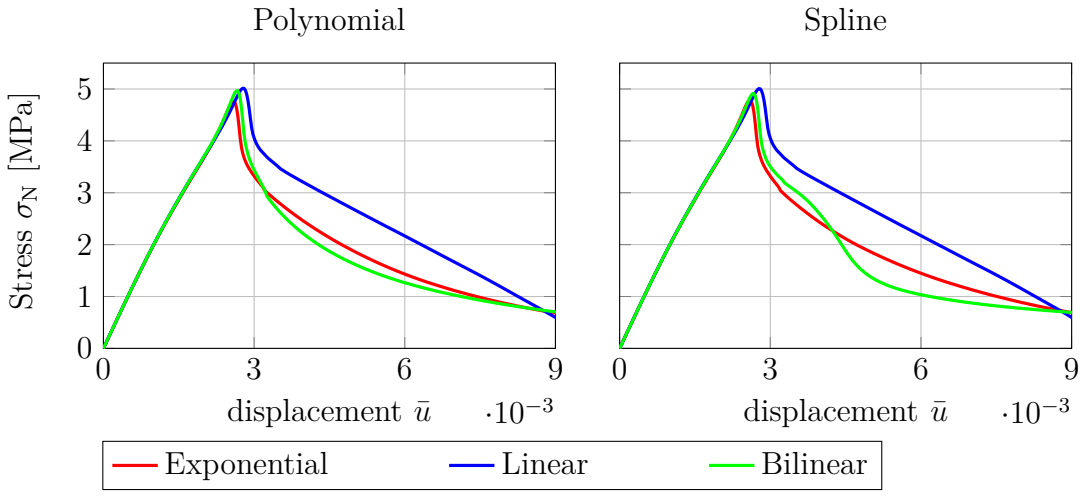

Figure 4.17: "CT-specimen – Notched plate under tension: Normal stresses σ_{N} at point A versus prescribed displacement $\bar{u}$ (point A is defined in Figure 4.13). The results correspond to the different approximations (polynomial and spline approximation of the degradation function) and three different traction-separation laws (exponential, linear and bilinear)." ([79, Sec. 4.2∗]). A geometrically exact theory is applied.

4.7.5 L-shaped plate

4.7.5.1 Geometrically exact setting

The following section is taken from [79, Sec. 4.3∗]:

"Finally, the two-dimensional L-shaped plate shown in Fig. 4.18, cf. [81], is investigated under a plane stress assumption. In contrast to the previous examples, a geometrically exact setting is adopted, i.e., finite strains.

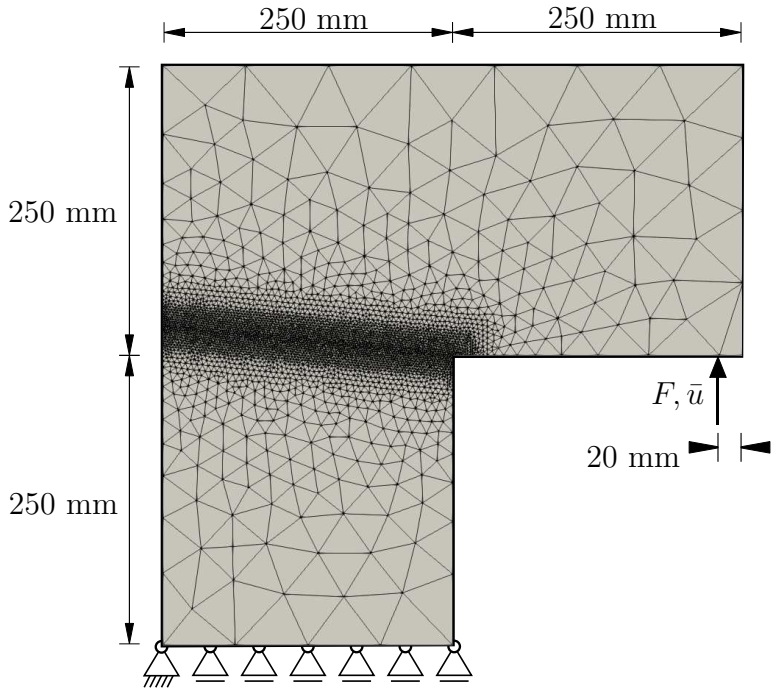

Material Parameter	
λ	4766.95 MPa
μ	8474.58 MPa
σ_c	2.5 MPa
γ	0.13 N/mm
E^*	19998.35 MPa
ε	2.5, 5 mm

Figure 4.18: Two-dimensional finite element analysis of an L-shaped plate. The material parameters have been taken from [51]. The L-shape has a thickness of 100 mm. Parameter E^* controlling the strength of the material has been computed in line with [81].

The plate is loaded by prescribing the vertical displacement $\bar{u}$. If the load has reached a certain threshold, a crack initiates at the inner corner of the structure. This crack then evolves in a curved manner – in contrast to the previous example.

Following [81], the MCR effect is captured. The energy associated with active damage Ψ_+ and that corresponding to compression Ψ_- are assumed of neo-Hooke-type, i.e.,

$$\Psi_+ = \begin{cases} \frac{1}{2} G \operatorname{tr}(\bar{\boldsymbol{C}} - \boldsymbol{I})^2 + \frac{1}{2} K (J-1)^2 & \text{if } J \geq 1 \,, \\ \frac{1}{2} G \operatorname{tr}(\bar{\boldsymbol{C}} - \boldsymbol{I})^2 & \text{if } J < 1 \,, \end{cases} \tag{4.152}$$

$$\Psi_- = \begin{cases} 0 & \text{if } J \geq 1 \,, \\ \frac{1}{2} K (J-1)^2 & \text{if } J < 1 \,, \end{cases} \tag{4.153}$$

where K is the bulk's modulus and G is the shear modulus. As far as the traction-separation-law is concerned, exponential model

$$t_n^0(\llbracket \boldsymbol{u} \rrbracket) = \sigma_c \exp\left(-\| \llbracket \boldsymbol{u} \rrbracket \| \frac{\sigma_c}{\gamma} \right) \tag{4.154}$$

is chosen. In order to approximate this law by the degradation function (phase-field model), the parameter vector $\boldsymbol{a}$ for $n_{\boldsymbol{a}} = 6$ of the polynomial ansatz for the exponential traction-separation-law evaluated in Section 4.7.2.3 is employed (see Table 6.1). Due to the non-differentiability of the degradation function at the onset of crack initiation, an approximation/convexification is again applied, cf. 4.6.1.

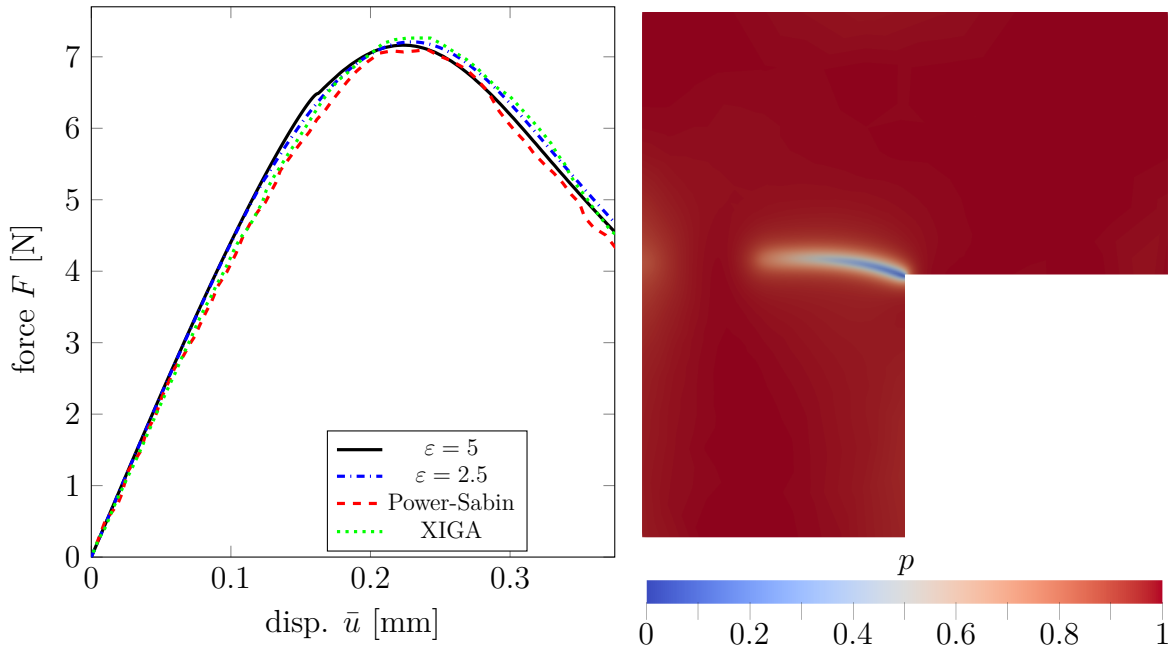

Figure 4.19: Two-dimensional finite element analysis of an L-shaped plate. (left) Force-displacement-diagram predicted by the novel phase-field model and predictions taken from [51], (right) phase-field distribution computed by the novel model at $\bar{u} = 0.4$ mm (final stage).

The force-displacement-diagram (left) as well as the final phase-field distribution (right) computed from the phase-field model is summarized in Figure 4.19.

According to Fig. 4.19, the force-displacement diagram is in good agreement with those of sharp interfaces models, see [51]. The same statement also holds true for the predicted crack geometry."

4.7.5.2 Geometrically linearized setting

The same free boundary problem as presented in Figure 4.18 is investigated for a geometrically linearized theory. The small strain model proposed in Section 4.5 with an included MCR effect using the spectral decomposition (cf. Section 6.3) is applied here. An explicit plane stress formulation as presented in Appendix 6.3 is applied. The model parameters remain the same as presented in Figure 4.18 besides $c^* = E = 20000$ MPa following Section 4.5. Again, the exponential traction-separation law is chosen using the polynomial fitting approach with $n_{\boldsymbol{a}} = 6$ free parameters. The phase field width is 5 mm.

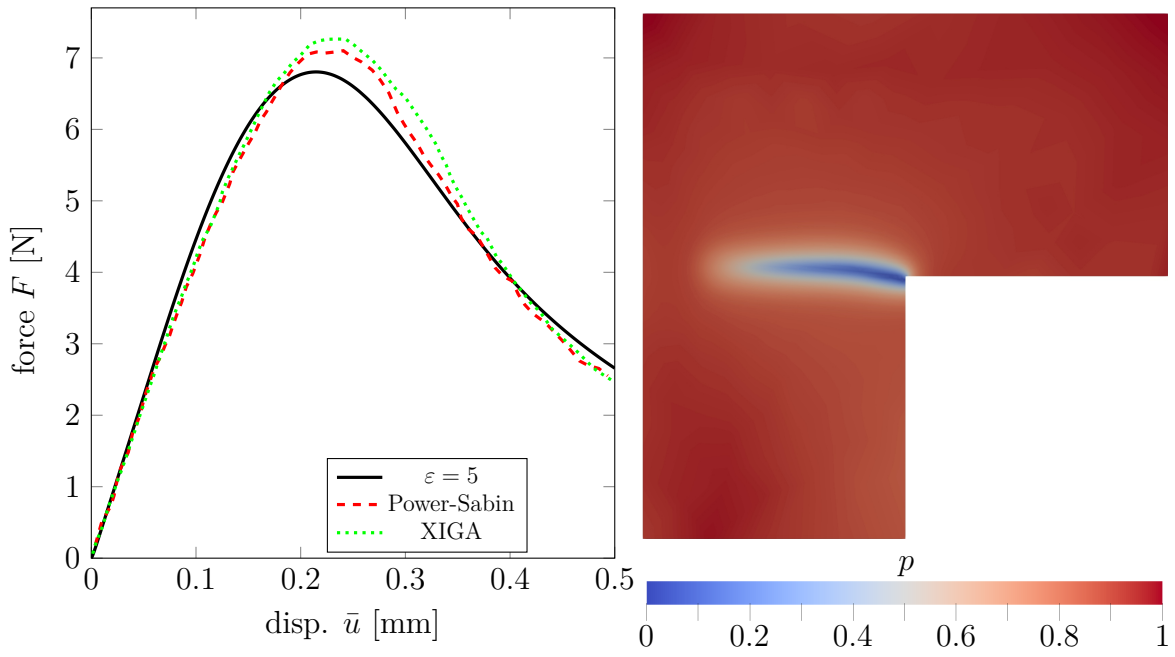

Figure 4.20: "Two-dimensional finite element analysis of an L-shaped plate. (left) Force-displacement-diagram predicted by the novel phase-field model and predictions taken from [51]" ([79, Sec. 4.3∗]). (right) Phase field distribution at latest time step $\bar{u} = 0.5$ mm. A geometrically linearized setting is adopted here.

Similar to the geometrically exact setting, the structural response in form of the force displacement curve approximates the sharp interface solutions well. However, a small deviation of the maximal force is visible. The main difference to the geometrically exact setting is the phase field distribution shown in Figure 4.20 (right). As the advanced

spectral decomposition is applied here in contrast to the volumetric deviatoric decomposition at finite strains, no damaged zone on the compressive region on the left edge is present. The crack can also emerge further in the structure highlighting the capabilities of the spectral decomposition in contrast to the rather straightforward approach for the geometrically exact setting.

4.8 Conclusion

In this section, the phase field approximation of cohesive zone models as presented in [35, 36, 55] was further extended. Although the approach introduced by [35] and extended by [36, 55] yields several advantages compared to other approaches (c.f. [52, 53, 90, 91, 150, 165, 166]) such as a proven Γ-convergence including the Cantor part, it leaves some points unconsidered. Several of these points were covered and included here, improving in particular the underlying physics of the model.

"The enhanced model allows to prescribe the fracture energy as well as the strength of the material interfaces — the probably two most important material parameters of cohesive interfaces. A rigorous mathematical convergence proof of the model was given." ([81, Sec. 5]). Furthermore, the shape of the traction-separation law was incorporated into the model. By redefining the calibration problem as minimization problem arbitrary potential-based traction-separation laws could be approximated. Two ansatz functions based on polynomials and splines were suggested. Both provide good approximations of the desired traction-separation laws. However, the regularity of the traction-separation law and the approximation space had an important impact on the calibration.

Regarding the bulk energy a geometrically exact setting was considered. To be more precise, arbitrary hyperelastic material models can be incorporated into the model. Furthermore, the MCR-effect is considered in the new approach. For the introduction of arbitrary bulk materials, "the energy proposed in [35, 55] was re-interpreted in terms of effective strains (displacement gradients) and a scaling between surface and bulk energies. Subsequently, this interpretation was applied to general non-linear hyperelastic models. Second, an effective scalar-valued bulk stiffness was introduced in order to adjust the strength of the interface." ([81, Sec- 5]). With respect to the MCR effect a volumetric-deviatoric decomposition was employed. For linear bulk material, improved MCR models were introduced.

Numerical examples underlined the predictive capabilities of the novel approach. An exponential, linear, bilinear and trapezoidal (limit) traction-separation law were calibrated. These laws were applied to one-dimensional finite element simulation with linear and nonlinear material models. Finally, two-dimensional examples were also investigated. Both examples were carried for a geometrically exact and a geometrically linearized setting. A tensile test highlighted the impact of the traction-separation laws on the global structural responses. An L-shaped specimen showed the convergence to a

sharp interface reference solution for more complex structures. The importance of the chosen approach to model the MCR effect was also emphasized.

5 Concluding remarks

5.1 Conclusion

This thesis consists of three main parts. First an introduction to general interfaces was given. Phase field approaches for interface elasticity as well as cohesive fracture were presented next. The two phase field approaches are concluded in the following.

5.1.1 Coherent interface — Hyperelastic framework

Within the interface's hyperelastic framework, the energy of the interface depends on its deformation gradient resulting in stresses tangential to the interface and consequently in a traction jump. In order to introduce the interface's deformation to a phase field approximation the interface deformation gradient needed to be approximated. By establishing the normed phase field gradient as interface normal, local tangential vectors were introduced. With these vectors the interface deformation gradient could be approximated.

The novel phase field approach to coherent interfaces was able to reproduce the well-known "the smaller the stiffer" size effect and to interpret this effect by means of a competition between interface and bulk energies.

5.1.2 Cohesive fracture

A promising approach of a phase field approximation to cohesive fracture was proposed in Conti et al. [35, 36], Freddi and Iurlano [55]. It shows a mathematically rigorous structure including a proof of Γ-convergence to the sharp interface limit. However, the approach does not allow to prescribe the elastic response, the material's strength and the fracture energy independently. Furthermore, it does not account for the MCR effect. In this work the phase field approximation was extended to a more physical setting.

The interface energy of the converged, sharp interface setting depends only on the degradation function of the phase field model. Consequently, all aforementioned improvements were achieved by adjusting the degradation function. Rescaling the degradation function by using all material parameters allowed to prescribe the two main

interface material parameters — the fracture energy as well as the material's strength. By tracing the problem back to the original approach by Conti et al. [35, 36], Freddi and Iurlano [55] a rigorous proof of Γ-convergence was presented. Evidently, the interface energy is not uniquely defined by means of these two parameters. For instance, the shape of the traction-separation law is not uniquely defined by these two model parameters. However, the shape is indeed important for many applications. "For this reason, an inverse optimization problem was presented in this paper. It allows to identify the degradation function (phase-field approximation) for a given/measured traction-separation law (sharp interface). In order to derive the respective algorithm, the other direction was considered first (the forward problem). To be more precise, the traction-separation-law (sharp interface problem) implied by a certain degradation function (phase-field model) was computed. For that purpose, a variational principle proposed in [35] was solved by means of finite elements. Subsequently, the space of admissible degradation functions was discretized. In order to a priori fulfill the constraints associated with the space of degradation functions in [35], a novel ansatz was presented. Both a polynomial and a spline basis proved to be suitable. Piecewise-linear functions, on the other hand, led to numerical problems in the finite element simulations – at least for an implementation based on alternate minimization combined with a Newton method. Based on the solution of the forward problem, the inverse problem was solved: For a given traction-separation-law, the parameters defining the aforementioned approximation are computed by minimizing the distance (error) between the prescribed and the computed traction-separation law. Numerical experiments highlighted that the degradation function can indeed be identified for the most frequently applied traction-separation-laws including an exponential, a linear and a bilinear law. Since both approximations of the space of admissible degradation functions yield similar results (polynomials and cubic splines), a polynomial basis is recommended due to its simplicity, the nested structure $\mathcal{D}_{\text{pol}}^{(n_a)} \subset \mathcal{D}_{\text{pol}}^{(n_a+1)}$ and the smoothness." ([79, Sec. 5∗]).

"Furthermore and in contrast to Conti et al. [35], Freddi and Iurlano [55], the final enhanced model is based on a geometrically exact setting. This setting, in turn, makes it possible to incorporate arbitrary hyperelastic bulk models. The generalization to the geometrically exact setting required two ideas. First, the energy proposed in Conti et al. [35], Freddi and Iurlano [55] was re-interpreted in terms of effective strains (displacement gradients) and a scaling between surface and bulk energies. Subsequently, this interpretation was applied to general non-linear hyperelastic models. Secondly, an effective scalar-valued bulk stiffness was introduced in order to adjust the strength of the interface. Finally, the MCR effect was included in the final model by applying the well-established volumetric-deviatoric decomposition. Other decompositions such as the spectral decomposition are not applicable here, as the polynomial structure of the effective strains vanishes. Numerical experiments highlighted the predictive capabilities of the model and emphasized that a sound implementation of the MCR effect is indeed important." ([81, Sec. 5]). A mathematical treatment of the geometrically exact setting is presented in [37].

5.2 Outlook

The probably most important contribution of this work is the phase field description of sharp cohesive interface models. Although the model does capture several phenomena realistically, some extensions are still required. Two of them are summarized next.

Advanced MCR effect within a geometrcally exact phase field approach The employed volumetric-deviatoric decomposition (see [9]) does not capture the MCR effect very realistically. In particular, the anisotropy induced by cracks is not accounted for. Thus decompositions such as the spectral decomposition (see [101, 104]) are to be considered. However, due to the scaling of the different terms within the energy, their adaptions and implementations are scientifically very challenging.

Anisotropy So far, only isotropic traction-separation laws are considered in this thesis. Consequently, the tractions are colinear to the displacement jump. The introduction of anisotropic interface energies would be a major enhancement to the model. This often comes along with a decomposition of the jump into normal and tangent components. As the jump is only included implicitly in the displacement field for the given approach, the extension to anisotropy remains an open question.

6 Appendix

6.1 Γ-convergence in the setting of phase field approximations

In the following, Γ-convergence in the setting of phase field approximations is briefly introduced. While the functional of the phase field approximation is denoted by $\mathcal{E}_\varepsilon$ the sharp interface functional reads $\mathcal{E}$. The diffuse and the sharp interface solutions of free boundary problems belong to different function spaces. Therefore, a pointwise convergence ($\mathcal{E}_\varepsilon[\boldsymbol{u}_*, p_*] \to \mathcal{E}[\boldsymbol{u}_*, p_*]$ for any given pair $(\boldsymbol{u}_*, p_*)$) cannot be expected. However, phase field approximations often show Γ-convergence to the discrete solution. It is defined as follows.

Γ-convergence Let $\mathcal{X} := \mathbb{R}^{n_{\mathrm{dim},\boldsymbol{u}}} \times \mathbb{R}$ and $\overline{\mathbb{R}} = \mathbb{R} \cup \{\pm\infty\}$. A sequence of functionals $\mathcal{I}_\varepsilon : \mathcal{X} \to \overline{\mathbb{R}}$ Γ-converges to $\mathcal{I} : \mathcal{X} \to \overline{\mathbb{R}}$ ($\mathcal{E}_\varepsilon \xrightarrow{\Gamma} \mathcal{E}$) if

$$\begin{aligned} &\forall (\boldsymbol{u}_\varepsilon, p_\varepsilon)_{\varepsilon\in\mathbb{R}_+} \subset \mathcal{X} \text{ with } (\boldsymbol{u}_\varepsilon, p_\varepsilon) \to (\boldsymbol{u}_*, p_*) \in \mathcal{X} && \mathcal{E}[\boldsymbol{u}_*, p_*] \leq \liminf_{\varepsilon \searrow 0} \mathcal{E}_\varepsilon[\boldsymbol{u}_\varepsilon, p_\varepsilon]\,, \\ &\forall (\boldsymbol{u}_*, p_*) \in \mathcal{X}\ \exists (\boldsymbol{u}_\varepsilon, p_\varepsilon)_{\varepsilon\in\mathbb{R}_+} \subset \mathcal{X} \text{ with } (\boldsymbol{u}_\varepsilon, p_\varepsilon) \to (\boldsymbol{u}_*, p_*) && \mathcal{E}[\boldsymbol{u}_*, p_*] \geq \limsup_{\varepsilon \searrow 0} \mathcal{E}_\varepsilon[\boldsymbol{u}_\varepsilon, p_\varepsilon]. \end{aligned} \tag{6.1}$$

Thus, Γ-convergence states that for any pair $(\boldsymbol{u}_*, p_*) \in \mathcal{X}$, value $\mathcal{E}^{\mathrm{int},\Omega}[\boldsymbol{u}_*, p_*]$ is the lowest possible limit of the sequence $\mathcal{E}_\varepsilon^{\mathrm{int},\Omega}[\boldsymbol{u}_\varepsilon, p_\varepsilon]$ over all possible sequences $(\boldsymbol{u}_\varepsilon, p_\varepsilon)$ which converge in $L^1(\Omega; \mathbb{R}^{n_{\mathrm{dim},\boldsymbol{u}}}) \times L^1(\Omega)$ to $(\boldsymbol{u}_*, p_*)$. Assuming appropriate coercivity, minimizers of $\mathcal{E}_\varepsilon$ converge to minimizers of $\mathcal{E}$ up to subsequences. Accordingly, the phase field approach $\mathcal{E}_\varepsilon$ asymptotically approximates the variational sharp interface problem $\mathcal{E}$. Interested readers are referred to [25] for an extensive introduction to the concept of Γ-convergence.

6.2 Variational description and free boundary problem

Although the balance laws have already been discussed in Section 2.3 for sharp interfaces, they are re-derived here for the phase-field setting by using the variational structure of the problem.

As the additional condition $\dot{p} \leq 0$ applies in order to prevent selfhealing (see Section 4.1.2), the stationary condition of the constrained optimization reads

$$\delta\mathcal{E} = \delta_{\boldsymbol{\varphi}}\mathcal{E} \cdot \delta\boldsymbol{\varphi} + \delta_p\mathcal{E}\,\delta p \overset{!}{\geq} 0 \qquad \forall \delta\boldsymbol{\varphi}, \delta p \quad \text{with} \quad \delta p(\boldsymbol{X}) \leq 0 \,\forall \boldsymbol{X} \in \Omega\,. \tag{6.2}$$

The total energy takes the form

$$\mathcal{E} = \mathcal{E}^{\text{int}} + \mathcal{E}^{\text{ext}}\,, \tag{6.3}$$

with contributions

$$\mathcal{E}^{\text{int}} = \int_{\mathcal{V}_0} \widetilde{\Psi}(\boldsymbol{F}, p)\,\mathrm{d}V\,, \tag{6.4}$$

$$\mathcal{E}^{\text{ext}} = -\int_{\mathcal{V}_0} \boldsymbol{B} \cdot \boldsymbol{\varphi}\,\mathrm{d}V - \int_{\partial\mathcal{V}_0} \boldsymbol{T} \cdot \boldsymbol{\varphi}\,\mathrm{d}\boldsymbol{A}\,. \tag{6.5}$$

Helmholtz energy $\widetilde{\Psi}$ is defined by

$$\widetilde{\Psi}(\boldsymbol{F}, p, \nabla p) := \Psi^{\text{eff}}(\boldsymbol{F}, p) + \gamma\, f_\varepsilon(p, \nabla p) \tag{6.6}$$

The effective energy differs throughout the thesis. In the prototype model of brittle fracture it is defined by $\Psi^{\text{eff}}(\boldsymbol{F}, p) = d(p)\,\Psi(\boldsymbol{F})$ (cf. Section 4.1). For the enhanced cohesive model elaborated in Chapter 4 the effective Helmholtz energy of the bulk is defined in Equation (4.115). Following the procedure of Colemann and Noll [33], the dual variables take the form

$$\boldsymbol{P} = \frac{\partial\widetilde{\Psi}}{\partial\boldsymbol{F}} = \frac{\partial\Psi^{\text{eff}}}{\partial\boldsymbol{F}}\,, \tag{6.7}$$

$$\pi = \frac{\partial\widetilde{\Psi}}{\partial p} = \frac{\partial\Psi^{\text{eff}}}{\partial p} + \gamma\,\frac{\partial f_\varepsilon}{\partial p} = \frac{\partial\Psi^{\text{eff}}}{\partial p} + \frac{\gamma}{4\,c_0\,\varepsilon}\,\frac{\partial\vartheta}{\partial p}\,, \tag{6.8}$$

$$\boldsymbol{\chi} = \frac{\partial\widetilde{\Psi}}{\partial\nabla p} = \gamma\,\frac{\partial f_\varepsilon}{\partial\nabla p} = \frac{2\,\varepsilon\,\gamma}{c_0}\,\nabla p\,. \tag{6.9}$$

Since stationary condition (6.2) needs to hold for all $\delta\boldsymbol{\varphi}$ and δp with $\delta p(\boldsymbol{X}) \leq 0 \,\forall \boldsymbol{X} \in \Omega$ it can be separated into

$$\delta_{\boldsymbol{\varphi}}\mathcal{E} \cdot \delta\boldsymbol{\varphi} = \delta_{\boldsymbol{\varphi}}\mathcal{E}^{\text{int}} \cdot \delta\boldsymbol{\varphi} + \delta_{\boldsymbol{\varphi}}\mathcal{E}^{\text{ext}} \cdot \delta\boldsymbol{\varphi} \overset{!}{=} 0 \qquad \forall \delta\boldsymbol{\varphi}\,, \tag{6.10}$$

$$\delta_p\mathcal{E}\,\delta p = \delta_p\mathcal{E}^{\text{int}}\,\delta p + \delta_p\mathcal{E}^{\text{ext}}\,\delta p \overset{!}{\geq} 0 \qquad \forall \delta p \text{ with } \delta p(X) \leq 0 \,\forall \boldsymbol{X} \in \Omega\,. \tag{6.11}$$

The inequality is only present for the variation regarding the phase field p, as this field is restricted by condition $\dot{p}(\boldsymbol{X}) \leq 0 \,\forall \boldsymbol{X} \in \Omega$.

First the variation with respect to $\boldsymbol{\varphi}$ is considered. The variation of energy contribution $\mathcal{E}^{\text{int}}$ takes the form

$$\begin{aligned} \delta_{\boldsymbol{\varphi}}\mathcal{E}^{\text{int}} \cdot \delta\boldsymbol{\varphi} &= \int_{\mathcal{V}_0} \boldsymbol{P} \colon \text{Grad}(\delta\boldsymbol{\varphi})\,\mathrm{d}V \\ &= \int_{\mathcal{V}_0} -\text{Div}(\boldsymbol{P}) \cdot \delta\boldsymbol{\varphi}\,\mathrm{d}V + \int_{\partial\mathcal{V}_0} [\boldsymbol{P} \cdot \boldsymbol{N}] \cdot \delta\boldsymbol{\varphi}\,\mathrm{d}\boldsymbol{A}\,, \end{aligned} \tag{6.12}$$

where identities

$$\boldsymbol{P} \colon \text{Grad}(\delta\boldsymbol{\varphi}) = \text{Div}(\delta\boldsymbol{\varphi} \cdot \boldsymbol{P}) - \text{Div}(\boldsymbol{P}) \cdot \delta\boldsymbol{\varphi}\,, \tag{6.13}$$

$$\int_{\mathcal{V}_0} \text{Div}(\delta\boldsymbol{\varphi} \cdot \boldsymbol{P})\mathrm{d}V = \int_{\partial\mathcal{V}_0} [\boldsymbol{P} \cdot \boldsymbol{N}] \cdot \delta\boldsymbol{\varphi}\,\mathrm{d}\boldsymbol{A} \tag{6.14}$$

are used within the reformulation of the variation. Together with the variation of external energy $\mathcal{E}^{\text{ext}}$

$$\delta_{\boldsymbol{\varphi}}\mathcal{E}^{\text{ext}} \cdot \delta\boldsymbol{\varphi} = -\int_{\mathcal{V}_0} \boldsymbol{B} \cdot \delta\boldsymbol{\varphi}\,\mathrm{d}V - \int_{\partial\mathcal{V}_0} \boldsymbol{T} \cdot \delta\boldsymbol{\varphi}\,\mathrm{d}\boldsymbol{A} \tag{6.15}$$

the variation of the total energy $\mathcal{E}$ takes the form

$$\delta_{\boldsymbol{\varphi}}\mathcal{E} \cdot \delta\boldsymbol{\varphi} = \int_{\mathcal{V}_0} [-\text{Div}(\boldsymbol{P}) - \boldsymbol{B}] \cdot \delta\boldsymbol{\varphi}\,\mathrm{d}V + \int_{\partial\mathcal{V}_0} [\boldsymbol{P} \cdot \boldsymbol{N} - \boldsymbol{T}] \cdot \delta\boldsymbol{\varphi}\,\mathrm{d}\boldsymbol{A} \quad \overset{!}{=} 0 \quad \forall\, \delta\boldsymbol{\varphi}\,. \tag{6.16}$$

The local form of the equilibrium condition thus results in

$$\text{Div}(\boldsymbol{P}) + \boldsymbol{B} = \boldsymbol{0} \qquad \forall\, \boldsymbol{X} \in \Omega\,, \tag{6.17}$$

$$\boldsymbol{P} \cdot \boldsymbol{N} - \boldsymbol{T} = \boldsymbol{0} \qquad \forall\, \boldsymbol{X} \in \partial\Omega_{\text{N}}\,. \tag{6.18}$$

Regarding the order parameter p the variation of total energy $\mathcal{E}$ reads

$$\begin{aligned}\delta_p\mathcal{E}\cdot\delta p &= \delta_p\mathcal{E}^{\text{int}}\cdot\delta p \\ &= \int_{\mathcal{V}_0} \pi\,\delta p + \boldsymbol{\chi}\cdot\delta\nabla p\,\mathrm{d}V \\ &= \int_{\mathcal{V}_0} \pi\,\delta p + \mathrm{Div}(\boldsymbol{\chi}\,\delta p) - \mathrm{Div}(\boldsymbol{\chi})\,\delta p\,\mathrm{d}V \\ &= \int_{\mathcal{V}_0} [\pi - \mathrm{Div}(\boldsymbol{\chi})]\;\delta p\,\mathrm{d}V + \int_{\partial\mathcal{V}_0} [\boldsymbol{\chi}\cdot\boldsymbol{N}]\;\delta p\,\mathrm{d}\boldsymbol{A} \quad \overset{!}{\geq} 0 \\ &\qquad\qquad \forall\,\delta p \quad \text{with} \quad \delta p(X)\leq 0\;\forall \boldsymbol{X}\in\Omega\,,\end{aligned} \tag{6.19}$$

as the variation of $\mathcal{E}^{\text{ext}}$ vanishes. Identities

$$\boldsymbol{\chi}\cdot\delta\nabla p = \mathrm{Div}(\delta p\cdot\boldsymbol{\chi}) - \mathrm{Div}(\boldsymbol{\chi})\,\delta p\,, \tag{6.20}$$

$$\int_{\mathcal{V}_0}\mathrm{Div}(\delta p\cdot\boldsymbol{\chi})\mathrm{d}V = \int_{\partial\mathcal{V}_0}[\boldsymbol{\chi}\cdot\boldsymbol{N}]\;\delta p\,\mathrm{d}\boldsymbol{A} \tag{6.21}$$

are used in order to derive the final form of the variation. The strong form reads

$$\mathrm{Div}(\boldsymbol{\chi}) - \pi \leq 0 \qquad \forall\;\boldsymbol{X}\in\Omega\,, \tag{6.22}$$

$$\boldsymbol{\chi}\cdot\boldsymbol{N} = \boldsymbol{0} \qquad \forall\;\boldsymbol{X}\in\partial\Omega\,. \tag{6.23}$$

Following [93] variation $\delta p(\boldsymbol{X}) = \dot{p}(\boldsymbol{X}) \leq 0\,\forall\,\boldsymbol{X}\in\Omega$ is chosen in Equation (6.19) resulting in

$$\int_{\mathcal{V}_0}[\pi - \mathrm{Div}(\boldsymbol{\chi})]\;\dot{p}\,\mathrm{d}V = 0\,,\quad \int_{\mathcal{V}_0}[\pi - \mathrm{Div}(\boldsymbol{\chi})]\;\delta p\,\mathrm{d}V \geq 0\,,\quad \dot{p}(\boldsymbol{X})\leq\boldsymbol{X}\,\forall\,\boldsymbol{X}\in\Omega. \tag{6.24}$$

Different approaches to handle the condition $\dot{p}\leq 0$ are discussed in Section 4.1.2.

6.3 Explicit plane stress formulation for Hooke's model including the MCR effect

The plane stress assumption states, that no stresses emerge orthogonal to a plane. For isotropic material models, this can be formulated as $\sigma_{33} = 0$ when assuming the plane normal to be $\boldsymbol{e}_3$. For the standard linear Hooke's model

$$\Psi = \frac{1}{2}\,\lambda\,\mathrm{trace}(\nabla\boldsymbol{u}^{\text{sym}})^2 + \mu\,\nabla\boldsymbol{u}^{\text{sym}}\colon\nabla\boldsymbol{u}^{\text{sym}}\,. \tag{6.25}$$

The condition $\sigma_{33} = 0$ can be solved analytically resulting in a stress energy density

$$\Psi = \frac{1}{2}\,\lambda^{\text{2d}}\,\mathrm{trace}(\nabla\boldsymbol{u}^{\text{sym}})^2 + \mu\,\nabla\boldsymbol{u}^{\text{sym}}\colon\nabla\boldsymbol{u}^{\text{sym}}\,, \tag{6.26}$$

where $n_{\mathrm{dim}} = 2$. Parameter $\lambda^{2\mathrm{d}}$ takes the form

$$\lambda^{2\mathrm{d}} = \frac{2\,\lambda\,\mu}{\lambda + 2\,\mu}\,. \tag{6.27}$$

When no MCR effect is assumed in the phase field approximation (see Section 4.1) the same explicit formulation can be adopted because the degradation function is applied to the full energy. However, a more complex explicit formulation is required when a decomposition of the bulk energies into a tensile and a compressive part is introduced (see Section 4.1.1). In [88] an explicit formulation regarding the volumetric-deviatoric as well as the spectral decomposition is presented. It is recapitulated in the following.

6.3.1 Volumetric deviatoric decomposition

The bulk energy density for a volumetric-deviatoric decomposition reads

$$\Psi_+ = \frac{1}{2}\,\lambda_+^{2\mathrm{d}}\,\mathrm{trace}(\nabla \boldsymbol{u}^{\mathrm{sym}})^2 + \mu\,\nabla \boldsymbol{u}^{\mathrm{sym}} \colon \nabla \boldsymbol{u}^{\mathrm{sym}}\,, \tag{6.28}$$

$$\Psi_- = \frac{1}{2}\,\lambda_-^{2\mathrm{d}}\,\mathrm{trace}(\nabla \boldsymbol{u}^{\mathrm{sym}})^2\,, \tag{6.29}$$

with

$$\lambda_+^{2\mathrm{d}} = \begin{cases} \dfrac{2\,\lambda\,\mu}{\lambda + 2\,\mu} & \text{if } \mathrm{trace}(\nabla \boldsymbol{u}^{\mathrm{sym}}) > 0\,, \\[2ex] \dfrac{2\,\lambda^2\,\mu}{(\lambda + 2\,\mu\,d)^2} & \text{if } \mathrm{trace}(\nabla \boldsymbol{u}^{\mathrm{sym}}) \leq 1\,, \end{cases} \tag{6.30}$$

and

$$\lambda_-^{2\mathrm{d}} = \begin{cases} 0 & \text{if } \mathrm{trace}(\nabla \boldsymbol{u}^{\mathrm{sym}}) > 0\,, \\[2ex] \dfrac{4\,\lambda\,\mu^2\,d}{(\lambda + 2\,\mu\,d)^2} & \text{if } \mathrm{trace}(\nabla \boldsymbol{u}^{\mathrm{sym}}) \leq 1\,. \end{cases} \tag{6.31}$$

Degradation function d used here fulfills Properties (4.4) to (4.8). For the approximation to cohesive fracture presented in Chapter 4 it takes the form $d = d^2_{\varepsilon,c^*,\gamma,\sigma_{\mathrm{c}}}$.

6.3.2 Spectral decomposition

The bulk energy density for a spectral decomposition reads

$$\Psi_+ = \frac{1}{2}\,\lambda_+^{2\mathrm{d}}\,\mathrm{trace}(\nabla \boldsymbol{u}^{\mathrm{sym}})^2 + \mu\,\nabla \boldsymbol{u}_+^{\mathrm{sym}} \colon \nabla \boldsymbol{u}_+^{\mathrm{sym}}\,, \tag{6.32}$$

$$\Psi_- = \frac{1}{2}\,\lambda_-^{2\mathrm{d}}\,\mathrm{trace}(\nabla \boldsymbol{u}^{\mathrm{sym}})^2 + \mu\,\nabla \boldsymbol{u}_-^{\mathrm{sym}} \colon \nabla \boldsymbol{u}_-^{\mathrm{sym}}\,, \tag{6.33}$$

with $\nabla \boldsymbol{u}_+^{\mathrm{sym}}$ and $\nabla \boldsymbol{u}_+^{\mathrm{sym}}$ as defined in Equations (4.25) and (4.25). The parameters take the form

$$\lambda_+^{2\mathrm{d}} = \begin{cases} \dfrac{4\,\lambda\,\mu^2}{(\lambda\,d + 2\,\mu)^2} & \text{if}\,\mathrm{trace}(\nabla \boldsymbol{u}^{\mathrm{sym}}) > 0\,, \\[2ex] \dfrac{2\,\lambda^2\,\mu}{(\lambda + 2\,\mu\,d)^2} & \text{if}\,\mathrm{trace}(\nabla \boldsymbol{u}^{\mathrm{sym}}) \leq 1\,, \end{cases} \tag{6.34}$$

and

$$\lambda_-^{2\mathrm{d}} = \begin{cases} \dfrac{2\,\lambda^2\,\mu\,d^2}{(\lambda\,d + 2\,\mu)^2} & \text{if}\,\mathrm{trace}(\nabla \boldsymbol{u}^{\mathrm{sym}}) > 0\,, \\[2ex] \dfrac{4\,\lambda\,\mu^2\,d^2}{(\lambda + 2\,\mu\,d)^2} & \text{if}\,\mathrm{trace}(\nabla \boldsymbol{u}^{\mathrm{sym}}) \leq 1\,. \end{cases} \tag{6.35}$$

Degradation function d used here fulfills Properties (4.4) to (4.8). For the approximation to cohesive fracture presented in Chapter 4 it takes the form $d = d^2_{\varepsilon,c^*,\gamma,\sigma_{\mathrm{c}}}$. The total effective energy can be formulated as

$$\Psi^{\mathrm{eff}} = \frac{1}{2}\,\lambda^{2\mathrm{d}}\,\mathrm{trace}(\nabla \boldsymbol{u}^{\mathrm{sym}})^2 + d\,\mu\,\nabla \boldsymbol{u}_+^{\mathrm{sym}} \colon \nabla \boldsymbol{u}_+^{\mathrm{sym}} + \mu\,\nabla \boldsymbol{u}_-^{\mathrm{sym}} \colon \nabla \boldsymbol{u}_-^{\mathrm{sym}}, \tag{6.36}$$

with

$$\lambda^{2\mathrm{d}} = \begin{cases} \dfrac{2\,\lambda\,\mu\,d}{\lambda\,d + 2\,\mu} & \text{if}\,\mathrm{trace}(\nabla \boldsymbol{u}^{\mathrm{sym}}) > 0 \\[2ex] \dfrac{2\,\lambda\,\mu\,d}{\lambda + 2\,\mu\,d} & \text{if}\,\mathrm{trace}(\nabla \boldsymbol{u}^{\mathrm{sym}}) \leq 1. \end{cases} \tag{6.37}$$

6.4 Approximated/convexified damage function for $d = p/(1-p)$

For the well established degradation function $d(p) = p/(1-p)$ (cf. [35, 55]) the $\mathcal{C}^1$-approximation

$$\hat{d}_{\varepsilon,c^*,\gamma,\sigma_c}(p) := \begin{cases} d_{\varepsilon,c^*,\gamma,\sigma_c}(p), & p \in [0, p_{\text{th}}[\,, \\ \left.\dfrac{\partial d_{\varepsilon,c^*,\gamma,\sigma_c}(\tilde{p})}{\partial \tilde{p}}\right|_{\tilde{p}=p_{\text{th}}} (p - p_{\text{th}}) + d_{\varepsilon,c^*,\gamma,\sigma_c}(p_{\text{th}}), & p = [p_{\text{th}}, 1]\,. \end{cases} \tag{6.38}$$

As presented in Section 4.6.2 can be derived analytically. The resulting threshold value takes the form

$$p_{\text{th}} = \frac{1 - \sqrt{\frac{2\varepsilon\sigma_c^2}{\gamma c \ell^2}}}{1 + \sqrt{\frac{2\varepsilon\sigma_c^2}{\gamma c \ell^2}}}\,. \tag{6.39}$$

This value also proves to be useful as initial guess to solve for p_{th} for general degradation functions $d(p)$. The unknown coefficients for $d(p) = p/(1-p)$ follow as

$$\left.\frac{\partial d_{\varepsilon,c^*,\gamma,\sigma_c}(\tilde{p})}{\partial \tilde{p}}\right|_{\tilde{p}=p_{\text{th}}} = \frac{\left[1 + \sqrt{\frac{2\varepsilon\sigma_c^2}{\gamma c \ell^2}}\right]^2}{4\sqrt{\frac{2\varepsilon\sigma_c^2}{\gamma c \ell^2}}} \quad \text{and} \quad d_{\varepsilon,c^*,\gamma,\sigma_c}(p_{\text{th}}) = \frac{1 - \sqrt{\frac{2\varepsilon\sigma_c^2}{\gamma c \ell^2}}}{2}\,. \tag{6.40}$$

6.5 Degradation functions (phase-field method) for different traction-separation-laws

The following section is taken from [79, App. A∗]:

"This appendix summarizes the degradation functions $d(p) = \tilde{d}(p)/(1-p)$ optimized for different traction-separation-laws. In line with Subsection 4.3.2.2, two different approximations for $\tilde{d}(p)$ have been considered: Polynomials (6.5.1) and cubic splines (6.5.2).

6.5.1 Polynomial functions

For $\tilde{d}$ spanned by polynomials, the optimized model parameters are given below. While $n_{\boldsymbol{a}} = 0$ corresponds to linear function $\tilde{d}(p) = p$, $n_{\boldsymbol{a}} = 6$ is associated with a polynomial of degree 7.

$n_{\boldsymbol{a}}$	Parameter vector $\boldsymbol{a}$	Error $r_{\boldsymbol{a}}$
exponential traction-separation-law		
0	$[1.0000]^{\mathrm{t}}$	$5.1219 \cdot 10^{-3}$
1	$[0.8194, 0.1806]^{\mathrm{t}}$	$1.5356 \cdot 10^{-3}$
2	$[0.5730, 1.2643, -0.8373]^{\mathrm{t}}$	$5.7578 \cdot 10^{-6}$
3	$[0.5580, 1.3916, -1.1137, 0.1641,]^{\mathrm{t}}$	$3.0170 \cdot 10^{-6}$
4	$[0.5582, 1.3922, -1.1160, 0.1616, 0.0040,]^{\mathrm{t}}$	$2.9883 \cdot 10^{-6}$
5	$[0.5582, 1.3922, -1.1160, 0.1616, 0.0040, 0.0000]^{\mathrm{t}}$	$2.9883 \cdot 10^{-6}$
6	$[0.5581, 1.3923, -1.1162, 0.1616, 0.0040, 0.0002, -0.0000]^{\mathrm{t}}$	$2.9870 \cdot 10^{-6}$
linear traction-separation-law		
0	$[1.0000]^{\mathrm{t}}$	$1.8479 \cdot 10^{-2}$
1	$[1.5360, -0.5360]^{\mathrm{t}}$	$3.4116 \cdot 10^{-6}$
2	$[1.5348, -0.5326, -0.0022]^{\mathrm{t}}$	$3.2524 \cdot 10^{-6}$
3	$[1.5348, -0.5326, -0.0022, 0.0000]^{\mathrm{t}}$	$3.2524 \cdot 10^{-6}$
4	$[1.5371, -0.5778, \quad 0.0363, 0.1695, -0.1652,]^{\mathrm{t}}$	$1.4702 \cdot 10^{-7}$
5	$[1.5418, -0.5989, \quad 0.0465, 0.1870, -0.1542, -0.0223]^{\mathrm{t}}$	$2.8962 \cdot 10^{-8}$
6	$[1.5416, -0.5987, \quad 0.0471, 0.1875, -0.1538, -0.0221, -0.0017]^{\mathrm{t}}$	$2.1548 \cdot 10^{-8}$
bilinear traction-separation-law		
0	$[1.0000]^{\mathrm{t}}$	$1.0456 \cdot 10^{-2}$
1	$[0.7768, 0.2232]^{\mathrm{t}}$	$2.2608 \cdot 10^{-3}$
2	$[0.4767, 1.4428, -0.9195]^{\mathrm{t}}$	$2.2411 \cdot 10^{-3}$
3	$[0.4651, 1.4694, -0.8761, -0.0585,]^{\mathrm{t}}$	$2.4870 \cdot 10^{-4}$
4	$[0.5974, 0.7231, -0.1079, \quad 0.6566, -0.8692,]^{\mathrm{t}}$	$2.4870 \cdot 10^{-4}$
5	$[0.5974, 0.7231, -0.1079, \quad 0.6566, -0.8692, 0.0000]^{\mathrm{t}}$	$2.4870 \cdot 10^{-4}$
6	$[0.5974, 0.7231, -0.1079, \quad 0.6566, -0.8692, 0.0000, 0.0000]^{\mathrm{t}}$	$2.4870 \cdot 10^{-4}$
limit traction-separation-law		
0	$[1.0000]^{\mathrm{t}}$	$7.8246 \cdot 10^{\ 2}$
1	$[3.1500, -2.1500]^{\mathrm{t}}$	$2.8972 \cdot 10^{-15}$
2	$[3.1500, -2.1500, 0.0000]^{\mathrm{t}}$	$2.8972 \cdot 10^{-15}$
3	$[3.1502, -2.1500, 0.0000, -0.0002]^{\mathrm{t}}$	$1.5283 \cdot 10^{-15}$
4	$[3.1505, -2.1494, 0.0000, -0.0002, -0.0009]^{\mathrm{t}}$	$2.6919 \cdot 10^{-16}$
5	$[3.5600, -2.1146, 0.0050, \quad 0.0133, 0.0009, -0.4645]^{\mathrm{t}}$	$1.2537 \cdot 10^{-16}$
6	$[3.5619, -2.1146, 0.0052, \quad 0.0133, 0.0011, -0.4647, -0.0020]^{\mathrm{t}}$	$9.7087 \cdot 10^{-17}$

Table 6.1: Optimized model parameters for degradation function $\tilde{d}$ spanned by polynomials.

6.5.2 Cubic splines

For cubic splines, the optimized model parameters are given below.

$n_{\boldsymbol{a}}$	Parameter vector $\boldsymbol{a}$	Error $r_{\boldsymbol{a}}$
exponential traction-separation-law		
0	$[\quad]^{\mathrm{t}}$	$5.1219 \cdot 10^{-2}$
1	$[0.4562]^{\mathrm{t}}$	$1.5091 \cdot 10^{-3}$
2	$[0.3018, 0.6971]^{\mathrm{t}}$	$5.8797 \cdot 10^{-6}$
3	$[0.2111, 0.5004, 0.7845]^{\mathrm{t}}$	$4.7106 \cdot 10^{-6}$
4	$[0.1596, 0.3800, 0.6140, 0.8365]^{\mathrm{t}}$	$1.6795 \cdot 10^{-6}$

5	$[0.1273, 0.3031, 0.4968, 0.6913, 0.8693]^{\mathrm{t}}$	$1.3621 \cdot 10^{-6}$
6	$[0.1054, 0.2521, 0.4114, 0.5809, 0.7448, 0.8913]^{\mathrm{t}}$	$1.2154 \cdot 10^{-6}$
linear traction-separation-law		
0	$[\quad]^{\mathrm{t}}$	$1.8479 \cdot 10^{-2}$
1	$[0.6355]^{\mathrm{t}}$	$2.8988 \cdot 10^{-6}$
2	$[0.4527, 0.7882]^{\mathrm{t}}$	$2.2699 \cdot 10^{-6}$
3	$[0.3509, 0.6342, 0.8575]^{\mathrm{t}}$	$1.3318 \cdot 10^{-7}$
4	$[0.2866, 0.5281, 0.7315, 0.8933]^{\mathrm{t}}$	$1.1418 \cdot 10^{-7}$
5	$[0.2421, 0.4518, 0.6352, 0.7908, 0.9155]^{\mathrm{t}}$	$1.0220 \cdot 10^{-7}$
6	$[0.2097, 0.3949, 0.5596, 0.7053, 0.8298, 0.9302]^{\mathrm{t}}$	$9.7301 \cdot 10^{-8}$
bilinear traction-separation-law		
0	$[\quad]^{\mathrm{t}}$	$1.0456 \cdot 10^{-2}$
1	$[0.4370]^{\mathrm{t}}$	$2.2437 \cdot 10^{-3}$
2	$[0.2862, 0.6878]^{\mathrm{t}}$	$5.4330 \cdot 10^{-4}$
3	$[0.1923, 0.4769, 0.8512]^{\mathrm{t}}$	$2.1517 \cdot 10^{-4}$
4	$[0.1483, 0.3462, 0.6582, 0.8461]^{\mathrm{t}}$	$6.0561 \cdot 10^{-5}$
5	$[0.1234, 0.2675, 0.5182, 0.7399, 0.8918]^{\mathrm{t}}$	$1.8379 \cdot 10^{-5}$
6	$[0.1068, 0.2167, 0.3997, 0.6227, 0.7706, 0.9218]^{\mathrm{t}}$	$1.7089 \cdot 10^{-5}$
limit traction-separation-law		
0	$[\quad]^{\mathrm{t}}$	$7.7549 \cdot 10^{-2}$
1	$[1.0320]^{\mathrm{t}}$	$5.2682 \cdot 10^{-16}$
2	$[0.8062, 1.1396]^{\mathrm{t}}$	$1.5322 \cdot 10^{-15}$
3	$[0.6490, 1.0320, 1.1490]^{\mathrm{t}}$	$9.9431 \cdot 10^{-17}$
4	$[0.5405, 0.9107, 1.1107, 1.1405]^{\mathrm{t}}$	$1.9640 \cdot 10^{-15}$
5	$[0.4623, 0.8062, 1.0321, 1.1396, 1.1290]^{\mathrm{t}}$	$2.8539 \cdot 10^{-18}$
6	$[0.4035, 0.7200, 0.9498, 1.0927, 1.1486, 1.1178]^{\mathrm{t}}$	$6.6534 \cdot 10^{-16}$

Table 6.2: Optimized model parameters for degradation function $\tilde{d}$ spanned by cubic splines

"

6.6 One-dimensional reference solution for sharp interfaces

6.6.1 Geometrically linearized setting — Hooke's model

The following section is taken from [79, App. C∗]:

"In the following the determination of a reference sharp interface solution for the one-dimensional setting is presented. Due to the equilibrium condition, the stresses within the bulk and the interface are identical, i.e., $\sigma = t(\llbracket u \rrbracket)$. Furthermore, the imperfection leads to an opening of the interface, while the bulk material unloads elastically. Denoting the total elongation of the truss as u, the (elastic) strains within the homogeneously

deforming bulk material read $\varepsilon = (u - [\![u]\!])/l$ and the equilibrium condition takes the format

$$\sigma = E\,\frac{u - [\![u]\!]}{l} = t([\![u]\!]). \tag{6.41}$$

Within a displacement-driven analysis, u is prescribed and the above equation allows to compute the displacement jump. Once the jump is computed, the stresses follow from the traction-separation-law – or from Hooke's model."

6.6.2 Geometrically exact setting — arbitrary hyperelastic model

Regarding general finite strain formulations a similar derivation is possible. The equilibrium condition reads

$$P = \frac{\partial \Psi}{\partial F} = t([\![u]\!]), \tag{6.42}$$

where P denotes the one-dimensional first Piola-Kirchhoff stress and F denotes the one-dimensional deformation gradient. The latter depends on the displacement as well as the displacement jump and reads

$$F = \frac{l + u - [\![u]\!]}{l}, \tag{6.43}$$

for a homogeneous deformation. Similar to above, the displacement jump $[\![u]\!]$ can be obtained by solving Problem (6.42).

It bears emphasis that independent of the bulk material model, the problem above remains implicit. Therefore, a solution method such as bisection or Newton's scheme is necessary for both, the geometrically linearized and the geometrically exact setting.

6.7 Alternative calibration of the material's strength for an interface with finite thickness

In Section 4.4.2 a procedure for calibrating the material's strength is derived. Equation (4.109) provides a procedure to calculate parameter c^* for arbitrary hyperelastic material models. A vanishing phase field length $\varepsilon \to 0$ is assumed to derive this equation. The one-dimensional finite element problems presented in Section 4.7.3 suggest, that the material strength converges to the desired one. However, it deviates for larger phase field length ε. In this appendix the parameters are computed for a finite diffuse interface. Hooke's model is assumed.

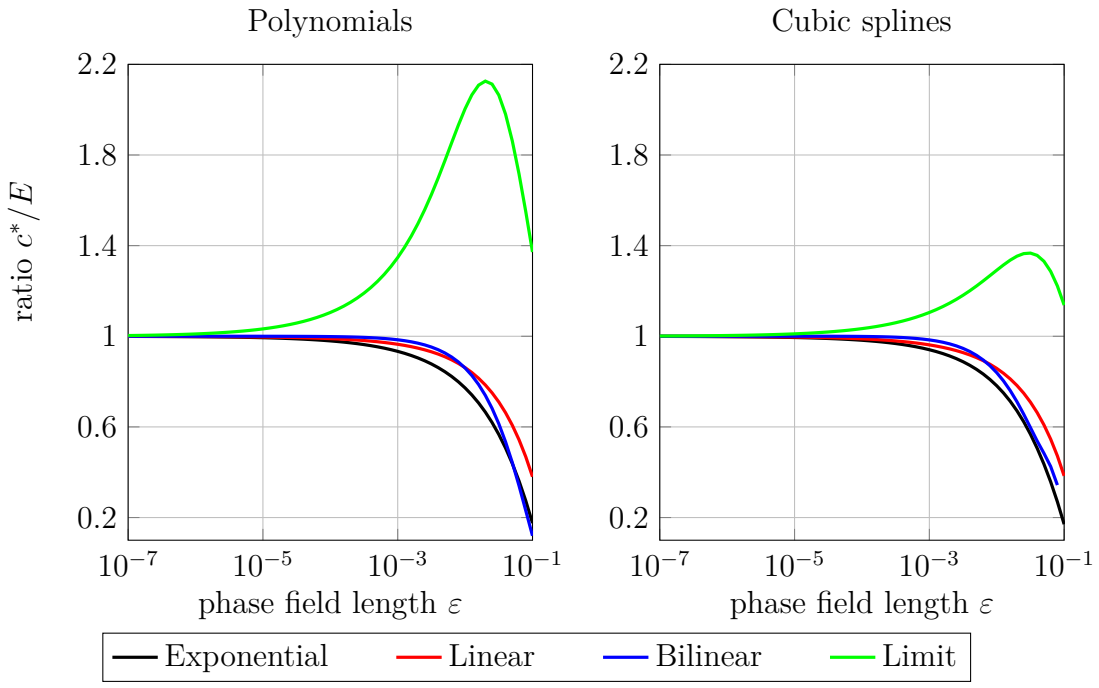

Figure 6.1: Calibration of the material's strength for finite phase field length ε. Ratio c^*/E between the newly calibrated parameter c_* and the parameter for vanishing phase field length $c^* = E$ for the polynomial and the spline based approximation approaches. The considered exponential, linear, bilinear and limit traction-separation laws are calibrated with $n_{\boldsymbol{a}} = 6$ free parameters.

For $\varepsilon \to 0$ and Hooke's model the parameter reduces to $c^* = E$, where E denotes Young's modulus (see Section 4.5). When assuming finite phase field length $\varepsilon > 0$ the parameter reads

$$c^* = E \, \frac{d^3(p_\mathrm{c}) \, (1 - p_\mathrm{c})}{\ell^2 \left. \dfrac{\partial d}{\partial p} \right|_\mathrm{c}} \,, \tag{6.44}$$

where subscript c denotes values at the moment of crack initiation. Accordingly, p_c needs to be obtained from condition

$$d_{\varepsilon, c^*, \gamma, \sigma_\mathrm{c}}(p_\mathrm{c}) = \sqrt{\frac{2 \, \varepsilon \, \sigma_\mathrm{c}^2}{c^* \, \gamma}} \, d(p_\mathrm{c}) \stackrel{!}{=} 1 \tag{6.45}$$

and depends on c^*. Threshold value p_c can be calculated by e.g. Newton's method or bisection. Furthermore, Equation (6.44) yields a natural structure for a fix-point scheme if the right side provides a contraction. Following these numeric schemes, a value for c^* can be derived.

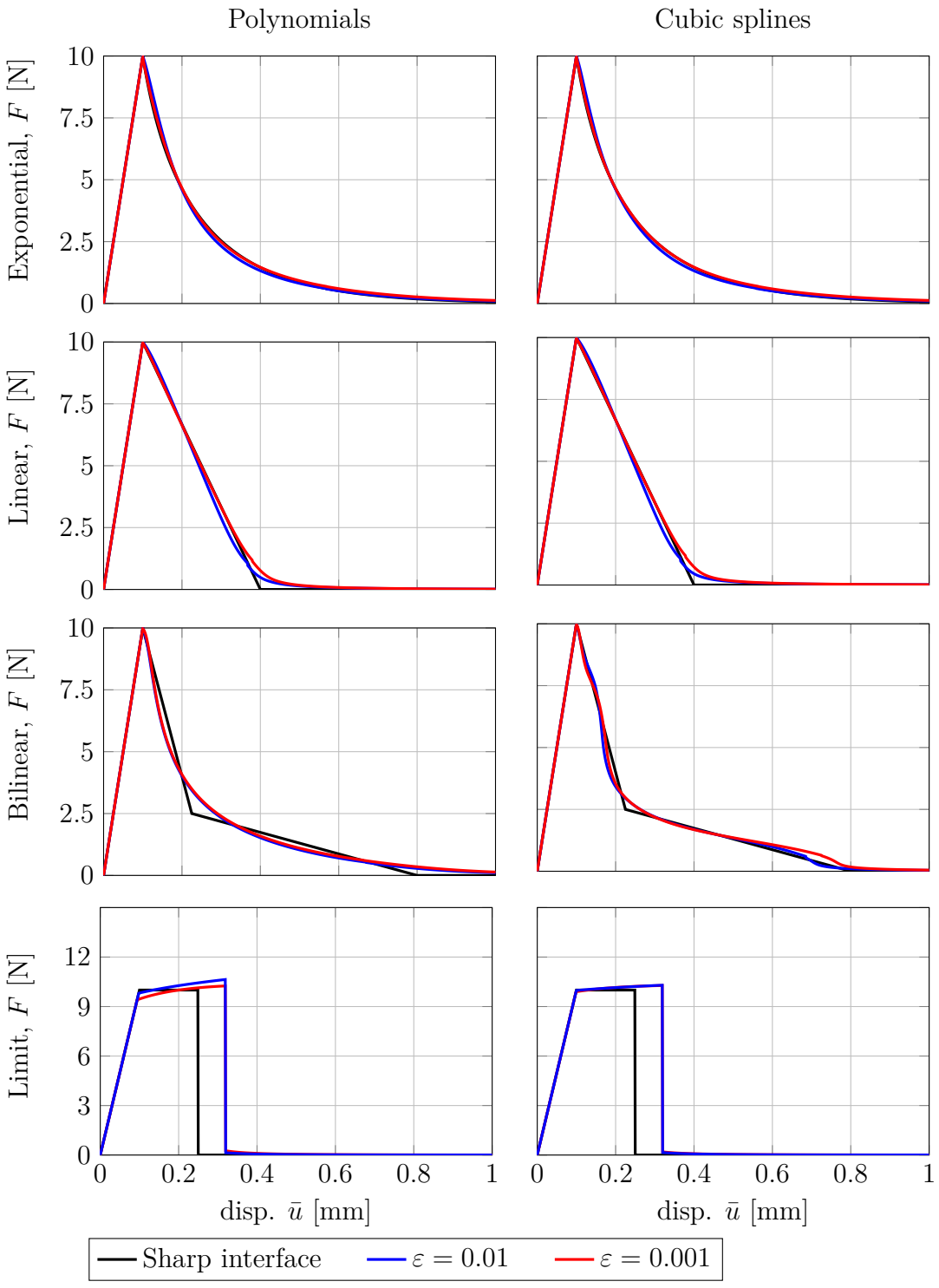

Figure 6.2: "1D finite element analysis of a truss subjected to tension: force-displacement diagrams obtained from the phase-field model for different degradation functions. The underlying sharp interface solution is also shown for the sake of comparison." ([79, Sec. 4.1∗]). The underlying sharp interface solution is also shown for the sake of comparison. The artificial parameter c^* is obtained via Equation (4.105).

Figure 6.1 presents the ratios c^*/E for varying phase field length ε. Degradation functions following from the polynomial approach for the four presented traction-separation laws (exponential, linear, bilinear, limit) are assumed here with $n_{\boldsymbol{a}} = 6$ free parameters. The material parameters utilized are taken from the finite element examples below and are summarized in Table 6.3. They coincide with the parameters applied in Section 4.7.3.1. Clearly, the artificial parameter c^* is converging to E for all considered approaches. However, for larger phase field length of about $\varepsilon = 0.01$ mm, such as used in Section 4.7.3.1, larger deviations are visible.

Material parameter				Geometry parameter	
E	σ_{c}	γ	c^*	l	A
100 MPa	10 MPa	2 N/mm	varying	1 mm	1 mm^2

Table 6.3: 1D finite element analysis of a truss subjected to tension: Material parameters and geometry

In the following, finite element simulations from Section 4.7.3.1 of a truss under tension are reevaluated with the newly introduced derivation of c^*. Figure 6.2 presents the structural results in form of force-displacement diagrams for all investigated traction-separation-laws and approximation spaces. The material parameters are summarized in Table 6.3.

The approximation of the maximum force, i.e. the material's strength, is superior compared to the approach for $\varepsilon \to 0$ (see Section 4.7.3.1). In fact only deviations of less than 1 % in the maximum force compared to the sharp interface reference solution are present. Only the limit law shows higher deviations but sill presents a superior fit compared to the results from Section 4.7.3.1.

6.8 CT-Specimen — Notched plate under tension — Phase field distributions

In this appendix, the distributions of the phase field corresponding to the results presented on Section 4.7.4 are summarized. As expected, the crack evolves in a horizontal path from the notch to the right edge for all investigated cases.

The responses for all considered traction-separation laws behave similarly for the polynomial and the spline based ansatz space as well as for the linear and the non-linear geometrical setting. However, a difference in the evolution of the crack can be seen when comparing the different traction separation laws. For instance, it evolves slower in the case of the linear traction-separation law.

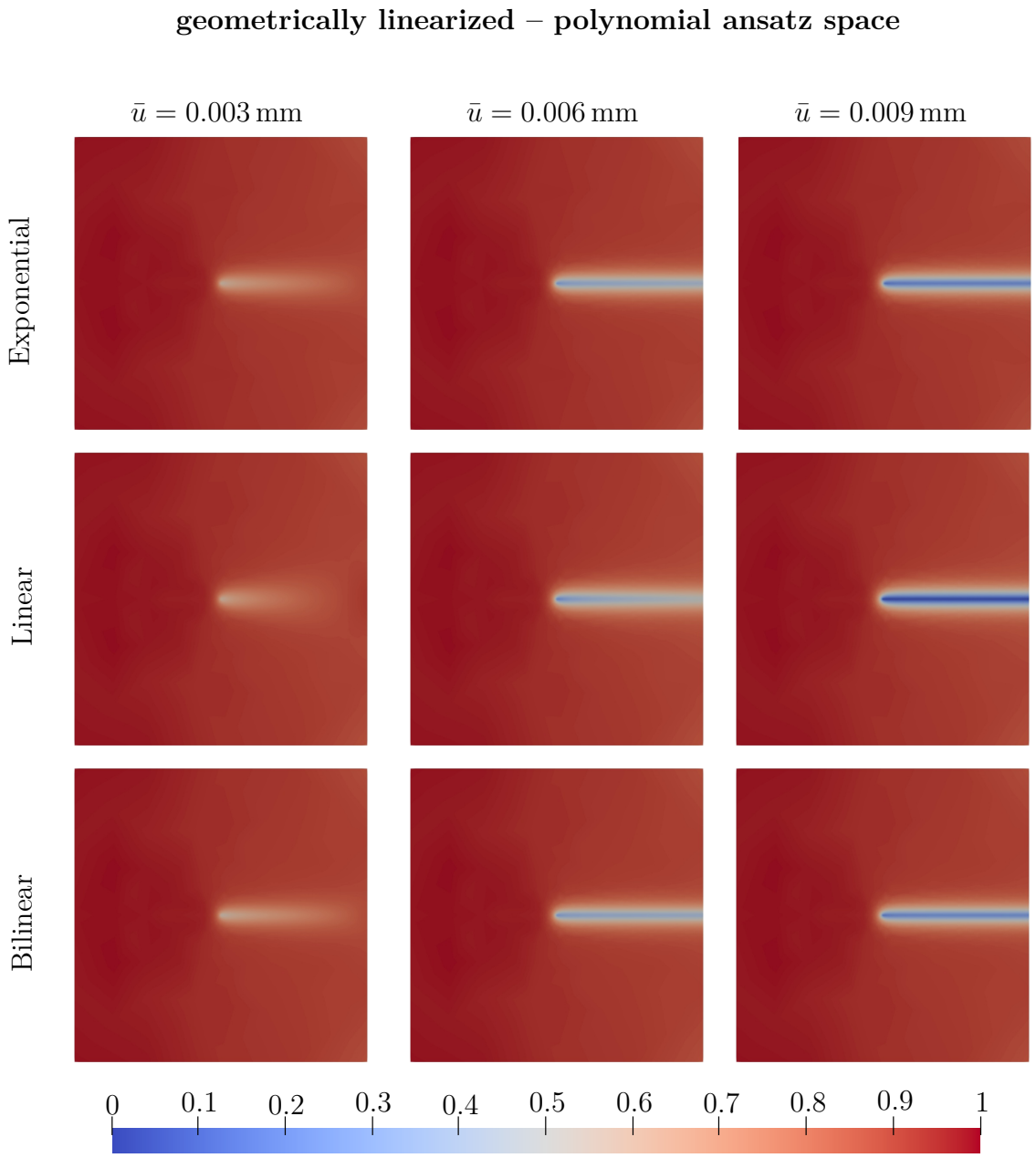

Figure 6.3: CT-specimen – Notched Plate under tension: Phase field distribution for loadings $\bar{u} = 0.003/0.006/0.009\,\mathrm{mm}$ for all traction-separation laws in a geometrically linearized setting. The polynomial based approximation of degradation functions is used with $n_{\boldsymbol{a}} = 6$ free parameters.

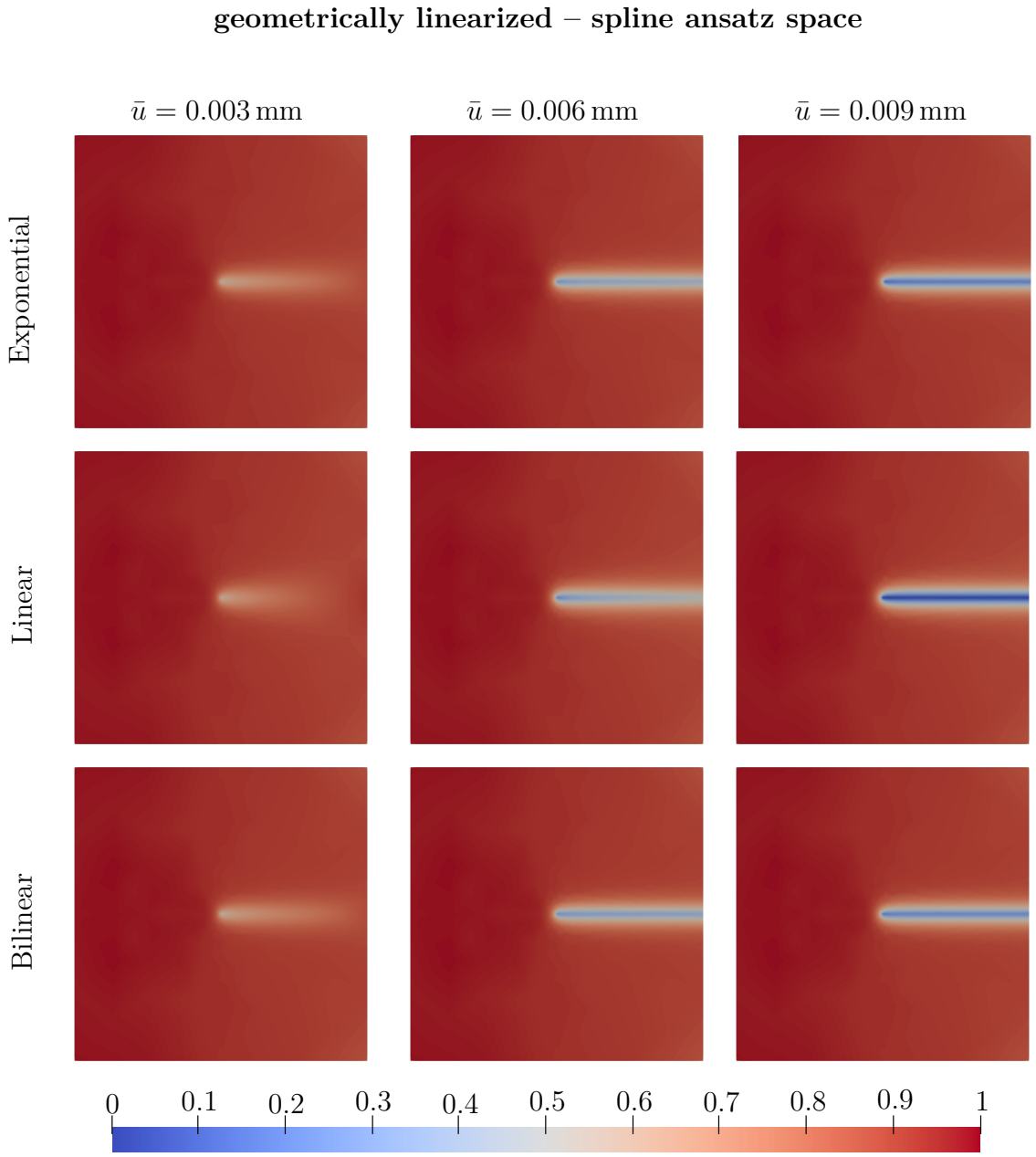

Figure 6.4: CT-specimen – Notched Plate under tension: Phase field distribution for loadings $\bar{u} = 0.003/0.006/0.009\,\mathrm{mm}$ for all traction-separation laws in a geometrically linearized setting. The spline based approximation of degradation functions is used with $n_{\boldsymbol{a}} = 6$ free parameters.

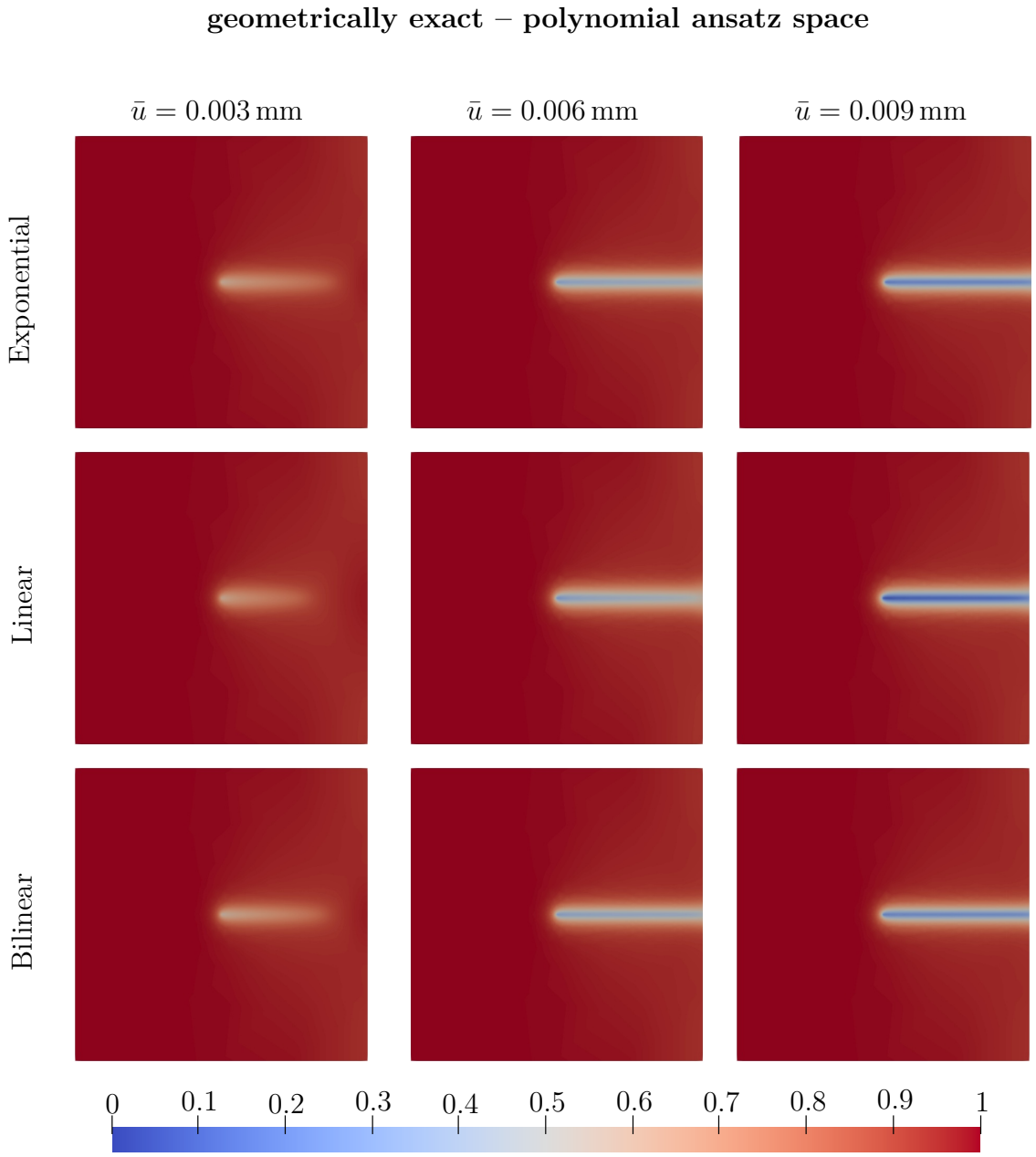

Figure 6.5: CT-specimen – Notched Plate under tension: Phase field distribution for loadings $\bar{u} = 0.003/0.006/0.009\,\mathrm{mm}$ for all traction-separation laws in a geometrically exact setting. The polynomial based approximation of degradation functions is used with $n_{\boldsymbol{a}} = 6$ free parameters.

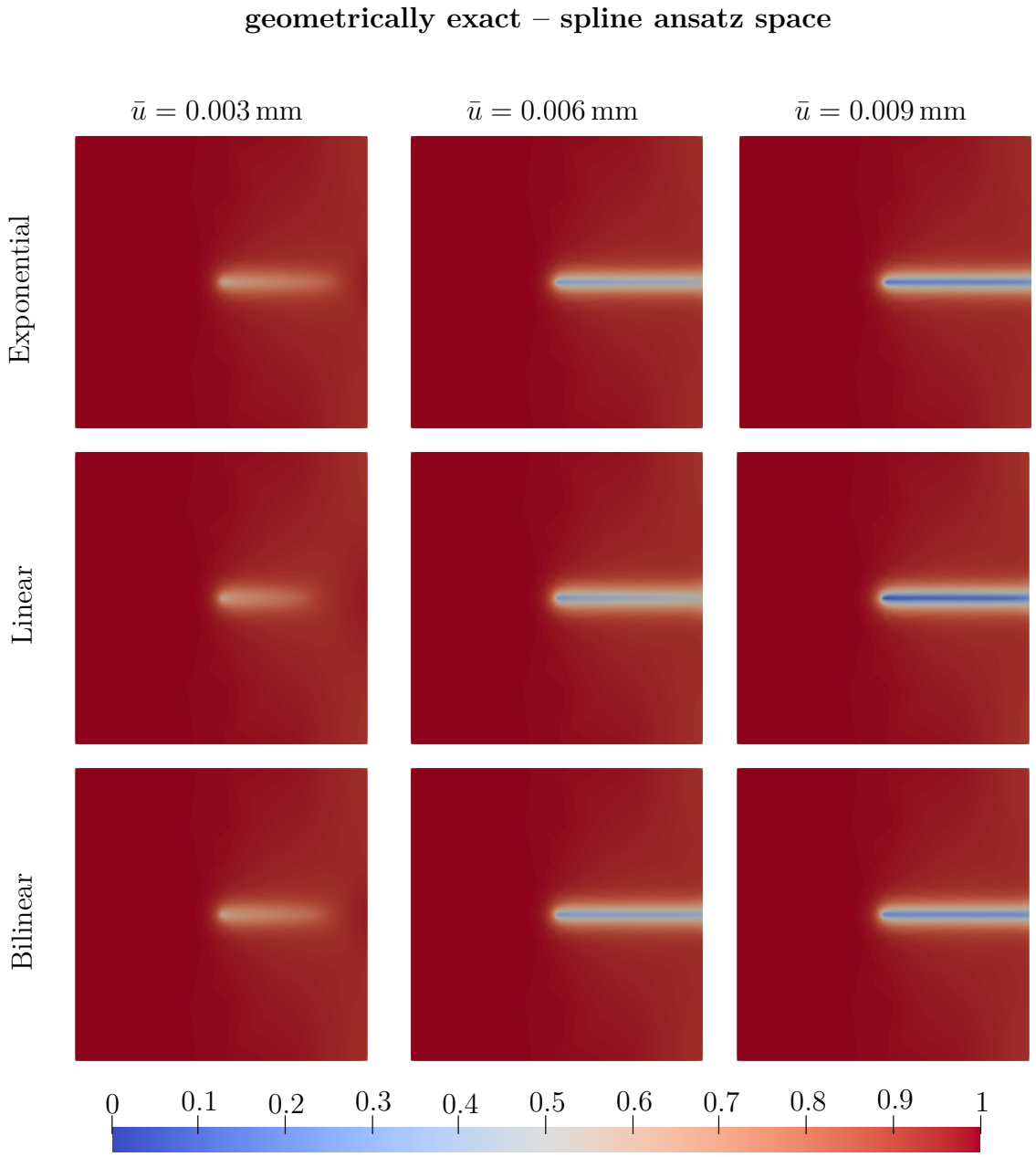

Figure 6.6: CT-specimen – Notched Plate under tension: Phase field distribution for loadings $\bar{u} = 0.003/0.006/0.009\,\mathrm{mm}$ for all traction-separation laws in a geometrically exact setting. The spline based approximation of degradation functions is used with $n_{\boldsymbol{a}} = 6$ free parameters.

Bibliography

[1] B. Akbari and R. Bagheri. Deformation mechanism of epoxy/clay nanocomposite. *European Polymer Journal*, 43(3):782–788, 2007. ISSN 0014-3057. doi:10.1016/j.eurpolymj.2006.11.028.

[2] G. Alfano and M. Crisfield. Finite element interface models for the delamination analysis of laminated composites: mechanical and computational issues. *International Journal for Numerical Methods in Engineering*, 50(7):1701–1736, 2001. doi:10.1002/nme.93.

[3] O. Allix, P. Ladevéze, and A. Corigliano. Damage analysis of interlaminar fracture specimens. *Composite Structures*, 31(1):61–74, 1995. ISSN 0263-8223. doi:10.1016/0263-8223(95)00002-X.

[4] O. Allix and A. Corigliano. Modeling and simulation of crack propagation in mixed-modes interlaminar fracture specimens. *International journal of Fracture*, 77(2):111–140, 1996. doi:10.1007/BF00037233.

[5] M. Ambati, R. Kruse, and L. D. Lorenzis. A phase-field model for ductile fracture at finite strains and its experimental verification. *Comput. Mech.*, 57:149–167, 2016. doi:10.1007/s00466-015-1225-3.

[6] M. Ambati, T. Gerasimov, and L. De Lorenzis. A review on phase-field models of brittle fracture and a new fast hybrid formulation. *Computational Mechanics*, 55: 383–405, 2015. doi:10.1007/s00466-014-1109-y.

[7] L. Ambrosio, N. Fusco, and D. Pallara. *Functions of Bounded Variation and Free Discontinuity Problems*. Mathematical Monographs. Oxford University Press, 2000.

[8] L. Ambrosio and V. M. Tortorelli. Approximation of functional depending on jumps by elliptic functional via Γ-convergence. *Communications on Pure and Applied Mathematics*, 43(8):999–1036, 1990. doi:10.1002/cpa.3160430805.

[9] H. Amor, J.-J. Marigo, and C. Maurini. Regularized formulation of the variational brittle fracture with unilateral contact: Numerical experiments. *Journal of the Mechanics and Physics of Solids*, 57(8):1209–1229, 2009. ISSN 0022-5096. doi:10.1016/j.jmps.2009.04.011.

[10] J. Ast, M. Ghidelli, K. Durst, M. Göken, M. Sebastiani, and A. Korsunsky. A review of experimental approaches to fracture toughness evaluation at the micro-scale. *Materials & Design*, 173:107762, 2019. ISSN 0264-1275.

doi:10.1016/j.matdes.2019.107762.

[11] B. K. Atkinson. Introduction to fracture mechanics and its geophysical applications. *Fracture mechanics of rock*, pages 1–26, 1987.

[12] S. Aubry, M. Fago, and M. Ortiz. A constrained sequential-lamination algorithm for the simulation of sub-grid microstructure in martensitic materials. *Computer Methods in Applied Mechanics and Engineering*, 192(26):2823–2843, 2003. ISSN 0045-7825. doi:10.1016/S0045-7825(03)00260-3.

[13] I. Babuška, U. Banerjee, and J. E. Osborn. Generalized finite element methods - main ideas, results and perspective. *International Journal of Computational Methods*, 01(01):67–103, 2004. doi:10.1142/S0219876204000083.

[14] D. P. Bach, D. Brancherie, and L. Cauvin. Size effect in nanocomposites: Xfem/level set approach and interface element approach. *Finite Elements in Analysis and Design*, 165:41–51, 2019. ISSN 0168-874X. doi:10.1016/j.finel.2019.07.005.

[15] G. Barenblatt. The mathematical theory of equilibrium cracks in brittle fracture. 7:55–129, 1962. ISSN 0065-2156. doi:10.1016/S0065-2156(08)70121-2.

[16] G. I. Barenblatt. The formation of equilibrium cracks during brittle fracture. general ideas and hypotheses. axially-symmetric cracks. *Journal of applied mathematics and mechanics*, 23(3):622–636, 1959.

[17] T. Belytschko and T. Black. Elastic crack growth in finite elements with minimal remeshing. *International Journal for Numerical Methods in Engineering*, 45(5): 601–620, 1999.

[18] J. Bernoulli. Problema novum ad cujus solutionem mathematici invitantur. *Acta Eruditorum*, 15:264–269, 1696.

[19] R. Bharali, F. Larsson, and R. Jänicke. Phase-field fracture irreversibility using the slack variable approach. 2022.

[20] M. A. Biot. *Mechanics of incremental deformations*. 1965.

[21] M. Bonacini, S. Conti, and F. Iurlano. Cohesive fracture in 1d: Quasi-static evolution and derivation from static phase-field models. *Archive for Rational Mechanics and Analysis*, 239:1501–1576, 2021. doi:10.1007/s00205-020-01597-1.

[22] B. Bourdin, G. Francfort, and J.-J. Marigo. Numerical experiments in revisited brittle fracture. *Journal of the Mechanics and Physics of Solids*, 48(4):797–826, 2000. ISSN 0022-5096. doi:10.1016/S0022-5096(99)00028-9.

[23] B. Bourdin. Numerical implementation of the variational formulation for quasi-static brittle fracture. *Interfaces Free Bound.*, 9(3):411–430, 2007. doi:10.4171/ifb/171.

[24] R. M. Bowen and C.-C. Wang. *Introduction to vectors and tensors*, volume 2. Courier Corporation, 2008.

[25] A. Braides. *Gamma-convergence for Beginners*, volume 22. Clarendon Press, 2002.

[26] M. J. Buehler and A. Misra. Mechanical behavior of nanocomposites. *MRS Bulletin*, 44(1):19–24, 2019. doi:10.1557/mrs.2018.323.

[27] C. Carstensen, K. Hackl, and A. Mielke. Non-convex potentials and microstructures in finite-strain plasticity. *Proceedings of the Royal Society of London. Series A: Mathematical, Physical and Engineering Sciences*, 458(2018):299–317, 2002. doi:10.1098/rspa.2001.0864.

[28] K. W. Cassel. *Variational methods with applications in science and engineering*. Cambridge University Press, 2013.

[29] A. Chambolle, S. Conti, and G. A. Francfort. Approximation of a brittle fracture energy with a constraint of non-interpenetration. *Archive for Rational Mechanics and Analysis*, 228:867–889, 2018. doi:10.1007/s00205-017-1207-z.

[30] N. Chandra, H. Li, C. Shet, and H. Ghonem. Some issues in the application of cohesive zone models for metal-ceramic interfaces. *International Journal of Solids and Structures*, 39(10):2827–2855, 2002. ISSN 0020-7683. doi:10.1016/S0020-7683(02)00149-X.

[31] T. Chen, G. J. Dvorak, and C. Yu. Size-dependent elastic properties of unidirectional nano-composites with interface stresses. *Acta Mechanica*, 188(1):39–54, 2007. ISSN 1619-6937. doi:10.1007/s00707-006-0371-2.

[32] P. G. Ciarlet. An introduction to differential geometry with applications to elasticity. *Journal of elasticity*, 78(1-3):1–215, 2005. doi:10.1007/s10659-005-4738-8.

[33] B. D. Coleman and W. Noll. On the thermostatics of continuous media. *Arch. Rational Mech. Anal.*, 4:97–128, 1959.

[34] C. Comi and U. Perego. A unified approach for variationally consistent finite elements in elastoplasticity. *Computer Methods in Applied Mechanics and Engineering*, 121(1):323–344, 1995. ISSN 0045-7825. doi:10.1016/0045-7825(94)00703-P.

[35] S. Conti, M. Focardi, and F. Iurlano. Phase field approximation of cohesive fracture models. *Annales de l'Institut Henri Poincaré C, Analyse non linéaire*, 33(4):1033 – 1067, 2016. ISSN 0294-1449. doi:10.1016/j.anihpc.2015.02.001.

[36] S. Conti, M. Focardi, and F. Iurlano. Phase-field approximation of a vectorial, geometrically nonlinear cohesive fracture energy. *arXiv Preprint arXiv:2205.06541*, 2022.

[37] S. Conti, M. Focardi, and F. Iurlano. Phase-field approximation of a vectorial, geometrically nonlinear cohesive fracture energy. *Archive for Rational Mechanics and Analysis*, 248(2):21, 2024. doi:10.1007/s00205-024-01962-4.

[38] R. de Borst and C. V. Verhoosel. Gradient damage vs phase-field approaches for fracture: Similarities and differences. *Computer Methods in Applied Mechanics and Engineering*, 312:78–94, 2016. ISSN 0045-7825. doi:10.1016/j.cma.2016.05.015.

Phase Field Approaches to Fracture.

[39] L. De Lorenzis and C. Maurini. Nucleation under multi-axial loading in variational phase-field models of brittle fracture. *International Journal of Fracture*, pages 1573–2673, 2021. doi:10.1007/s10704-021-00555-6.

[40] E. De Luycker, D. J. Benson, T. Belytschko, Y. Bazilevs, and M. C. Hsu. X-FEM in isogeometric analysis for linear fracture mechanics. *International Journal for Numerical Methods in Engineering*, 87(6):541–565, 2011. doi:10.1002/nme.3121.

[41] G. Del Piero and D. R. Owen. Structured deformations of continua. *Archive for Rational Mechanics and Analysis*, 124:99–99, 1993. doi:http://repository.cmu.edu/math/417.

[42] R. Dimitri, M. Trullo, L. De Lorenzis, and G. Zavarise. Coupled cohesive zone models for mixed-mode fracture: A comparative study. *Engineering Fracture Mechanics*, 148:145–179, 2015. ISSN 0013-7944. doi:10.1016/j.engfracmech.2015.09.029.

[43] N. Dourado, S. Morel, M. de Moura, G. Valentin, and J. Morais. Comparison of fracture properties of two wood species through cohesive crack simulations. *Composites Part A: Applied Science and Manufacturing*, 39(2):415–427, 2008. ISSN 1359-835X. doi:10.1016/j.compositesa.2007.08.025.

[44] T. Doyle and J. Ericksen. *Nonlinear Elasticity.* Advances in Applied Mechanics. Academic Press, 1956.

[45] H. Duan, J. Wang, and B. Karihaloo. Theory of elasticity at the nanoscale. volume 42 of *Advances in Applied Mechanics*, pages 1–68. Elsevier, 2009. doi:10.1016/S0065-2156(08)00001-X.

[46] D. Dugdale. Yielding of steel sheets containing slits. *Journal of the Mechanics and Physics of Solids*, 8(2):100–104, 1960. ISSN 0022-5096. doi:10.1016/0022-5096(60)90013-2.

[47] Éamonn Ó Máirtín, G. Parry, G. E. Beltz, and J. P. McGarry. Potential-based and non-potential-based cohesive zone formulations under mixed-mode separation and over-closure - part ii: Finite element applications. *Journal of the Mechanics and Physics of Solids*, 63:363–385, 2014. ISSN 0022-5096. doi:10.1016/j.jmps.2013.08.019.

[48] M. Ekh, A. Menzel, K. Runesson, and P. Steinmann. Anisotropic damage with the mcr effect coupled to plasticity. *International Journal of Engineering Science*, 41 (13):1535–1551, 2003. ISSN 0020-7225. doi:10.1016/S0020-7225(03)00032-6. Damage and failure analysis of materials.

[49] European Space Agency. *Sentinel-2 captures Antarctica's new iceberg*, 2023. `https://www.esa.int/ESA_Multimedia/Images/2023/01/Sentinel-2_captures_Antarctica_s_new_iceberg` [Accessed: 14.08.2024], © ESA Standard Licence.

[50] F. Fathi and R. de Borst. Geometrically nonlinear extended isogeometric analysis for cohesive fracture with applications to delamination in composites. *Finite Elements in Analysis and Design*, 191:103527, 2021. ISSN 0168-874X. doi:10.1016/j.finel.2021.103527.

[51] F. Fathi, L. Chen, and R. de Borst. Extended isogeometric analysis for cohesive fracture. *International Journal for Numerical Methods in Engineering*, 121(20): 4584–4613, 2020. doi:10.1002/nme.6453.

[52] Y. Feng and J. Li. A unified regularized variational cohesive fracture theory with directional energy decomposition. *International Journal of Engineering Science*, 182:103773, 2023. ISSN 0020-7225. doi:10.1016/j.ijengsci.2022.103773.

[53] Y. Feng, J. Fan, and J. Li. Endowing explicit cohesive laws to the phase-field fracture theory. *Journal of the Mechanics and Physics of Solids*, 152:104464, 2021. ISSN 0022-5096. doi:10.1016/j.jmps.2021.104464.

[54] G. Francfort and J.-J. Marigo. Revisiting brittle fracture as an energy minimization problem. *Journal of the Mechanics and Physics of Solids*, 46(8):1319–1342, 1998. ISSN 0022-5096. doi:10.1016/S0022-5096(98)00034-9.

[55] F. Freddi and F. Iurlano. Numerical insight of a variational smeared approach to cohesive fracture. *Journal of the Mechanics and Physics of Solids*, 98:156 – 171, 2017. ISSN 0022-5096. doi:10.1016/j.jmps.2016.09.003.

[56] F. Freddi and G. Royer-Carfagni. Regularized variational theories of fracture: A unified approach. *Journal of the Mechanics and Physics of Solids*, 58(8):1154–1174, 2010. ISSN 0022-5096. doi:10.1016/j.jmps.2010.02.010.

[57] T.-P. Fries and T. Belytschko. The extended/generalized finite element method: An overview of the method and its applications. *International Journal for Numerical Methods in Engineering*, 84(3):253–304, 2010. doi:10.1002/nme.2914.

[58] X. Gao, Z. Huang, J. Qu, and D. Fang. A curvature-dependent interfacial energy-based interface stress theory and its applications to nano-structured materials: (i) general theory. *Journal of the Mechanics and Physics of Solids*, 66:59–77, 2014. ISSN 0022-5096. doi:10.1016/j.jmps.2014.01.010.

[59] X. Gao, Z. Huang, and D. Fang. Curvature-dependent interfacial energy and its effects on the elastic properties of nanomaterials. *International Journal of Solids and Structures*, 113-114:100–107, 2017. ISSN 0020-7683. doi:10.1016/j.ijsolstr.2017.01.021.

[60] T. C. Gasser and G. A. Holzapfel. Geometrically non-linear and consistently linearized embedded strong discontinuity models for 3d problems with an application to the dissection analysis of soft biological tissues. *Computer Methods in Applied Mechanics and Engineering*, 192(47):5059–5098, 2003. ISSN 0045-7825. doi:10.1016/j.cma.2003.06.001.

[61] F. Gómez, M. Elices, and J. Planas. The cohesive crack concept: application to PMMA at -60° C. *Engineering Fracture Mechanics*, 72(8):1268–1285, 2005. ISSN 0013-7944. doi:10.1016/j.engfracmech.2004.09.005.

[62] A. Greer, Y. Cheng, and E. Ma. Shear bands in metallic glasses. *Materials Science and Engineering: R: Reports*, 74(4):71–132, 2013. ISSN 0927-796X. doi:10.1016/j.mser.2013.04.001.

[63] A. A. Griffith. Vi. the phenomena of rupture and flow in solids. *Philosophical transactions of the royal society of london. Series A, containing papers of a mathematical or physical character*, 221(582-593):163–198, 1921. doi:10.1098/rsta.1921.0006.

[64] M. E. Gurtin and A. Ian Murdoch. A continuum theory of elastic material surfaces. *Archive for rational mechanics and analysis*, 57:291–323, 1975. doi:10.1007/BF00261375.

[65] M. E. Gurtin and A. I. Murdoch. Addenda to our paper a continuum theory of elastic material surfaces. *Archive for Rational Mechanics and Analysis*, 59:389–390, 1975. doi:10.1007/BF00250426.

[66] T. Heitbreder, N. S. Ottosen, M. Ristinmaa, and J. Mosler. Consistent elastoplastic cohesive zone model at finite deformations - variational formulation. *International Journal of Solids and Structures*, 106-107:284–293, 2017. ISSN 0020-7683. doi:10.1016/j.ijsolstr.2016.10.027.

[67] T. Heitbreder, N. S. Ottosen, M. Ristinmaa, and J. Mosler. On damage modeling of material interfaces: Numerical implementation and computational homogenization. *Computer Methods in Applied Mechanics and Engineering*, 337:1–27, 2018. ISSN 0045-7825. doi:10.1016/j.cma.2018.03.023.

[68] T. Heitbreder, P. Kurzeja, and J. Mosler. On general imperfect interfaces with spatially non-constant displacement jumps. *International Journal of Solids and Structures*, 232:111068, 2021. ISSN 0020-7683. doi:10.1016/j.ijsolstr.2021.111068.

[69] R. Hill. On constitutive inequalities for simple materials - i. *Journal of the Mechanics and Physics of Solids*, 16(4):229–242, 1968. ISSN 0022-5096. doi:10.1016/0022-5096(68)90031-8.

[70] A. Hillerborg, M. Modéer, and P.-E. Petersson. Analysis of crack formation and crack growth in concrete by means of fracture mechanics and finite elements. *Cement and Concrete Research*, 6(6):773–781, 1976. ISSN 0008-8846. doi:10.1016/0008-8846(76)90007-7.

[71] F. Hirsch and M. Kästner. Microscale simulation of adhesive and cohesive failure in rough interfaces. *Engineering Fracture Mechanics*, 178:416–432, 2017. ISSN 0013-7944. doi:10.1016/j.engfracmech.2017.02.026.

[72] J. P. Hirth. The influence of grain boundaries on mechanical properties. 1972. doi:10.1007/BF02661312.

[73] M. Homayonifar and J. Mosler. Efficient modeling of microstructure evolution in magnesium by energy minimization. *International Journal of Plasticity*, 28(1): 1–20, 2012. ISSN 0749-6419. doi:10.1016/j.ijplas.2011.05.011.

[74] A. Javili, G. Chatzigeorgiou, A. T. McBride, P. Steinmann, and C. Linder. Computational homogenization of nano-materials accounting for size effects via surface elasticity. *GAMM-Mitteilungen*, 38(2):285–312, 2015. doi:10.1002/gamm.201510016.

[75] A. Javili, P. Steinmann, and J. Mosler. Micro-to-macro transition accounting for general imperfect interfaces. *Computer Methods in Applied Mechanics and Engineering*, 317:274–317, 2017. ISSN 0045-7825. doi:10.1016/j.cma.2016.12.025.

[76] A. Javili, N. S. Ottosen, M. Ristinmaa, and J. Mosler. Aspects of interface elasticity theory. *Mathematics and Mechanics of Solids*, 23(7):1004–1024, 2018. doi:10.1177/1081286517699041.

[77] G. C. Kais Ammar, Benoît Appolaire and S. Forest. Combining phase field approach and homogenization methods for modelling phase transformation in elastoplastic media. *European Journal of Computational Mechanics*, 18(5-6):485–523, 2009. doi:10.3166/ejcm.18.485-523.

[78] E. Kreyszig. *Differential geometry*. Courier Corporation, 2013.

[79] H. Lammen, S. Conti, and J. Mosler. Approximating arbitrary traction-separation-laws by means of phase-field theory – mathematical foundation and numerical implementation. *Journal of the Mechanics and Physics of Solids*, 197:106038, 2025. ISSN 0022-5096. doi:https://doi.org/10.1016/j.jmps.2025.106038.

[80] H. Lammen and J. Mosler. On the approximation of surface elasticity theory by means of phase-field theory. *PAMM*, 19(1):e201900375, 2019. doi:10.1002/pamm.201900375.

[81] H. Lammen, S. Conti, and J. Mosler. A finite deformation phase field model suitable for cohesive fracture. *Journal of the Mechanics and Physics of Solids*, 178:105349, 2023. ISSN 0022-5096. doi:10.1016/j.jmps.2023.105349.

[82] O. Lampron, D. Therriault, and M. Lévesque. An efficient and robust monolithic approach to phase-field quasi-static brittle fracture using a modified newton method. *Computer Methods in Applied Mechanics and Engineering*, 386:114091, 2021. ISSN 0045-7825. doi:10.1016/j.cma.2021.114091.

[83] G. Lancioni and G. Royer-Carfagni. The variational approach to fracture mechanics. a practical application to the french panthéon in paris. *Journal of elasticity*, 95:1–30, 2009. doi:10.1007/s10659-009-9189-1.

[84] C. Lanczos. *The variational principles of mechanics*. Courier Corporation, 2012.

[85] B. Lawn. *Fracture of Brittle Solids*. Cambridge Solid State Science Series. Cambridge University Press, 2 edition, 1993. doi:10.1017/cbo9780511623127.

[86] V. I. Levitas. Phase field approach to martensitic phase transformations with large strains and interface stresses. *Journal of the Mechanics and Physics of Solids*, 70: 154–189, 2014. ISSN 0022-5096. doi:10.1016/j.jmps.2014.05.013.

[87] T. Li, J.-J. Marigo, D. Guilbaud, and S. Potapov. Gradient damage modeling of brittle fracture in an explicit dynamics context. *International Journal for Numerical Methods in Engineering*, 108(11):1381–1405, 2016. doi:10.1002/nme.5262.

[88] Z. Li, Y. Shen, F. Han, and Z. Yang. A phase field method for plane-stress fracture problems with tension-compression asymmetry. *Engineering Fracture Mechanics*, 257:107995, 2021. ISSN 0013-7944. doi:10.1016/j.engfracmech.2021.107995.

[89] I.-S. Liu et al. *Continuum mechanics*, volume 5. Springer, 2002.

[90] E. Lorentz and V. Godard. Gradient damage models: Toward full-scale computations. *Computer Methods in Applied Mechanics and Engineering*, 200(21): 1927–1944, 2011. ISSN 0045-7825. doi:10.1016/j.cma.2010.06.025.

[91] E. Lorentz, S. Cuvilliez, and K. Kazymyrenko. Modelling large crack propagation: from gradient damage to cohesive zone models. *International Journal of Fracture*, 178:85–95, 2012. ISSN 1573-2673. doi:10.1007/s10704-012-9746-7.

[92] H. Luo, X. Zhou, C. Ellingford, Y. Zhang, S. Chen, K. Zhou, D. Zhang, C. R. Bowen, and C. Wan. Interface design for high energy density polymer nanocomposites. *Chem. Soc. Rev.*, 48:4424–4465, 2019. doi:10.1039/C9CS00043G.

[93] A. Marengo, A. Patton, M. Negri, U. Perego, and A. Reali. A rigorous and efficient explicit algorithm for irreversibility enforcement in phase-field finite element modeling of brittle crack propagation. *Computer Methods in Applied Mechanics and Engineering*, 387:114137, 2021. ISSN 0045-7825. doi:https://doi.org/10.1016/j.cma.2021.114137.

[94] J.-J. Marigo, C. Maurini, and K. Pham. An overview of the modelling of fracture by gradient damage models. *Meccanica*, 51:3107–3128, 2016. doi:10.1007/s11012-016-0538-4.

[95] J. P. McGarry, Éamonn Ó Máirtín, G. Parry, and G. E. Beltz. Potential-based and non-potential-based cohesive zone formulations under mixed-mode separation and over-closure. part i: Theoretical analysis. *Journal of the Mechanics and Physics of Solids*, 63:336–362, 2014. ISSN 0022-5096. doi:10.1016/j.jmps.2013.08.020.

[96] A. Menzel, M. Ekh, P. Steinmann, and K. Runesson. Anisotropic damage coupled to plasticity: Modelling based on the effective configuration concept. *International Journal for Numerical Methods in Engineering*, 54(10):1409–1430, 2002. doi:10.1002/nme.470.

[97] J. Mergheim and P. Steinmann. A geometrically nonlinear fe approach for the simulation of strong and weak discontinuities. *Computer Methods in Applied Mechanics and Engineering*, 195(37):5037–5052, 2006. ISSN 0045-7825. doi:10.1016/j.cma.2005.05.057. John H. Argyris Memorial Issue. Part I.

[98] C. Mi and D. Kouris. Nanoparticles under the influence of surface/interface elasticity. *Journal of Mechanics of Materials and Structures*, 1(4):763–791, 2006.

[99] Y. Mi, M. Crisfield, H. Hellweg, G. Davies, and J. Owen. Finite element method and progressive failure modelling of composite structures. *Computational plasticity: Fundamentals and Applications. Part*, 1:239–254, 1997.

[100] Y. Mi, M. A. Crisfield, G. A. O. Davies, and H. B. Hellweg. Progressive delamination using interface elements. *Journal of Composite Materials*, 32(14):1246–1272, 1998. doi:10.1177/002199839803201401.

[101] C. Miehe, F. Welschinger, and M. Hofacker. Thermodynamically consistent phase-field models of fracture: Variational principles and multi-field fe implementations. *International Journal for Numerical Methods in Engineering*, 83(10):1273–1311, 2010. doi:10.1002/nme.2861.

[102] C. Miehe and M. Lambrecht. Algorithms for computation of stresses and elasticity moduli in terms of seth hill's family of generalized strain tensors. *Communications in Numerical Methods in Engineering*, 17(5):337–353, 2001. doi:10.1002/cnm.404.

[103] C. Miehe and M. Lambrecht. A two-scale finite element relaxation analysis of shear bands in non-convex inelastic solids: small-strain theory for standard dissipative materials. *Computer Methods in Applied Mechanics and Engineering*, 192(5):473–508, 2003. ISSN 0045-7825. doi:10.1016/S0045-7825(02)00547-9.

[104] C. Miehe, M. Hofacker, and F. Welschinger. A phase field model for rate-independent crack propagation: Robust algorithmic implementation based on operator splits. *Computer Methods in Applied Mechanics and Engineering*, 199(45): 2765–2778, 2010. ISSN 0045-7825. doi:10.1016/j.cma.2010.04.011.

[105] R. E. Miller and V. B. Shenoy. Size-dependent elastic properties of nanosized structural elements. *Nanotechnology*, 11(3):139, 2000.

[106] N. Moelans, B. Blanpain, and P. Wollants. Quantitative analysis of grain boundary properties in a generalized phase field model for grain growth in anisotropic systems. *Phys. Rev. B*, 78:024113, Jul 2008. doi:10.1103/PhysRevB.78.024113.

[107] N. Moës, J. Dolbow, and T. Belytschko. A finite element method for crack growth without remeshing. *International Journal for Numerical Methods in Engineering*, 46(1):131–150, 1999.

[108] J. Mosler and I. Scheider. A thermodynamically and variationally consistent class of damage-type cohesive models. *Journal of the Mechanics and Physics of Solids*, 59(8):1647–1668, 2011. ISSN 0022-5096. doi:10.1016/j.jmps.2011.04.012.

[109] J. Mosler, O. Shchyglo, and H. M. Hojjat. A novel homogenization method for phase field approaches based on partial rank-one relaxation. *Journal of the Mechanics and Physics of Solids*, 68:251–266, 2014. ISSN 0022-5096. doi:10.1016/j.jmps.2014.04.002.

[110] W. Müller and S. Schmauder. Interface stresses in fiber-reinforced materials with regular fiber arrangements. *Composite Structures*, 24(1):1–21, 1993. ISSN 0263-8223. doi:10.1016/0263-8223(93)90050-Z.

[111] A. I. Murdoch. A Thermodynamical Theory of Elastic Material Interfaces. *The Quarterly Journal of Mechanics and Applied Mathematics*, 29(3):245–275, 08 1976. ISSN 0033-5614. doi:10.1093/qjmam/29.3.245.

[112] M. Musto and G. Alfano. A novel rate-dependent cohesive-zone model combining damage and visco-elasticity. *Computers & Structures*, 118:126–133, 2013. ISSN 0045-7949. doi:10.1016/j.compstruc.2012.12.020. Special Issue: UK Association for Computational Mechanics in Engineering.

[113] L. Nazarenko, S. Bargmann, and H. Stolarski. Influence of interfaces on effective properties of nanomaterials with stochastically distributed spherical inclusions. *International Journal of Solids and Structures*, 51(5):954–966, 2014. ISSN 0020-7683. doi:10.1016/j.ijsolstr.2013.11.024.

[114] A. Needleman. A Continuum Model for Void Nucleation by Inclusion Debonding. *Journal of Applied Mechanics*, 54(3):525–531, 09 1987. ISSN 0021-8936. doi:10.1115/1.3173064.

[115] A. Needleman. An analysis of tensile decohesion along an interface. *Journal of the Mechanics and Physics of Solids*, 38(3):289–324, 1990. ISSN 0022-5096. doi:10.1016/0022-5096(90)90001-K.

[116] A. Niehüser and J. Mosler. Numerically efficient and robust interior-point algorithm for finite strain rate-independent crystal plasticity. *Computer Methods in Applied Mechanics and Engineering*, 416:116392, 2023. ISSN 0045-7825. doi:10.1016/j.cma.2023.116392.

[117] R. W. Ogden and E. Sternberg. Nonlinear elastic deformations. *Journal of Applied Mechanics*, 52(3):740–741, 09 1985. ISSN 0021-8936. doi:10.1115/1.3169137.

[118] M. Ortiz and A. Pandolfi. Finite-deformation irreversible cohesive elements for three-dimensional crack-propagation analysis. *International Journal for Numerical Methods in Engineering*, 44(9):1267–1282, 1999.

[119] M. Ortiz and E. Repetto. Nonconvex energy minimization and dislocation structures in ductile single crystals. *Journal of the Mechanics and Physics of Solids*, 47 (2):397–462, 1999. ISSN 0022-5096. doi:10.1016/S0022-5096(97)00096-3.

[120] N. S. Ottosen, M. Ristinmaa, and J. Mosler. Framework for non-coherent interface models at finite displacement jumps and finite strains. *Journal of the Mechanics and Physics of Solids*, 90:124–141, 2016. ISSN 0022-5096. doi:10.1016/j.jmps.2016.02.034.

[121] K. Park and G. Paulino. Cohesive zone models: A critical review of traction-separation relationships across fracture surfaces. *Applied Mechanics Reviews*, 64: 1002–, 11 2011. doi:10.1115/1.4023110.

[122] K. Park, G. H. Paulino, and J. R. Roesler. A unified potential-based cohesive model of mixed-mode fracture. *Journal of the Mechanics and Physics of Solids*, 57(6):891–908, 2009. ISSN 0022-5096. doi:10.1016/j.jmps.2008.10.003.

[123] K. Park, G. H. Paulino, and J. R. Roesler. A unified potential-based cohesive model of mixed-mode fracture. *Journal of the Mechanics and Physics of Solids*, 57(6):891–908, 2009. ISSN 0022-5096. doi:10.1016/j.jmps.2008.10.003.

[124] R. H. J. Peerlings, R. de Borst, W. A. M. Brekelmans, and M. G. D. Geers. Gradient-enhanced damage modelling of concrete fracture. *Mechanics of Cohesive-frictional Materials*, 3(4):323–342, 1998.

[125] H. Petryk. A consistent energy approach to defining stability of plastic deformation processes. 1982.

[126] D. PITSA and M. G. DANIKAS. Interfaces features in polymer nanocomposites: A review of proposed models. *Nano*, 06(06):497–508, 2011. doi:10.1142/S1793292011002949.

[127] Y. Qiao and M. Salviato. Strength and cohesive behavior of thermoset polymers at the microscale: A size-effect study. *Engineering Fracture Mechanics*, 213:100–117, 2019. ISSN 0013-7944. doi:10.1016/j.engfracmech.2019.03.033.

[128] D. Raabe, M. Herbig, S. Sandlöbes, Y. Li, D. Tytko, M. Kuzmina, D. Ponge, and P.-P. Choi. Grain boundary segregation engineering in metallic alloys: A pathway to the design of interfaces. *Current Opinion in Solid State and Materials Science*, 18(4):253–261, 2014. ISSN 1359-0286. doi:10.1016/j.cossms.2014.06.002. Slip Localization and Transfer in Deformation and Fatigue of Polycrystals.

[129] R. Radulovic, O. T. Bruhns, and J. Mosler. Effective 3d failure simulations by combining the advantages of embedded strong discontinuity approaches and classical interface elements. *Engineering Fracture Mechanics*, 78(12):2470–2485, 2011. ISSN 0013-7944. doi:10.1016/j.engfracmech.2011.06.007.

[130] A. Reuß. Berechnung der fließgrenze von mischkristallen auf grund der plastizitätsbedingung für einkristalle . *Zamm-zeitschrift Fur Angewandte Mathematik Und Mechanik*, 9:49–58, 1929.

[131] J. R. Rice et al. Mathematical analysis in the mechanics of fracture. *Fracture: an advanced treatise*, 2:191–311, 1968.

[132] J. B. Rundle, P. B. Rundle, W. Klein, J. De Sa Martins, K. F. Tiampo, A. Donnellan, and L. H. Kellogg. Gem plate boundary simulations for the plate boundary observatory: A program for understanding the physics of earthquakes on complex fault networks via observations, theory and numerical simulation. pages 2357–2381, 2002. doi:10.1007/978-3-0348-8197-5_11.

[133] I. Scheider and W. Brocks. Simulation of cup-cone fracture using the cohesive model. *Engineering Fracture Mechanics*, 70(14):1943–1961, 2003. ISSN 0013-7944. doi:10.1016/S0013-7944(03)00133-4. Cohesive Models.

[134] A. Schlüter, A. Willenbücher, C. Kuhn, and R. Müller. Phase field approximation of dynamic brittle fracture. *Computational Mechanics*, 54(5):1141–1161, 2014. doi:10.1007/s00466-014-1045-x.

[135] P. Sharma, S. Ganti, and N. Bhate. Effect of surfaces on the size-dependent elastic state of nano-inhomogeneities. *Applied Physics Letters*, 82(4):535–537, 2003. doi:10.1063/1.1539929.

[136] M. Silhavy. *The mechanics and thermodynamics of continuous media*. Springer Science & Business Media, 2013.

[137] R. Sondershaus, R. Müller, D. Gross, and A. Humbert. *Phase Field Modeling of Cracks in Ice*, pages 281–304. Springer International Publishing, Cham, 2024. ISBN 978-3-031-45554-4. doi:10.1007/978-3-031-45554-4_11.

[138] D. J. Steigmann and R. Ogden. Plane deformations of elastic solids with intrinsic boundary elasticity. *Proceedings of the Royal Society of London. Series A: Mathematical, Physical and Engineering Sciences*, 453(1959):853–877, 1997. doi:10.1098/rspa.1997.0047.

[139] P. Steinmann. On boundary potential energies in deformational and configurational mechanics. *Journal of the Mechanics and Physics of Solids*, 56(3):772–800, 2008. ISSN 0022-5096. doi:10.1016/j.jmps.2007.07.001.

[140] P. Steinmann. Geometrical foundations of continuum mechanics. *Lecture Notes in Applied Mathematics and Mechanics*, 2, 2015.

[141] P. J. Tackley. Self-consistent generation of tectonic plates in time-dependent, three-dimensional mantle convection simulations. *Geochemistry, Geophysics, Geosystems*, 1(8), 2000. doi:10.1029/2000GC000036.

[142] H. Tran and H. B. Chew. Cohesive zone interpretations of phase-field fracture models. *Journal of Applied Mechanics*, 89(12):121005, 10 2022. ISSN 0021-8936. doi:10.1115/1.4055660.

[143] V. Tvergaard and J. W. Hutchinson. The relation between crack growth resistance and fracture process parameters in elastic-plastic solids. *Journal of the Mechanics and Physics of Solids*, 40(6):1377–1397, 1992. ISSN 0022-5096. doi:10.1016/0022-5096(92)90020-3.

[144] V. Tvergaard and J. W. Hutchinson. The influence of plasticity on mixed mode interface toughness. *Journal of the Mechanics and Physics of Solids*, 41(6):1119–1135, 1993. ISSN 0022-5096. doi:10.1016/0022-5096(93)90057-M.

[145] United States. Department of the Army. Mathematics Research Center. and B. Seth. *Generalized Strain Measure with Application to Physical Problems*. United States. Department of the Army. Mathematics Research Center., 1964.

[146] A. Ural. Cohesive modeling of bone fracture at multiple scales. *Procedia Engineering*, 10:2827–2832, 2011. ISSN 1877-7058. doi:10.1016/j.proeng.2011.04.470.

11th International Conference on the Mechanical Behavior of Materials (ICM11).

[147] M. van den Bosch, P. Schreurs, and M. Geers. An improved description of the exponential xu and needleman cohesive zone law for mixed-mode decohesion. *Engineering Fracture Mechanics*, 73(9):1220–1234, 2006. ISSN 0013-7944. doi:10.1016/j.engfracmech.2005.12.006.

[148] M. van den Bosch, P. Schreurs, and M. Geers. A cohesive zone model with a large displacement formulation accounting for interfacial fibrilation. *European Journal of Mechanics - A/Solids*, 26(1):1–19, 2007. ISSN 0997-7538. doi:10.1016/j.euromechsol.2006.09.003.

[149] M. van den Bosch, P. Schreurs, and M. Geers. Identification and characterization of delamination in polymer coated metal sheet. *Journal of the Mechanics and Physics of Solids*, 56(11):3259–3276, 2008. ISSN 0022-5096. doi:10.1016/j.jmps.2008.07.006.

[150] C. V. Verhoosel and R. de Borst. A phase-field model for cohesive fracture. *International Journal for numerical methods in Engineering*, 96(1):43–62, 2013. doi:10.1002/nme.4553.

[151] J. Vignollet, S. May, R. De Borst, and C. V. Verhoosel. Phase-field models for brittle and cohesive fracture. *Meccanica*, 49:2587–2601, 2014. doi:10.1007/s11012-013-9862-0.

[152] W. Voigt. Ueber die beziehung zwischen den beiden elasticitätsconstanten isotroper körper. *Annalen der Physik*, 274(12):573–587, 1889. doi:10.1002/andp.18892741206.

[153] H. D. Wagner and R. A. Vaia. Nanocomposites: issues at the interface. *Materials Today*, 7(11):38–42, 2004. ISSN 1369-7021. doi:10.1016/S1369-7021(04)00507-3.

[154] J. Wambacq, J. Ulloa, G. Lombaert, and S. François. A dissipation-based path-following technique for the phase-field approach to brittle and ductile fracture. *International Journal for Numerical Methods in Engineering*, 122(15):3919–3940, 2021. doi:10.1002/nme.6687.

[155] J. Wambacq, J. Ulloa, G. Lombaert, and S. François. Interior-point methods for the phase-field approach to brittle and ductile fracture. *Computer Methods in Applied Mechanics and Engineering*, 375:113612, 2021. ISSN 0045-7825. doi:10.1016/j.cma.2020.113612.

[156] M. Wang and W. Ye. Size-dependent elastic field of nano-inhomogeneity: from interface effect to interphase effect. *Archive of Applied Mechanics*, 90(10):2319–2333, 2020. doi:10.1007/s00419-020-01722-2.

[157] M. Wheeler, T. Wick, and W. Wollner. An augmented-lagrangian method for the phase-field approach for pressurized fractures. *Computer Methods in Applied Mechanics and Engineering*, 271:69–85, 2014. ISSN 0045-7825. doi:10.1016/j.cma.2013.12.005.

[158] J. White and S. White. On the structure of grain boundaries in tectonites. *Tectonophysics*, 78(1):613–628, 1981. ISSN 0040-1951. doi:10.1016/0040-1951(81)90032-9. The Effect of Deformation on Rocks.

[159] T. Wick. Modified newton methods for solving fully monolithic phase-field quasi-static brittle fracture propagation. *Computer Methods in Applied Mechanics and Engineering*, 325:577–611, 2017. ISSN 0045-7825. doi:10.1016/j.cma.2017.07.026.

[160] T. Wick. An error-oriented newton/inexact augmented lagrangian approach for fully monolithic phase-field fracture propagation. *SIAM Journal on Scientific Computing*, 39(4):B589–B617, 2017. doi:10.1137/16M1063873.

[161] H. Wilbuer, H. Lammen, and J. Mosler. Phase field modeling with deformation-dependent interface energies. *PAMM*, 21(1):e202100114, 2021. doi:10.1002/pamm.202100114.

[162] H. Wilbuer, P. Kurzeja, and J. Mosler. Phase field modeling of hyperelastic material interfaces - theory, implementation and application to phase transformations. *Computer Methods in Applied Mechanics and Engineering*, 426:116972, 2024. ISSN 0045-7825. doi:10.1016/j.cma.2024.116972.

[163] A. Wojcik, E. Olejnik, A. Bigos, R. Chulist, P. Bobrowski, P. Kurtyka, A. Tarasek, N. Rylko, L. Szymanski, and W. Maziarz. Microstructural characterization and mechanical properties of in situ cast nanocomposites al/tic type. *Journal of Materials Research and Technology*, 9(6):12707–12715, 2020. ISSN 2238-7854. doi:10.1016/j.jmrt.2020.09.012.

[164] T. W. Wright. *The physics and mathematics of adiabatic shear bands*. Cambridge University Press, 2002.

[165] J.-Y. Wu. A unified phase-field theory for the mechanics of damage and quasi-brittle failure. *Journal of the Mechanics and Physics of Solids*, 103:72–99, 2017. ISSN 0022-5096. doi:10.1016/j.jmps.2017.03.015.

[166] J.-Y. Wu and V. P. Nguyen. A length scale insensitive phase-field damage model for brittle fracture. *Journal of the Mechanics and Physics of Solids*, 119:20–42, 2018. ISSN 0022-5096. doi:10.1016/j.jmps.2018.06.006.

[167] J.-Y. Wu, V. P. Nguyen, C. T. Nguyen, D. Sutula, S. Sinaie, and S. P. Bordas. Chapter one - phase-field modeling of fracture. 53:1–183, 2020. ISSN 0065-2156. doi:10.1016/bs.aams.2019.08.001.

[168] X.-P. Xu and A. Needleman. Numerical simulations of fast crack growth in brittle solids. *Journal of the Mechanics and Physics of Solids*, 42(9):1397–1434, 1994. ISSN 0022-5096. doi:10.1016/0022-5096(94)90003-5.

[169] X.-P. Xu and A. Needleman. Void nucleation by inclusion debonding in a crystal matrix. *Modelling and Simulation in Materials Science and engineering*, 1(2):111, 1993.

[170] Y. Yao, S. Chen, and D. Fang. An interface energy density-based theory considering the coherent interface effect in nanomaterials. *Journal of the Mechanics and Physics of Solids*, 99:321–337, 2017. ISSN 0022-5096. doi:10.1016/j.jmps.2016.12.009.

[171] S. Yin, Y. Gong, W. Li, L. Zhao, J. Zhang, and N. Hu. A novel four-linear cohesive law for the delamination simulation in composite dcb laminates. *Composites Part B: Engineering*, 180:107526, 2020. ISSN 1359-8368. doi:10.1016/j.compositesb.2019.107526.

[172] J. Yvonnet, A. Mitrushchenkov, G. Chambaud, Q.-C. He, and S.-T. Gu. Characterization of surface and nonlinear elasticity in wurtzite zno nanowires. *Journal of Applied Physics*, 111(12), 2012.

[173] W. Zhang, T. Wang, and X. Chen. Effect of surface/interface stress on the plastic deformation of nanoporous materials and nanocomposites. *International Journal of Plasticity*, 26(7):957–975, 2010. ISSN 0749-6419. doi:10.1016/j.ijplas.2009.12.002.

[174] L. Zhu and X. Zheng. Influence of interface energy and grain boundary on the elastic modulus of nanocrystalline materials. *Acta mechanica*, 213(3):223–234, 2010. doi:10.1007/s00707-009-0263-3.

Publication series of the Institute of Mechanics

published to date:

2010/01 Palnau, V.: Implementierung eines netzfreien Diskretisierungsverfahrens und seine Anwendung auf die Scherbandanalyse.
ISBN 978-3-921823-51-4

2010/02 Klusemann, B.: Application of homogenization methods and crystal plasticity to the modeling of heterogeneous materials of technological interest.
ISBN 978-3-921823-53-8

2011/01 Hortig, C.: Local and non-local thermomechanical modeling and finite-element simulation of high-speed cutting.
ISBN 978-3-921823-54-5

2011/02 Parvizian, F.: Modeling of microstructure evolution in aluminum alloys during hot extrusion.
ISBN 978-3-921823-56-9

2011/03 Noman, M.: Characterization and model identification for the simulation of the forming behavior of ferritic steels.
ISBN: 978-3-921823-55-2

2011/04 Kayser, T.: Characterization of microstructure in aluminum alloys based on electron backscatter diffraction.
ISBN: 978-3-921823-57-6

2011/05 Bargmann, S.: Computational modeling of material behavior on different scales based on continuum mechanics.
ISBN: 978-3-921823-58-3

2013/01 Waffenschmidt, T.: Modelling and simulation of adaptation and degradation in anisotropic biological tissues.
ISBN: 978-3-921823-61-3

2015/01 Ostwald, R.: Modelling and simulation of phase-transformations in elastoplastic polycrystals.
ISBN: 978-3-921823-66-8

2016/01 Subramanian, M.: Phenomenological modelling and simulation of ferroelectric ceramics.
ISBN: 978-3-921823-74-3

2016/02 Clausmeyer, T.: Evolution of plastic anisotropy in metals.
ISBN: 978-3-921823-76-7

2017/01 Holtermann, R.: Computational multiscale modelling of grinding processes.
ISBN: 978-3-921823-86-6

2017/02 Bartels, A.: Modelling of evolving microstructures at different scales.
ISBN: 978-3-921823-93-4

2017/03 Dusthakar Kumar Rao, D. K.: Computational modelling of single and polycrystalline ferroelectric materials.
ISBN 978-3-921823-94-1

2019/01 Buckmann, K.: Microstructure evolution in functional magnetic materials.
ISBN 978-3-947323-09-8

2019/02 Kaiser, T.: Computational modelling of non-simple and anisotropic materials.
ISBN 978-3-947323-14-2

2019/03 Heitbreder, T.: Modelling of material interfaces at different length scales.
ISBN 978-3-947323-18-0

2020/01 Berthelsen, R.: Computational homogenisation of thermomechanical problems.
ISBN 978-3-947323-19-7

2020/02 Sievers, C.: Describing the macroscopic behavior of surfaces based on atomistic models.
ISBN 978-3-947323-24-1

2022/01 Rose, L.: Optimisation based parameter identification using optical field measurements.
ISBN 978-3-947323-31-9

2023/01 Langenfeld, K.: Continuum modeling of brittle and ductile damage: theory and computational frameworks.
ISBN 978-3-947323-41-8

2023/02 Schulte, R.: Parameter identification approaches with application to different classes of materials.
ISBN 978-3-947323-45-6

2023/03 Kaiser, T.: Multiscale multiphysics material modelling.
ISBN 978-3-947323-46-3

2024/01 Noll, I.: Thermomechanical modelling and simulation of laser powder bed fusion processes.
ISBN 978-3-947323-49-4

2024/02 Witt, C.: Isogeometric analysis of anisotropic mechanical and electromechanical higher-gradient continua.
ISBN 978-3-947323-50-0

2025/01 Kurzeja, P.: Modeling, Control and Opportunities of Mechanical Interfaces Across the Scales.
ISBN 978-3-947323-51-7